Metal-organic framework-based photocatalysts for fuels production

Celia María Rueda Navarro

Supervised by:

Dr. Sergio Navalón Oltra

Dr. Hermenegildo García Baldoví

UNIVERSITAT POLITÈCNICA DE VALÈNCIA

Departamento de Química

Metal-organic framework-based photocatalysts for fuels production

DOCTORAL THESIS

Submitted by

Celia María Rueda Navarro

Supervisors

Dr. Sergio Navalón Oltra
Dr. Hermenegildo García Baldoví

València, November 2024

UNIVERSITAT POLITÈCNICA DE VALÈNCIA

Sergio Navalón Oltra, PhD in Chemical Engineering and Full Professor at the Universitat Politècnica de València (UPV) and Hermenegildo García Baldoví, PhD in Chemistry and Ramón y Cajal postdoctoral researcher at the UPV.

CERTIFY:

The work “Metal-organic framework-based photocatalysts for fuels production” has been developed by Celia María Rueda Navarro under their supervision at the Departament de Química of the Universitat Politècnica de València, as a Thesis Project to obtain the degree of PhD.

Dr. Sergio Navalón Oltra

Dr. Hermenegildo García Baldoví

“To attain freedom in the world of nature, man must use knowledge to build, in collaboration with nature, a better environment”

Report of the United Nations Conference on the Human Environment.
Sweden, **1972**

“*You must unite behind the science. You must take action. You must do the impossible. Because giving up can never ever be an option*”

Greta Thunberg, **2019**

Acknowledgements

I would like to express my deepest gratitude to everyone who has played a role throughout my PhD journey. I would like to mention some of the people that has surrounded me during this intense period of 4 years, apart from thanking them, just not to forget their names in the future to be able to contact them even if time goes by.

Firstly, to the people from my lab, starting from Sergio Navalón for giving me the opportunity of starting the PhD four years ago. And moreover, for his guidance and commitment during the research. And to Herme G. Baldoví, for creating a good environment and for his guidance in the laboratory. Moorthy, for his dedication with the projects even if they are not for him. Thanks to the colleagues in my current laboratory for all the nice experiences that have given me, and especially for the support this last period just before the stay and while staying abroad (they are always willing to help when it is necessary): Antón López, who usually seems calm to the outside but in deep he is always running out of time; Juanjo Ramírez, who has reached the top of his collagen production at this stage; Maykel De Miguel, the reporter and fix everything of the group, helped to build up everything by Vitor Fernandes; and Marta González, for her commitment even when she is not feeling perfectly; Inés Saiz, that I hope she is ideally in Mallorca visiting Joan Truyols. The recently incorporated as PhD students: Joan García and Athenea. Miguel, who had been around before María Nóvoa left to her home. I would like to mention also some more people who have already left the lab as the talkative future pharmacist Cristina Vallés; the international researcher Arianna Melillo; Eva Montero, who was here when I had just entered the lab, and her sister

Ana Montero. The people who had been in the lab during several months like Sergio Valverde; the ones who were also my students Nieves and Pedro; Andrea Parreño who is happily back in CS; Andrea, who came back from Belgium; the italians Emanuela and Fátima; and the responsible for the water of the city the named Paco Aguas.

I would like to mention as well some of the people who were around in the department that had been present during these years: firstly, mention the people who had been on the left side of the lab during these years who have been a very great company for the breaks: Dani Álvarez, Jorges: Herrera and Castellanos, Lorena Tamarit, Angie, Ainhoa, Pilar, Mery, Alejandro. And for the rest of the department, starting with Manolo for letting us share the office, the lab technicians Enrique and Susana, the cleaner Concha, the secretary people (María, for her commitment of doing everything as soon as possible, Pilar, Inma), people from the IDM group, especially the ones participating in the padel tour; the teachers: José Luis López, for his help with the lab practices; Raúl Pérez, Luis Villaescusa and Ignacio Vayá, for their presence when the coffee machine was in the second floor; Chelo, Inma, Loles, Elena, etc. Belén Ferrer and Mercedes Álvaro, who are part of the group. And also, I will mention people from the same group being at the ITQ: Firstly, Hermenegildo García, boss of the HG-Energy group, whose presence causes respect in everybody; ITQ members (or old ones): Amparo, Esther, María Cabrero, Alberto, Rubén, Andrés, Jonas, Horatiu, Adbe, Dawid, Kevin, Aisha, Adrián, Jiajun, Elena, Ana, Yong, Manuel, Sara, Sabine. I would also like to thank ITQ technicians: XRD (Jose Luis); XPS (Dolo); BET, TGA (Maribel, Amparo); UV (Mª Jesús); Raman (Adelina); solid NMR (Alejandro). More people contributing in the present thesis were the microscopy technicians (Manolo, Alicia, Merche, etc.), and the responsible for first assembling the

reactors, José Gaona. A small part of the thesis was also developed in the CPI, meeting Pedro Atienzar, Roberto and Elena.

And I would like to mention the people that were in Caen who were very kind with me since the beginning of my stay doing pellets and giving me an everyday life differently but very great: Especially to Zahraa, Akash Nath, Sina, Chunzheng Wang, Taha, Rayanne, Mohamad, Marco Daturi, Marco Fabbiani, Adisak, Joël, Pedram, Jihane, Ying, Edwin, Selua, Abdallah, Jaouad, Fatim, Ali, Maya, Mathias, Pascal, Elisabeth, Shadi and a long etc.

I would like to thank all the collaborators of the published papers during these years, from inside the UPV: Pedro Atienzar, and Ignacio Vayá; from the UV: Paula Escamilla and the technicians Chema and Gloria from the EPR; from UPV/EHU: Virginia Martínez-Martínez, Raúl Montero and Asier Longarte; and three parts of France, from Montpellier: Valentín Díez-Cabanes, Dong Fan, Guillaume Maurin, and from Caen: Zahraa Abou Khalil, Mohamad El-Roz, Marco Daturi, Philippe. And from París: Bingbing Chen, Georges Mouchaham, Christian Serre.

Finally, I want to recognise that being part of the UPV has given me the opportunity to access lots of activities during these years, meeting a lot of wonderful people in all of them, from young people starting their degree, passing to people as me doing the PhD and to titular teachers or workers of the university, making the stressful days when experiments do not work as they might, easily.

P.S. I would like to say as well that the people I have met living in this city, as well as my lifemate, my family and my friends, have been very nice company and support for all these years.

Style

This doctoral thesis assembles a collection of three published journal research articles, organized into seven chapters and an annexure. In Chapter 1, a literature review explores current energy challenges, emphasizing the generation of solar fuels from H_2O and CO_2 using inorganic semiconductors and metal-organic frameworks as heterogeneous photocatalysts. Chapter 2 outlines the objectives addressed in this work. Chapters 3, 4, and 5 present the photocatalytic results obtained and published, indicating the author's contribution in each case. They also present separate supporting information and bibliography. Chapter 6 summarizes the conclusions drawn from the preceding chapters, and Chapter 7 provides an overview of the thesis, firstly in English and then, in the two official languages of the university where the thesis is developed. The annexure compiles the list of publications and conferences derived from this thesis as well as the information of the international research stay carried out by the PhD candidate.

Abbreviations and Acronyms

AA	Acetic acid
AM	Air mass
AQY	Apparent quantum yield
BET	Brunauer−Emmett−Teller
BDC	1,4-benzene-dicarboxylate
CC BY 4.0	Creative Commons Attribution 4.0 International
CC BY-NC-ND 4.0	Creative Commons Attribution. NonCommercial-NoDerivatives. 4.0 International
CC BY-SA 2.0 DE	Creative Commons Attribution-ShareAlike 2.0 Germany
CCDC	Cambridge crystallographic data center
CCSU	Carbon capture, storage and utilisation
CT	Charge transfer
COF	Covalent organic frameworks
COP	Conference of the Parties
DF-STEM	Dark-field scanning transmission electron microscopy
DFT	Density functional theory
DMF	N,N-dimethylformamide
DRS	Diffuse reflectance spectroscopy
e^-	Electron
Ea	Activation energy
EDX	Energy-dispersive X-ray
EIS	Electrochemical impedance spectroscopy
EPR	Electron paramagnetic resonance
Eq.	Equivalents

fs-TAS	Femtosecond transient absorption spectroscopy
FT-IR	Fourier transform-infrared spectroscopy
FTO	Fluoride-doped tin oxide
GC	Gas chromatography
GC-MS	Gas chromatograph coupled to mass spectrometer
GO	Graphene oxide
h^+	Hole
HER	Hydrogen evolution reaction
HOCO	Highest occupied crystal orbital
HPLC	High-performance liquid chromatography
HR-SEM	High-resolution scanning electron microscopy
HR-TEM	High-resolution transmission electron microscopy
ICP-OES	Inductively coupled plasma optic emission spectroscopy
LFP	Laser flash photolysis
LMCT	Ligand-to-metal charge transfer
LSV	Linear sweep voltammetry
LUCO	Lowest unoccupied crystal orbital
MIL	Materiaux de l'Institute Lavoiser
MMCT	Metal-to-metal charge transfer
MOFs	Metal-organic frameworks
NBu_4PF_6	Tetrabutylammonium hexafluorophosphate
NHE	Normal hydrogen electrode
NTO	Natural transition orbital
NP	Nanoparticle
OER	Oxygen evolution reaction
OWS	Overall water splitting

PL	Photoluminescence
PSM	Post-synthetic modification
PXRD	Powder X-Ray Diffraction
QDs	Quantum dots
RDS	rate-determining step
SBU	Secondary inorganic building units
SEM	Scanning electron microscopy
STH	Solar-to-hydrogen
TAS	Transient absorption spectroscopy
TD-DFT	Time-dependent DFT
TD-DFPT	Time-dependent density functional perturbation theory
TEM	Transmission electron microscopy
TEOA	Triethanolamine
TFA	Trifluoroacetic acid
TGA	Thermogravimetric analysis
THF	Tetrahydrofuran
UiO	Universitet i Oslo
US	United States
UV-Vis DRS	UV–vis diffuse reflectance spectroscopy
XPS	X-ray photoelectron spectroscopy
ZPE	Zero-point energy
τ	Lifetime
λ	Wavenumber

Index

Chapter 1. Introduction

1.1 Fossil fuels and climate change

The present energy demand is estimated to be around 165,000 TWh worldwide and is increasing by about 1-2 % each year[1], although this demand differs considerably from one country to another, as can be seen in Figure 1.

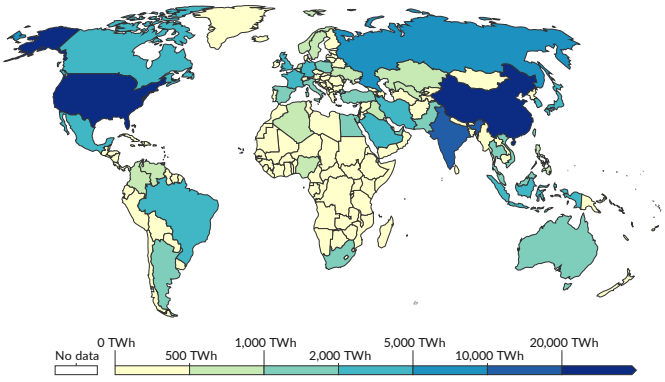

Figure 1. Energy consumption in 2022 by different countries worldwide. Licensed under CC BY 4.0 from ref.[2]

Fossil fuels were discovered as a new energy resource during the Industrial Revolution and have been the essential driver of technological, social, economic and other advances[3], despite emitting large amounts of CO_2, the greenhouse gas considered to be the main contributor to global warming and climate change[4]. Conventional fuels like coal, oil and gas have dominated global energy systems and continue to be intensively used[5, 6]. Figure 2 shows the evolution over time of the different fuel sources in global energy consumption.

It is widely accepted that climate change causes significant and long-lasting changes in the Earth's climate patterns and is primarily driven by human activities such as burning fossil fuels in different sectors like producing automobiles, power plants, deforestation to clear land for agriculture, building

and many other industrial processes[7,8]. These activities increase the atmospheric greenhouse gas concentrations such as CO_2, in the atmosphere. The heat trapped in these gases raises global temperatures, a phenomenon commonly referred to as global warming, which is currently more than ten times faster than it was at the end of the last Ice Age, marking the fastest sustained global natural change on record[8].

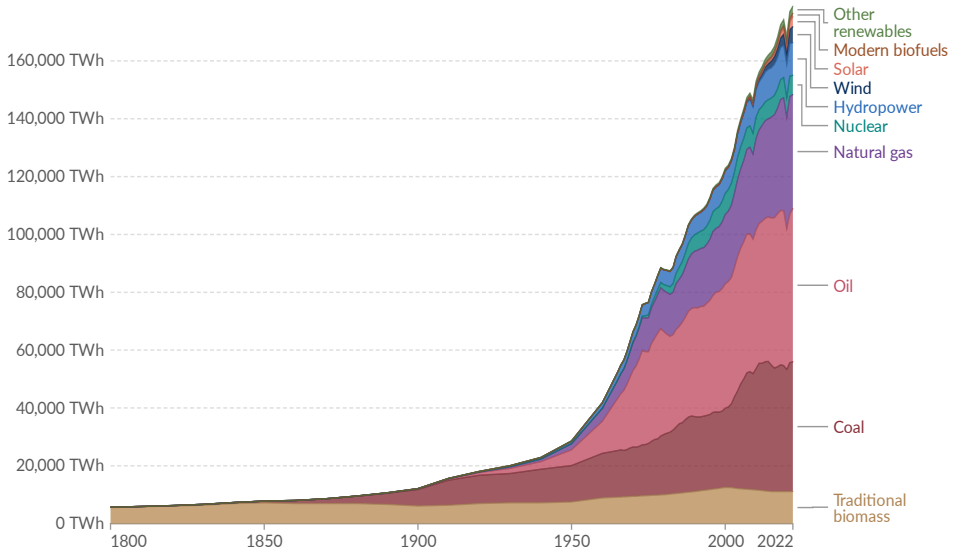

Figure 2. Global energy consumption by source. Licensed under CC BY 4.0 from ref.[9]

Some of the consequences of climate change have already been confirmed. The Earth's average surface air temperature has risen by about 1°C since 1900[7]. Both the lower atmosphere and the upper layers of the ocean have warmed up, while the snow and ice coverage in the Northern Hemisphere is declining, Greenland's ice sheet is shrinking, sea levels are rising and forests all over the world are facing climatic challenges, including storms, droughts, flash floods and heavy rainfall[8]. Climate change induces specific alterations in the typical structure and functions of ecosystems[10]. The urgency of the situation is also

confirmed by climate models, which show that if CO_2 emissions are not stopped, the temperature will continue to rise exponentially (Figure 3). The National Aeronautics and Space Administration (NASA) has confirmed that 2023 was the warmest year on record[11] and registered the highest summer temperatures in the last 2,000 years[12].

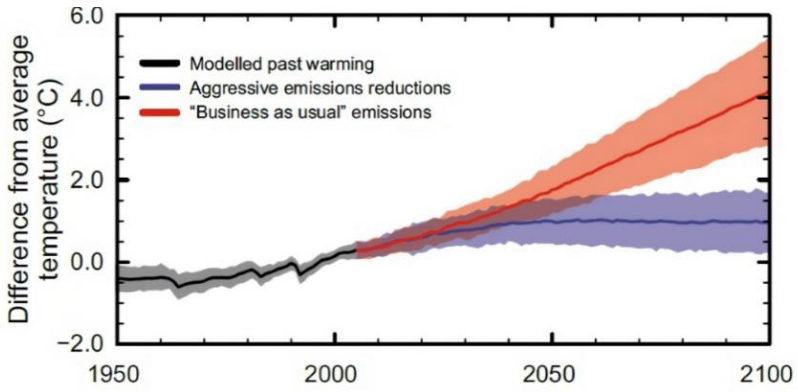

Figure 3. Rate of warming modelled for the 21st century in two different scenarios. Figure adapted with permission from ref.[7]

Direct CO_2 measurements in the atmosphere and from air trapped in ice have shown that human activity has a significant impact on the rise in temperature. These measurements indicate that atmospheric CO_2 levels have increased by over 40 % since 1800[7]. The rise in atmospheric CO_2 concentrations is mainly from burning fossil fuels, as confirmed by the analysis of carbon isotopes. Isotopes from burning fossil fuels are known to have low ^{13}C and no ^{14}C fractions, confirming that the rise in temperature is mainly due to human activities[13].

As the current rate of climate change is faster than ever, this makes it harder for society and natural ecosystems to adapt. Recent estimates indicate that the average global temperature has increased by 1 °C since the end of the last Ice Age, a change that has taken place over about 7,000 years, while atmospheric CO_2

levels have risen by more than 40 % in only the past 200 years, with much of this increase occurring since the 1970s[7].

In view of these alarming facts, governments all over the world agree on the need to be aware of natural cycles. Environmental concerns were first raised in a conference in Sweden in 1972 by a few countries, including Spain[14]. A second conference was held in Rio 20 years later, but it was not until 1995 that the Conferences of the Parties (COP) was created in the United Nations Framework Convention on Climate Change, agreed to hold an annual conference with the aim of enforcing a commitment to reducing greenhouse gas emissions and curbing global warming. In the Kyoto Protocol, drafted in 1997, Article 3 aimed to reduce total gas emissions of CO_2, CH_4, hydrofluorocarbons, perfluorocarbons, N_2O, and SF_6 by at least 5 % below the 1990 levels over the period from 2008 to 2012[15]. At the COP 21 in 2015 a legally binding international treaty, known as the *Paris Climate Agreement* was adopted to make an effort to limit the rise in temperature to 1.5 ^oC above pre-industrial levels[16, 17]. In 2019, the *Chile-Madrid Time to Act* agreement aimed to motivate all the participating nations to intensify their efforts in addressing climate change. In the last COP held in Dubai in 2023 it was decided to reduce net CO_2 emissions to zero by 2050. A significant number of countries are now committed to addressing climate solutions. Figure 4 shows a comparison of the CO_2 emitted by different countries over a period of time[18].

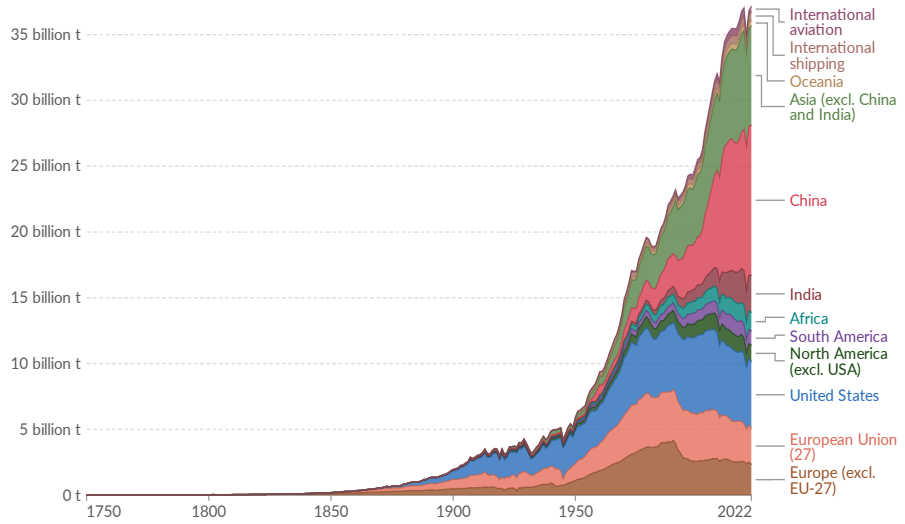

Figure 4. Annual CO_2 emissions from fossil fuels and industry by different world regions and separately some ways of transportation. Figure licensed under CC BY 4.0 from ref.[18]

1.2 Circular carbon economy

Worldwide anthropogenic emissions of CO_2 up to 2023 were about 37.4 billion tons[19, 20]. The goal of net-zero emission of CO_2 by 2050 is hoped to be achieved by the so-called circular carbon economy by applying the '4R' solutions[21]: (1) Reduce carbon emissions by enhancing energy efficiency and adopting clean energy sources like solar and wind power. (2) Reuse the captured CO_2 to provide valuable products such as fuels, CH_3OH or fertilizers. (3) Recycle biological systems by naturally recycling carbon; plants absorb CO_2 and release it when decomposing, while bioenergy crops can be harvested for energy. (4) Remove CO_2 from the atmosphere by capturing and storing carbon or using natural processes like reforestation.

Green H_2 (Section 1.3.1) stands at the forefront of the circular carbon economy. The scheme of an example for a potential sustainable plant for generating H_2 and

using CO_2 is given in Figure 5. This technology combines solar energy with water to perform solar water splitting to obtain H_2, which is reacted with CO_2 to produce solar fuels such as CH_3OH and other products. One of the foremost challenges in achieving these goals is to develop efficient and cost-effective water decomposition on a scale that can meet global energy demands.

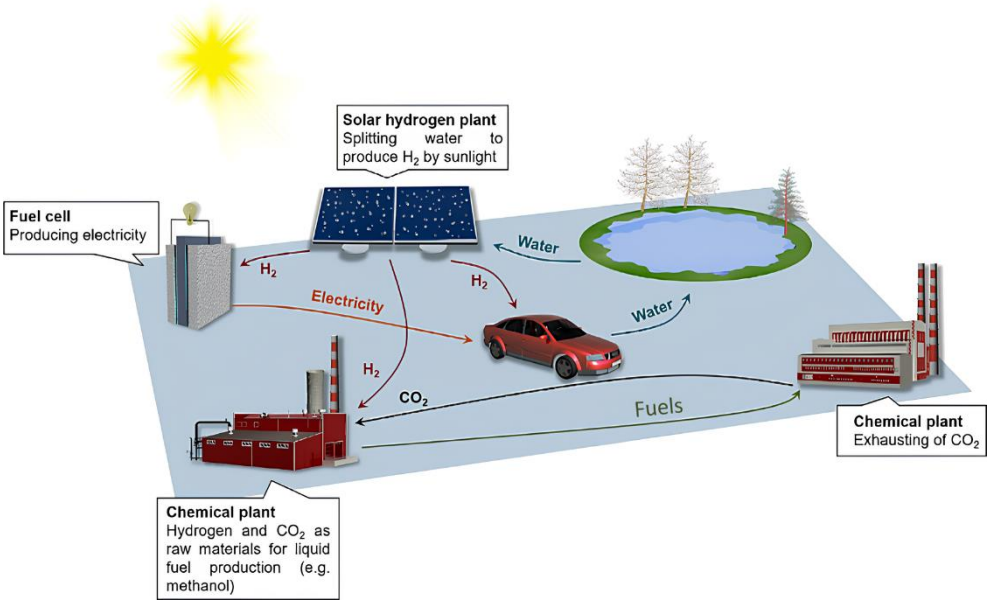

Figure 5. Sustainable plant for H_2 production and CO_2 reduction. Adapted with permission from ref.[22] Copyright 2020, American Chemical Society.

Despite green H_2's promise of a sustainable future, there are a series of critical short-term steps that must be addressed to mitigate the climate impact, the immediate priority being effective carbon dioxide capture and storage[21]. To achieve these goals, several complementary actions will have to be carried out. In the context of CO_2 use, different CO_2 transformation processes will have to be evaluated, including chemical, electrochemical and photochemical reduction processes, biological conversions, reforming and inorganic transformations[23]. Another possibility is to increase the use of renewable energy sources, which are still far from being able to satisfy the world's energy requirements. The

importance of enhancing energy efficiency, meeting the high energy demand and reducing fossil fuel consumption must be recognized in fields as varied as agriculture, industry, forestry, transport and land use[24]. All of these are crucial for mitigating the undesirable effects of CO_2, global warming and global climate change, which have a great impact on ecosystems, human health and the global economy.

1.3 Solar fuels

In the search for renewable, non-polluting and cost-efficient energy sources, fuels in the form of chemical energy vectors from solar energy[25] have been identified as a promising alternative. The idea of using artificial systems to mimic natural photosynthesis and generate fuels from CO_2 and H_2O using only sunlight as an energy source dates back to the 1970s. This concept has inspired active global research efforts to turn this idea into reality and lay the foundations of a solar fuels industry[26]. These fuels are chemical compounds generated from solar energy using photochemical, photobiological, photothermal and photoelectrochemical processes[27] and ideally allow renewable energy to be stored in an energy carrier such as H_2 for later use as a power source.

However, despite its detrimental effect on the global climate, CO_2 could still be an effective building block for generating valuable fuel compounds through reductive reactions like formic acid, CH_3OH,[28] CH_4,[29] among others. Although CH_4 is a powerful greenhouse gas and, after CO_2, the second largest contributor to global climate change[29], it is also a high energy density fuel. So developing technologies to convert CO_2 into solar fuels from renewable energy sources or through the so-called artificial photosynthesis[30] could help to reduce the dependence on non-renewable fossil fuels over time[16].

1.3.1 Hydrogen

H_2 is an attractive molecule as an energy vector due to its high mass-specific energy density, water emissions on combustion, and its versatility for use in various applications. H_2-based fuel cells and other storage systems are gaining increasing importance for large-scale exports. For instance, H_2 can be used to store energy on both the utility and residential scales, as fuel for fuel-cell electric vehicles, heavy-duty transport[31] and for producing chemicals (e.g. NH_3, CH_3OH)[32].

One of the main limitations of H_2 from renewable sources is its high cost of production. In 2022, these technologies represented less than 1 % of global H_2 production[32]. In 2020, the US Department of Energy set a target price of 2 $/kg H_2 by 2026[33]. In the same year, the European Union launched the European Clean Hydrogen Alliance with the aim of installing at least 40 GW of renewable H_2 electrolysers by 2030[34]. H_2 is, at present, primarily produced through the steam reforming of hydrocarbons at high temperatures and pressures[35], or the so-called *grey H_2*, which does not implement carbon capture and storage processes. However, more sustainable methods like water electrolysis technologies are under study but are still costly due to their energy requirements[36]. The key for generating net-zero CO_2 when producing H_2 is by obtaining green H_2 with free-carbon emissions through water electrolysis using renewable sources like sun- or wind-power to generate electricity. Some of the most promising technologies for green H_2 production are included in Figure 6[37]. Photovoltaic-electrolysis and photoelectrochemistry have reached a solar-to-hydrogen efficiency of up to 30 and 20 %, respectively[38, 39]. However, the problem of scaling up is difficult due to the high material and manufacturing costs[40]. The most promising technique that stands out for its cost-efficiency and commitment to zero waste discharge[41], which will be described here in depth, is therefore photocatalysis. There are also

other methods under study for producing light-assisted green H_2, such as solar thermochemical water splitting, photothermal catalysis and photobiological H_2 production[37].

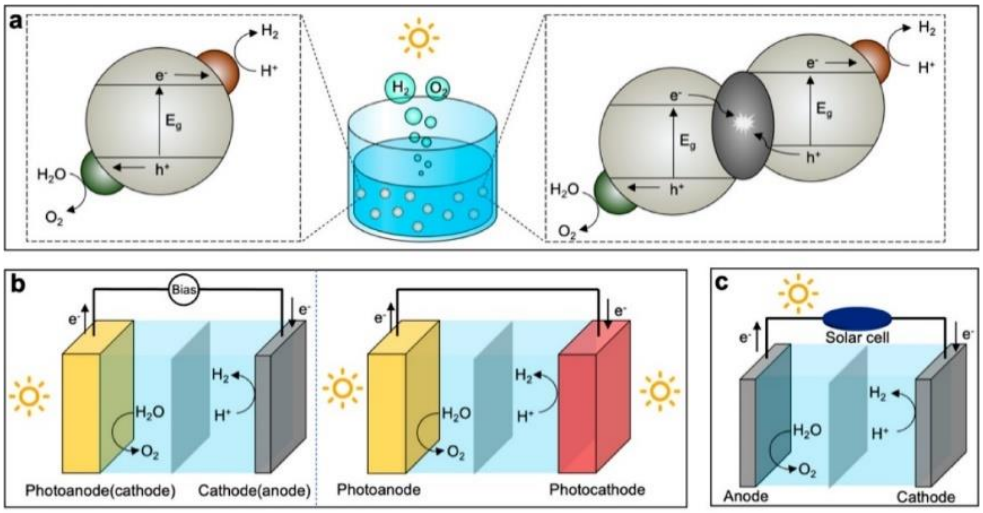

Figure 6. Solar-driven H_2 production approaches: (a) photocatalytic, (b) photoelectrochemical, (c) photovoltaic–electrochemical. Figure adapted from ref.[37] and licensed under CC BY 4.0.

Nonetheless, for H_2 to truly become the fuel of the future, significant progress in advanced green H_2 production technologies and establishing supportive energy policies are crucial[42].

1.3.2 CO_2 as solar fuel precursor

Converting CO_2 into added value chemicals and fuels is an important step in the process of mitigating the negative impact of this greenhouse gas in the environment. Some techniques for using CO_2 include its conversion to chemical feedstock, mineralization, direct use of synthesis of polymers and enhanced oil recovery, building materials and biofuels[43,44]. For instance, one of the key aspects in converting CO_2 into a biofuel will be to use H_2O as the reducing agent. However,

water oxidation to oxygen is a kinetically and thermodynamically demanding process that greatly hampers the overall efficiency of the process[40]. Alternatively, CO_2 hydrogenations involve a series of thermodynamically exothermic and spontaneous reactions with considerable kinetic challenges, such as the high activation energy (Ea) barrier in reducing CO_2 into C_1 fuel products like CH_4[29], CH_3OH[28], CO and HCOOH and even more into C_{2+} products. These reactions are outlined below together with their reduction potential relative to the normal hydrogen electrode (NHE)[45].

$CO_2 + 8H^+ + 8e^- \rightarrow CH_4 + 2H_2O$, $E^0 = -0.24$ V

$CO_2 + 6H^+ + 6e^- \rightarrow CH_3OH + H_2O$ $E^0 = -0.38$ V

$CO_2 + 2H^+ + 2e^- \rightarrow CO + H_2O$ $E^0 = -0.53$ V

$CO_2 + 2H^+ + 2e^- \rightarrow HCOOH$ $E^0 = -0.61$ V

As the average bond energy of C=O bond in CO_2 is 805 kJ mol^{-1}, these transformations require high reaction temperatures and the presence of catalysts[46]. CH_3OH is considered to be the most promising product of CO_2 conversion as it is a liquid energy carrier with a high energy density, making it easy to transport and store. CH_3OH can be used as a source of energy, as a chemical feedstock and as a raw material for synthesizing alcohols and gasoline[47], although efficiently and selectively transforming CO_2 into CH_3OH is a challenging reaction typically carried out at high temperatures (i.e. 300 – 350 °C) and pressures (i.e. 20-40 bar)[48, 49]. Alternatively, selective CO_2 hydrogenation to CH_4, a process also known as the Sabatier reaction, can be carried out under relatively milder reaction conditions, especially by using noble metal-based co-catalysts[50]. The obtained synthetic CH_4 also known as synthetic natural gas can be directly used as a fuel in existing natural gas facilities. CO_2 can be converted into CH_4 by

several methods, including oxidation-reduction, esterification, reforming and reverse-water gas shift reaction. 400-500 °C are typical hydrogenation reaction conditions with non-noble metal co-catalysts such as Ni, while lower temperatures (i.e. 250-350 °C) can be used with RuO_x nanoparticles (NPs), and even lower by using the high-cost Rh species (i.e. 160 – 220 °C)[51,52,53]. In addition, photocatalytic solar-driven CO_2 reduction, is attracting increasing interest. In this process, the temperature can be reduced to 200 °C and the pressure to < 2 atm[52], while achieving similar results to analogous thermocatalytic processes.

1.4 Heterogeneous photocatalysis

1.4.1 Fundamentals

Reactants and catalysts co-exist in different phases in heterogeneous catalysis, typically with the catalyst in a solid and the reactants in liquid or gas form. This biphasic system often impedes the reactants from accessing the active center due to mass transfer limitations. This reduces catalytic activity and needs more severe reaction conditions, such as higher temperatures or pressures than homogeneous catalysis, in which the substrates and catalysts are in the same phase[54]. However, most industrial catalytic processes use heterogeneous catalysts, whose solid state and increased stability make them easily recyclable and enhance their efficiency and appeal for industrial applications[55]. Catalyst efficiency is then generally studied in greater depth by evaluating its catalytic activity, selectivity and stability over time under various reaction conditions[54].

In inorganic semiconductors, band theory is essential to understand their electronic properties. Atoms are densely packed, causing their atomic orbitals to overlap and form energy bands. The valence band, filled with electrons, and the

conduction band, packed with empty electronic states. As can be seen in Figure 7a, these bands overlap in metals, allowing free electrons to conduct electricity by applying an external electric field. For semiconductors and insulators, a band gap separates the valence band from the conduction band. The primary difference between these materials is their band gap values, semiconductors commonly have a band gap value of less than about 3 eV, while the band gap for insulators is typically above 3 eV. However, there are some exceptions, like anatase TiO_2, which has a band gap of 3.2 eV and is considered a semiconductor[56]. This variation in band gap value for different metal oxides (Figure 7b) has a significant impact on their electrical conductivity[57].

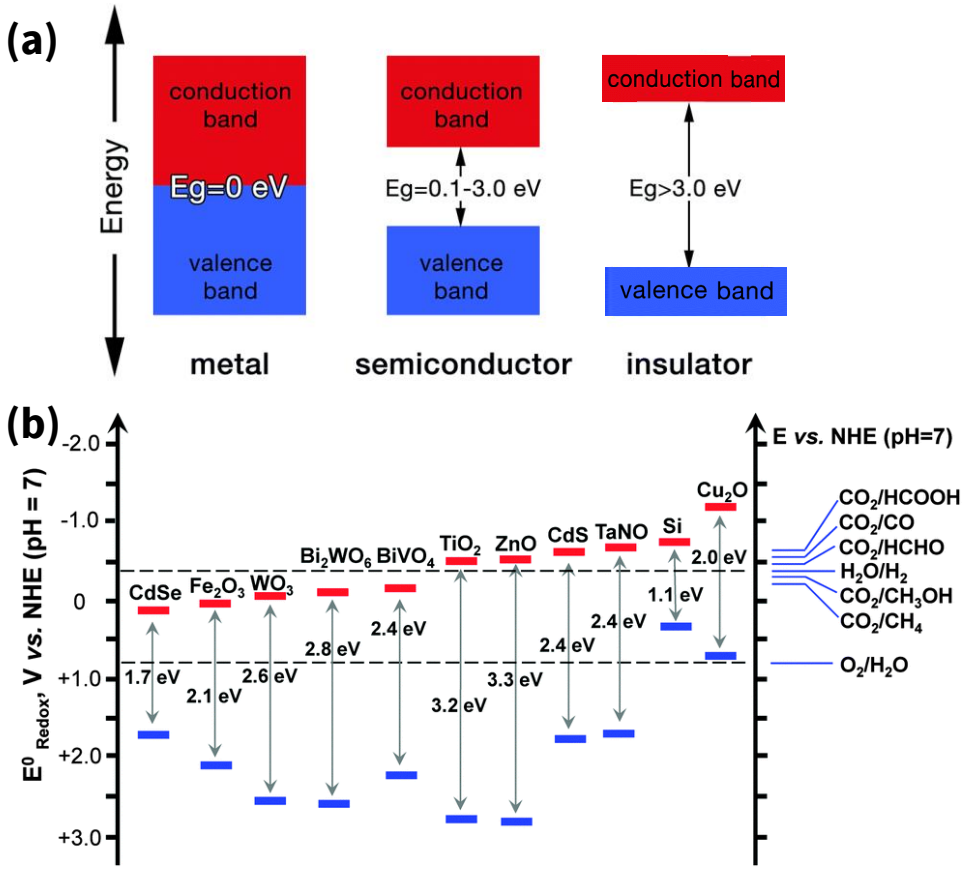

Figure 7. Energy band diagram for (a) in general conductors, semiconductors and insulators, and (b) different materials mainly metal oxides. Reproduced with permission from ref.[58, 59]

Heterogeneous photocatalysis could be described as a process in which a photocatalyst absorbs light with enough energy to generate reactive electron-hole pairs that facilitate chemical reactions on the photocatalyst's surface. This process has been typically used for environmental remediation and energy conversion[60]. It includes several steps (Figure 8a): (1) Absorption of photons with equal or higher energy than the semiconductor band gap. (2) Photoexcitation, leading to the separation of charges with an electron moving from the valence band to the conduction band of the semiconductor. (3) Migration of charge

carriers to the surface of the particle. (4) Reduction reaction, which takes place with photogenerated electrons and oxidation reaction occurring in the positive holes. Recombination of charges in the bulk (5a) or on the particle surface (5b).

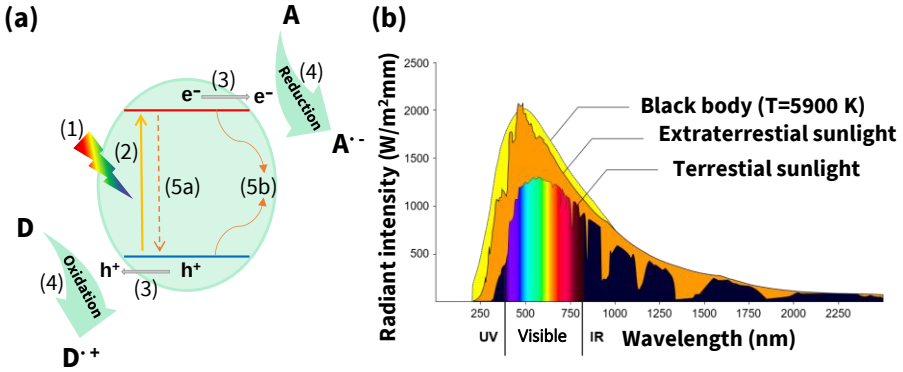

Figure 8. (a) Elemental steps occurring in a photocatalytic reaction. A is an electron acceptor and D an electron donor. (b) Standard solar radiation spectrum. Adapted from ref.[61] Licensed under the CC BY-SA 2.0 DE.

Despite decades of research since the discovery of ultraviolet-irradiated TiO_2 an efficient and economically viable photocatalyst has not been developed to generate H_2 in natural sunlight irradiation. A major limitation of TiO_2 and other inorganic semiconductors is their poor absorption of light above 380 nm, resulting in low efficiency under sunlight irradiation. The most important aim of developing heterogeneous photocatalysts that can absorb visible light, achieve efficient charge separation and have the appropriate energy band level diagram to accomplish the thermodynamic requisites of the redox reactions has still not been achieved. As most of the inorganic semiconductors do not meet all these criteria[62], there is a considerable interest in developing techniques to modify these materials to accomplish these requisites. It should be noted that the solar spectrum consists (Figure 8b) of roughly 4 % ultraviolet-visible light (290- 80 nm), 43 % visible light (380-780 nm) and 53 % infrared light (780- 2500 nm)[63].

One area of research focuses on developing visible-light responsive metal oxide photocatalysts, such as $BiVO_4$, α-Fe_2O_3, Bi_2WO_6, WO_3, and metal sulfides like CdS and Bi_2S_3[64]. These photocatalysts' efficiency in producing solar fuel still remains far from practical applications. Another widely used strategy to increase photocatalytic efficiency consists of modifying it by incorporating various co-catalysts such as metal or metal oxide NPs[65]. These NPs supported in the photocatalyst not only act as co-catalysts but also partially avoid electron-hole recombination by accumulating the photogenerated charge carriers. Also, metal substitution to create bimetallic assemblies has proven to be an effective method of improving the performance of inorganic semiconductors. In these cases, the metal used can serve as an electron mediator, facilitating metal-to-metal charge transfer (MMCT) and thereby promoting photocatalysis[66].

1.4.2 Efficiency of photocatalytic process

The activity of the photocatalytic reaction is usually measured by product yields (micro- or millimoles) per unit mass of a photocatalyst or per unit mass of the photocatalyst and time. However, the product yields are not directly proportional to the mass, so that for an appropriate comparison the mass used during the experiment should be indicated in each case. Other factors that greatly influence photocatalytic performance are the experimental setups themselves and the reaction conditions used (e.g. type of reactor, temperature, power and wavelength of the irradiation source). It is therefore essential to accurately describe all the experimental conditions of the reaction.

Several metrics such as quantum efficiency $\left(\frac{number\ of\ reacted\ electrons}{number\ of\ photons\ absorbed}\right)$ are used to evaluate the activity. However, as it is difficult to measure the absorbed

photons in heterogeneous photocatalysts, an alternative indicator commonly cited in the literature is the apparent quantum yield (AQY) $\left(\frac{number\ of\ reacted\ electrons}{number\ of\ incident\ photons}\right)$. Particular metrics have been used to compare the different research works conducted on solar fuels, such as solar-to-fuel, or particularly solar-to-hydrogen (STH) applied to processes that use only water as the H_2 source[22,37,67].

1.4.3 Photocatalytic water splitting

Regarding the thermodynamics of a photocatalytic process, the photocatalyst's valence and conduction band edge should ideally align with the redox potentials. In water splitting reactions, the valence band energy must be at a more positive potential than that of the oxygen evolution reaction (OER) (E^0 = +1.23 V_{RHE})[13], $H_2O \leftrightarrow 2H^+ + 1/2O_2(g) + 2e^-$; and the conduction band energy should be lower than that of the hydrogen evolution reaction (HER) (E^0 = 0 V_{RHE}), $2H^+ + 2e^- \leftrightarrow H_2(g)$. The reduction and oxidation of water start at 0 V_{RHE} and +1.23 V_{RHE}, respectively, meaning that the overall water splitting reaction can start from 1.23 V[68]. From the practical point of view however an overpotential (i.e. 0.4 – 0.6 V) is needed. To properly understand the process, it is very important to know the timescales of the steps in the reaction (example in Figure 9a). The initial photoinduced charge separation happens on the femtosecond timescale in the linker region, leading to charge separation. This is followed by rapid, unwanted electron-hole recombination at the charge separation site or after charge carrier migration on the picosecond to millisecond timescale. The chemical reaction is relatively slow in comparison to these processes, taking place on a time scale from hundreds of picoseconds to microseconds[62, 69], since photocatalytic overall water splitting (OWS) presents significant challenges due to the strong and stable

O-H bonds, while the reaction is thermodynamically unfavorable with a free energy of ΔG = +237 kJ mol^{-1}.[70] In addition, the OWS back reaction is a thermodynamically favored reaction, as can be seen in Figure 9b, and a co-catalyst is required to improve the reaction (Figure 9c). While numerous articles on H_2 production have used sacrificial agents, which are expensive chemicals such as CH_3OH and triethanolamine (TEOA)[71], there has recently been an increasing number of studies on alternative biomass feedstocks for hydrogen production[72]. Some studies also highlight the possibility of using biowaste photoreforming as a promising addition to the portfolio of sustainable hydrogen production technologies, offering competitive H_2 production rates and sustainable operation lifetimes for future development[73].

Some of the recently reported active materials and their metrics can be briefly described as follows: in the case of photocatalytic HER, an AQY up to 93 % has been reported for H_2 evolution under visible light irradiation (420 nm) using Na_2S/Na_2SO_3 as the sacrificial electron donor in the presence of Pt-PdS/CdS as photocatalyst (with less than 1 wt % Pt loading)[75].

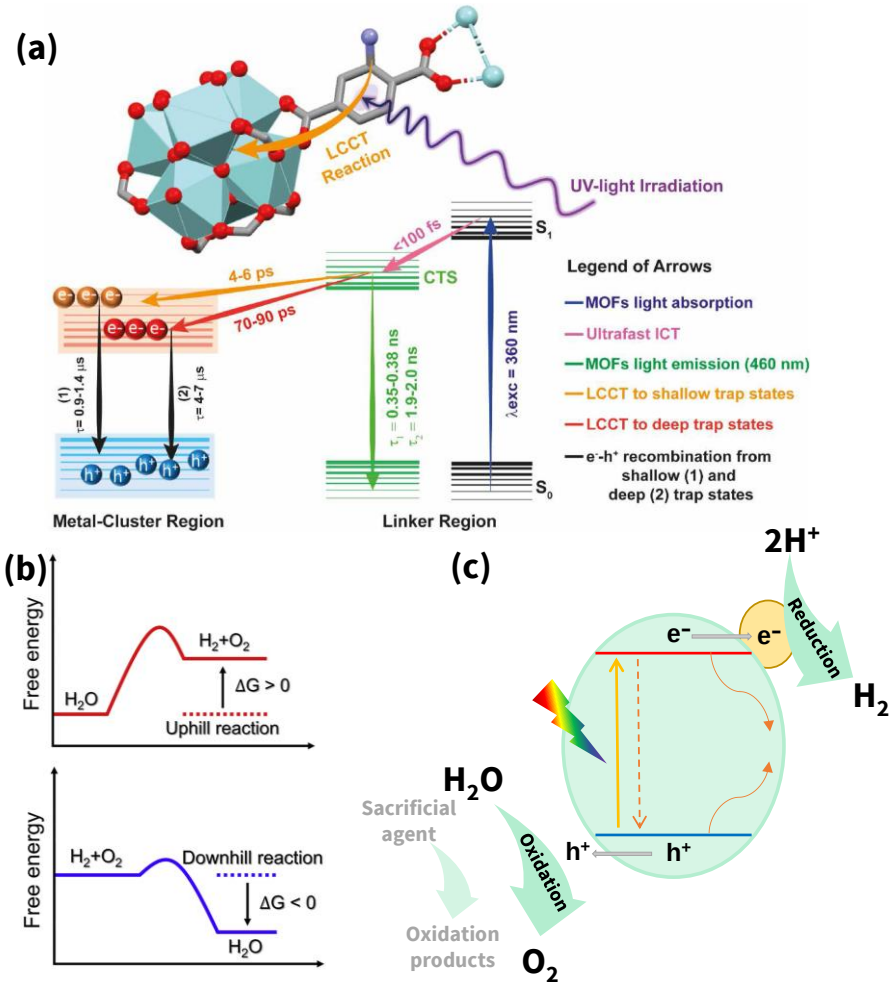

Figure 9. (a) Excited state events that occur upon photoexcitation of UiO-66(NH_2). Acronyms refer to ligand-to-cluster charge transfer (LCCT), intramolecular charge transfer (ICT), charge transfer state (CTS). Adapted from ref.[69] Licensed under CC BY-NC-ND 4.0. (b) Thermodynamic feasibility of OWS (red) versus its back reaction (blue). Adapted from ref.[74] Copyright 2022, with permission from Elsevier. (c) Photocatalytic water splitting reaction with a co-catalyst.

The current state-of-the-art STH values for particulate photocatalysts still remain around 1-2 %[19], indicating significant research and development gaps that will have to be solved before they can be practically applied[67]. A large-scale hydrogen production system on a 100 m^2 panel made of $SrTiO_3$:Al, incorporating

Rh, Cr, and Co as co-catalysts, achieved a solar-to-hydrogen efficiency of 0.76 % under natural sunlight[76]. However, to achieve economically viable solar hydrogen production, the STH efficiency would need to reach 5-10 %. A strategy has recently been developed to achieve a high (9.2 %) solar-to-hydrogen efficiency using pure water, concentrated solar light and an indium gallium nitride-based photocatalyst. This effectiveness is due to the combined effects of enhancing forward hydrogen–oxygen evolution and preventing reverse hydrogen–oxygen recombination by maintaining an optimal reaction temperature of approximately 70 °C. This temperature is achieved by capturing the previously unused infrared light from sunlight[77].

1.4.4 Photocatalytic CO_2 reduction

Pioneering works on CO_2 photoreduction were reported in 1978 by Inoue et al., where they highlighted the possibility of reducing CO_2 in an aqueous suspension of a semiconductor photocatalyst producing formaldehyde, formic acid, CH_3OH, and CH_4[78]. Further, Hemminger et al. reported the conversion of gaseous water and CO_2 to CH_4 using Pt-$SrTiO_3$[79]. This process closely resembles photosynthesis in plants, in which CO_2 and water are converted into glucose and oxygen. This reaction should ideally be produced from CO_2 and water, as shown in Figure 10a, but using hydrogen instead of water is an easier way of reducing CO_2 due to being a thermodynamically exothermic reaction, although the kinetics are challenging. The conduction band energy should exceed the energy level of the CO_2 reduction reaction[80]. The most common products of the reduction of CO_2 are shown in Figure 10b, together with the electrons and protons required to develop the reaction, with indications of the process timescales. It is very important to find an effective photocatalyst which activates the π–bond of the CO_2 molecule[81]. When the surface of the photocatalyst adsorbs CO_2, the C–O bond elongates and the

molecule bends to form $CO_2^{\cdot-}$ to be able to perform the reaction (Figure 10c)[82]. Figure 10c also shows the different pathways of the mechanisms under study. The different possibilities begin with the CO_2 binding modes on the photocatalyst's surface, including oxygen coordination, carbon coordination and mixed coordination. These pathways are determined by whether the subsequent reaction proceeds via electron transfer, proton transfer or concerted electron-proton transfer[83].

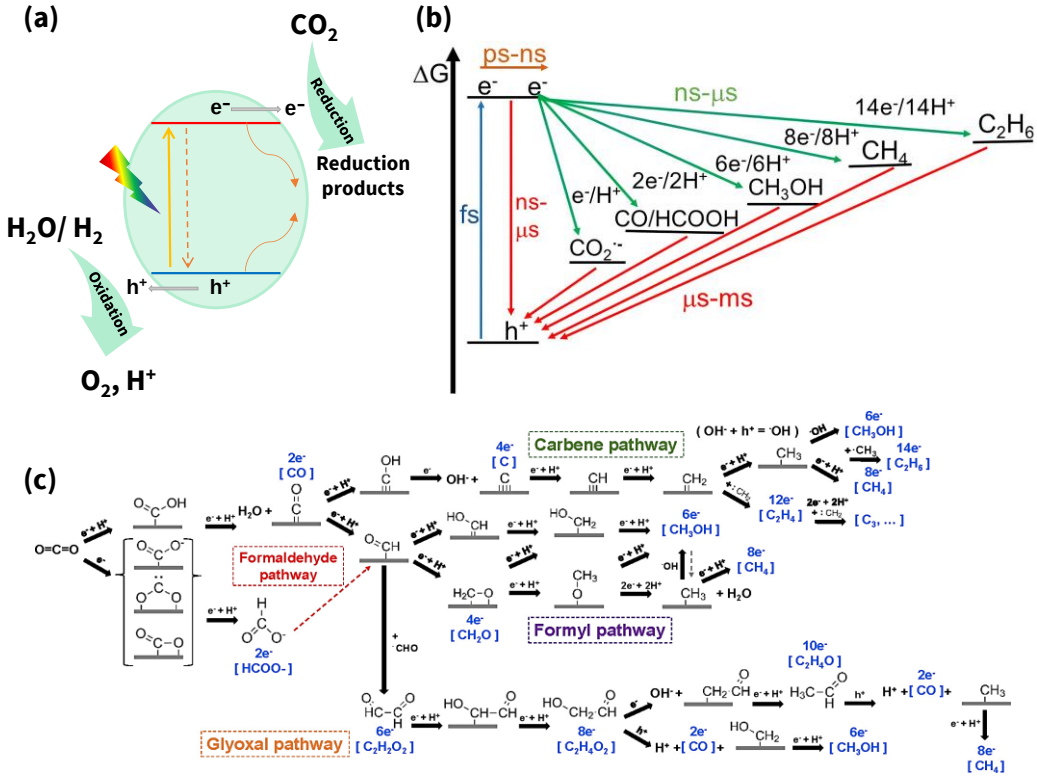

Figure 10. (a) Photocatalytic CO_2 reduction scheme and (b) energy diagram of CO_2 reduction products, highlighting the number of e^- and H^+ required and the timescale of charge transfer reactions. The timescale of charge transfer reactions encompasses light absorption (blue), charge migration (orange), charge transfer and reaction kinetics, and charge recombination (red). Reprinted with permission from ref.[83] Copyright 2020, American Chemical Society (c) Mechanistic routes for the reduction of CO_2. Reprinted with permission from ref.[84]

The commonly used photocatalysts for CO_2 photoreduction to CH_4 include metal oxides like TiO_2, ZnO_2, Cu_2O or CuO, among others. Efficient photothermal CO_2 methanation (277 mmol h^{-1} g^{-1} ; 300 W Xe lamp) was achieved under a continuous flow operation using ultrathin Mg-Al layered double hydroxide nanosheets with Ru NPs as co-catalysts[85]. Some other materials used to conduct CO_2 photomethanation include carbon nitride (g-C_3N_4), semiconducting nanocrystals like quantum dots (QDs)[16]. A series of crystalline and porous materials classified as metal-organic frameworks have also emerged recently as promising heterogeneous photocatalysts for this purpose[86].

1.5 Metal-Organic Frameworks

1.5.1 Description

MOFs, also known as porous coordinating polymers, are porous crystalline materials made up of metal ions, metal clusters or metal-oxo chains coordinated to multitopic organic ligands, forming one-, two-, or three-dimensional structures. These materials are the result of the reaction of organic linkers with inorganic secondary building units (SBUs) through establishing coordination bonds[87, 88].

The discovery of these materials has been attributed to a number of research groups in different countries: e.g. in Australia by Richard Robson[89], in the US by the group led by Omar Yaghi[90, 91], in France by Gerard Ferey[92] and in Japan by the group led by Kitagawa[93]. A standard system was devised to denote these materials[94] by means of an alphanumeric code followed by a number to denote the universities or research center in which the materials were discovered, e.g. HKUST-1, which stands for “Hong Kong University of Science and Technology”,

UiO-66 which indicates “Universitet i Oslo”, or MIL-125, that refers to “Materiaux de l’Institut Lavoisier”.

The flexibility in the geometry, size, and functionality of their constituents has led to the development and study of over 20,000 different MOFs[87, 95, 96]. These can be synthesized by a wide range of methods like precipitation, microwave, evaporation, sonochemical, electrochemical and solvothermal processes. The wide range of MOFs, are highly versatile and adjustable materials suitable for many applications, including gas storage and separation[97, 98], biomedicine[99], catalysis[100], electrocatalysis[101], photocatalysis[62] and many others.

The properties of MOFs include a large surface area, ranging from 100 to 10,000 m^2/g, tunable topography, high metal site density (20-30 wt %), they can function catalytically as Lewis or redox active centers, high porosity, with sizes from 3 to 100 Å, with volumes between 0.5 to 2 cm^3/g, high crystallinity and thermal stability[102]. As Ti- and Zr-based MOFs offer high thermal and chemical stability, they have attracted significant research interest, making them the most extensively studied MOF-based photocatalysts[103]. UiO-66 is benchmark MOF with remarkable stability that will be described in the present thesis, with zirconium as the node and was developed in 2008[104]. MIL-125 is another benchmark MOF, composed of titanium and was first synthesized in 2009 (also used as a photocatalyst in the present thesis)[105].

1.5.1.1 UiO-66(Zr)

The ideal crystalline cell formula of this material is $Zr_6O_4(OH)_4(C_8H_4O_4)_6$. Its structure (Figure 11) consists of metallic nodes containing six Zr(IV) atoms forming an octahedron, with each face coordinated by a μ_3 oxygen atom or an HO^- group. These metal nodes are coordinated with six terephthalic ligands, defining pores with a size of approximately 1.2 nm. In its ideal crystal structure, each Zr(IV) metal center is completely coordinated by 12 organic 1,4- benzenedicarboxylate (BDC) linkers, forming a highly interconnected framework[106].

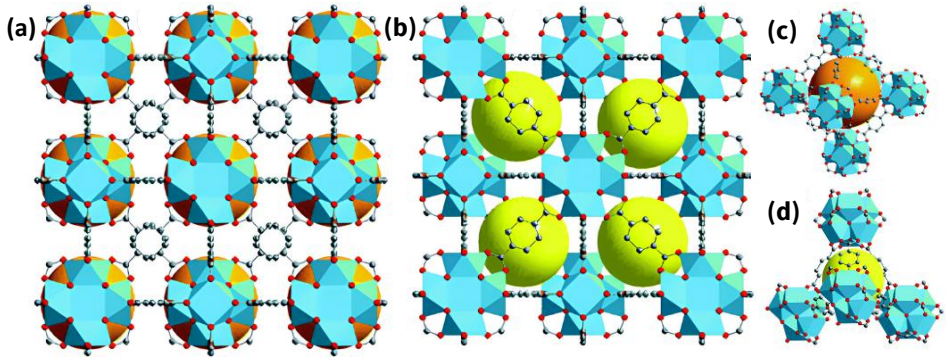

Figure 11. UiO-66(Zr) structure representation. (a, b) Parts of the framework showing spatial arrangements of the octahedral and the tetrahedral cages, represented by orange and yellow spheres, respectively. (c, d) Magnified views of the octahedral and the tetrahedral cages. Zr atoms are displayed as octahedra (color codes: Zr, blue; C, gray; O, red). For clarity, the hydrogen atoms have been removed from all structural plots. Reproduced with permission from ref.[107]

Monometallic UiO-66 materials have been widely used as photocatalysts due to their excellent porosity, their exceptional stability and the potential for a rational design to enhance their photoresponse and charge separation efficiency[108]. UiO-66 has been extensively studied for gas adsorption and storage applications, especially for H_2 and CO_2. Its robustness also makes it a promising candidate for catalytic applications and environmental remediation[109].

1.5.1.2 MIL-125(Ti)

The structural analysis of MIL-125(Ti) indicates that the ideal crystalline cell is constructed from $Ti_8O_8(OH_4)(O_2C\text{-}C_6H_4\text{-}CO_2)$ units, capable of forming body-centered cubic structures with cyclic octamers (designated as SBU-8 of $TiO_5(OH)$) replacing the atoms. These octamers are interconnected by BDC linkers, resulting in the final 3D structure which can be seen in Figure 12. Similar to a close-packed cubic structure, each octamer is surrounded by 12 neighboring SBUs linked by BDC ligands. This 3D arrangement creates two octahedral cages that correspond to the vacant and tetrahedral positions in a typical close-packed cubic structure. As in UiO-66-based MOFs, MIL-125-based materials are considered benchmark Ti-MOFs and can be used in several applications, including (photo)catalysis.

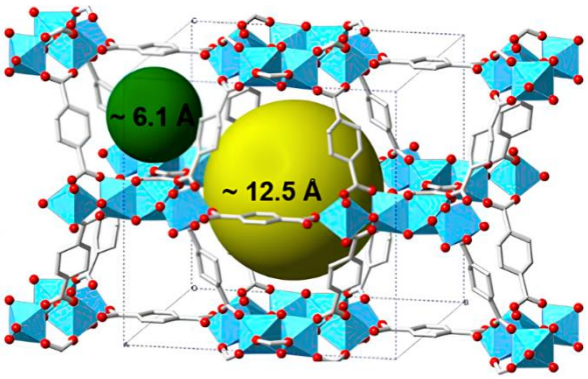

Figure 12. MIL-125(Ti) structure, showing the spaces within the cages represented by yellow and green spheres. Reproduced from ref.[110] licensed under CC BY 4.0.

1.5.2 Metal-organic frameworks as photocatalysts

Unlike inorganic semiconductors, despite their relatively low electrical conductivity, MOFs are capable of achieving electron/hole pair separation during irradiation, facilitating redox reactions[111]. One widely accepted reaction mechanism for MOFs as photocatalysts consists of irradiating the MOF organic

ligand using photons with enough energy to generate a charge-separated state through organic ligand-to-metal charge transfer (LMCT) processes[103]. In this procedure, MOFs absorb photons of specific energy via the organic ligands, converting initial excitons into a charge-separated state by transferring electrons from the organic ligand to the metal nodes[112]. The diverse composition of organic ligands and the potential for post-synthetic modifications (PSM) of both metals and organic ligands allow MOFs to be optimized for efficient solar energy use[103]. Other MOF mechanisms include MMCT, ligand-to-ligand charge transfer and metal-to-ligand charge transfer, plus various other possibilities[111].

1.5.2.1 Tuning MOF properties

Several approaches have been documented for engineering the MOF-based photocatalysts while maintaining their crystalline structure to enhance their photocatalytic activity, some of which are similar to those outlined above for inorganic materials. These include organic ligand functionalization, metal node composition, structural defects and incorporating metal NPs as co-catalysts, among others.

1.5.2.1.1 Ligand functionalization

Different studies have been carried out on the effect of functionalizing ligands to enhance the properties of MOF-based materials[113]. In heterogeneous photocatalysis, determining the band energy diagram level of the solid is crucial to obtain information on the photocatalyst's thermodynamic capabilities when performing different reactions. In MOFs, this band energy level diagram is mainly influenced by three factors, the band gap, the highest occupied crystal orbital (HOCO), and the lowest unoccupied crystal orbital (LUCO). Linker

functionalization significantly influences the electronic structure, including the band gap modification in UiO-66(Zr) (Figure 13a) combining theoretical[105] and experimental studies to show how linker functionalization can alter the band gap. Functionalizing MOFs with -NH_2 groups is often used to narrow the band gap by facilitating n → π* electronic transitions, which require less energy than π → π* electron excitation. It also alters the position of the HOCO. For example, in Figure 13b it can be seen that when the BDC linker is replaced by an electron-donating group like NH_2, new filled states often emerge near the middle of the original HOCO–LUCO gap of pristine UiO-66(Ce). Conversely, substituting the BDC linker by an electron-withdrawing group (e.g. NO_2) introduces new filled states located just above the original HOCO of the pristine solid, in line with previous findings on UiO-66[80].

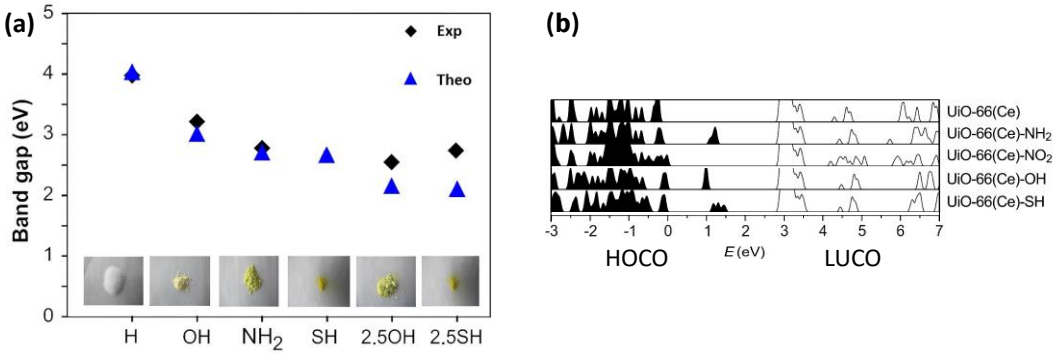

Figure 13. (a) Linker functionalization of UiO-66(Zr) solid modifying the band gap. Adapted with permission from ref.[114] Copyright 2015, American Chemical Society (b) Filled states of the functionalized UiO-66(Ce). Adapted with permission from ref.[80] Copyright 2018, American Chemical Society.

1.5.2.1.2 Metal node composition

Truhlar, Gagliardi et al. assessed the theoretical influence of metal node composition (M: Zr, Hf, Th, Ti, U, or Ce) in UiO-66 structures on the resulting

electronic properties (i.e. band gap, HOCO, LUCO values)[80], as can be seen in Figure 14. It has been suggested that UiO-66(Ce) could be the most efficient photocatalyst of the series for OWS under visible light irradiation, due to the favorable photoinduced LMCT. Serre, Navalón et al. experimentally confirmed the higher efficiency of UiO-66(Ce)-based MOFs than UiO-66(Zr) as photocatalysts for HER, OER[13] and OWS[115]. This study also confirmed that UiO-66(Ce) solids had relatively lower photostability than UiO- 66(Zr) solids.

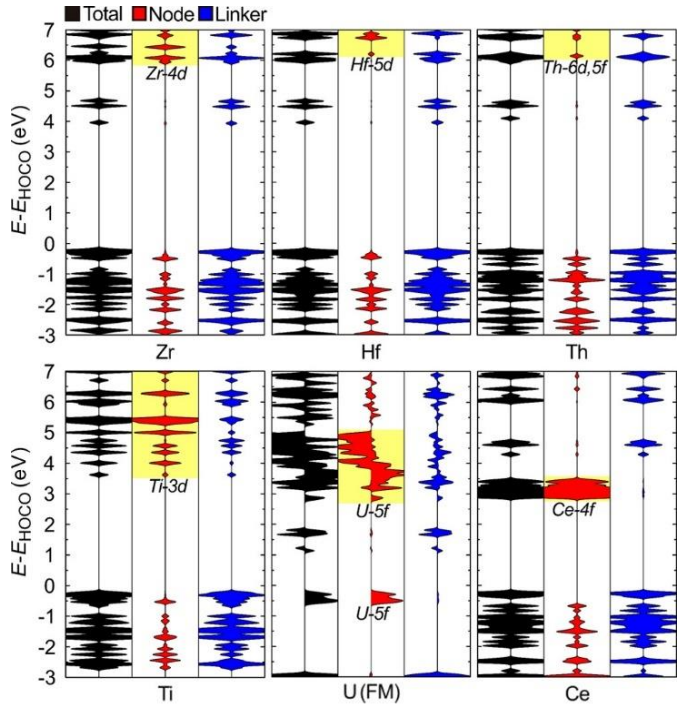

Figure 14. Density states total (black) and projected (red and blue) of UiO-66(M) where M represents Zr, Hf, Th, Ti, U, and Ce. Reproduced with permission from ref.[80] Copyright 2018, American Chemical Society.

Theoretical calculations in 2018 also suggested that the photocatalytic activity of UiO-66(Ce) materials could be improved by developing bimetallic UiO- 66(Ce/Zr) or UiO-66(Ce/Ti) solids for a favorable overlap between the HOCO

in the organic ligand and the LUCO of the metal nodes, combined with a narrow band gap to obtain a more efficient LMCT pathway[116]. The effect of the heterogeneity of mixed metal-MOFs implies that synergistic interactions between the metal orbitals within the framework significantly enhance the catalytic properties[117]. Ti(IV) is now commonly introduced as a metal node alongside the original Zr(IV) metal node in UiO-66(Zr), due to the photoaccessible unoccupied Ti(III) state. In 2014, the successful preparation of Ti-substituted UiO- 66(Zr/Ti)- NH_2 was pioneered using a PSM[66]. It is now generally accepted that two main modifications can occur during this process (Figure 15). Ti(IV) can either be integrated into the inorganic SBU through Zr(IV) exchange or attached to the surface of the SBU at a linker vacancy site[118].

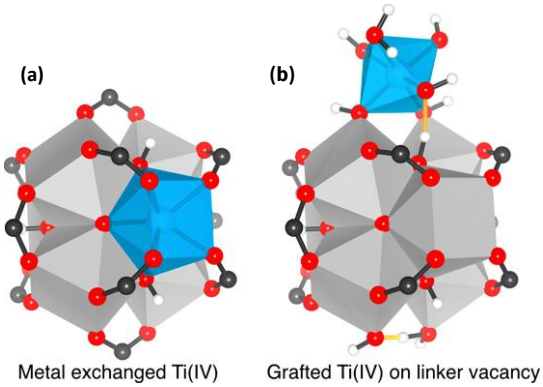

Figure 15. Proposed coordination sites of Ti in UiO-type materials: (a) Incorporation of Ti(IV) into the cluster through metal exchange, and (b) Attachment of Ti(IV) to the cluster surface at a linker vacancy defect site. Adapted with permission from ref.[118] Copyright 2017, American Chemical Society.

UiO-66 materials are among the most extensively researched mixed-metal MOFs due to their promising photocatalytic properties. In 2015, Li et al. synthesized a UiO-66(Zr/Ti)–NH_2 solid that had a better photocatalytic performance for both CO_2 reduction and H_2 evolution than the Zr-based UiO-66 solid[66]. Other studies have also found a preparation of mixed-metal

Ce(IV)/Zr(IV) UiO-66 solids with a better photocatalytic performance than monometallic UiO-66(Zr), due to the favorable overlap between the HOCO in the organic ligand and the LUCO in the metal nodes, as well as a narrow band gap, leading to a more efficient LMCT pathway. Density functional theory (DFT) and electron paramagnetic resonance (EPR) studies revealed that the incorporated metal acts as an electron mediator during the photoinduced electron transfer from the HOCO of the organic ligand to the metal node, facilitating electron transfer from the excited 2-aminoterephthalic acid ligand to the Zr- O oxo- clusters, forming the catalytically active species Zr(III)[66]. In the case of Ti, it is therefore seen that the initial formation of Ti(III)–O–Zr(IV) species in the metal node of the MOF then transforms into Ti(IV)–O–Zr(III) via metal–metal electron exchange[108], as can be seen in Figure 16.

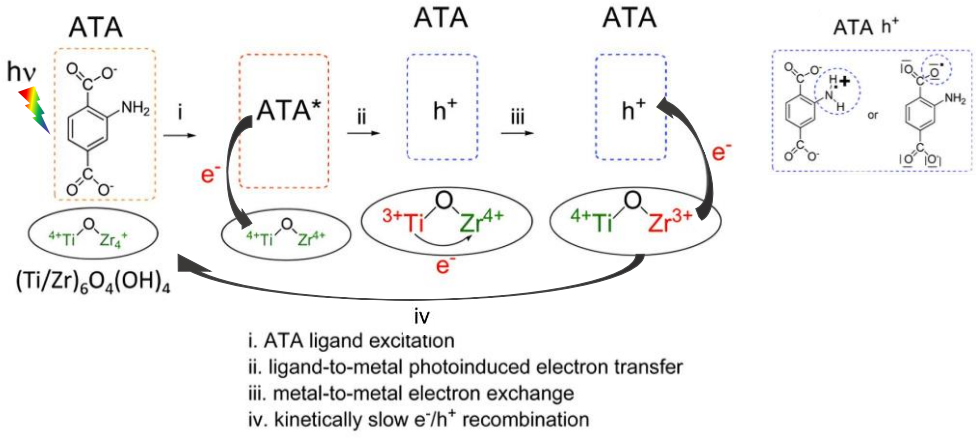

Figure 16. Mechanism of UiO-66(Zr/Ti)-NH_2. Adapted with permission from ref.[119] Copyright 2017, American Chemical Society.

1.5.2.1.3 Structural defects

Defects in MOFs involving metal nodes or organic ligands can be due to PSM, such as thermal, chemical, or plasma treatments[94,120-122], or by *in situ* synthesis[120,122-126]. Theoretical studies have suggested that the partial removal of

organic linkers, particularly in UiO-66(Zr), reduces the unoccupied d orbitals in Zr atoms, potentially enhancing charge transfer in the photocatalytic process[127]. A notable modulated synthesis of UiO-66(Zr) materials[128] involves using modulators such as monocarboxylic acids (i.e. formic acid, acetic acid, trifluoroacetic acid, benzoic acid) or inorganic compounds such as HCl during synthesis. These modulators fully interact with multitopic organic ligands during their coordination with metal nodes, especially within the highly connected SBU of UiO-66, resulting in structural defects like missing linkers or clusters[129], as seen in Figure 17. The type and number of modulators not only influence these structural defects but also affect the physical, chemical, morphological and textural properties of the MOFs. Both theoretical and experimental studies have suggested that these modulators can modify MOFs' electronic properties and enhance the photocatalytic activity of UiO-66 solids[130], while recent studies emphasize the significance of moderate structural defects[127].

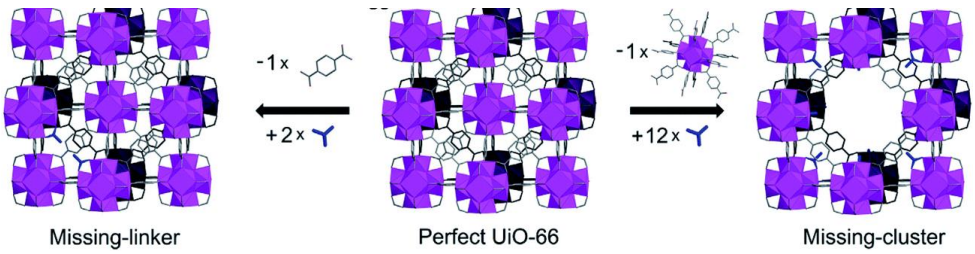

Figure 17. Structural UiO-66 differences between the ideal unit cell and those with missing linker or missing cluster defects. Reproduced with permission from ref.[129] Copyright 2017, with permission from Elsevier.

1.5.2.1.4 Co-catalyst incorporation

Due to their low Fermi energy levels, metal NPs serve as electron acceptors and mediators. In some cases, such as Au, Ag, Cu or RuO_x these NPs enhance

visible and near-infrared light absorption, e.g. through the localized surface plasmon resonance effect[113]. The efficiency of photocatalytic reactions is generally improved by metal NPs as co-catalysts, as they reduce both the charge carrier recombination and the activation energy barrier and serve as reactive sites[131].

1.5.2.1.5 Other approaches

MOF properties can also be modified by encapsulating organic photosensitizers, creating heterojunctions like MOF-on-MOF or MOF/inorganic semiconductors, and designing MOFs with specific exposed facets[62, 132].

A simplified timeline summarizing the discovery of MOFs, including those with UiO-66 and MIL-125 topologies, and the first examples of photocatalytic water splitting reactions or CO_2 reduction as it concerns the present thesis is shown in Figure 18.

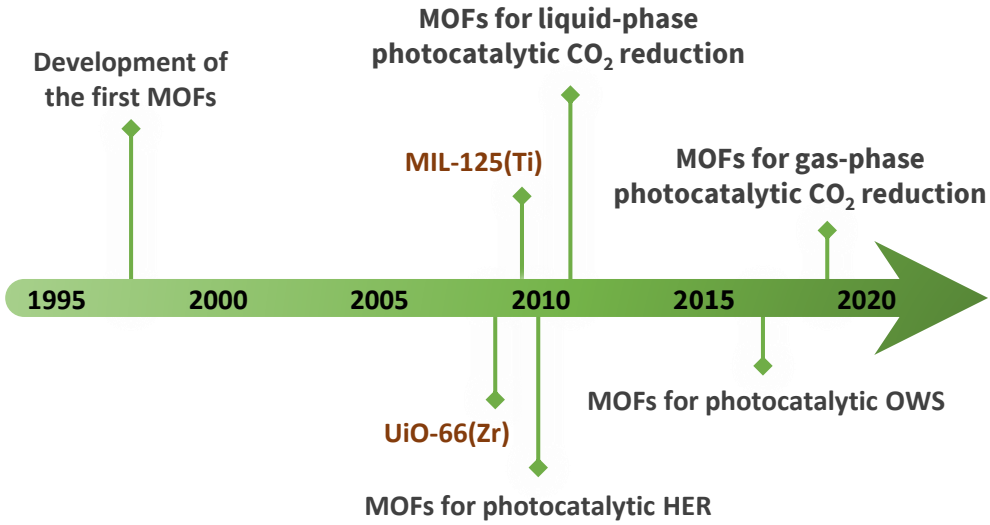

Figure 18. Timeline of the discovery and the photocatalytic applications of MOFs appearing in the present document.

1.5.3 Photocatalytic water splitting reactions

The most frequently reported MOFs as water splitting photocatalysts are terephthalate-based MOFs like UiO-66(Zr)-NH_2, MIL-125(Ti)-NH_2 or MIL-101-NH_2. These processes aim to perform the reaction under natural sunlight irradiation. For this reason, many reported MOFs are functionalized with amino ligands since they can expand the visible light absorption up to about 450 nm, with respect to the parent non-functionalized MOFs. In other cases, MOFs' visible absorption properties have been further expanded in the entire visible region by the

development of porphyrin-based MOFs[111]. Photocatalytic HER is typically enhanced by the presence of co-catalysts such as Pt, Pd, Rh, Au, or Ni NPs[62]. Of these NPs, Pt, especially in the form of NPs or clusters, is the most widely studied HER with noble-metal-based co-catalyst, due to its high work function and better efficiency. As Pt NPs of around 1 nm in size are considered optimal for HER[133], many studies have been reported that combine these MOFs with Pt as the reference co-catalysts for HER.

1.5.3.1 Photocatalytic hydrogen evolution reaction

Photocatalytic HER involves reducing protons to produce hydrogen gas and is facilitated by organic (i. e. CH_3OH, TEOA) or inorganic (i.e. $Na_2S{\cdot}9H_2O/Na_2SO_3$) sacrificial electron donors. It should be mentioned that the use of organic sacrificial electron donors during this process can result in the formation of H_2 via the so-called photoreforming, an additional reaction pathway to that of the proton reduction reaction. In a seminal study, Garcia et al. first reported the possibility of using MOFs as heterogeneous photocatalysts for HER[128]. In particular, UiO-66(Zr)-X (X: H or NH_2) solids with or without Pt NPs as co-catalysts were used for the photocatalytic HER in the presence of CH_3OH as a sacrificial electron donor under UV-vis irradiation. An AQY of 3.5 % at 370 nm using UiO - 66(Zr)-NH_2 as the photocatalyst has been reported[134] and since then many other studies have reported the use of MOF-based photocatalysts for this purpose. Table 1 highlights notable outcomes of H_2 production using different benchmark MOFs as photocatalysts under visible light, including their activities and the specific reaction conditions. It can be seen that amino linker functionalization in combination with the incorporation of NPs has had a significant impact on this field. TEOA is one of the most representative sacrificial agents.

Table 1. Photocatalytic water splitting using MOF-based materials under simulated sunlight irradiation. Modified from ref.[62] with the CC BY 4.0 license. Standing COF as covalent-organic-frameworks.

Material	Reaction conditions	H_2 produced	AQY (%)	Ref
UiO-66(Zr)-NH_2 with Pt NPs	Photocatalyst (10 mg), solution (18 mL CH_3CN, 0.2 mL H_2O), TEOA (2 mL), irradiation source (300 W Xe lamp, λ > 380 nm)	0.275 mmol g^{-1} h^{-1}		135
UiO-66(Zr/Ti)-NH_2 with Pt NPs	Photocatalyst (50 mg), solvent (H_2O, H_2O/TEOA (5/1), 60 mL), irradiation source (300 W Xe lamp, λ > 420 nm)	0.35 mmol g^{-1} h^{-1}		66
UiO-66(Zr)-NH_2/ GO MoS_2(5 wt %)	Photocatalyst (30 mg), aqueous solution (100 mL, 10 vol % TEOA, pH 7), MoS_2 (5 wt %), eosin Y (0.4 mM), irradiation source (300 W Xe lamp, λ > 420 nm)	2.07 mmol g^{-1} h^{-1}	At 430 is 40.5 %	136
MIL-125(Ti)-NH_2-COF with Pt NPs (3 wt %)	Photocatalyst (20 mg), solution (80 mL; H_2O/TEOA 72:8), irradiation source (300 W Xe lamp, λ > 420 nm),6 °C	0.36 mmol g^{-1} h^{-1}	At 420 nm is 0.87 %	137
$Zn_{0.5}Cd_{0.5}S$(40 %)/ MIL-125-NH_2(Ti)	Photocatalyst (20 mg), aqueous solution (45 mmol $Na_2S{\cdot}9H_2O$ and 100 mmol Na_2SO_3), irradiation source (300 W Xe lamp, λ > 400 nm)	92.5 mmol g^{-1} h^{-1}	At 420 nm is 30.8%	138
Au_{core}@CdS_{shell}/ MIL-101[48] (60 %)	Photocatalyst (10 mg), aqueous solution (100 mL; 20 mmol of Na_2S and Na_2SO_3 as sacrificial agents), irradiation source (300 W Xe lamp, λ > 420 nm)	25 mmol g^{-1} h^{-1}	At 420 nm is 8.8 %	139
Porphyrin-Ti-MOF Pt NPs (3 wt %)	Photocatalyst (10 mg), aqueous solution (270 mL; 10 mmol ascorbic acid), irradiation source (300 W Xe lamp, λ > 420 nm)	8.52 mmol g^{-1} h^{-1}	At 380–420 nm ~0.26 %	140

1.5.3.2 Photocatalytic overall water splitting

MOF-based photocatalysts were first used for OWS in 2017, when Huang Liu et al. described the use of an aluminum-based MOF (MIL-53(Al)-NH_2) modified with Ni(II) ions coordinated to the amino group of the material as photocatalyst for OWS in the absence of sacrificial electron donors. This photocatalyst provided a production rate of 36 and 155 $\mu mol \cdot h^{-1}$ of H_2 and O_2, respectively[131]. This groundbreaking study represented a crucial advance in harnessing the potential of MOFs for OWS applications. Since then, other studies have been reported for the same purpose[62]. Table 2 gives the significant results of photocatalytic OWS using various MOF-based photocatalysts, detailing their activities and specific reaction conditions. MOFs with amino-functionalized organic ligands and mixed- metal SBUs have proved to be active for conducting the reaction under simulated sunlight, while porphyrin-based MOFs have so far achieved the highest efficiencies for this process.

Table 2. Photocatalytic OWS using MOF-based materials under visible or simulated sunlight irradiation. Modified with permission from CC BY 4.0 by license from ref.[62]

Material	Reaction conditions	H_2 and O_2 production	AQY (%)	Ref.
UiO-66(Zr)-NH_2(core)@UiO-66(Ce)(shell)	Photocatalyst (10 mg), H_2O (20 mL), simulated sunlight irradiation (Hg−Xe lamp 150 W equipped with an AM 1.5G filter), and 35 °C	375 and 170 μmol g^{-1} in 22 h	0.034 % at 400 nm	132
UiO-66(Ce)-NH_2 with Pt NPs (1 wt %) as co-catalyst	Photocatalyst (20 mg), H_2O (20 mL), simulated sunlight irradiation (150 W Hg-Xe lamp equipped with an AM 1.5G filter), 35 °C	208 and 80 μmol g^{-1} in 22 h	-	115
UiO-66(Zr)-NH_2 with Pt and MnO_x NPs as co-catalyst	Photocatalyst (10 mg), H_2O (100 mL), 5 °C, irradiation source (Xe lamp $\lambda > 400$ nm)	19.6 and 10.1 μmol g^{-1} h^{-1}	-	141
UiO-66(Zr/Ce/Ti)	Photocatalyst (20 mg), H_2O (20 mL), visible light irradiation (Hg-Xe lamp 150 W with a $\lambda >$ 450 nm cut-off filter)	210 and 70 μmol g^{-1} in 22 h	-	142
MIL-125(Ti)-NH_2 treated with oxygen-plasma	Photocatalyst (20 mg), H_2O (20 mL), 35 °C, solar simulator (1 sun)	83 and 29 μmol g^{-1} in 22 h	-	143
Ti-MOF: IEF-11	Photocatalyst (10 mg), H_2O (20 mL), simulated sunlight irradiation (Xe_Hg lamp 150 W, 1.5 AM filter), 35 °C	260 and 107 μmol g^{-1} in 22 h	-	144
Ni-MOF: IEF-13	Photocatalyst (5 mg), H_2O (20 mL), simulated sunlight irradiation (solar simulator; Oriel, 1 sun) 20 °C	160 and 14 μmol g^{-1} in 22 h	-	145
Porphyrin-based MOF: MIL-173(Zr/Ti)-40 (40 wt % of Ti content)	Photocatalyst (10 mg), H_2O (20 mL), simulated sunlight irradiation (Xe-Hg lamp 150 W, 1.5 AM filter), 35 °C	381 and 145 μmol g^{-1} in 22 h	0.11 % at 450 nm	146

1.5.3.3 CO_2 photoreduction

Most of the information gained to date on CO_2 photoreduction by MOFs has been derived from liquid-phase reactions. MIL-125(Ti)-NH_2 was used as a photocatalyst for carbon dioxide reduction to liquid-phase formate anion ($HCOO^-$)[147] in 2012. Most of these studies were conducted with organic solvents and sacrificial electron donors, such as TEOA[50], under UV-vis or visible light irradiation. After donating an electron, this tertiary amine forms an aminyl radical cation, which then transfers a hydride to CO_2, reducing it to formic acid[62]. An example is shown in Figure 19, in which the mixed-metal UiO-66(Zr/Ti)-NH_2, where Ti(IV) acts as electron mediator to favor photoinduced LMCT processes from the organic ligand to the metal node, thus enhancing the CO_2 reduction capacity. In this example sacrificial agents were used to almost linearly raise the production of $HCOO^-$ over time and was 1.7 times more active than the pristine sample UiO-66(Zr)[66].

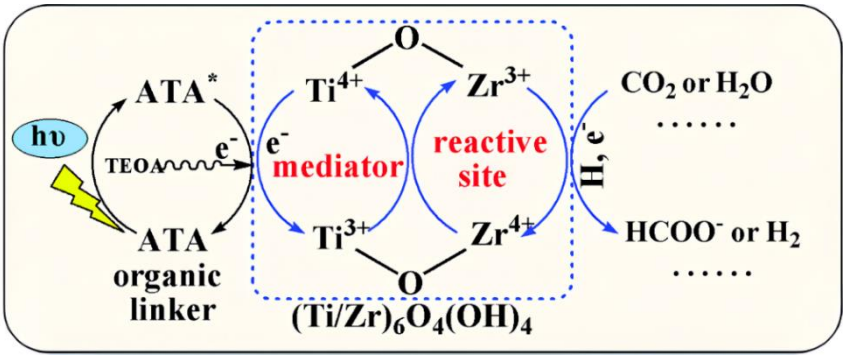

Figure 19. Mechanism to produce $HCOO^-$ using UiO-66(Zr/Ti)-NH_2. Reproduced with permission from ref.[66]

However, it was not until 2019 photocatalytic gaseous CO_2 hydrogenation to CH_4 under UV-Vis light irradiation and at a reaction temperature of 215 °C with a modified or unmodified Zn-MOF with Cu_2O NPs as a co-catalyst was reported for

the first time[86]. Co-catalysts are known to be able to significantly enhance photocatalytic activity, while noble metals like Rh offer greater activity and stability[52]. Ru/RuO_x NPs is considered to be the benchmark co-catalyst for achieving remarkable efficiency in CO_2 methanation[148], e.g. the high CH_4 production achieved with MIL-125(Ti)-NH_2 combined with RuO_x NPs when exposed to solar energy and H_2 gas at a temperature of 200°C. The optimal material was with a 10 % wt of RuO_x NPs, yielding 18.5 mmol·g^{-1} of CH_4 after 22 hours of reaction. A dual photothermal mechanism was found to contribute to the process. This mechanism can be seen in Figure 20, combining photochemical charge separation and the generation of electrons and holes with thermochemical local heating caused by irradiated photons. In the photochemical mechanism, light irradiation with sufficient energy generates electrons and holes, which drive the reduction and oxidation reactions, respectively. Conversely, in the photothermal mechanism, light energy is converted into heat promoted with RuO_x NPs, enhancing the thermocatalytic process[108]. The plasmon band of RuO_x significantly enhanced CH_4 production efficiency, particularly with increased absorption at 800 nm[149].

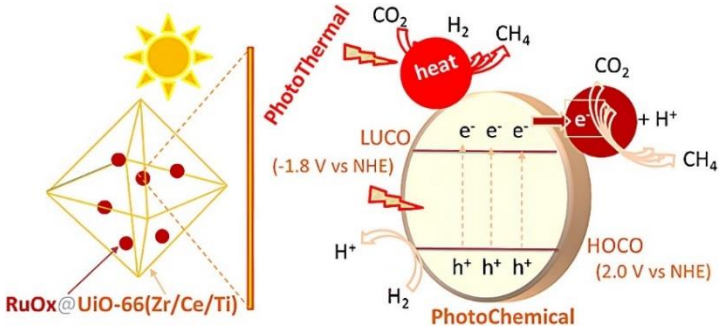

Figure 20. Mechanism of CO_2 reduction by H_2 during photocatalysis using RuO_x@UiO-66(Zr/Ce/Ti). Reproduced with permission from ref.[108]

1.6 References

(1) Ritchie, H.; Rosado, P.; Roser, M. Energy production and consumption. Our World in Data, **2020**.

(2) Ritchie, H.; Rosado, P.; Roser, M. Primary energy consumption. Our World in Data, **2023**.

(3) Hannah, R. P., Rosado. Fossil fuels. Our World in Data: **2017**.

(4) Karayil, A.; Elseragy, A.; Aliyu, A. M. An assessment of CO_2 capture technologies towards global carbon net neutrality. *Energies* **2024**, *17* (6), 1460.

(5) Yanguas-Parra, P. A.; Malz, N.; Oei, P.-Y.; Furnaro, A.; Hauenstein, C.; Quiceno, G.; Corral-Montoya, F.; Mitterecker, T.; Hanto, J. Perspective: How a short-term relapse to coal could put exporting countries and just transition processes at risk. *Energy Res. Soc. Sci.* **2023**, *97*, 102989.

(6) Wang, Z.; Li, S.; Jin, Z.; Li, Z.; Liu, Q.; Zhang, K. Oil and gas pathway to net-zero: Review and outlook. *Energy Strateg. Rev.* **2023**, *45*, 101048.

(7) Climate change: evidence and causes: update 2020; the national academies press, **2020**.

(8) Abbass, K.; Qasim, M. Z.; Song, H.; Murshed, M.; Mahmood, H.; Younis, I. A review of the global climate change impacts, adaptation, and sustainable mitigation measures. *Environ. Sci. Pollut. Res.* **2022**, *29* (28), 42539-42559.

(9) Institute, E. *Statistical Review of World Energy.* Our World in Data, **2023**.

(10) Zhang, M.; Liu, N.; Harper, R.; Li, Q.; Liu, K.; Wei, X.; Ning, D.; Hou, Y.; Liu, S. A global review on hydrological responses to forest change across multiple spatial scales: Importance of scale, climate, forest type and hydrological regime. *J. Hydrol.* **2017**, *546*, 44-59.

(11) Bardan, R. NASA analysis confirms 2023 as warmest year on record. NASA, **2024**.

(12) Esper, J.; Torbenson, M.; Büntgen, U. 2023 summer warmth unparalleled over the past 2,000 years. *Nature* **2024**.

(13) Graven, H.; Keeling, R. F.; Rogelj, J. Changes to carbon isotopes in atmospheric CO_2 over the industrial era and into the future. *Global Biogeochem. Cycles* **2020**, *34* (11), e2019GB006170.

(14) Nations, U. Report of the United Nations conference on the human environment; Stockholm, **1972**.

(15) Kyoto protocol to the united nations framework convention on climate change. United Nations, Treaty Series: Kyoto, **1997**; Vol. 2303, p 173.

(16) Chen, J. J.; Oh, P. C.; Saleh, S. B. M. Recent development on photocatalysts and membrane processes for photoreduction of CO_2 into C1 solar fuels. *Korean J. Chem. Eng.* **2024**, *41* (3), 609-637.

(17) Paris Agreement. **2015**; Vol. UNTC XXVII 7.d.

(18) Ritchie, H.; Roser, M. CO_2 emissions. Our World in Data, **2020**.

(19) Zhao, Y.; Ding, C.; Zhu, J.; Qin, W.; Tao, X.; Fan, F.; Li, R.; Li, C. A hydrogen farm strategy for scalable solar hydrogen production with particulate photocatalysts. *Angew. Chem. Int. Ed.* **2020**, *59* (24), 9653-9658.

(20) Agency, I. E. *CO_2 Emissions in 2023 – Analysis*. 2024.

(21) Alsarhan, L. M.; Alayyar, A. S.; Alqahtani, N. B.; Khdary, N. H. Circular Carbon Economy (CCE): A way to Invest CO_2 and protect the environment, a review. *Sustain.* **2021**, *13* (21), 11625.

(22) Wang, Q.; Domen, K. Particulate photocatalysts for light-driven water splitting: mechanisms, challenges, and design strategies. *Chem. Rev.* **2020**, *120* (2), 919-985.

(23) Mikkelsen, M.; Jørgensen, M.; Krebs, F. C. The teraton challenge. A review of fixation and transformation of carbon dioxide. *Energy Environ. Sci.* **2010**, *3* (1), 43-81.

(24) Waheed, A.; Bernward Fischer, T.; Khan, M. I. Climate change policy coherence across policies, plans, and strategies in pakistan—implications for the china–pakistan economic corridor plan. *Environ. Manage.* **2021**, *67* (5), 793-810.

(25) Styring, S. Artificial photosynthesis for solar fuels. *Faraday Discuss.* **2012**, *155* (0), 357-376.

(26) Segev, G.; Kibsgaard, J.; Hahn, C.; Xu, Z. J.; Cheng, W.-H.; Deutsch, T. G.; Xiang, C.; Zhang, J. Z.; Hammarström, L.; Nocera, D. G.; et al. The 2022 solar fuels roadmap. *J. Phys. D: Appl. Phys.* **2022**, *55* (32), 323003.

(27) Tuller, H. L. Solar to fuels conversion technologies: a perspective. *Mat. Renew. Sust. Energ.* **2017**, *6* (1), 3.

(28) Guil-López, R.; Mota, N.; Llorente, J.; Millán, E.; Pawelec, B.; Fierro, J.; Navarro, R. Methanol synthesis from CO_2: a review of the latest developments in heterogeneous catalysis. *Materials* **2019**, *12* (23), 3902.

(29) Mar, K. A.; Unger, C.; Walderdorff, L.; Butler, T. Beyond CO_2 equivalence: The impacts of methane on climate, ecosystems, and health. *Environ. Sci. Policy* **2022**, *134*, 127-136.

(30) Yamada, T.; Nishiyama, H.; Akatsuka, H.; Nishimae, S.; Ishii, Y.; Hisatomi, T.; Domen, K. Production of methane by sunlight-driven photocatalytic water splitting and carbon dioxide methanation as a means of artificial photosynthesis. *ACS Eng. Au* **2023**, *3* (5), 352-363.

(31) Younas, M.; Shafique, S.; Hafeez, A.; Javed, F.; Rehman, F. An overview of hydrogen production: current status, potential, and challenges. *Fuel* **2022**, *316*, 123317.

(32) Al-Douri, A.; Groth, K. M. Hydrogen production via electrolysis: State-of-the-art and research needs in risk and reliability analysis. *Int. J. Hydrogen Energy* **2024**, *63*, 775-785.

(33) Liu, Q. Unlocking the potential of hydrogen in intermittent electricity systems: a global assessment of levelized cost of hydrogen and low carbon industrial hub profitability. Massachusetts Institute of Technology, **2023**.

(34) Commission, E. European Clean Hydrogen Alliance. European Commission. **2024**

(35) Parkinson, B.; Balcombe, P.; Speirs, J. F.; Hawkes, A. D.; Hellgardt, K. Levelized cost of CO_2 mitigation from hydrogen production routes. *Energy Environ. Sci.* **2019**, *12* (1), 19-40.

(36) Parra, D.; Valverde, L.; Pino, F. J.; Patel, M. K. A review on the role, cost and value of hydrogen energy systems for deep decarbonisation. *Renew. Sust. Energ. Rev.* **2019**, *101*, 279-294.

(37) Song, H.; Luo, S.; Huang, H.; Deng, B.; Ye, J. Solar-driven hydrogen production: recent advances, challenges, and future perspectives. *ACS Energy Lett.* **2022**, *7* (3), 1043-1065.

(38) Tembhurne, S.; Nandjou, F.; Haussener, S. A thermally synergistic photo-electrochemical hydrogen generator operating under concentrated solar irradiation. *Nat. Energy* **2019**, *4* (5), 399-407.

(39) Qureshi, F.; Tahir, M. Photoelectrochemical water splitting with engineering aspects for hydrogen production: Recent advances, strategies and challenges. *Int. J. Hydrogen Energy* **2024**, *69*, 760-776.

(40) Gunawan, D.; Zhang, J.; Li, Q.; Toe, C. Y.; Scott, J.; Antonietti, M.; Guo, J.; Amal, R. Materials advances in photocatalytic solar hydrogen production: integrating systems and economics for a sustainable future. *Adv. Mater.* **2024**, *n/a* (n/a), 2404618.

(41) Hassaan, M. A.; El-Nemr, M. A.; Elkatory, M. R.; Ragab, S.; Niculescu, V.-C.; El Nemr, A. Principles of photocatalysts and their different applications: a review. *Top. Curr. Chem.* **2023**, *381* (6), 31.

(42) Rambhujun, N.; Salman, M. S.; Wang, T.; Pratthana, C.; Sapkota, P.; Costalin, M.; Lai, Q.; Aguey-Zinsou, K.-F. Renewable hydrogen for the chemical industry. *MRS Energy Sustain.* **2020**, *7* (1), 33.

(43) Zhang, Z.; Pan, S.-Y.; Li, H.; Cai, J.; Olabi, A. G.; Anthony, E. J.; Manovic, V. Recent advances in carbon dioxide utilization. *Renew. Sust. Energ. Rev.* **2020**, *125*, 109799.

(44) Mahmoudi Kouhi, R.; Jebrailvand Moghaddam, M. M.; Doulati Ardejani, F.; Mirheydari, A.; Maghsoudy, S.; Gholizadeh, F.; Ghobadipour, B. Carbon Utilization technologies & methods. in carbon capture, utilization, and storage technologies: towards more sustainable cities, Ahmadian, A., Elkamel, A., Almansoori, A. Eds.; Springer International Publishing, **2024**; pp 1-50.

(45) Jiao, X.; Zheng, K.; Hu, Z.; Sun, Y.; Xie, Y. Broad-spectral-response photocatalysts for CO_2 reduction. *ACS Cent. Sci.* **2020**, *6* (5), 653-660.

(46) Hou, S.-L.; Dong, J.; Zhao, B. Formation of CX bonds in CO_2 chemical fixation catalyzed by metal−organic frameworks. *Adv. Mater.* **2020**, *32* (3), 1806163.

(47) Li, P.; Gong, S.; Li, C.; Liu, Z. Analysis of routes for electrochemical conversion of CO_2 to methanol. *Clean Energy* **2022**, *6* (1), 202-210.

(48) Ghosh, S.; Sebastian, J.; Olsson, L.; Creaser, D. Experimental and kinetic modeling studies of methanol synthesis from CO_2 hydrogenation using In_2O_3 catalyst. *Chem. Eng. J.* **2021**, *416*, 129120.

(49) Ticali, P.; Salusso, D.; Ahmad, R.; Ahoba-Sam, C.; Ramirez, A.; Shterk, G.; Lomachenko, K. A.; Borfecchia, E.; Morandi, S.; Cavallo, L.; et al. CO_2 hydrogenation to methanol and hydrocarbons over bifunctional Zn-doped ZrO_2/zeolite catalysts. *Catal. Sci. Technol.* **2021**, *11* (4), 1249-1268.

(50) Özsoysal, S.; Oral, B.; Yıldırım, R. Analysis of photocatalytic CO_2 reduction over MOFs using machine learning. *J. Mater. Chem. A* **2024**, *12* (10), 5748-5759.

(51) Remiro-Buenamañana, S.; García, H. Photoassisted CO_2 conversion to fuels. *ChemCatChem* **2019**, *11* (1), 342-356.

(52) A Review of current developments in Sabatier reaction-based methanation of carbon dioxide: thermocatalytic approach. **2024**

(53) Younas, M.; Sethupathi, S.; Kong, L. L.; Mohamed, A. R. CO_2 methanation over Ni and Rh based catalysts: Process optimization at moderate temperature. *Int. J. Energy Res.* **2018**, *42* (10), 3289-3302.

(54) Dumesic, J. A.; Huber, G. W.; Boudart, M. Principles of heterogeneous catalysis. In *Handbook of Heterogeneous Catalysis*. **2008**.

(55) Wegener, S. L.; Marks, T. J.; Stair, P. C. Design strategies for the molecular level synthesis of supported catalysts. *Acc. Chem. Res.* **2012**, *45* (2), 206-214.

(56) Ahmed, T. Y.; Abdullah, O. G.; Mamand, S. M.; Aziz, S. B. Band structure study of pure and doped anatase titanium dioxide (TiO_2) using first-principle-calculations: role of atomic mass of transition metal elements (TME) on band gap reduction. *Opt. Quantum Electron.* **2024**, *56* (7), 1249.

(57) Morab, S.; Sundaram, M. M.; Pivrikas, A. Review on Charge Carrier Transport in Inorganic and Organic Semiconductors. *Coatings* **2023**, *13* (9), 1657.

(58) Abdelhamid, M. E.; O'Mullane, A. P.; Snook, G. A. Storing energy in plastics: a review on conducting polymers & their role in electrochemical energy storage. *RSC Advances* **2015**, *5* (15), 11611-11626.

(59) Xie, S.; Zhang, Q.; Liu, G.; Wang, Y. Photocatalytic and photoelectrocatalytic reduction of CO_2 using heterogeneous catalysts with controlled nanostructures. *Chem. Commun.* **2016**, *52* (1), 35-59.

(60) Ibhadon, A. O.; Fitzpatrick, P. Heterogeneous photocatalysis: recent advances and applications. *Catalysts* **2013**, *3* (1), 189-218.

(61) Degreen. Sonne Strahlungsintensitaet. **2006**.

(62) Navalón, S.; Dhakshinamoorthy, A.; Álvaro, M.; Ferrer, B.; García, H. Metal–organic frameworks as photocatalysts for solar-driven overall water splitting. *Chem. Rev.* **2023**, *123* (1), 445-490.

(63) Wang, L.; Yu, J. Chapter 1 - Principles of photocatalysis. In *Interface Science and Technology*, Vol. 35; Elsevier, **2023**; pp 1-52.

(64) Quan, H.; Gao, Y.; Wang, W. Tungsten oxide-based visible light-driven photocatalysts: crystal and electronic structures and strategies for photocatalytic efficiency enhancement. *Inorg. Chem. Front.* **2020**, *7* (4), 817-838.

(65) Schuurmans, J. H. A.; Masson, T. M.; Zondag, S. D. A.; Buskens, P.; Noël, T. Solar-Driven Continuous CO_2 Reduction to CO and CH_4 using Heterogeneous Photothermal Catalysts: Recent Progress and Remaining Challenges. *ChemSusChem* **2024**, *17* (4), e202301405.

(66) Sun, D.; Liu, W.; Qiu, M.; Zhang, Y.; Li, Z. Introduction of a mediator for enhancing photocatalytic performance via post-synthetic metal exchange in metal–organic frameworks (MOFs). *Chem. Commun.* **2015**, *51* (11), 2056-2059.

(67) Wang, Z.; Hisatomi, T.; Li, R.; Sayama, K.; Liu, G.; Domen, K.; Li, C.; Wang, L. Efficiency accreditation and testing protocols for particulate photocatalysts toward solar fuel production. *Joule* **2021**, *5* (2), 344-359.

(68) Saruyama, M.; Pelicano, C. M.; Teranishi, T. Bridging electrocatalyst and co-catalyst studies for solar hydrogen production via water splitting. *Chem. Sci.* **2022**, *13* (10), 2824-2840.

(69) Bhattacharyya, A.; Gutiérrez, M.; Cohen, B.; Valverde-González, A.; Iglesias, M.; Douhal, A. How does the metal doping in mixed metal MOFs influence their photodynamics? A direct evidence for improved photocatalysts. *Mater. Today Energy* **2022**, *29*, 101125.

(70) Lakhera, S. K.; Rajan, A.; T.P, R.; Bernaurdshaw, N. A review on particulate photocatalytic hydrogen production system: Progress made in achieving high energy conversion efficiency and key challenges ahead. *Renew. Sust. Energ. Rev.* **2021**, *152*, 111694.

(71) Pal, U.; Ghosh, S.; Chatterjee, D. Effect of sacrificial electron donors on hydrogen generation over visible light–irradiated nonmetal-doped TiO_2 photocatalysts. *Trans. Met. Chem.* **2012**, *37* (1), 93-96.

(72) Romito, D.; Govind, C.; Nikolaou, V.; Fernández-Terán, R. J.; Stoumpidi, A.; Agapaki, E.; Charalambidis, G.; Diring, S.; Vauthey, E.; Coutsolelos, A. G.; et al. Dye-sensitized photocatalysis: hydrogen evolution and alcohol-to-aldehyde oxidation without sacrifical electron donor. *Angew. Chem. Int. Ed.* **2024**, *63* (12), e202318868.

(73) Rumayor, M.; Corredor, J.; Rivero, M. J.; Ortiz, I. Prospective life cycle assessment of hydrogen production by waste photoreforming. *J. Clean. Prod.* **2022**, *336*, 130430.

(74) Bie, C.; Wang, L.; Yu, J. Challenges for photocatalytic overall water splitting. *Chem* **2022**, *8* (6), 1567-1574.

(75) Yan, H.; Yang, J.; Ma, G.; Wu, G.; Zong, X.; Lei, Z.; Shi, J.; Li, C. Visible-light-driven hydrogen production with extremely high quantum efficiency on Pt–PdS/CdS photocatalyst. *J. Catal.* **2009**, *266* (2), 165-168.

(76) Nishiyama, H.; Yamada, T.; Nakabayashi, M.; Maehara, Y.; Yamaguchi, M.; Kuromiya, Y.; Nagatsuma, Y.; Tokudome, H.; Akiyama, S.; Watanabe, T.; et al. Photocatalytic solar hydrogen production from water on a 100-m^2 scale. *Nature* **2021**, *598* (7880), 304-307.

(77) Zhou, P.; Navid, I. A.; Ma, Y.; Xiao, Y.; Wang, P.; Ye, Z.; Zhou, B.; Sun, K.; Mi, Z. Solar-to-hydrogen efficiency of more than 9% in photocatalytic water splitting. *Nature* **2023**, *613* (7942), 66-70.

(78) Halmann, M. Photoelectrochemical reduction of aqueous carbon dioxide on p-type gallium phosphide in liquid junction solar cells. *Nature* **1978**, *275* (5676), 115-116.

(79) Hemminger, J. C.; Carr, R.; Somorjai, G. A. The photoassisted reaction of gaseous water and carbon dioxide adsorbed on the $SrTiO_3$ (111) crystal face to form methane. *Acc. Chem. Res.* **1978**, *57* (1), 100-104.

(80) Wu, X.-P.; Gagliardi, L.; Truhlar, D. G. Cerium metal–organic framework for photocatalysis. *J. Am. Chem. Soc.* **2018**, *140* (25), 7904-7912.

(81) Nguyen, T. D.; Van Tran, T.; Singh, S.; Phuong, P. T. T.; Bach, L. G.; Nanda, S.; Vo, D.-V. N. Conversion of carbon dioxide into formaldehyde. In conversion of carbon dioxide into hydrocarbons Vol. 2 Technology, Inamuddin, Asiri, A. M., Lichtfouse, E. Eds.; Springer International Publishing, **2020**; pp 159-183.

(82) Kovačič, Ž.; Likozar, B.; Huš, M. Photocatalytic CO_2 Reduction: A review of ab initio mechanism, kinetics, and multiscale modeling simulations. *ACS Catal.* **2020**, *10* (24), 14984-15007.

(83) Wang, Y.; Chen, E.; Tang, J. Insight on reaction pathways of photocatalytic CO_2 conversion. *ACS Catal.* **2022**, *12* (12), 7300-7316.

(84) Albero, J.; Peng, Y.; García, H. Photocatalytic CO_2 Reduction to C_{2+} Products. *ACS Catal.* **2020**, *10* (10), 5734-5749.

(85) Ren, J.; Ouyang, S.; Xu, H.; Meng, X.; Wang, T.; Wang, D.; Ye, J. Targeting Activation of CO_2 and H_2 over Ru-loaded ultrathin layered double hydroxides to achieve efficient photothermal CO_2 methanation in flow-type system. *Adv. Energy Mater.* **2017**, *7*.

(86) Cabrero-Antonino, M.; Remiro-Buenamañana, S.; Souto, M.; García-Valdivia, A. A.; Choquesillo-Lazarte, D.; Navalón, S.; Rodríguez-Diéguez, A.; Mínguez Espallargas, G.; García, H. Design of cost-efficient and photocatalytically active Zn-based MOFs decorated with Cu_2O nanoparticles for CO_2 methanation. *Chem. Commun.* **2019**, *55* (73), 10932-10935.

(87) Furukawa, H.; Cordova, K. E.; O'Keeffe, M.; Yaghi, O. M. The Chemistry and Applications of Metal-Organic Frameworks. *Science* **2013**, *341* (6149), 1230444.

(88) Zhou, H.-C. J.; Kitagawa, S. Metal–Organic Frameworks (MOFs). *Chem. Soc. Rev.* **2014**, *43* (16), 5415-5418.

(89) Robson, R.; Abrahams, B. F.; Batten, S. R.; Gable, R. W.; Hoskins, B. F.; Liu, J. Crystal engineering of novel materials composed of infinite two- and three-dimensional frameworks. In *Supramolecular Architecture*, ACS Symposium Series, Vol. 499; American Chemical Society, **1992**; pp 256-273.

(90) Yaghi, O. M.; Li, G.; Li, H. Selective binding and removal of guests in a microporous metal–organic framework. *Nature* **1995**, *378* (6558), 703-706.

(91) Li, H.; Eddaoudi, M.; O'Keeffe, M.; Yaghi, O. M. Design and synthesis of an exceptionally stable and highly porous metal-organic framework. *Nature* **1999**, *402* (6759), 276-279.

(92) Ferey, G. The new microporous compounds and their design. *Comptes Rendus de l'Académie des Sciences - Series IIC - Chemistry* **1998**, *1* (1), 1-13.

(93) Kitagawa, S.; Kondo, M. Functional micropore chemistry of crystalline metal complex-assembled compounds. *Bull. Chem. Soc. Jpn.* **2006**, *71* (8), 1739-1753.

(94) Vermoortele, F. B., B.; Le Bars, G.; Van de Voorde, B.; Vandichel, M.; Houthoofd, K.; Vimont, A.; Daturi, M.; Waroquier, M.; Van Speybroeck, V.; Kirschhock, C.; De Vos, D. . Synthesis modulation as a tool to increase the catalytic activity of metal-organic frameworks: the unique case of UiO-66(Zr). *J. Am. Chem. Soc.* **2013**, *135*, 11465−11468.

(95) Férey, G. Hybrid porous solids: past, present, future. *Chem. Soc. Rev.* **2008**, *37* (1), 191-214.

(96) Dhakshinamoorthy, A.; Asiri, A. M.; Garcia, H. Metal–organic framework (MOF) compounds: photocatalysts for redox reactions and solar fuel production. *Angew. Chem. Int. Ed.* **2016**, *55* (18), 5414-5445.

(97) Li, J.; Bhatt, P. M.; Li, J.; Eddaoudi, M.; Liu, Y. Recent progress on microfine design of metal–organic frameworks: structure regulation and gas sorption and separation. *Adv. Mater.* **2020**, *32* (44), 2002563.

(98) Cui, W.-G.; Hu, T.-L.; Bu, X.-H. Metal–organic framework materials for the separation and purification of light hydrocarbons. *Adv. Mater.* **2020**, *32* (3), 1806445.

(99) Lázaro, I. A.; Forgan, R. S. Application of zirconium MOFs in drug delivery and biomedicine. *Coord. Chem. Rev.* **2019**, *380*, 230-259.

(100) Bavykina, A.; Kolobov, N.; Khan, I. S.; Bau, J. A.; Ramirez, A.; Gascon, J. Metal–organic frameworks in heterogeneous catalysis: recent progress, new trends, and future perspectives. *Chem. Rev.* **2020**, *120* (16), 8468-8535.

(101) Downes, C. A.; Marinescu, S. C. Electrocatalytic metal–organic frameworks for energy applications. *ChemSusChem* **2017**, *10* (22), 4374-4392.

(102) Felix Sahayaraj, A.; Joy Prabu, H.; Maniraj, J.; Kannan, M.; Bharathi, M.; Diwahar, P.; Salamon, J. Metal–organic frameworks (MOFS): the next generation of materials for catalysis, gas storage, and separation. *J. Inorg. Organomet. Polym. Mater.* **2023**, *33* (7), 1757-1781.

(103) Sun, D.; Li, Z. Robust Ti- and Zr-based metal-organic frameworks for photocatalysis. *Chin. J. Chem.* **2017**, *35* (2), 135-147.

(104) Cavka, J. H.; Jakobsen, S.; Olsbye, U.; Guillou, N.; Lamberti, C.; Bordiga, S.; Lillerud, K. P. A new zirconium inorganic building brick forming metal organic frameworks with exceptional stability. *J. Am. Chem. Soc.* **2008**, *130* (42), 13850-13851.

(105) Dan-Hardi, M.; Serre, C.; Frot, T.; Rozes, L.; Maurin, G.; Sanchez, C.; Férey, G. A New photoactive crystalline highly porous titanium(iv) dicarboxylate. *J. Am. Chem. Soc.* **2009**, *131* (31), 10857-10859.

(106) Wu, H.; Chua, Y. S.; Krungleviciute, V.; Tyagi, M.; Chen, P.; Yildirim, T.; Zhou, W. Unusual and highly tunable missing-linker defects in zirconium metal–organic framework UiO-66 and their important effects on gas adsorption. *J. Am. Chem. Soc.* **2013**, *135* (28), 10525-10532.

(107) Biswas, S.; Zhang, J.; Li, Z.; Liu, Y.-Y.; Grzywa, M.; Sun, L.; Volkmer, D.; Van Der Voort, P. Enhanced selectivity of CO_2 over CH_4 in sulphonate-, carboxylate- and iodo-functionalized UiO-66 frameworks. *Dalton Trans.* **2013**, *42* (13), 4730-4737.

(108) Cabrero-Antonino, M.; Melillo, A.; Montero-Lanzuela, E.; Álvaro, M.; Ferrer, B.; Vayá, I.; Baldoví, H. G.; Navalón, S. Solar-driven gas phase photocatalytic CO_2 methanation by multimetallic UiO-66 solids decorated with RuOx nanoparticles. *Chem. Eng. J.* **2023**, *468*, 143553.

(109) Zhang, H.-M.; Wang, Y.-L.; Zhu, X.-F.; Huang, Z.-Z.; Pang, D.-D.; Wang, K.; Wang, C.-H.; Song, Z.-X.; Yin, S.-Q.; Chang, L.-L.; et al. Application of UiO-66 and its composites for remediation and resource recovery of typical environmental contaminants: a review. *Rare Metals* **2024**, *43* (6), 2498-2526.

(110) Vilela, S. M. F.; Salcedo-Abraira, P.; Colinet, I.; Salles, F.; De Koning, M. C.; Joosen, M. J. A.; Serre, C.; Horcajada, P. Nanometric MIL-125-NH_2 metal–organic framework as a potential nerve agent antidote carrier. *Nanomaterials* **2017**, *7* (10), 321.

(111) Liu, F.; Rincón, I.; Baldoví, H. G.; Dhakshinamoorthy, A.; Horcajada, P.; Rojas, S.; Navalón, S.; Fateeva, A. Porphyrin-based MOFs for photocatalysis in water: advancements in solar fuels generation and pollutants degradation. *Inorg. Chem. Front.* **2024**, *11* (8), 2212-2245.

(112) Nasalevich, M. A.; van der Veen, M.; Kapteijn, F.; Gascon, J. Metal–organic frameworks as heterogeneous photocatalysts: advantages and challenges. *CrystEngComm* **2014**, *16* (23), 4919-4926.

(113) Wang, Q.; Gao, Q.; Al-Enizi, A. M.; Nafady, A.; Ma, S. Recent advances in MOF-based photocatalysis: environmental remediation under visible light. *Inorg. Chem. Front.* **2020**, *7* (2), 300-339.

(114) Hendrickx, K.; Vanpoucke, D. E. P.; Leus, K.; Lejaeghere, K.; Van Yperen-De Deyne, A.; Van Speybroeck, V.; Van Der Voort, P.; Hemelsoet, K. Understanding Intrinsic light absorption properties of UiO-66 Frameworks: A combined theoretical and experimental study. *Inorg. Chem.* **2015**, *54* (22), 10701-10710.

(115) Dai, S. M.-L., E.; Tissot, A.; Baldoví, H. G.; García, H.; Navalón, S.; Serre, C. . Room temperature design of Ce(IV)-MOFs: from photocatalytic HER and OER to overall water splitting under simulated sunlight irradiation. *Chem. Sci.* **2023**, *14*, 3451–3461.

(116) Wu, X.-P.; Gagliardi, L.; Truhlar, D. G. Metal doping in cerium metal-organic frameworks for visible-response water splitting photocatalysts. *J. Chem. Phys.* **2019**, *150* (4).

(117) Jaryal, R.; Kumar, R.; Khullar, S. Mixed metal-metal organic frameworks (MM-MOFs) and their use as efficient photocatalysts for hydrogen evolution from water splitting reactions. *Coord. Chem. Rev.* **2022**, *464*, 214542.

(118) Santaclara, J. G.; Olivos-Suarez, A. I.; Gonzalez-Nelson, A.; Osadchii, D.; Nasalevich, M. A.; van der Veen, M. A.; Kapteijn, F.; Sheveleva, A. M.; Veber, S. L.; Fedin, M. V.; et al. Revisiting the Incorporation of Ti(IV) in UiO-type Metal–organic frameworks: metal exchange versus grafting and their implications on photocatalysis. *Chem. Mater.* **2017**, *29* (21), 8963-8967.

(119) Santiago Portillo, A.; Baldoví, H. G.; García Fernandez, M. T.; Navalón, S.; Atienzar, P.; Ferrer, B.; Alvaro, M.; Garcia, H.; Li, Z. Ti as mediator in the photoinduced electron transfer of mixed-metal NH2–UiO-66(Zr/Ti): Transient absorption spectroscopy study and application in photovoltaic cell. *J. Phys. Chem. C* **2017**, *121* (12), 7015-7024.

(120) Xiang, W. Z., Y.; Chen, Y.; Liu, C.-J.; Tu, X. Synthesis, characterization and application of defective metal-organic frameworks: Current status and perspectives. *J. Mater. Chem. A* **2020**, *8*, 21526–21546.

(121) Hou, X. W., J.; Mousavi, B.; Klomkliang, N.; Chaemchuen, S. Strategies for induced defects in metal-organic frameworks for enhancing adsorption and catalytic performance. *Dalton Trans.* **2022**, *51*, 8133–8159.

(122) Yuan, S. F., L.; Wang, K.; Bosch, M.; Lollar, C.; Sun, Y.; Qin, J.; Yang, X.; Zhang, P.; Wang, Q.; Zou, L.; Zhang, Y.; Zhang, L.; Fang, Y.; Li, J.; Zhou, H.-C. Stable metal–organic frameworks: design, synthesis, and applications. *Adv. Mater.* **2018**, *30*, 1704303.

(123) Bagheri, M. M., M.Y. Quasi-metal organic frameworks: Preparation, applications and future perspectives. *Coord. Chem. Rev.* **2022**, *468*, 214643.

(124) Forgan, R. S. Modulated self-assembly of metal–organic frameworks. *Chem. Sci.* **2020**, *11*, 4546-4562.

(125) Bueken, B. V., N.V.; Krajnc, A.; Smolders, S.; Taulelle, F.; Mellot-Draznieks, C.; Mali, G.; Bennett, T.D.; De Vos, D. Tackling the defect conundrum in UiO-66: a

mixed-linker approach to engineering missing linker defects. *Chem. Mater.* **2017**, *29*, 10478–10486.

(126) Ren, J. L., M.; Musyoka, N.M.; Langmi, H.W.; Mathe, M.; Liao, S.; Pang, W. Structural defects in metal–organic frameworks (MOFs): Formation, detection and control towards practices of interests. *Coord. Chem. Rev.* **2017**, *349*, 169–197.

(127) Ma, X.; Wang, L.; Zhang, Q.; Jiang, H.-L. Switching on the photocatalysis of metal–organic frameworks by engineering structural defects. *Angew. Chem. Int. Ed.* **2019**, *58*, 12175 –12179.

(128) Gomes Silva, C.; Luz, I.; Llabres i Xamena, F. X.; Corma, A.; Garcia, H. Water stable Zr–benzenedicarboxylate metal–organic frameworks as photocatalysts for hydrogen generation. *Chem. Eur. J.* **2010**, *16*, 11133-11138.

(129) Taddei, M. When defects turn into virtues: The curious case of zirconium-based metal-organic frameworks. *Coord. Chem. Rev.* **2017**, *343*, 1-24.

(130) Shearer, G. C.; Chavan, S.; Bordiga, S.; Svelle, S.; Olsbye, U.; Lillerud, K. P. Defect engineering: tuning the porosity and composition of the metal–organic framework UiO-66 via modulated synthesis. *Chem. Mater.* **2016**, *28* (11), 3749-3761.

(131) An, Y.; Liu, Y.; An, P.; Dong, J.; Xu, B.; Dai, Y.; Qin, X.; Zhang, X.; Whangbo, M.-H.; Huang, B. NiII Coordination to an Al-based metal–organic framework made from 2-Aminoterephthalate for photocatalytic overall water splitting. *Angew. Chem. Int. Ed.* **2017**, *56* (11), 3036-3040.

(132) Melillo, A. C.-A., M.; Ferrer, B.; Dhakshinamoorthy, A.; Baldoví, H.G.; Navalón, S. MOF-on-MOF composites with UiO-66-based materials as photocatalysts for the overall water splitting under sunlight Irradiation. *Energy Fuels* **2023**, *37*, 5457–5468.

(133) Yang, J.; Wang, D.; Han, H.; Li, C. Roles of co-catalysts in photocatalysis and photoelectrocatalysis. *Acc. Chem. Res.* **2013**, *46* (8), 1900-1909.

(134) Gomes Silva, C.; Luz, I.; Llabrés i Xamena, F. X.; Corma, A.; García, H. Water Stable Zr–benzenedicarboxylate metal–organic frameworks as photocatalysts for hydrogen generation. *Chem. Eur. J.* **2010**, *16* (36), 11133-11138.

(135) Xiao, J.-D.; Shang, Q.; Xiong, Y.; Zhang, Q.; Luo, Y.; Yu, S.-H.; Jiang, H.-L. Boosting photocatalytic hydrogen production of a metal–organic framework decorated with platinum nanoparticles: The Platinum Location Matters. *Angew. Chem. Int. Ed.* **2016**, *55* (32), 9389-9393.

(136) Hao, X.; Jin, Z.; Yang, H.; Lu, G.; Bi, Y. Peculiar synergetic effect of MoS2 quantum dots and graphene on Metal-Organic Frameworks for photocatalytic hydrogen evolution. *Appl. Catal. B. Environ.* **2017**, *210*, 45-56.

(137) Li, F.; Wang, D.; Xing, Q.-J.; Zhou, G.; Liu, S.-S.; Li, Y.; Zheng, L.-L.; Ye, P.; Zou, J.-P. Design and syntheses of MOF/COF hybrid materials via postsynthetic covalent modification: An efficient strategy to boost the visible-light-driven photocatalytic performance. *Appl. Catal. B. Environ.* **2019**, *243*, 621-628.

(138) Guo, Y.; Li, J.; Yang, X.; Lou, Y.; Chen, J. $Zn_{0.5}Cd_{0.5}S$/MIL-125-NH2(Ti) nanocomposites: Highly efficient and stable photocatalyst for hydrogen production under visible light. *Inorg. Chem. Commun.* **2020**, *112*, 107714.

(139) Wang, Y.; Zhang, Y.; Jiang, Z.; Jiang, G.; Zhao, Z.; Wu, Q.; Liu, Y.; Xu, Q.; Duan, A.; Xu, C. Controlled fabrication and enhanced visible-light photocatalytic hydrogen production of Au@CdS/MIL-101 heterostructure. *Appl. Catal. B. Environ.* **2016**, *185*, 307-314.

(140) Wang, X.; Zhang, X.; Zhou, W.; Liu, L.; Ye, J.; Wang, D. An ultrathin porphyrin-based metal-organic framework for efficient photocatalytic hydrogen evolution under visible light. *Nano Energy.* **2019**, *62*, 250-258.

(141) Zhang, J. B., T.; Huang, H.; Yu, M.-H.; Fan, X.; Chang, Z.; Bu, X.-H. Metal-organic-framework-based photocatalysts optimized by spatially separated co-catalysts for overall water splitting. *Adv. Mater.* **2020**, *32*, 2004747.

(142) Melillo, A.; Cabrero-Antonino, M.; Navalón, S.; Alvaro, M.; Ferrer, B.; García, H. Enhancing visible light photocatalytic activity for overall water splitting in UiO-

66 by controlling metal node composition. *Appl. Catal. B. Environ.* **2020**, *278*, 119345.

(143) Cabrero-Antonino, M.; Albero, J.; García-Vallés, C.; Álvaro, M.; Navalón, S.; García, H. Plasma-induced defects enhance the visible-light photocatalytic activity of MIL-125(Ti)-NH_2 for overall water splitting. *Chem. Eur. J.* **2020**.

(144) Salcedo-Abraira, P.; Babaryk, A. A.; Montero-Lanzuel, E.; Contreras-Almengor, O. R.; Cabrero-Antonino, M.; Svensson Grape, E. S.; Willhammar, T.; Navalón, S.; Elkäim, E.; García, H.; et al. A novel porous Ti-squarate as efficient photocatalyst in the overall water splitting reaction under simulated sunlight irradiation. *Adv. Mater.* **2021**, *33*, 2106627.

(145) Salcedo-Abraira, P.; Vilela, S. M. F.; Babaryk, A. A.; Cabrero-Antonino, M.; Gregorio, P.; Salles, F.; Navalón, S.; García, H.; Horcajada, P. Nickel phosphonate MOF as efficient water splitting photocatalyst. *Nano Res.* **2021**, *14*, 450–457.

(146) Gikonyo, B. M.-L., E.; Baldovi, H.G.; De, S.; Journet, C.; Devic, T.; Guillou, N.; Tiana, D.; Navalon, S.; Fateeva, A. . Mixed-metal Zr/Ti MIL-173 porphyrinic metal-organic frameworks as efficient photocatalysts towards solar-driven overall water splitting. *J. Mater. Chem. A* **2022**, *10*, 24938-24950.

(147) Fu, Y.; Sun, D.; Chen, Y.; Huang, R.; Ding, Z.; Fu, X.; Li, Z. An amine-functionalized titanium metal–organic framework photocatalyst with visible-light-induced activity for CO_2 reduction. *Angew. Chem. Int. Ed.* **2012**, *51* (14), 3364-3367.

(148) Memon, M. A.; Jiang, Y.; Hassan, M. A.; Ajmal, M.; Wang, H.; Liu, Y. Heterogeneous catalysts for carbon dioxide methanation: a view on catalytic performance. *Catalysts* **2023**, *13* (12), 1514.

(149) Cabrero-Antonino, M.; Ferrer, B.; Baldoví, H. G.; Navalón, S. Toward solar-driven photocatalytic CO_2 methanation under continuous flow operation using benchmark MIL-125(Ti)–NH2 supported ruthenium nanoparticles. *Chem. Eng. J.* **2022**, *445*, 136426.

Chapter 2. Objectives

The aim of the present thesis was to develop MOF-based photocatalysts to produce solar fuels from sustainable feedstocks, water and CO_2.

The specific objectives of the chapters of the thesis can be described as follows:

Chapter 3 - To evaluate the photocatalytic activity of UiO-66(Zr)-X (X: H, NH_2 or NO_2) and MIL-125(Ti)-NH_2 solids for solar-driven hydrogen generation from glycerol aqueous solutions as sustainable feedstocks. To study the influence of supported platinum NPs as co-catalysts on the most active MOF and to evaluate the photocatalytic activity and assess photocatalyst stability over time by reusing the photocatalyst for consecutive cycles. To study the reaction mechanism by means of transient absorption and photoluminescence spectroscopies together with photocurrent measurements. The results are given in Chapter 3, Section 3.4 - Results and discussion.

Chapter 4 - To study the photocatalytic water splitting reaction using defective UiO-66(Zr)-X (X: NH_2 or NO_2) solids prepared by modulated synthesis. To prepare defective UiO-66 solids with different equivalents of acetic acid or trifluoroacetic acid as modulators with respect to the MOF organic ligand. To evaluate the photocatalytic activity of defective MOFs for HER and OWS under simulated sunlight irradiation. To study the photocatalytic stability of the most active sample after repeated consecutive reuse. To study in depth the observed order of photocatalytic activity for the series of samples by spectroscopic, analytical, electrochemical and computational methods, among others. These results are given in Chapter 4, Section 4.4 - Results and discussion.

Chapter 5 - To develop MOF-based photocatalysts consisting of RuO_x NPs supported on UiO-66(Zr)-X (X: NH_2 or NO_2) or on UiO-66(Zr/Ti)-X (X: NH_2 or NO_2) for the gas-phase CO_2 hydrogenation under simulated sunlight irradiation. To

compare the photocatalytic activity of the materials and study the stability of the most active sample after reuse. To further study the observed order of activity of the samples and the reaction mechanism by spectroscopic techniques including transient absorption spectrocopy (TAS), spin resonance, photoluminescence (PL) and electrochemical impedance spectroscopy (EIS) methods, among others. To investigate the photocatalytic CO_2 hydrogenation pathway by Fourier transform-infrared spectroscopy (FT-IR) spectroscopy. These results are given in Chapter 5, Section 5.4 - Results and discussion.

Chapter 3. Photocatalytic hydrogen production from glycerol aqueous solutions as sustainable feedstocks using Zr-based UiO-66 materials under simulated sunlight irradiation

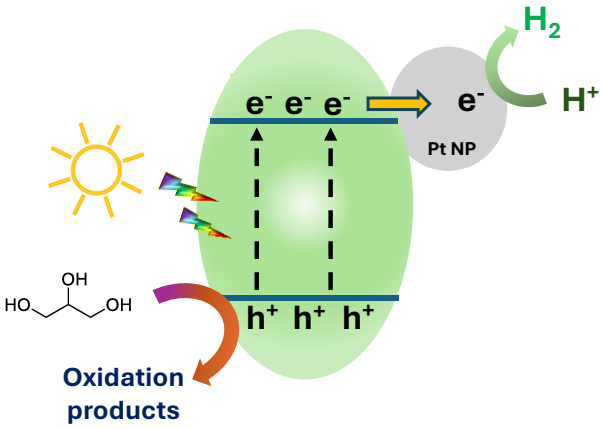

3.1 Abstract

There is an increasing interest in developing cost-effective technologies to produce hydrogen from sustainable resources. Herein, a comprehensive study on the use of MOFs as heterogeneous photocatalysts for H_2 generation from photoreforming of glycerol aqueous solutions under simulated sunlight irradiation is shown. The list of materials employed in this study include some of the benchmark Zr-MOFs such as UiO-66(Zr)-X (X: H, NO_2, NH_2) as well as MIL-125(Ti)-NH_2 as reference Ti-MOF. Among these solids, UiO-66(Zr)-NH_2 exhibits the highest photocatalytic H_2 production, and this observation is attributed due to its adequate energy level. The photocatalytic activity of UiO-66(Zr)-NH_2 can be increased by deposition of small Pt NPs as reference noble metal co-catalyst within the MOF network. This photocatalyst is effectively used for H_2 generation at least for 70 h without loss of activity. The crystallinity of MOF and Pt particle size were maintained as revealed by powder X-ray diffraction and transmission electron microscopy measurements, respectively. Evidence in support of the occurrence of photoinduced charge separation with Pt@UiO-66(Zr)-NH_2 is provided from transient absorption and photoluminescence spectroscopies together with photocurrent measurements. This study exemplifies the possibility of using MOFs as photocatalysts for the solar-driven H_2 generation using sustainable feedstocks.

3.2 Introduction

Fossil fuels are still employed to supply more than 80 % of the world energy demand[1]. The combustion of fossil fuels is directly connected to air pollution, emissions of greenhouse gases and climate change, resulting in negative impacts for the environment and the human health[1-3]. For these reasons, there is an urgent need to develop alternative sustainable and renewable energy vectors that favor the decarbonization of the current energy system[4, 5]. In this context, H_2 is recognized as an ideal carbon-free energy vector candidate[6-8]. Today, however, mostly H_2 is produced via steam reforming of hydrocarbons at high temperature (> 650-1000 °C), with most energy requirements from non-renewable fossil fuels[6, 9]. Therefore, important scientific and technological efforts are being made to produce H_2 in a sustainable and renewable manner[7, 8]. Electrolysis processes are relatively efficient and mature technologies for decomposing H_2O into H_2 and O_2 that can operate using, for example, renewable photovoltaic energy[10]. The economic viability of this technology is, however, still hampered due to the investment and operation costs[7, 8, 11, 12]. Alternatively, solar-driven photocatalytic water splitting into H_2 and O_2 using heterogeneous catalysts is a simpler and cheaper technology with potential application at medium-large scale[13-15]. For this purpose, it would be necessary further increase the relatively low efficiencies achieved using inorganic semiconductors or investigate other type of photocatalysts[13, 15, 16].

MOFs[17-19] are considered among the most versatile and tunable materials to act as active photocatalysts[20-23]. Photocatalytic overall water splitting using MOFs is still a challenging process which is in its infancy[24-26]. A more efficient though less ambitious process closer to real small to medium industrial applications is the

photocatalytic HER in the presence of sacrificial electron donors[27]. The research in the field of photocatalytic HER using MOFs is exceptional, and excellent achievements have been reached even under visible or sunlight irradiation[27-40]. Most of the reports in this area have employed sacrificial electron donors such as CH_3OH, TEOA or triethylamine to enhance the H_2 production[27-40]. The use of these sacrificial agents limits, however, the cost-effective real application. Alternatively, in a similar way to that reported for inorganic semiconductors[27, 41], the use of biomass or industrial byproducts feedstocks for H_2 production is envisioned as a promising solution[42, 43]. In this context, it is worth mentioning that biodiesel production generates about a 10 wt % of crude glycerol as by-product[44]. In this scenario, the development of technologies such as photoreforming of glycerol aqueous solution (Figure 1) will contribute to both the viability of biodiesel market and the production of sustainable H_2[42, 44]. Theoretically, complete glycerol photoreforming results in a H_2-to-CO_2 molar ratio of 2.33 (Figure 1a). The proposed reaction mechanism of glycerol photoreforming mainly using inorganic semiconductors is complicated and still under investigation.[45] Some studies have proposed that the oxidation process could proceed through different parallel reaction pathways involving initial oxidative C-C scission, oxidation of primary or secondary carbons (carbonyl group formation) or light-driven dehydration (Figure 1b)[46] Importantly, the reaction pathway determines the H_2-to-CO_2 molar ratio[46]. The higher extent of carbonyl group formation with respect to oxidative C-C rupture leads to the higher H_2:CO_2 molar ratio[47]. Some studies have also reported the formation of byproducts such as formaldehyde, CH_4 or CO among other possible products during glycerol photoreforming[45]. Other processes such as photocatalytic water splitting might also occur simultaneously. In the area of MOF-based materials, as far as it is known, there is only one example reporting the use of an inorganic semiconductor/MOF

composite termed as TiO_2@HKUST-1 was used for H_2 production from photoreforming of glycerol aqueous solutions (Figure 1a)[48].

(a) $$C_3H_8O_3 + 3\,H_2O + h\upsilon \geq Eg_{photocatalyst} \rightarrow 3\,CO_2 + 7\,H_2$$

(b)

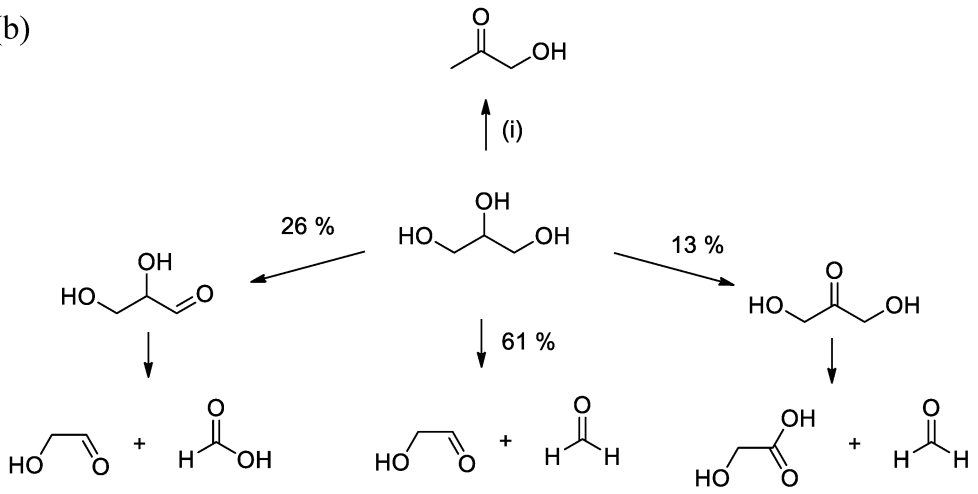

Figure 1. (a) Stoichiometry of glycerol photoreforming. (b) Proposed initial reaction sequences of glycerol photoreforming using Rh/TiO_2. Note: Light-driven dehydration to hydroxyacetone constitutes a side reaction (i)[46].

With these precedents in mind, the present study investigates in a comprehensive manner the H_2 generation from photoreforming of glycerol aqueous solution using Zr-based UiO-66 materials under simulated sunlight irradiation. Particularly, three UiO-66(Zr)-X (X: H, NH_2, NO_2) solids having different energy band levels were selected for the study. For comparison, the photoactivity of a Ti-based MOF reference material such as MIL-125(Ti)-NH_2 was tested. The most active UiO-66(Zr)-NH_2 photocatalyst of the series was further modified with Pt NPs as the noble metal reference co-catalyst. The photocatalyst activity and stability of the Pt@UiO-66(Zr)-NH_2 was also studied. The reaction mechanism of

the most active sample was further studied by transition absorption and photoluminescence spectroscopies as well as by photocurrent measurements.

3.3 Experimental section

3.3.1 Materials

All the chemicals employed in this work were of analytical or high- performance liquid chromatography (HPLC) grade and supplied by Merck.

3.3.2 Synthesis and characterization of the MOF- based materials

The MOFs under study, namely, UiO-66(Zr), UiO-66(Zr)-NH_2, UiO-66(Zr)-NO_2 and MIL-125(Ti)-NH_2, were prepared according to previously reported procedures[49, 50]. Pt NPs (1 wt %) were supported on UiO-66(Zr)-NH_2 by using the photodeposition method (Section 3.8.1). The series of materials were characterized by several techniques including powder X-ray diffraction (PXRD), UV-Vis spectroscopy, X-ray photoelectron spectroscopy (XPS), thermogravimetric analysis (TGA), isothermal N_2 adsorption, and scanning (SEM) and transmission (TEM) electron microscopies equipped with an energy-dispersive X-ray (EDX) detector. The most active Pt@UiO-66(Zr)-NH_2 and/or UiO-66(Zr)-NH_2 photocatalysts were also characterized by means of TAS and PL spectroscopies and photocurrent measurements. Section 3.8 summarizes the details of these experimental procedures and the characterization techniques employed in this study.

3.3.3 Photocatalytic hydrogen generation from glycerol aqueous solution

Briefly, 5 mg of MOF photocatalyst was placed in a quartz reactor (50 mL) containing a glycerol aqueous mixture (20 mL), and then the system was sonicated (450 W) for 20 min to obtain a good MOF dispersion. To remove the air from the reactor, the system was purged with argon for 1 h. The MOF suspension while stirring was irradiated under simulated sunlight irradiation (Hamamatsu Hg-Xe lamp-150W-L8253; Hamamatsu spotlight source-L9566-04; Hamamatsu light guide A10014-50-0110; Lasing air mass (AM) 1.5 G type filter-81094). During the irradiation, the temperature and the pressure of the system were monitored. At the required time, the evolved gases were analyzed from the head space of the quartz reactor by direct connection to a Micro gas chromatography (GC) system (Agilent 490 Micro GC system equipped with a Molsieve 5 Å column and a Pore Plot Q column) that employed argon as the carrier gas. These photocatalytic measurements were carried out at least in triplicate trials, and the presented data correspond to the average of these experiments.

3.4 Results and discussion

3.4.1 Photocatalyst preparation and characterization

The selected MOFs under study include the series of Zr-based MOF with UiO-66 topology, namely, UiO-66(Zr), UiO-66(Zr)-NH_2 and UiO-66(Zr)-NO_2. It should be remembered that the UiO-66 solids are considered as benchmark Zr-MOF photocatalysts[51]. One of the important features of these MOFs is that the presence of the electron donor or acceptor functional groups in the organic ligand can tune the energy level of the solids[51]. The photocatalytic activity of the most active

UiO-66 solid under study was compared with that of MIL-125(Ti)-NH_2 as reference Ti-MOF[52]. These four MOFs have been prepared by solvothermal method as previously reported and described in Section 3.8.[49, 50]. Figure 2a,b shows the characteristic diffraction patterns of the four MOFs under study that are in good agreement with their respective simulated patterns. In Figure 2c,d the thermogravimetric analyses of the MOFs that confirmed the thermal stability for all of the materials up to about 350 °C can be seen, being UiO-66(Zr) the most stable. Higher temperatures caused combustion of the ligands and a residue associated with the formation of ZrO_2 (Figure 2c) or TiO_2 (Figure 2d) remains.

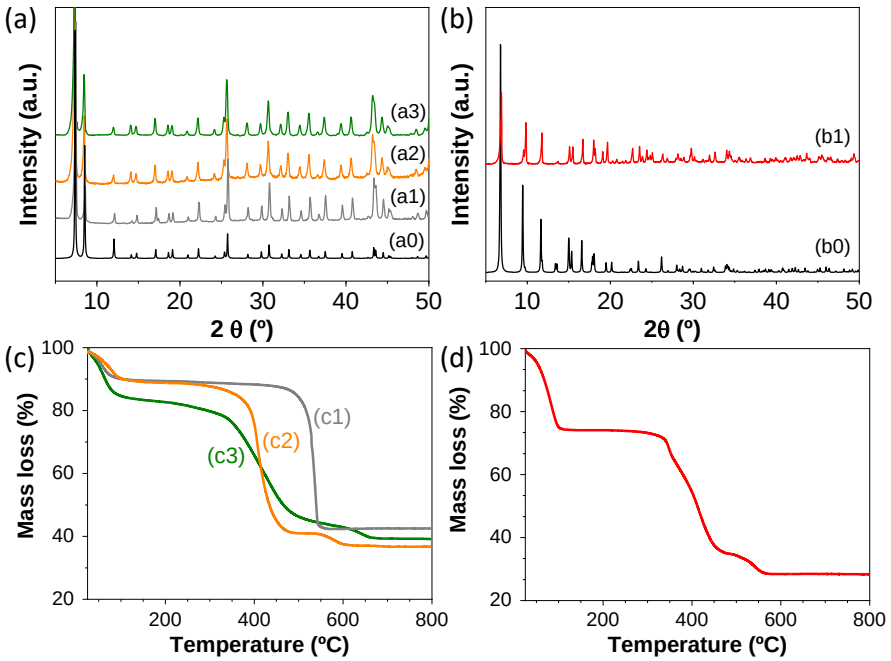

Figure 2. (a) XRD patterns of simulated UiO-66(Zr) (a0) and experimental UiO-66(Zr) (a1), UiO-66(Zr)-NO_2 (a2) and UiO-66(Zr)-NH_2 (a3). (b) XRD patterns of simulated (b0) and experimental MIL-125(Ti)-NH_2 (b1). (c) TGA of UiO-66(Zr) (c1), UiO-66(Zr)-NO_2 (c2), UiO-66(Zr)-NH_2 (c3) and MIL-125(Ti)-NH_2 (d).

XPS spectroscopy was used to characterize the oxidation state of the elements present in the MOFs under study. Figure 3 compiles the survey and XPS spectra of

MOFs, while the corresponding deconvolutions of the elements can be found in the Supporting Information (Section 3.8, Figures S1-S4). The C 1s spectra show the presence of a band centered at 284.4 eV assigned to C-C sp^2 of the terephthalate organic ligand. The C 1s spectra of UiO-66(Zr)-NH_2 and MIL- 125(Ti)- NH_2 exhibit an additional band at 285.5 eV due to the presence of the C-N bond in the amino functional groups. In the case of the UiO-66(Zr)-NO_2, a band appearing at 286 eV due to the nitro group's presence can be observed. The O 1s spectra of the four MOFs show a broad band that corresponds to the oxygen atoms present in the carboxylate (about 532 eV) and zirconium or titanium oxo clusters (529.8 eV). In the case of the UiO-66(Zr)-NO_2 sample, a band due to the oxygen atoms present in the nitro group (~532.5 eV) can be also assigned. The N 1s spectra of the amino- or nitro-based MOFs show their characteristic band centered at about 399 or 405 eV, respectively. The Zr 3d spectra of the UiO-66 samples exhibit two main bands characteristic of the Zr(IV) ions in the oxo clusters at 182.1 and 184.4 eV that correspond to the Zr $3d_{5/2}$ and Zr $3d_{3/2}$, respectively. In the case of the MIL-125(Ti)-NH_2 solid, the XPS Ti 2p due to the presence of Ti(IV) in the octameric oxo cluster resulted in the observation of Ti $2p_{1/2}$ (458 eV) and Ti $2p_{3/2}$ (464 eV) signals. In addition, FT-IR spectroscopy confirms the presence of the expected vibration bands of the carboxylates (around 1500 and 1300 cm^{-1}), amino (3518 - 3382 cm^{-1}) or nitro (1542 and 1498 cm^{-1}) groups present in the terephthalate organic ligand of the MOFs (Figure S5).

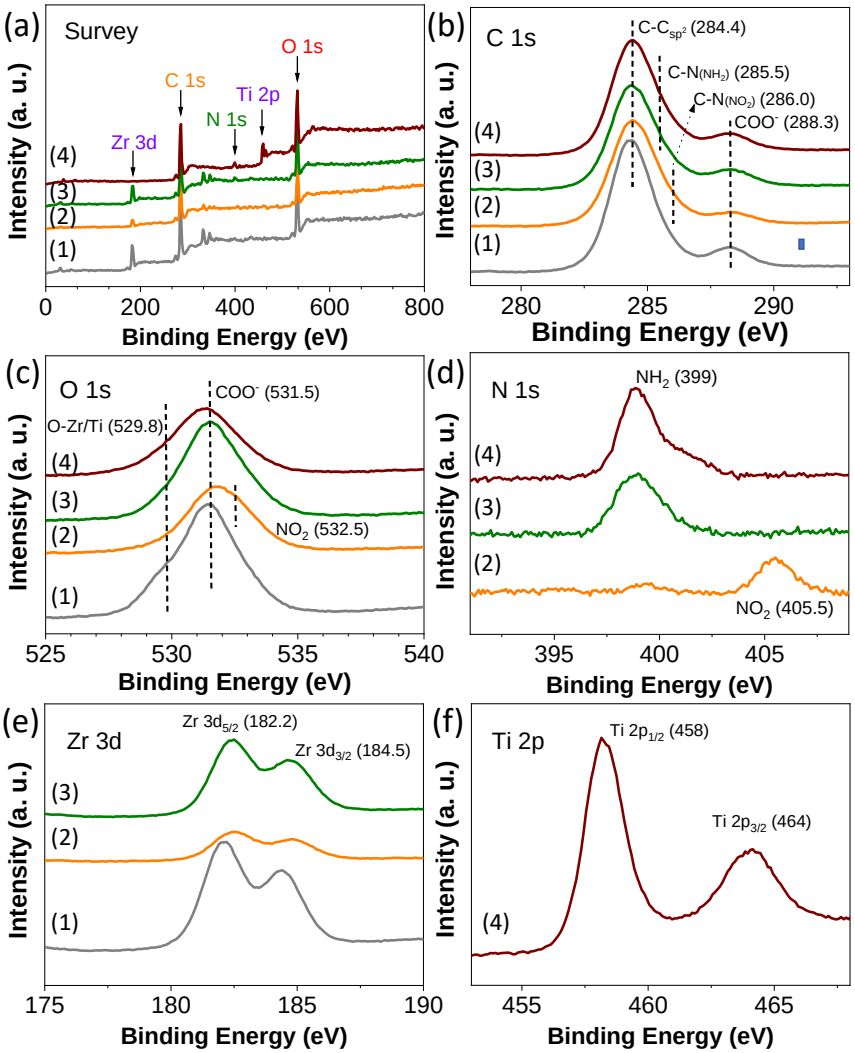

Figure 3. XPS survey spectrum (a) and high-resolution C 1s (b), O 1s (c), N 1s (d), Zr 3d (e) and Ti 2p (f) spectra of the MOFs under study. Legend: UiO-66(Zr) (grey), UiO-66(Zr)-NO_2 (orange), UiO-66(Zr)-NH_2 (green) and MIL-125(Ti)-NH_2 (wine red).

The porosity of the MOFs under study was measured by isothermal N_2 adsorption experiments (Table 1 and Figure S6). The estimated Brunauer–Emmett–Teller (BET) surface area and pore volumes are summarized in Table 1. Remarkably is the higher porosity of MIL-125(Ti)-NH_2 with respect to

the UiO-66 solids. SEM measurements showed that all the four MOFs under study exhibit average particle size distribution with values lower than 400 nm (Figures S7 and S8). Besides, SEM coupled to EDX reveals a good distribution of the elements in the samples (Figures S9-S12).

Table 1. BET surface area, pore volume, and average particle size and standard deviation of the MOFs under study.

	BET surface area (m^2/g)	**Pore volume (cm^3/g)**	**Average particle size and standard deviation (nm) [a]**
UiO-66(Zr)	650	0.23	114 / 92
UiO-66(Zr)-NO_2	782	0.42	109 / 48
UiO-66(Zr)-NH_2	922	0.43	366 / 201
MIL-125(Ti)-NH_2	1046	0.51	146 / 60

[a] Obtained from SEM measurements

One of the important aspects in heterogeneous photocatalysis is to determine the energy level of the solid employed for this purpose. Three main factors that determine this diagram in the case of MOFs include their band gap, HOCO and LUCO. Furthermore, the optical properties of the solids were studied by UV-Vis diffuse reflectance spectroscopy. Figure S13 shows that the UiO-66(Zr) exhibits a main broad absorption in the UV range due to the presence of the zirconium oxo clusters and the terephthalate organic ligands. The presence of the nitro and especially the amino group in the terephthalate ligand of the UiO-66(Zr) results in bathochromic shift in the absorption toward visible light region. From these optical absorption data and the corresponding Tauc plots, the optical band gap of UiO-66(Zr), UiO-66(Zr)-NO_2 and UiO-66(Zr)-NH_2 was estimated to be 3.91, 3.27 and 2.81 eV, respectively (Figure S13). Similarly, the optical band gap of the MIL- 125(Ti)-NH_2 was estimated as 2.65 eV (Figure S13). These results agree with previous analogous reports and confirm the simplicity to tune the band gap of MOFs by introducing one functional in the organic ligand[53]. Furthermore, XPS

spectroscopy was also employed to characterize the HOCO band maximum of the UiO-66(Zr)-X (X:H, NH_2, NO_2) and MIL-125(Ti)-NH_2 samples (Figure S14). From these values and the optical band gap the LUCO energy minimum was calculated (details in Supporting Information, Section 3.8.2. Characterization of the MOF-based materials). Figure 4 illustrates the energy band diagram of the MOF samples under study. The obtained results indicate that the presence of functional groups in the organic ligand reduces the band gap of the solids with respect to the parent MOF and determines the HOCO and LUCO values of the samples. As it is shown later, these energy level diagrams influence to a large extent the observed photocatalytic activity.

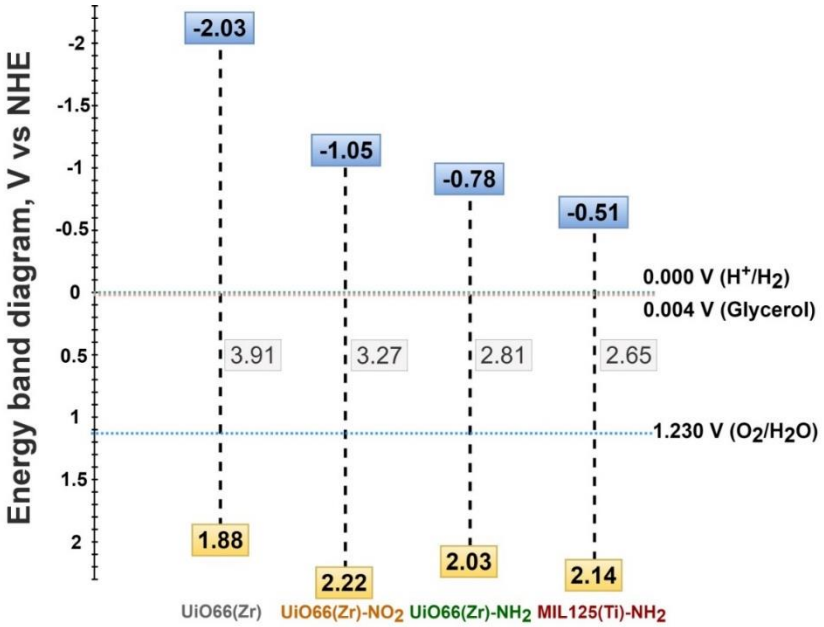

Figure 4. Energy band diagram for UiO-66(Zr)-H, UiO-66(Zr)-NO_2, UiO-66(Zr)-NH_2 and MIL-125(Ti)-NH_2. The proton and oxygen reduction and glycerol oxidation potentials are also indicated.

3.4.2 Photocatalytic results

Initially, the activity of UiO-66(Zr), UiO-66(Zr)-NH_2, UiO-66(Zr)-NO_2 and MIL- 125(Ti)-NH_2 was evaluated for the generation of H_2 from glycerol photoreforming in aqueous solution under simulated sunlight irradiation. The main role of glycerol is to act as an electron donor during the photocatalytic reaction by scavenging the photogenerated holes[45]. During this process, glycerol becomes oxidized through several possible steps resulting in the formation of CO_2 and H_2 (Figure 1). Furthermore, the photogenerated electrons have the ability to reduce protons to H_2[45]. Therefore, the evolved H_2 during the photocatalytic process is determined by the ability of the MOF-based photocatalyst for both glycerol oxidation and proton reduction towards H_2 production. As previously commented, glycerol photoreforming is a process that involves the generation of H_2:CO_2 with a molar ratio of 2.33 (Figure 1a). The results shown in Figure 5 indicate that the UiO-66(Zr)-NH_2 solid is the most active photocatalyst of the series for the HER with a H_2:CO_2 molar ratio of 7.3 after 3 h of reaction. It should be commented that, in all cases, the conversion of glycerol was below 0.5 %, and during the photocatalytic reaction, traces of CH_4 were also detected. The higher activity of UiO-66(Zr)-NH_2 respect to UiO-66(Zr)-NO_2 or UiO-66(Zr) is attributed to the higher ability of the former to absorb visible light. The higher photoactivity of UiO-66(Zr)-NH_2 compared to MIL - 125(Ti)-NH_2 is remarkable even though the slightly higher band gap, lower BET surface area and pore volume of the former solid (Table 1). This observation can be mainly attributed to the more negative LUCO value of UiO-66(Zr)-NH_2 respect to MIL-125(Ti)-NH_2 to favor the HER. In order to put in context of the achieved photocatalytic results, the most active UiO-66(Zr)-NH_2 was compared with the existing analogous study using MOFs. It should be mentioned that the photocatalytic activity can depend in large extent

of the reaction conditions such as glycerol aqueous solution concentration, catalyst amount, temperature, reactor design, irradiation source, among other parameters. Thus, comparison with literature results should be cautiously taken. With these comments in mind, the achieved H_2 activity of UiO-66(Zr)-NH_2 (0.62 mmol g^{-1} h^{-1} after 3 h; H_2:CO_2 7.3) is higher than that achieved using the Cu-MOF termed as HKUST-1 (0.1 mmol g^{-1} h^{-1} after 8 h, H_2:CO_2 ~0.9) both under simulated sunlight irradiation[48].

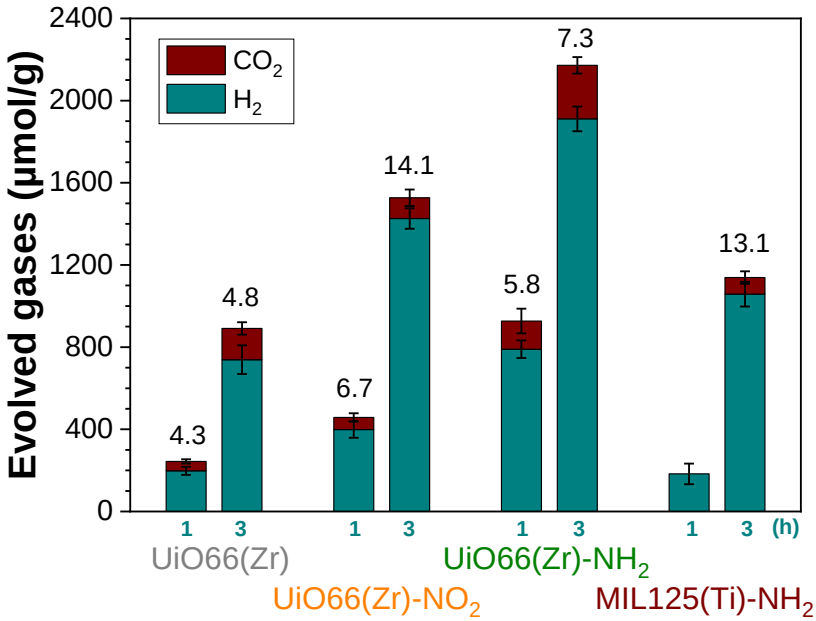

Figure 5. Photocatalytic H_2 and CO_2 generation from glycerol aqueous solution using the MOFs under study. The numbers indicated above the bars correspond to the H_2-to-CO_2 molar ratio. Reaction conditions: Photocatalyst (5 mg), H_2O:glycerol mixture (20 mL; 14 vol %), reaction time (h) as indicated, simulated sunlight irradiation (230 W/cm^2), 35 ºC.

Of particular interest is also the observation of different H_2-to-CO_2 ratios as a function of the MOF employed as the photocatalyst. These observations may be associated with the occurrence of different photochemical reactions taking place

simultaneously during the photoreforming of glycerol aqueous solutions with each specific MOF (Figure 1). As commented in the introduction of this chapter, the occurrence of primary or secondary carbon oxidation (carbonyl formation) to a larger extent than the oxidative C-C rupture (Figure 1) would favor a higher H_2- to-CO_2 molar ratio. Therefore, it can be assumed that the use of UiO - 66(Zr)- NO_2 as the photocatalyst might favor the carbonyl formation pathway in larger extent than UiO-66(Zr)-NH_2 or UiO-66(Zr) and, therefore the higher H_2-to-CO_2 molar ratio observed (Figure 5). This fact could be explained by considering the higher oxidation ability of UiO-66(Zr)-NO_2 with a more positive HOCO value (+2.22 V) than the other two UiO-66 solids (Figure 4). According to a previous study, the higher acidity of metals nodes of UiO-66(Zr)-NO_2 with respect to UiO-66(Zr)-NH_2 or UiO-66(Zr) may also influence some steps of the reaction mechanism of aqueous glycerol photoreforming[54]. Furthermore, the use of UiO - 66 photocatalysts results in an increase of H_2-to-CO_2 molar ratio as the reaction proceeds from 1 to 3 h, and these observations might be associated to the occurrence of the carbonyl pathways to a larger extent at the longer reaction time. For comparison, the similar H_2-to-CO_2 ratio at 3 h observed for MIL - 125(Ti) - NH_2 respect to UiO-66(Zr)-NO_2 may be also due to the fact that both photocatalysts exhibit similar HOCO values that would favor H_2 evolution through the carbonyl formation pathway. In the case of MIL-125(Ti)-NH_2, the formation of H_2 at 1 h is accompanied with only traces of CO_2 while as the reaction proceeds, more CO_2 is formed towards the theoretical 2.33 molar ratio. However, further studies are required to gain more insights about the complex reaction mechanism for glycerol photoreforming using MOF-based materials. Using the most active UiO-66(Zr)-NH_2 photocatalyst under study, the influence of the glycerol aqueous solution concentration on the H_2 production was studied. Figure 6 shows that the H_2 production increases along with the glycerol aqueous

solution concentration up to 14 vol %. Further increase in the glycerol concentration resulted in a slight decrease in activity. The optimum glycerol concentration observed of 14 vol % to maximize H_2 production can be interpreted considering that the number of photogenerated electron-hole pairs can efficiently react up to this value. The use of higher glycerol concentration might be responsible for deactivation of the MOF by either poisoning the redox active sites or blocking the porosity. For comparison, the use of CH_3OH instead of glycerol as the sacrificial agent, with the same number of moles, results in a relatively higher activity for H_2 production (4.46 mmol g^{-1} at 3 h) respect to glycerol (1.85 mmol g^{-1} at 3 h). Considering the relatively higher oxidation potential of CH_3OH (0.016 V *vs.* NHE) with respect to glycerol (0.004 V *vs.* NHE)[55], it can be assumed that better diffusion of the former through the porous structure of the UiO-66(Zr)-NH_2 plays a significant role in the observed photocatalytic activity. Regardless of these comments, it should be remembered that, currently, CH_3OH production is mainly through a catalytic reaction that involves the hydrogenation of CO with H_2 obtained from steam reforming of hydrocarbons, so that, its use as the sacrificial electron donor for H_2 production is far from practical applications[6, 9]. Therefore, the use of highly available glycerol as a byproduct of biodiesel can contribute simultaneously to the development of this market and to the development of sustainable technologies for H_2 generation.

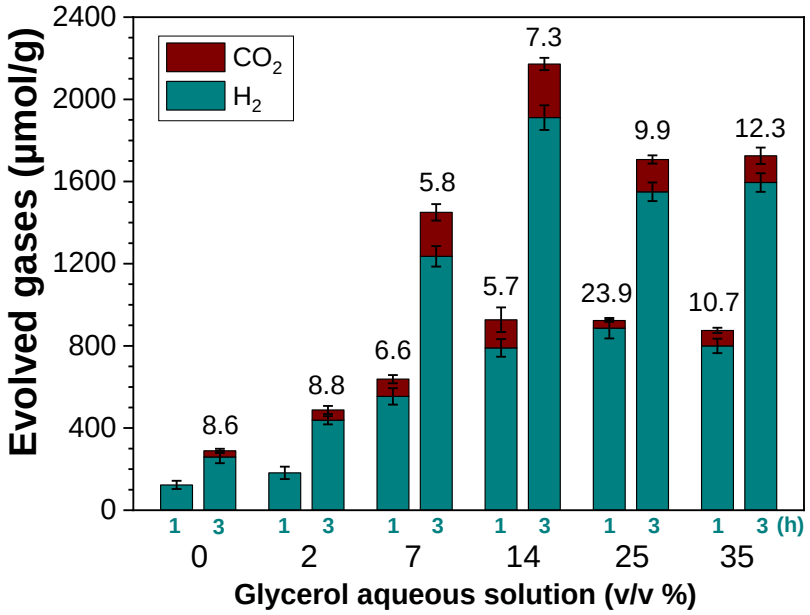

Figure 6. Influence of the glycerol aqueous solution concentration on the photocatalytic H_2 and CO_2 generation using UiO-66(Zr)-NH_2. The numbers indicated above the bars correspond to the H_2-to-CO_2 molar ratio. Reaction conditions: Photocatalyst (5 mg), H_2O:glycerol mixture (20 mL; vol % as indicated), reaction time (as indicated), simulated sunlight irradiation (230 W/cm^2), 35 °C.

To further study the H_2 generation from the photoreforming of glycerol aqueous solutions, the active UiO-66(Zr)-NH_2 material was modified with Pt NPs as the co-catalyst. Pt NPs are among the preferred reference noble metal NPs to promote the photocatalytic H_2 generation[47]. For example, previous studies have reported the use of Pt NPs supported on MOFs such as UiO-66(Zr)-NH_2 as photocatalysts for the HER using CH_3OH or TEOA as sacrificial agents[56,57,58]. Frequently, the use of Pt NPs loadings below 3 wt % is considered an adequate strategy to boost the photocatalytic activity for HER[56,58]. In the present study, the innovation resides in the use for the first time of Pt NPs- supported

UiO - 66(Zr) - NH_2 at low metal loading (1 wt %) as photocatalyst for H_2 production in a sustainable manner from glycerol photoreforming. PXRD of the as-prepared Pt NPs-supported UiO-66(Zr)-NH_2 by the photodeposition method shows that the resulting MOF-based material retains its initial crystallinity (Figure 7a). DF-STEM of the Pt@UiO-66(Zr)-NH_2 reveals an average particle size and standard deviation of Pt NPs of 1.27 and 0.43 nm, respectively (Figure 7b). Point EDX analyses confirmed the presence of Pt NPs within the MOF framework (Figure S20).

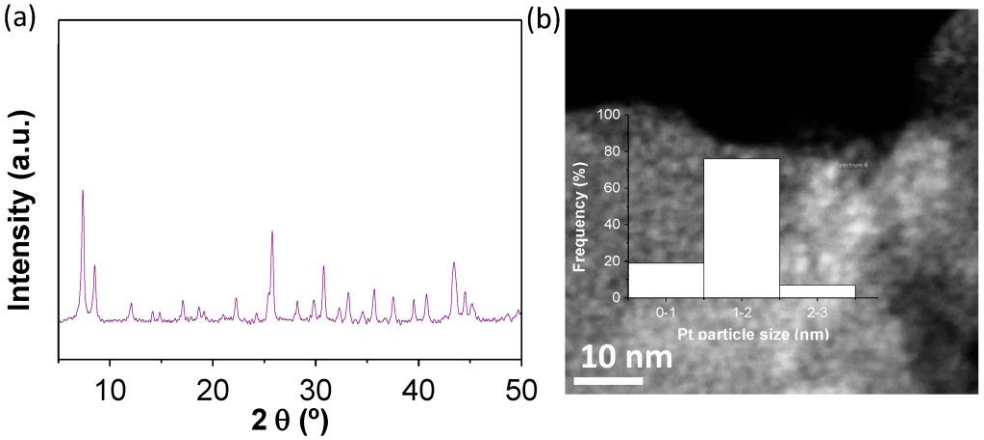

Figure 7. XRD (a) and representative DF-STEM image and platinum particle size distribution (b) of fresh Pt@UiO-66(Zr)-NH_2.

SEM measurements coupled to EDX analysis support that the small Pt NPs are well-distributed through the UiO-66(Zr)-NH_2 network (Figure 8). XPS allows for confirmation of the presence of supported Pt NPs in UiO-66(Zr)-NH_2 in its metallic form (Figure S16) based on the binding energies of Pt $4f_{7/2}$ and $4f_{5/2}$ at 69.6 and 72.6 eV, respectively.

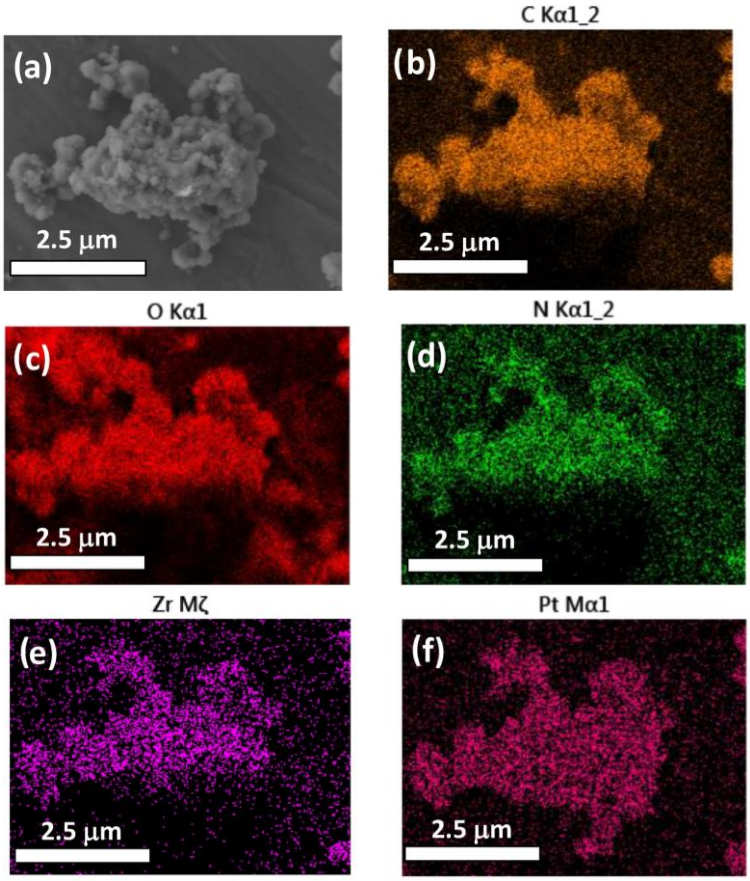

Figure 8. HR-SEM image of Pt@UiO66-(Zr)-NH_2 (a) and EDX mapping: carbon (b), oxygen (c), nitrogen (d), zirconium (e), platinum (f).

After the characterization of the Pt@UiO-66(Zr)-NH_2 sample, this solid was employed as the photocatalyst for H_2 generation from glycerol aqueous solution (14 vol %). The results show higher H_2 photocatalytic production when using Pt@UiO-66(Zr)-NH_2 (2.30 mmol g^{-1} in 3 h) with respect to the parent UiO-66(Zr)-NH_2 (1.85 mmol g^{-1} in 3 h). Remarkably, the Pt@UiO-66(Zr)-NH_2 material can be used under the same reaction conditions for 70 h (Figure 9a) while retaining its crystallinity and morphology, as revealed by XRD and SEM measurements, respectively (Figures 9b,c). DF-STEM measurements (Figure 9d) coupled with EDX

analyses (Figure S17) also allowed us to confirm the absence of significant Pt NP aggregation (1.34 ± 0.45 nm) with respect to the fresh sample (1.27 ± 0.43 nm).

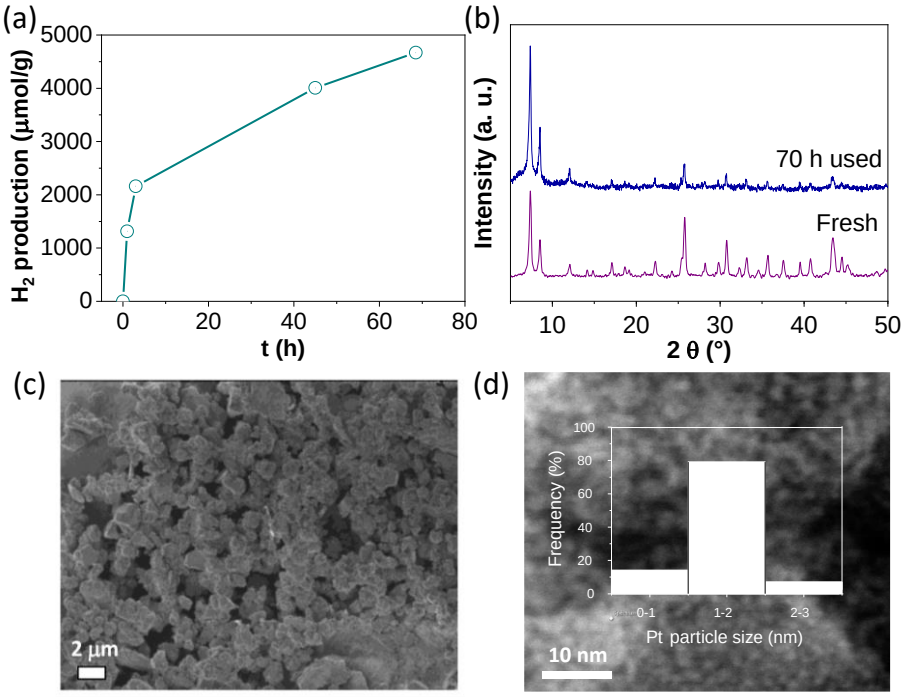

Figure 9. (a) H_2 evolution reaction after 70 h. (b) XRD patterns to confirm the stability of Pt@UiO-66(Zr)-NH_2. (c) Representative SEM and DF-STEM images of used Pt@UiO-66(Zr)-NH_2 together with platinum particle size distribution (d). Reaction conditions: Photocatalyst (5 mg), H_2O:glycerol mixture (20 mL; 14 vol %), reaction time as indicated, simulated sunlight irradiation (230 W/cm^2), 35 °C.

3.4.3 Reaction mechanism

To gain some understanding of the photocatalytic performance and reaction mechanism of Pt@UiO-66(Zr)-NH_2 and UiO-66(Zr)-NH_2 solids, several spectroscopic and electrochemical measurements were carried out. Initially, the PL response of Ar-purged acetonitrile MOF suspensions having the same absorbance value (*ca.* 0.35) at 340 nm, corresponding with the excitation

wavelength of the organic ligand, was measured. Figure 10 shows that the presence of Pt NPs (1 wt %) within the UiO-66(Zr)-NH_2 solid results in a decrease in PL of 66 % with respect to the parent UiO-66(Zr)-NH_2. These results are interpreted in a way that considers the fact that the presence of Pt NPs avoids, at least partially, the photoinduced charge recombination that is the process responsible for the observed photoluminescence emission. In fact, photocurrent measurements using a Pt@UiO-66(Zr)-NH_2/FTO (fluorine-doped tin oxide) working electrode upon polarization and dark/illumination cycles allow us to confirm the occurrence of photoinduced charge separation, a process that is favored in the presence of glycerol. This enhancement of photocurrent associated with the role of glycerol as the sacrificial electron donor can be explained considering that it quenches the photogenerated holes and increases the photocurrent intensity. This effect agrees with the previous photocatalytic data in which the presence of glycerol in water increases the photocatalytic H_2 production (Figure 6).

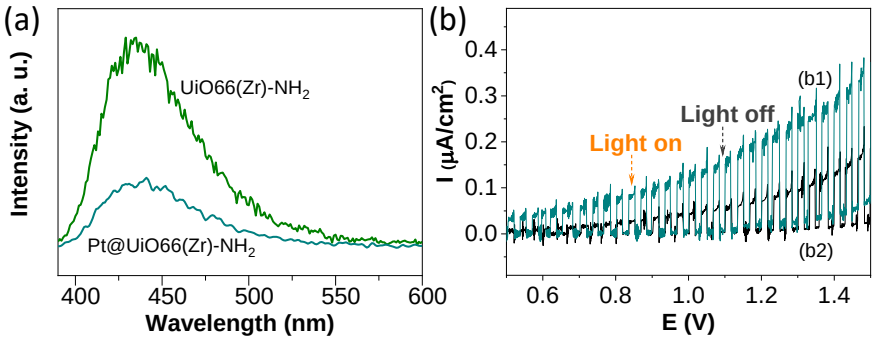

Figure 10. (a) PL of UiO-66(Zr)-NH_2 and Pt@UiO-66(Zr)-NH_2 upon excitation at 340 nm. (b) Photocurrent measurements upon electrode polarization and illumination/dark cycles using Pt@UiO-66(Zr)-NH_2/FTO as the working electrode in the presence (b1) and absence (b2) of glycerol.

TAS was also used to further study the reaction mechanism when using UiO- 66(Zr)-NH_2 or Pt@UiO-66(Zr)-NH_2 as photocatalysts. Specifically, TAS spectrum of both MOFs recorded upon irradiation at ligand-centered absorption at 355 nm under Ar atmosphere clearly shows the presence of two bands (Figure 11a). The first band appearing from 350 to 450 nm and second one from 550 to 750 nm, both exhibiting different decays of kinetics and profiles. This fact suggests that these two absorbance bands correspond to different species. In the case of UiO-66(Zr)-NH_2, the first region is characterized by transient absorbance decay kinetics with two components, one quick and intense, attributed to the occurrence of charge separation, and other residual, with a longer lifetime due to charge delocalization along the MOF crystal (Figure 11b). The second band observed in the region from 550–750 nm is mainly characterized by one component decay (Figure 11c, blue line). In the case of the Pt@UiO-66(Zr)-NH_2 sample, the presence of Pt mainly causes the quenching of the second component, inhibiting photoinduced charge delocalization in the MOF (Figure 11b). More specifically, the transient absorbance lifetime decay of UiO- 66(Zr)-NH_2 (65 ns) is quenched in the presence of Pt NPs in UiO-66(Zr)-NH_2 (40 ns) (Figure 11c). In addition, the presence of Pt NPs results in a quenching of the transient absorbance spectrum of UiO-66(Zr)-NH_2, particularly intense in the region from 550 to 750 nm. These observations can be interpreted considering that metallic Pt NPs have the ability of trapping photoinduced generated charges.

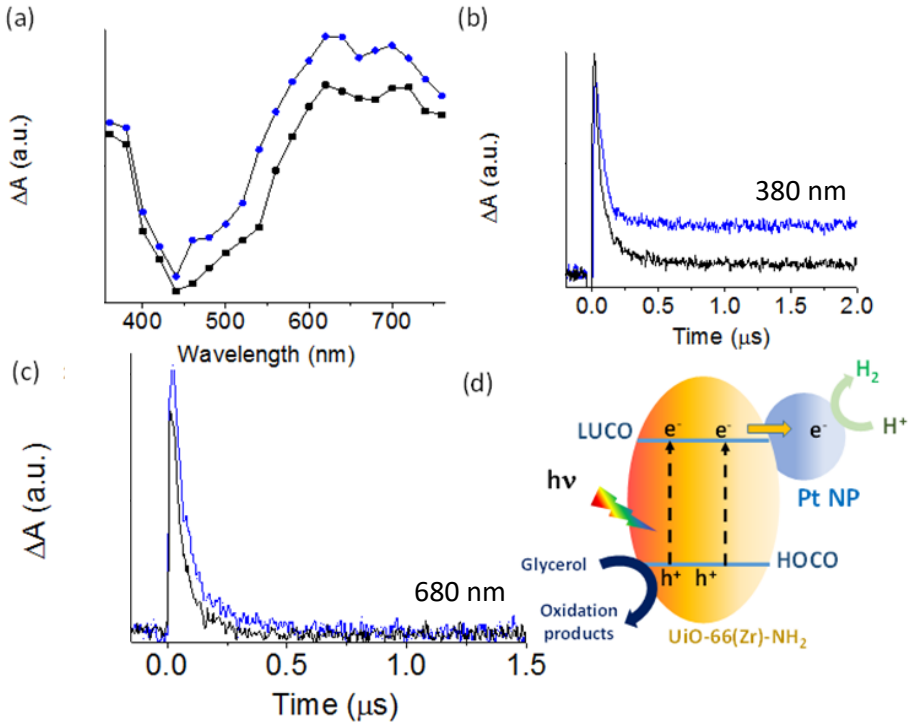

Figure 11. (a) Transient absorption spectra for UiO-66(Zr)-NH_2 (●) and Pt@UiO- 66-NH_2 (■) upon excitation at 365 nm under Ar atmosphere recorded at 25 ns. Transient absorption decay kinetics for UiO-66(Zr)-NH_2 (blue line) and Pt@UiO-66(Zr)-NH_2 (black line) recorded at 380 (b) or 680 (c) nm under Ar. (d) Simplified illustration of the proposed reaction mechanism using Pt@UiO- 66(Zr)- NH_2.

Aiming to bring light to the nature of the observed photoinduced charge separation species for the most active Pt@UiO-66(Zr)-NH_2 sample, additional TAS measurements in the presence of quenchers were carried out. CH_3OH was selected as the hole quencher due to its good electron-donor behaviour, while molecular oxygen was chosen as the electron acceptor. Figures S18 and S19 show that the use of these two quenchers results in significant changes to the TAS measurements. In particular, the presence of CH_3OH quenches the intensity signal and the spectra decay along the whole spectrum, specifically the region

between 350 and 450 nm (Figure S18). These observations suggest that the TAS observed mainly from 350 to 450 nm corresponds to photogenerated holes. The use of O_2 as the quencher also modifies the TAS profiles and decreases the decay lifetimes (Figure S19). For instance, the presence of O_2 decreases the decay lifetimes from 65 to 38 ns recorded at 380 nm or from 45 to 30 ns at 680 nm. The observed quenching of transient absorbance intensity due to the presence of O_2 in the region from 550 to 750 nm is associated with the presence of photogenerated electrons. These observations agree with the role of supported Pt NPs as an electron reservoir responsible for the observed decrease in both signal intensity and lifetime of the transient species in the region from 550 to 750 nm with respect to the parent MOF. Figure 11d illustrates a simplified reaction mechanism showing the photoinduced electron transfer from the organic ligand to the metal node of the MOF. Then, the electrons present in the LUCO are transferred to Pt NPs where the reduction reactions occur, while oxidations take place in the HOCO localized in the organic ligand.

In addition to the above spectroscopic and electrochemical characterization, the influence of the light irradiation source with Pt@UiO-66(Zr)-NH_2 was also investigated. Figure 12 shows the highest photocatalytic activity achieved using UV-Vis light, followed by simulated sunlight irradiation and then visible light irradiation. In any case, these results confirm unambiguously that Pt@UiO- 66(Zr)-NH_2 behaves as an efficient photocatalyst under both visible or simulated sunlight irradiation.

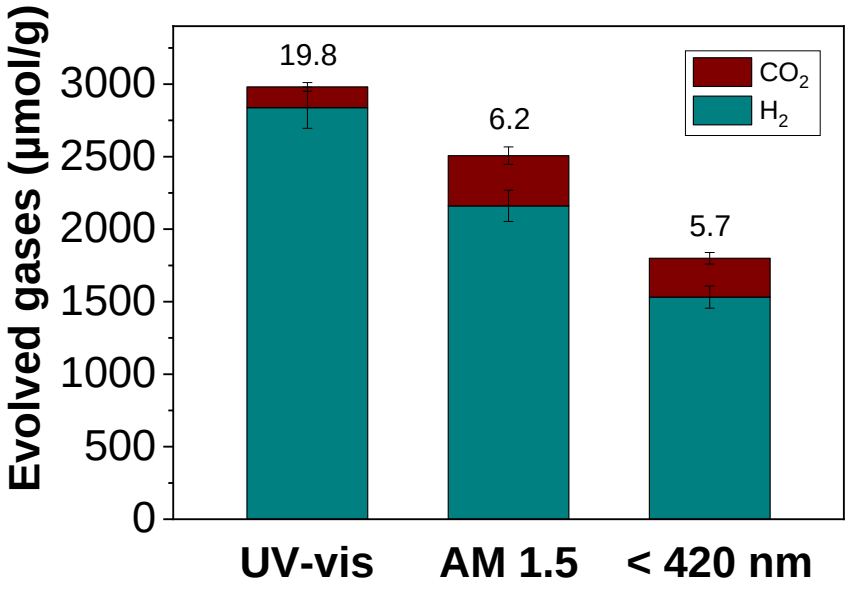

Figure 12. Evolved gases over the influence of the light irradiation source with Pt@UiO-66(Zr)-NH_2. Reaction conditions: Photocatalyst (5 mg), H_2O:glycerol mixture (20 mL; 14 vol %), reaction time 3 h, irradiation source as indicated, 35 °C.

3.5 Conclusions

The present study has shown the possibility of using UiO-66 topology for H_2 generation from photoreforming of glycerol aqueous solutions under simulated sunlight irradiation. The most active photocatalyst of the series was UiO- 66(Zr)- NH_2, followed by UiO-66(Zr)-NO_2 and the less active UiO-66(Zr). The activity of MIL-125(Ti)-NH_2 was lower than that of UiO-66(Zr)-NH_2. The observed order of activity was mainly attributed to the energy level difference of the solids, where UiO-66(Zr)-NH_2 has an appropriate band gap to absorb visible light together with adequate LUCO value to promote reduction reactions. Deposition of Pt NPs as the co-catalyst for H_2 generation within the UiO-66(Zr)-NH_2 network has significantly improved the photocatalytic activity of the MOF. In addition, the

Pt@UiO-66(Zr)-NH_2 photocatalyst was employed for about 70 h with good H_2 generation and without loss of crystallinity or change in its morphology based on PXRD and SEM measurements, respectively. Furthermore, Pt particle size distribution was also retained, as revealed by TEM measurements. Evidence in support of the occurrence of photoinduced charge separation with Pt@UiO- 66(Zr)-NH_2 was obtained by TAS and photocurrent measurements. In addition, PL measurements using Pt@UiO-66(Zr)-NH_2 and UiO-66(Zr)-NH_2 indicated that the use of the Pt NPs avoids to some extent the occurrence of undesirable photoinduced charge recombination. The study of the influence of light irradiation on H_2 generation from glycerol aqueous solution using Pt@UiO- 66(Zr)-NH_2 revealed that this photocatalyst exhibits good activity under both visible and simulated sunlight irradiation. The authors consider that this study will contribute to the field of solar-driven photocatalytic H_2 generation using MOFs and sustainable feedstocks as sacrificial agents.

3.6 Author contribution

Celia María Rueda Navarro performed the synthesis of the materials under study and tested their photocatalytic activities. Considering the characterization of the solids, she measured the XRD, FT-IR and the SEM and participated in TEM analyses. Moreover, she analyzed all characterization data of the BET, TGA, XPS, UV, that were carried out by technicians. Regarding the study of the mechanism, she did the photocurrent and Nyquist experiments and participated during the photoluminescence measurements.

3.7 References

(1) Bosa, K.; Gupta, J. Stranded assets and stranded resources: Implications for climate change mitigation and global sustainable development. *Energy Res. Soc. Sci.* **2019**, *56*, 101215.

(2) Paraschiv, S.; Paraschiv, L. S. Trends of carbon dioxide (CO_2) emissions from fossil fuels combustion (coal, gas and oil) in the EU member states from 1960 to 2018. *Energy Rep.* **2020,** *6*,237-242.

(3) Shahnazi, R.; Shabani, Z. D. The effects of renewable energy, spatial spillover of CO_2 emissions and economic freedom on CO_2 emissions in the EU. *Renew. Energy* **2021**, *169*, 293-307.

(4) Friedlingstein, P.; O'Sullivan, M.; Jones, M. W.; Andrew, R. M.; Hauck, J.; Olsen, A.; P. Peters, G. P.; Peters, W.; Pongratz, J.; Sitch, S.; et al. Global Carbon Budget. *Earth Syst. Sci. Data* **2020**, *12*, 3269-3340.

(5) Radovanović, M.; Filipović, S.; Vukadinović, S.; Trbojević, M.; Podbregar, I. Decarbonisation of eastern European economies: monitoring, economic, social and security concerns. *Energy Sustain. Soc.* **2022**, *12*, 16.

(6) Parkinson, B.; Balcombe, P.; Speirs, J. F.; Hawkes, A. D.; Hellgardt, K. Levelized cost of CO_2 mitigation from hydrogen production routes. *Energy Environ. Sci.* **2019**, *12*, 19-40.

(7) Parra, D.; Valverde, L.; Pino, F. J.; Patel, M. K. A review on the role, cost and value of hydrogen energy systems for deep decarbonisation. *Renew. Sust. Energy Rev.* **2019**, *101*, 279-294.

(8) Staffell, I.; Scamman, D.; Velazquez Abad, A.; Balcombe, P.; Dodds, P. E.; Ekins, P.; Shah, N.; Ward, K. R. The role of hydrogen and fuel cells in the global energy system. *Energ. Environ. Sci.* **2019**, *12*, 463-491.

(9) Younas, M.; Shafique, S.; Hafeez, A.; Javed, F.; Rehman, F. An overview of hydrogen production: current status, potential, and challenges. *Fuel* **2022**, *316*, 123317.

(10) Hosseini, S. E.; Wahid, M. A. Hydrogen from solar energy, a clean energy carrier from a sustainable source of energy. *Int. J. Energy Res.* **2020**, *44*, 4110-4131.

(11) Jia, J.; Seitz, L. C.; Benck, J. D.; Huo, Y.; Chen, Y.; Desmond Ng, J. W.; Bilir, T.; Harris, J. S.; Jaramillo, T. F. Solar water splitting by photovoltaic-electrolysis with a solar-to-hydrogen efficiency over 30 %. *Nat. Commun.* **2016**, *7*, 13237

(12) Saba, S. M.; Muller, M.; Robinius, M.; Stolten, D. The investment costs of electrolysis e A comparison of cost studies from the past 30 years. *Int. J. Hydrogen Energy* **2018**, *43*, 1209-1223.

(13) Hisatomi, T.; Domen, K. Reaction systems for solar hydrogen production via water splitting with particulate semiconductor photocatalyst. *Nat. Catal.* **2019**, *2*, 387–399.

(14) Kim, J.; Hansora, D.; Sharma, P.; Jang, J.-W.; Lee, J. S. Toward practical solar hydrogen production -an artificial photosynthetic leaf-to-farm challenge. *Chem. Soc. Rev.* **2019**, *48*, 1908-1971.

(15) Nishiyama, H.; Yamada, T.; Nakabayashi, M.; Yoshiki Maehara, Y.; Yamaguchi, M.; Kuromiya, Y.; Nagatsuma, Y.; Tokudome, H.; Akiyama, S.; Watanabe, T.; et al. Photocatalytic solar hydrogen production from water on a 100-m2 scale. *Nature.* **2021**, *598*, 304-307.

(16) Wang, Q.; Domen, K. Particulate photocatalysts for light-driven water splitting: mechanisms, challenges, and design strategies. *Chem. Rev.* **2020**, *120*, 919-985.

(17) Férey, G.; Mellot-Draznieks, C.; Serre, C.; Millange, F.; Dutour, J.; Surblé, S.; Margiolaki, I. A chromium terephthalate-based solid with unusually large pore volumes and surface area. *Science* **2005**, *23*, 2040-2042.

(18) Furukawa, H.; Cordova, K. E.; O'Keeffe, M.; Yaghi, O. M. The chemistry and applications of metal-organic frameworks. *Science* **2013**, *341*, 1230444.

(19) Kitagawa, S.; Kitaura, R.; Noro, S.-I. Functional Porous Coordination Polymers. *Angew. Chem. Int. Ed.* **2004**, *43*, 2334-2375.

(20) Dhakshinamoorthy, A.; Asiri, A. M.; García, H. Metal-organic framework (MOF) compounds: photocatalysts for redox reactions and solar fuel production. *Angew. Chem. Int. Ed.* **2016**, *55*, 5414-5445.

(21) Qiu, J.; Zhang, X.; Feng, Y.; Zhang, X.; Wang, H.; Yao, J. Modified metal-organic frameworks as photocatalysts. *Appl. Catal. B. - Environ.* **2018**, *231*, 317-342.

(22) Swetha, S.; Janani, B.; Khan, S. S. A critical review on the development of metal-organic frameworks for boosting photocatalysis in the fields of energy and environment. *J. Clean. Prod.* **2022**, *333*, 130164.

(23) Yoon, J.-W.; Kim, J.-H.; Kim, C.; Jang, H. W.; Lee, J.-H. MOF-based hybrids for solar fuel production. *Adv. Energy Mater.* **2021**, *11*, 2003052.

(24) Nguyen, H. L. Metal–organic frameworks for photocatalytic water splitting. *Sol. RRL* **2021**, *5*, 2100198.

(25) Nguyen, H. L. Metal–organic frameworks can photocatalytically split water—why not? *Adv. Mater.* **2022**, *34*, 2200465.

(26) Salcedo-Abraira, P.; Babaryk, A. A.; Montero-Lanzuel, E.; Contreras-Almengor, O. R.; Cabrero-Antonino, M.; Svensson Grape, E. S.; Willhammar, T.; Navalón, S.; Elkäim, E.; García, H.; et al. A novel porous ti-squarate as efficient photocatalyst in the overall water splitting reaction under simulated sunlight irradiation. *Adv. Mater.* **2021**, *33*, 2106627.

(27) Tahir, M.; Tasleem, S.; Tahir, B. Recent development in band engineering of binary semiconductor materials for solar driven photocatalytic hydrogen production. *Int. J. Hydrogen Energy* **2020**, *45*, 15985-16038.

(28) Hu, E.; Yao, Y.; Cui, Y.; Qian, G. Strategies for the enhanced water splitting activity over metal-organic frameworks-based electrocatalysts and photocatalysts. *Mater. Today Nano* **2021**, *15* 100124.

(29) Luo, H.; Zeng, Z.; Zeng, G.; Zhang, C.; Xiao, R.; Huang, D.; Lai, C.; Cheng, M.; Wang, W.; Xiong, W.; et al. Recent progress on metal-organic frameworks based- and derived- photocatalysts for water splitting. *Chem. Eng. J.* **2020**, *383*, 123196.

(30) Meyer, K.; Ranocchiari, M.; van Bokhoven, J. A. Metal Organic Frameworks for Photo-Catalytic Water Splitting. *Energy Environ. Sci.* **2015**, *8*, 1923-1937.

(31) Song, F.; Li, W.; Sun, Y. Metal–Organic Frameworks and their derivatives for photocatalytic water splitting. *Inorganics* **2017**, *5*, 40.

(32) Wang, W.; Xu, X.; Zhou, W.; Shao, Z. Recent progress in metal-organic frameworks for applications in electrocatalytic and photocatalytic water splitting. *Adv. Sci.* **2017**, *4*, 160037.

(33) Wen, M.; Mori, K.; Kuwahara, Y.; An, T.; Yamashita, H. Design of single-site photocatalyst using metal-orgnaic framework as matrix. *Chem. Asian J.* **2018**, *13*, 1767-1779.

(34) Xiang, W.; Zhang, Y.; Lin, H.; Liu, C.-j. Nanoparticle/Metal–Organic Framework composites for catalytic applications: current status and perspective. *Molecules* **2017**, *22*, 2103.

(35) Fang, Y.; Ma, Y.; Zheng, M.; Yang, P.; Asiri, A. M.; Wang, X. Metal–organic frameworks for solar energy conversion by photoredox catalysis. *Coord. Chem. Rev.* **2018**, *373*, 83-115.

(36) Jaryal, R.; Kumar, R.; Khullar, S. Mixed Metal-Metal Organic Frameworks (MM-MOFs) and their use as efficient photocatalysts for hydrogen evolution from water splitting reactions. *Coord. Chem. Rev.* **2022**, *464*, 214542.

(37) Reddy, D. A.; Kim, Y.; Gopannagari, M.; Kumar, D. P.; Kim, T. K. Recent advances in metal-organic framework-based photocatalysts for hydrogen production. *Sustain. Energy Fuels* **2021**, *5*, 1597-1618.

(38) Wang, Y.-C.; Liu, X.-Y.; Wang, X.-X.; Cao, M.-S. Metal-organic frameworks based photocatalysts: architecture strategies for efficient solar energy conversion. *Chem. Eng. J.* **2021**, *419*, 129459.

(39) Zhang, X.; Tong, S.; Huang, D.; Liu, Z.; Shao, B.; Liang, Q.; Wu, T.; Pan, Y.; Huang, J.; Liu, Y.; et al. Recent advances of zr based metal organic frameworks photocatalysis: energy production and environmental remediation. *Coord. Chem. Rev.* **2021**, *448*, 214177.

(40) Shi, Y.; Yang, A.-F.; Cao, C.-S.; Zhao, B. Applications of MOFs: Recent advances in photocatalytic hydrogen production from water. *Coord. Chem. Rev.* **2019**, *390*, 50-75.

(41) Seadira, T.; Sadanandam, G.; Ntho, T. A.; Lu, X.; M. Masuku, C. M.; Scurrell, M. Hydrogen production from glycerol reforming: conventional and green production. *Rev. Chem. Eng.* **2017**, *34*, 695-726.

(42) Rumayor, M.; Corredor, J.; Rivero, M. J.; Ortiz, I. Prospective life cycle assessment of hydrogen production by waste photoreforming. *J. Clean. Prod.* **2022**, *336* 130430.

(43) Karimi Estahbanati, M. R.; Feilizadeh, M.; Attar, F.; Iliuta, M. C. Current developments and future trends in photocatalytic glycerol valorization: process analysis. *React. Chem. Eng.* **2021**, *6*, 197-219.

(44) Abdul Raman, A. A.; Tan, H. W.; Buthiyappan, A. Two-step purification of glycerol as a value added by product from the biodiesel production process. *Front. Chem.* **2019**, *7*, 774.

(45) Puga, A. V. Photocatalytic production of hydrogen from biomass-derived feedstocks. *Coord. Chem. Rev.* **2016**, *315* 1-66.

(46) Sanwald, K. E.; Berto, T. F.; Eisenreich, W.; Gutiérrez, O. Y.; Lercher, J. A. Catalytic routes and oxidation mechanisms in photoreforming of polyols. *J. Catal.* **2016**, *344* 806-816.

(47) López-Tenllado, F. J.; Estévez, R.; Hidalgo-Carrillo, J.; López-Fernández, S.; Urbano, F. J.; Marinas, A. Hydrogen photo-production from glycerol on platinum, gold and silver-modified TiO_2-USY62 catalysts. *Catal. Today* **2022**, *390-391*, 92-98.

(48) Martínez, F. M.; Albiter, E.; Alfaro, S.; Luna, A. L.; Colbeau-Justin, C.; Barrera-Andrade, J. M.; Remita, H.; Valenzuela, M. A. Hydrogen production from glycerol photoreforming on TiO_2/HKUST-1 composites: effect of preparation method. *Catalysts* **2019**, *9*, 338.

(49) Melillo, A.; García-Vallés, C.; Ferrer, B.; Álvaro, M.; Navalón, S.; García, H. Bifunctional metal-organic frameworks for hydrogenation of nitrophenol using methanol as hydrogen source. *Org. Biomol. Chem.* **2021**, *19*, 794-800.

(50) Shearer, G. C.; Chavan, S.; Bordiga, S.; Svelle, S.; Olsbye, U.; Lillerud, K. P. Defect engineering: tuning the porosity and composition of the metal−organic framework UiO-66 via modulated synthesis. *Chem. Mater.* **2016**, *28*, 3749−3761.

(51) Liu, H.; Cheng, M.; Liu, Y.; Zhang, G.; Li, L.; Du, L.; Li, B.; Xiao, S.; Wang, G.; Yang, X. Modified UiO-66 as photocatalysts for boosting the carbon-neutral energy cycle and solving environmental remediation issues. *Coord. Chem. Rev.* **2022**, *458*, 214428.

(52) Sun, D.; Li, Z. Robust Ti- and Zr-Based metal-organic frameworks for photocatalysis. *Chin. J. Chem.* **2017**, *35*, 135-147.

(53) Musho, T.; Li, J.; Wu, N. Band gap modulation of functionalized metal–organic frameworks. *Phys. Chem. Chem. Phys.* **2014**, *16*, 23646--23653.

(54) Vermoortele, F.; Vandichel, M.; de Voorde, B. V.; Ameloot, R.; Waroquier, M.; Speybroeck, V.; De Vos, D. E. Electronic effects of linker substitution on lewis acid catalysis with metal–organic frameworks. *Angew. Chem. Int. Ed.* **2012**, *51*, 4887 -4890.

(55) Al-Azri, Z. H. N.; Chena, W.-T.; Chan, A.; Jovic, V.; Ina, T.; Idriss, H.; Waterhouse, G. I. N. The roles of metal co-catalysts and reaction media in photocatalytic hydrogen production: Performance evaluation of M/TiO2 photocatalysts (M = Pd, Pt, Au) in different alcohol–water mixtures. *J. Catal.* **2015**, *329*, 355-367.

(56) Chen, Y.-F.; Tan, L.-L.; Liu, J.-M.; Qin, S.; Xie, Z.-Q.; Huang, J.-F.; Xu, Y.-W.; Xiao, L.-M.; Su, C.-Y. Arene based dye-sensitized pt@uio-66-nh2 metal-organicframework for efficient visible-light photocatalytic hydrogenproduction. *Appl. Catal. B Environ*. **2017**, 206, 426–433.

(57) Wang, X.; Zhang, W.; Li, R.; Han, J.; Guo, J.; Liu, B. Platinum nanoparticles decorated and titanium incorporated with NH2-UiO-66 for photocatalytic hydrogen production. *React. Kinet. Mech. Catal*. **2020**, 129, 505–518.

(58) Xiao, J.-D.; Shang, Q.; Xiong, Y.; Zhang, Q.; Luo, Y.; Yu, S.-H.; Jiang, H.-L. Boosting photocatalytic hydrogen production of a metal–organic framework decorated with platinum nanoparticles: the platinum location matters. *Angew. Chem. Int.* Ed. **2016**, 55, 9389–9393.

3.8 Supporting Information

3.8.1 Synthesis of the MOF-based materials

Synthesis of UiO-66(Zr). $ZrCl_4$ (0.466 g, 2 mmol) and terephthalic acid (0.332 g, 2 mmol) were mixed with N,N-dimethylformamide (DMF, 6 mL), the system was sonicated for 20 min (450 W power) and then, transferred to a Teflon- lined autoclave [1]. The autoclaved was sealed and placed in a pre-heated oven at 220 °C and maintained the temperature for 12 h. After cooling the system to room temperature, the resulting white solid was recovered by filtration, and washed several times with DMF and CH_3OH while stirring. The recovered solid was further washed in a Soxhlet for 4 h using CH_3OH as solvent. The solid was dried under a vacuum at 150 °C overnight.

Synthesis of UiO-66(Zr)-NH_2. $ZrCl_4$ (0.466 g, 2 mmol) and 2-amino-terephthalic acid (0.362 g, 2 mmol) were mixed with DMF (6.0 mL), the system sonicated for 20 min and then, the mixture was transferred in a Teflon-lined autoclave[1]. The sealed autoclave was placed in a pre-heated oven at 100 ℃ for 24 hours. After cooling the system at room temperature, the solid was recovered by filtration, washed several times with DMF and CH_3OH, washed in a Soxhlet for 4 h using CH_3OH, and dried at room temperature.

Synthesis of UiO-66(Zr)-NO_2. $ZrCl_4$ (0.862 g, 3.699 mmol), nitro-terephthalic acid (0.620 g, 3.701 mmol), and H_2O (0.200 mL, 11.10 mmol) were mixed with DMF (100 mL, 1291 mmol) in 250 ml volumetric flask[2]. The system was heated at 70 °C and stirred during the preparation to ensure the complete dissolution of the reagents. Once all reagents were dissolved, the flask was placed in a pre-heated oven to 120 °C for 72 hours after removing the stirring magnet and closing the

system. The resulting precipitate was recovered by centrifugation. Then, it was washed with DMF and CH_3OH several times. It was further washed in a Soxhlet for 4 h using CH_3OH as solvent. And finally, the powder was dried under vacuum at 150 °C overnight.

Synthesis of MIL-125(Ti)-NH_2. 2-aminoterephthalic acid (1.43 g, 7.9 mmol) was initially dissolved in anhydrous DMF (20 mL) and then, anhydrous CH_3OH (5 mL) was added to the flask. The system was sonicated for 20 min (450 W power) and then, the reaction mixture was transferred to a Teflon-lined autoclave (50 mL) where titanium isopropoxide (1.36 g, 4.8 mmol) was added. The autoclave was then sealed, heated up to 110 ℃ for 72 h and cooled down to room temperature. The resulting precipitate was recovered by filtration, washed with DMF at room temperature for 12 h under stirring, and then, washed with DMF at 70 °C. This washing procedure was repeated using CH_3OH as solvent. The recovered solid was further washed in a Soxhlet for 4 h using CH_3OH as solvent. The recovered solid by filtration was dried in an oven at 100 ºC for 24 h.

Deposition of Pt NPs on UiO-66(Zr)-NH_2. Pt NPs were deposited in the as-prepared UiO-66(Zr)-NH_2 material using the so-called photodeposition method. Briefly, the MOF (50 mg) was dispersed in a mixture of Milli-Q water (8 mL) and CH_3OH (13 mL) using a quartz tube. Subsequently, the corresponding amount of $H_2PtCl_6 \cdot (H_2O)_6$ previously dissolved in water (1 mL) was added to this quartz tube. Then, the system was purged with Ar for 30 min and immediately irradiated using a UV-vis light lamp (150 W) for 4 h. The resulting solid was recovered by filtration, washed several times with Milli-Q water and dried in an oven at 100 °C for 24 h.

3.8.2 Characterization techniques

PXRD data was recorded on a Philips XPert diffractometer equipped with a graphite monochromator (40 kV and 45 mA) employing Ni filtered CuKα radiation (0.15418 nm).

Isothermal nitrogen adsorption data was collected using an ASAP 2010 Micromeritics device.

UV-Vis diffuse reflectance measurements of the solid samples were performed on a Varian spectrometer model Cary 5000.

Thermogravimetric analyses were carried out on a TGA/SDTA851e METTLER TOLEDO station.

SEM images were collected on a scanning electron microscope (SEM, Zeiss instrument, AURIGA Compact) equipped with an EDX detector.

Scanning transmission electron microscopy images in a dark field (DF-STEM) were recorded on a JEOL JEM2100F instrument operating at 200 kW.

Pt NP size distribution was estimated by measuring more than 100 particles from the Pt@UiO-66(Zr)-NH_2 sample.

XPS were recorded using a SPECS spectrometer equipped with an MCD-9 detector and using a monochromatic Al (K_α= 1486.6 eV) X-ray source. Spectra deconvolution was performed using the CASA software using the C 1s peak at 284.4 eV as binding energy reference. XPS HOCO band maximum versus the Fermi

level (E^f_u) was estimated from the intersection of the flat XPS energy and the linear fit of the leading valence band edge in the XPS graph. The valence band maximum versus the NHE can be calculated from the equation, $E_u^{NHE} = E_u^f + f_{sp} - 4.44$, where f_{sp} is the work function of the spectrometer with the value 4.244 eV. The LUCO band minimum can be determined from this value, and the optical band gap is estimated by the Tauc plot.

Photocurrent measurements were performed using a standard three-electrode electrochemical cell. The working electrons were composed of a transparent FTO-coated glass substrate on which a thin layer of the Pt@UiO- 66(Zr)-NH_2 or UiO-66(Zr)-NH_2 samples were deposited. A platinum wire was used as a counter electrode and a standard calomel electrode as the reference electrode. To remove the oxygen present in the cell the system was purged through the electrolyte solution with Ar for 15 min. The photocurrent was measured under dark or illumination conditions under continuous polarization of the working electrode at potentials from 1.5 to -0.5 V. The illumination of the working electrode was performed using an optical fiber connected to a 150 W Hg- Xe lamp.

Laser flash photolysis (LFP) measurements were performed with an OPO System Ekspla (EKS-NT342C-10) coupled with a UV extension (EKS-NT342C-SH-SFG) as the excitation source and an Edinburgh Instruments detection System (LP980) coupled with an ICCD camera (Andor iStar CCD 320T). The OPO System Ekspla light sources were adjusted to 340 nm. Similar acetonitrile suspensions to those employed for the PL measurements were also used in this case. In some cases, the cuvette was purged for 10 min with O_2 or N_2O as electron quenchers. In

other cases, CH_3OH (100 mL) was included in the cuvette as a hole quencher and the system was again sonicated with Ar for 10 min.

Photoluminescence (PL) measurements were carried out using JASCO FP- 8500 instrument. For this purpose, Ar purged acetonitrile suspensions of Pt@UiO-66(Zr)-NH_2 or UiO-66(Zr)-NH_2 with an adjusted absorption at 0.35 a.u. at the excitation wavelength of 340 nm were prepared using a quartz cuvette.

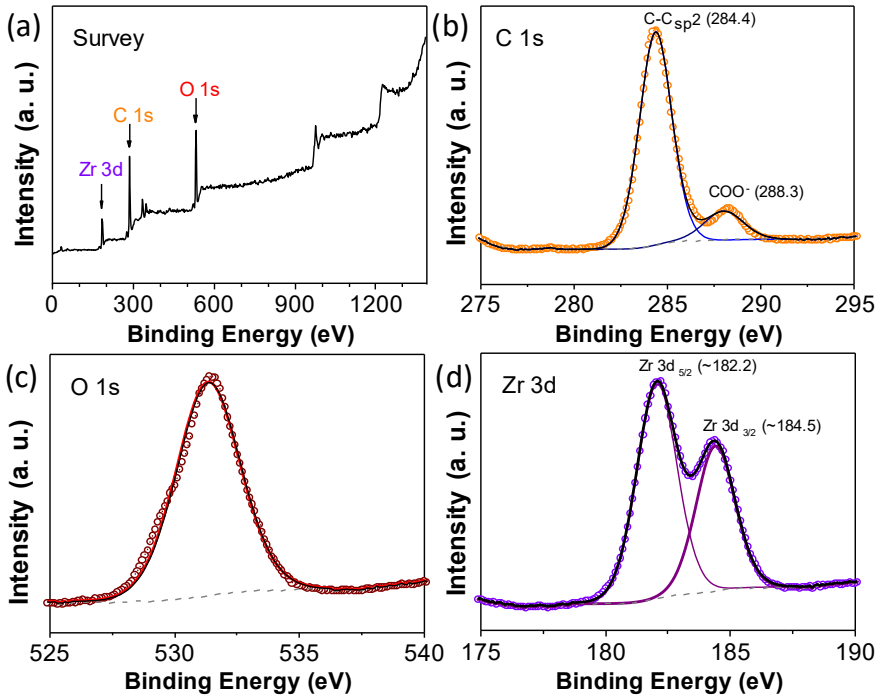

Figure S1. XPS of UiO-66(Zr): survey (a), C 1s (b), O 1s (c), Zr 3d (d).

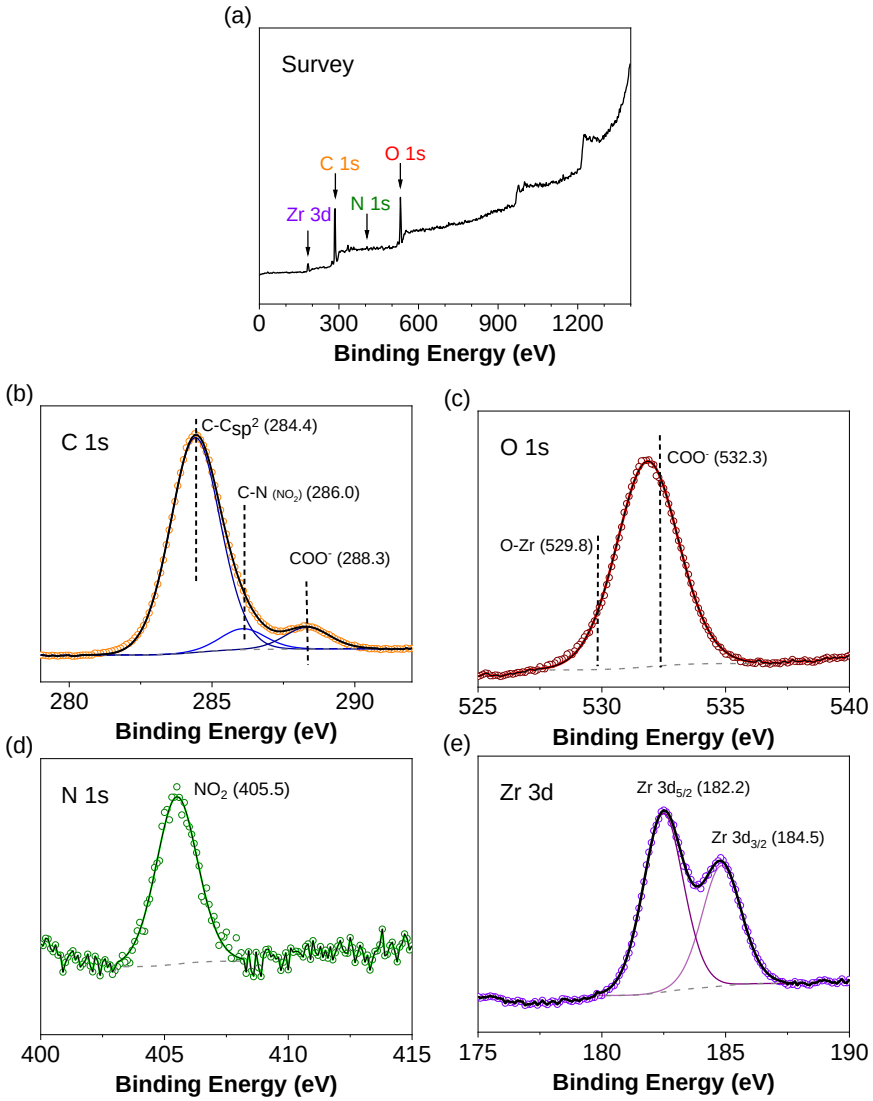

Figure S2. XPS of UiO-66(Zr)-NO_2: survey (a), C 1s (b), O 1s (c), N 1s (d), Zr 3d (e).

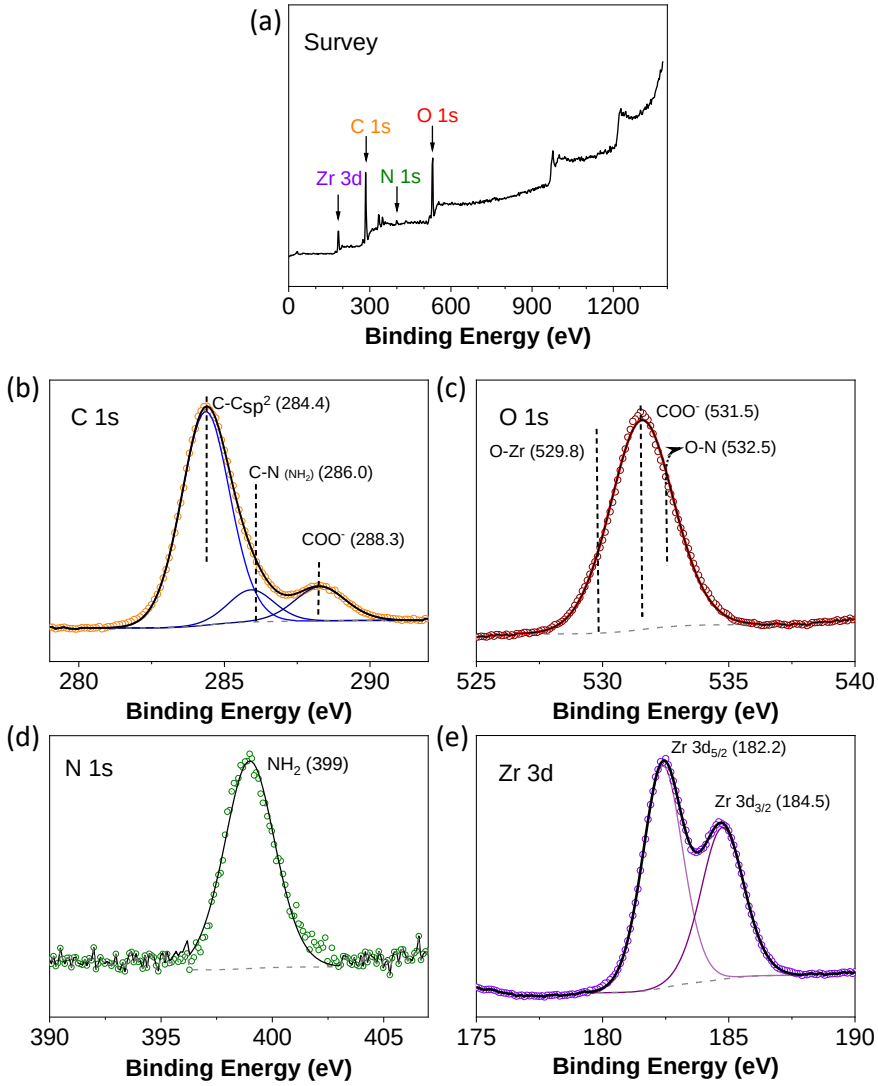

Figure S3. XPS of UiO-66(Zr)-NH_2: survey (a), C 1s (b), O 1s (c), N 1s (d), Zr 3d (e).

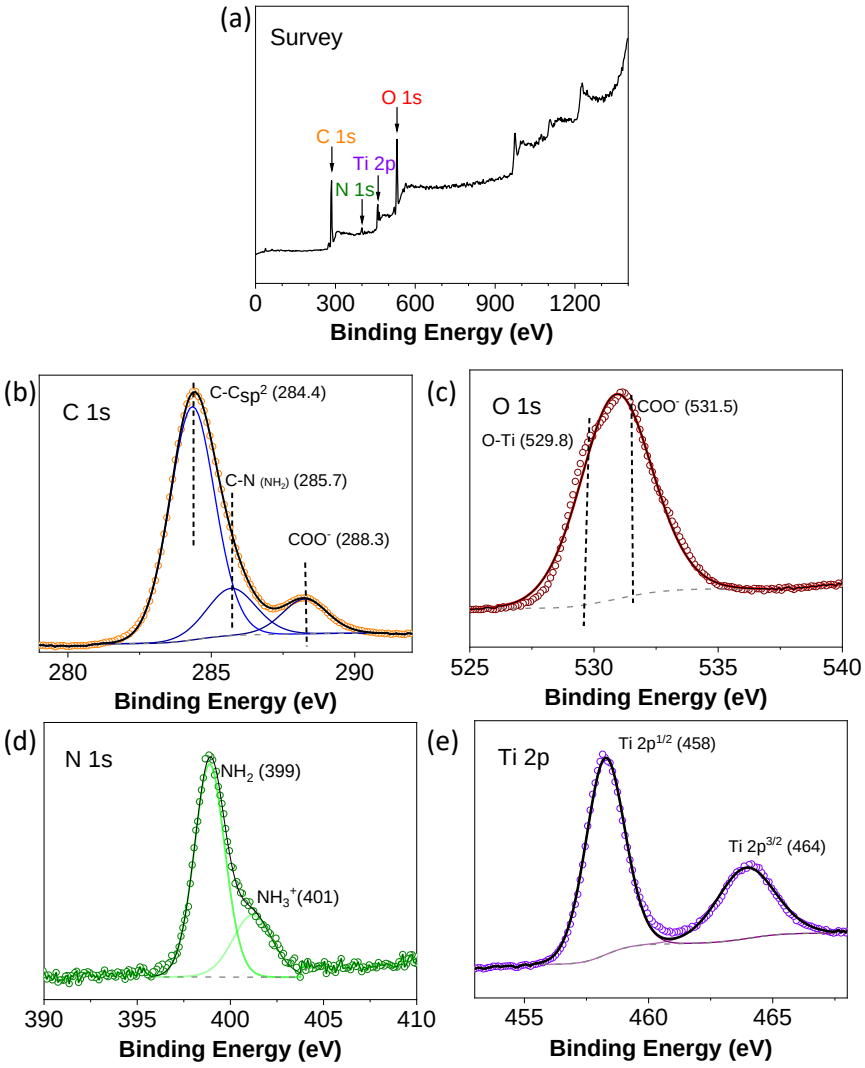

Figure S4. XPS of MIL-125(Ti)-NH_2: survey (a), C 1s (b), O 1s (c), N 1s (d), Ti 2p (e).

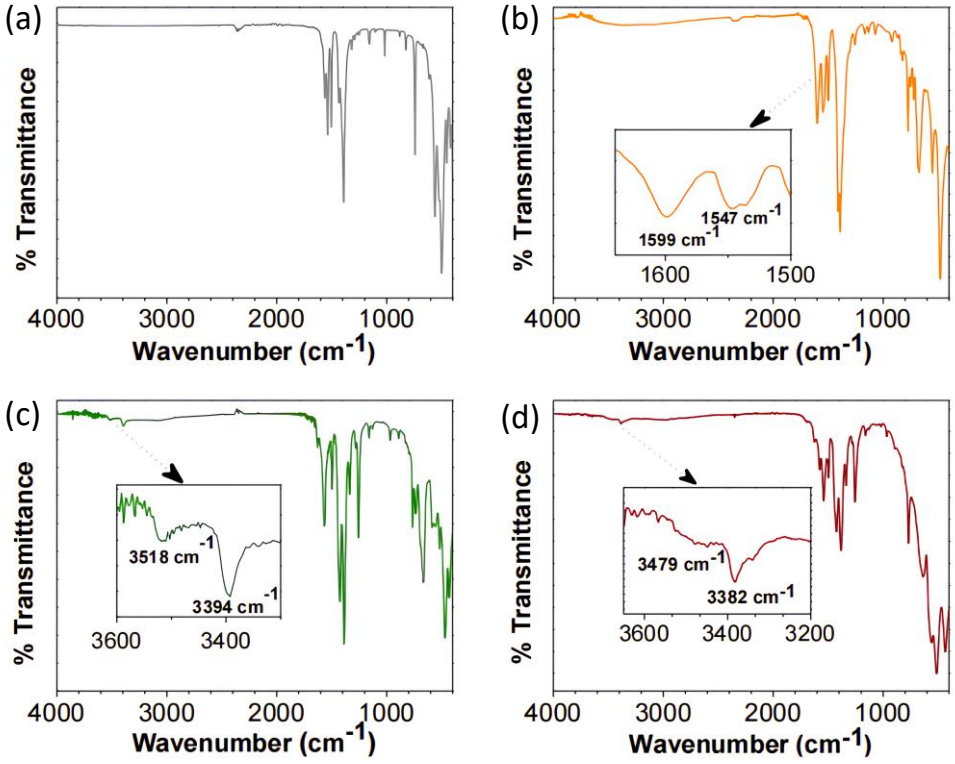

Figure S5. FT-IR spectroscopy of UiO-66(Zr) (a), UiO-66(Zr)-NO_2 (b), UiO-66(Zr)-NH_2 (c) and MIL-125(Ti)-NH_2 (d).

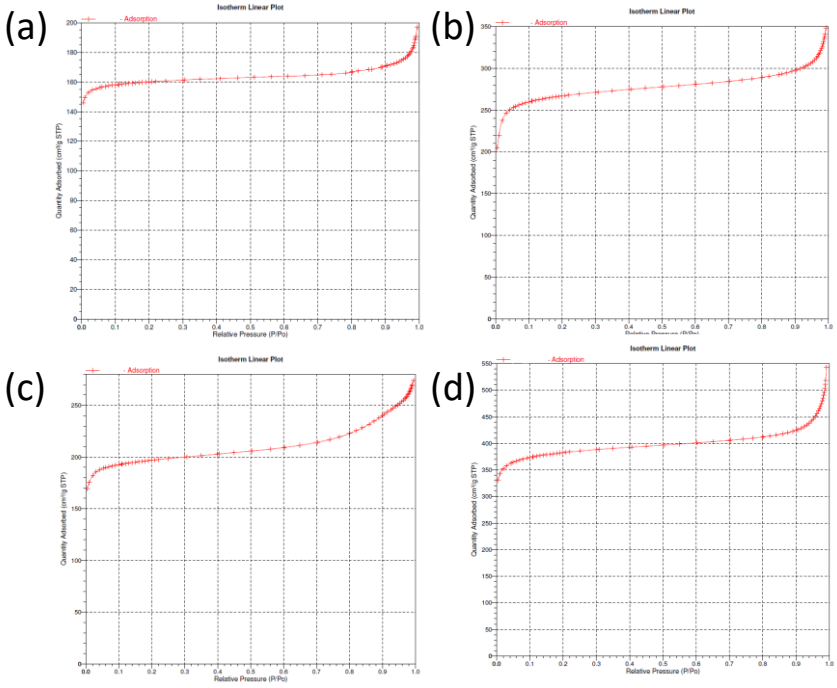

Figure S6. Isothermal N_2 adsorption curve of UiO-66(Zr) (a), UiO-66(Zr)-NO_2 (b), UiO-66(Zr)-NH_2 (c) and MIL-125(Ti)-NH_2 (d).

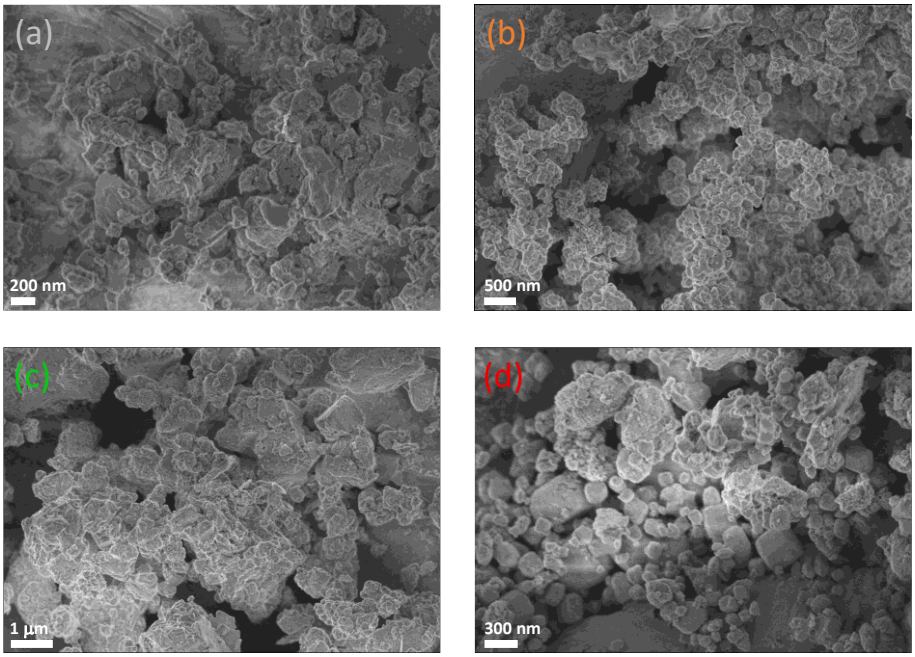

Figure S7. HR-SEM of UiO-66(Zr) (a), UiO-66(Zr)-NO_2 (b), UiO-66(Zr)-NH_2 (c) and MIL-125(Ti)-NH_2 (d).

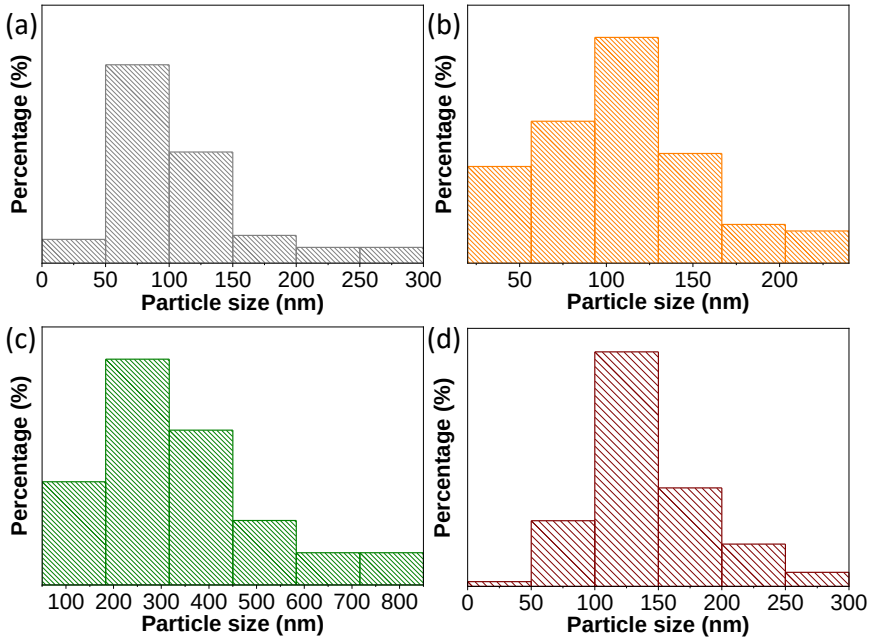

Figure S8. Particle size distribution of UiO-66(Zr) (a), UiO-66(Zr)-NO_2 (b), UiO-66(Zr)-NH_2 (c) and MIL-125(Ti)-NH_2 (d).

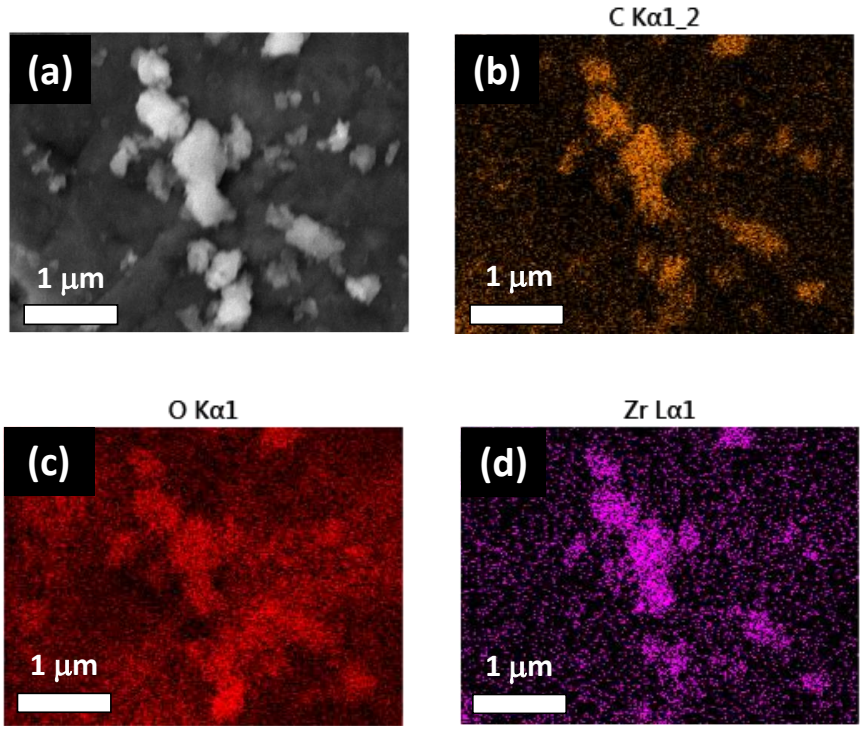

Figure S9. HR-SEM image of UiO66-(Zr) (a) and EDX mapping: carbon (b), oxygen(c), zirconium (d).

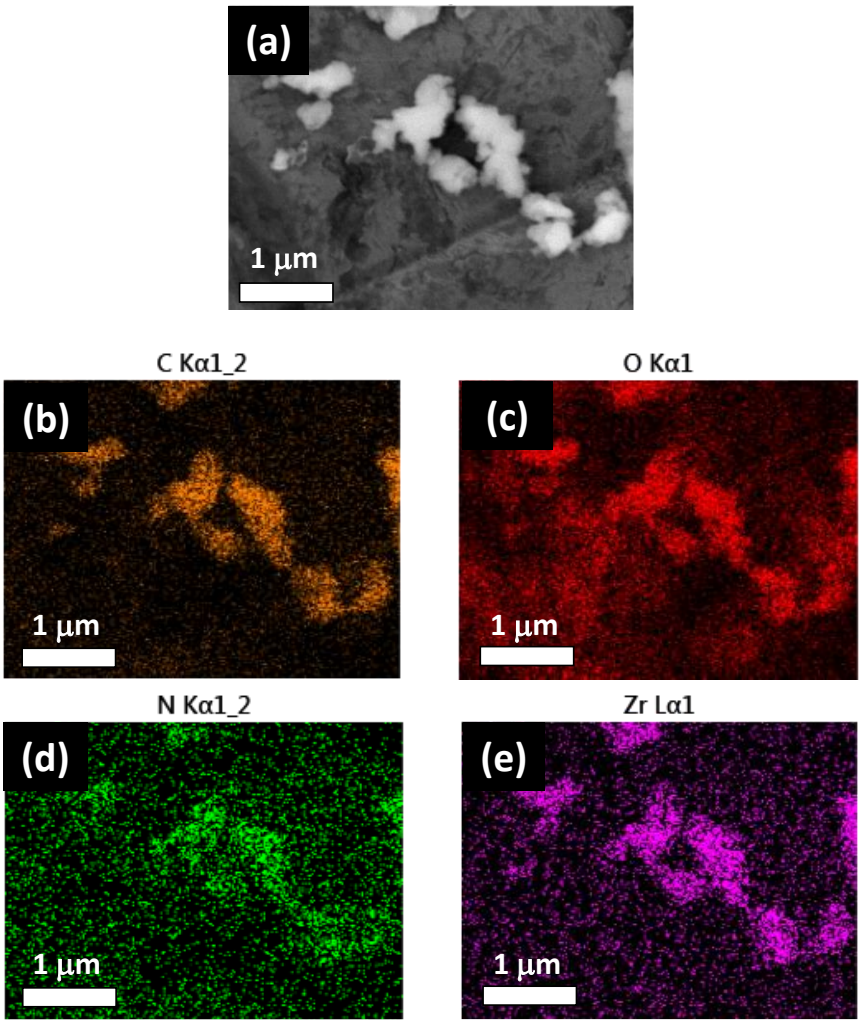

Figure S10. HR-SEM image of UiO66-(Zr)-NO_2 (a) and EDX mapping: carbon (b), oxygen(c), nitrogen (d), zirconium (e).

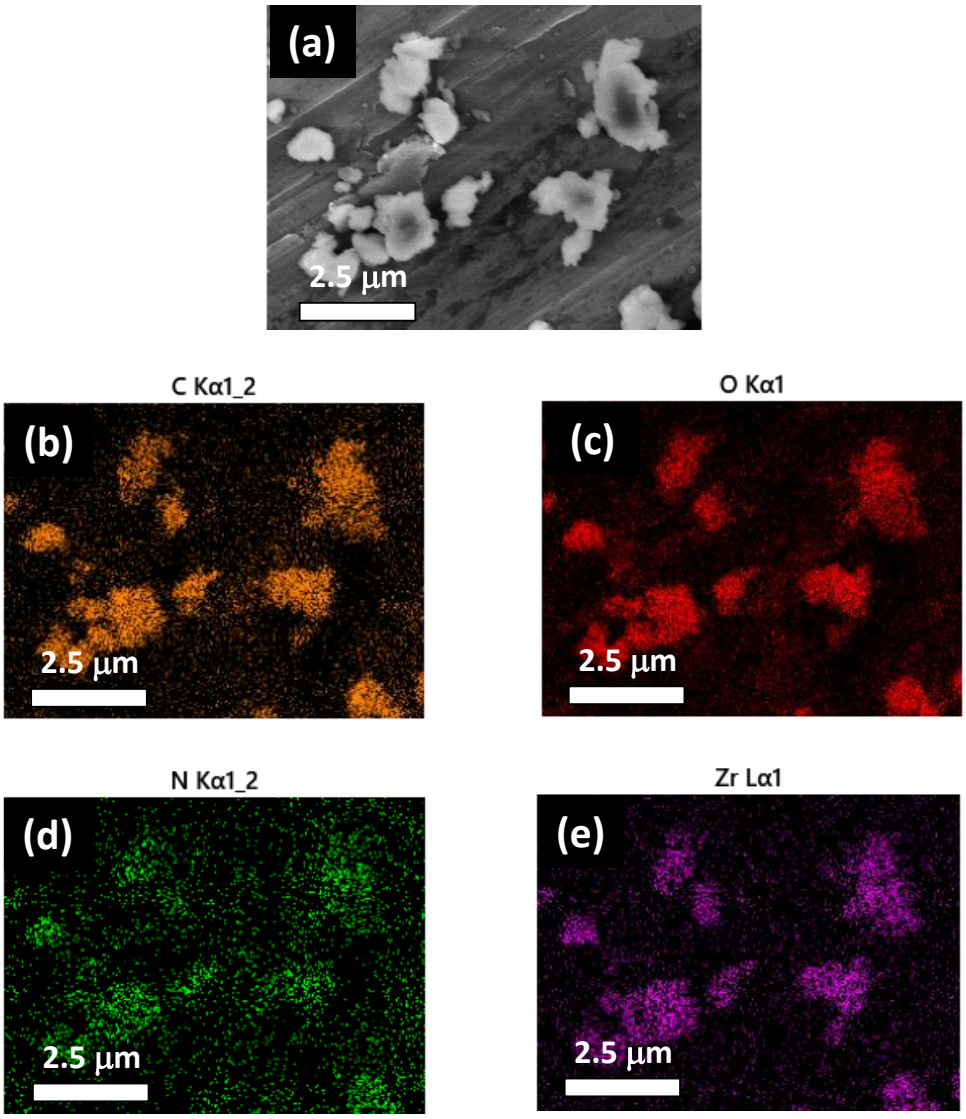

Figure S11. HR-SEM image of UiO66-(Zr)-NH_2 (a) and EDX mapping: carbon (b), oxygen(c), nitrogen (d), zirconium (e).

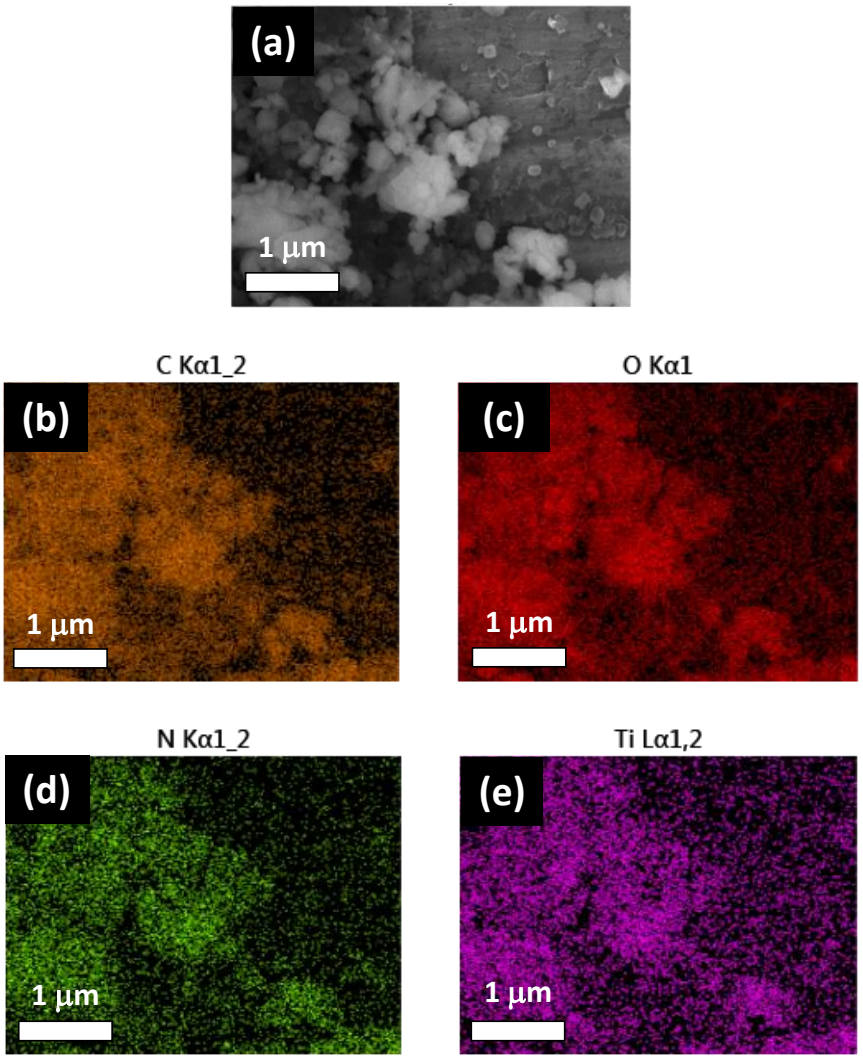

Figure S12. HR-SEM image of MIL-125-(Ti)-NH_2 (a) and EDX mapping: carbon (b), oxygen(c), nitrogen (d), titanium (e).

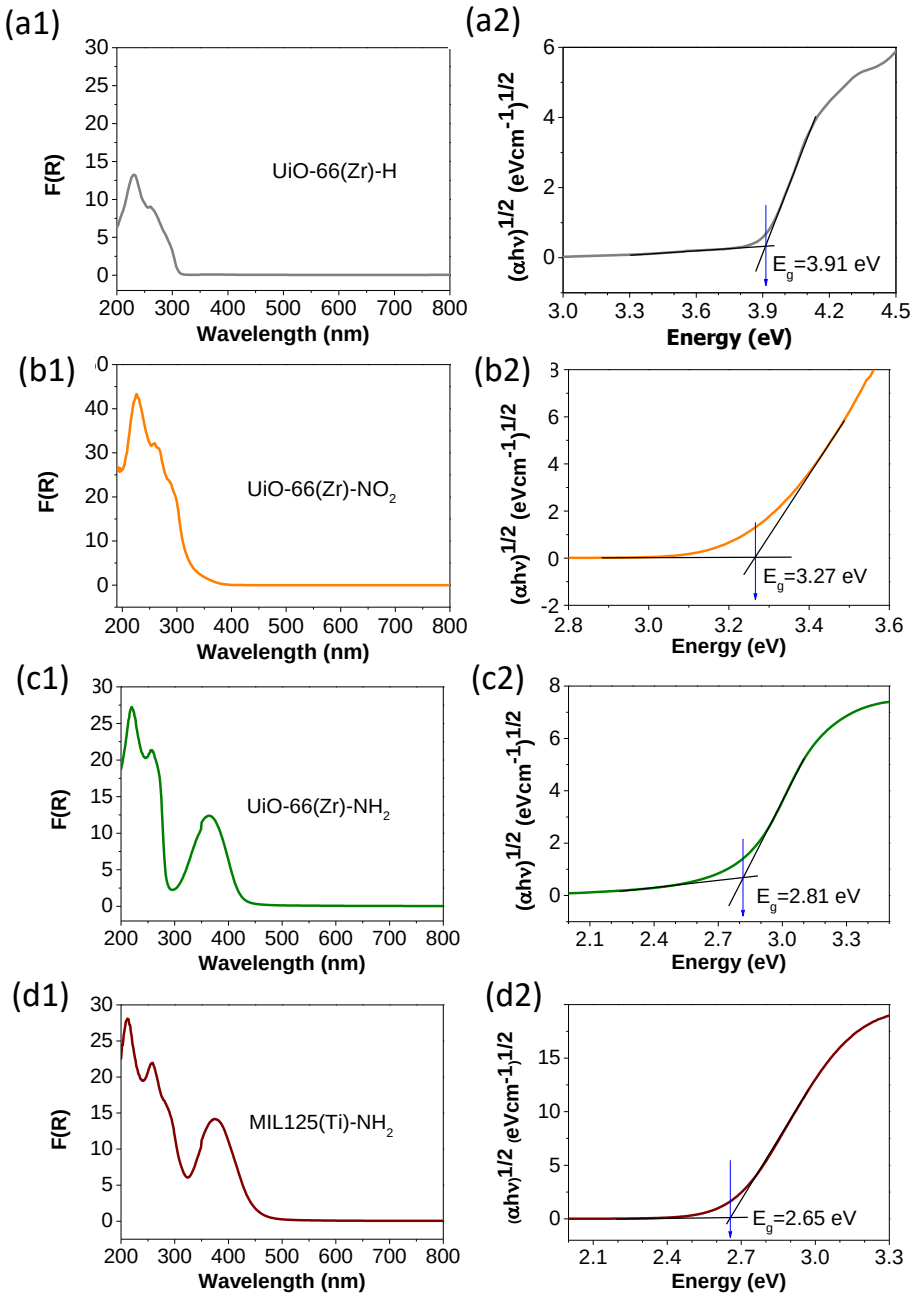

Figure S13. UV-Vis diffuse reflectance spectroscopy and its corresponding tauc plot: UiO-66(Zr) (a), UiO-66(Zr)-NO_2 (b), UiO-66(Zr)-NH_2 (c) and MIL-125(Ti)-NH_2 (d).

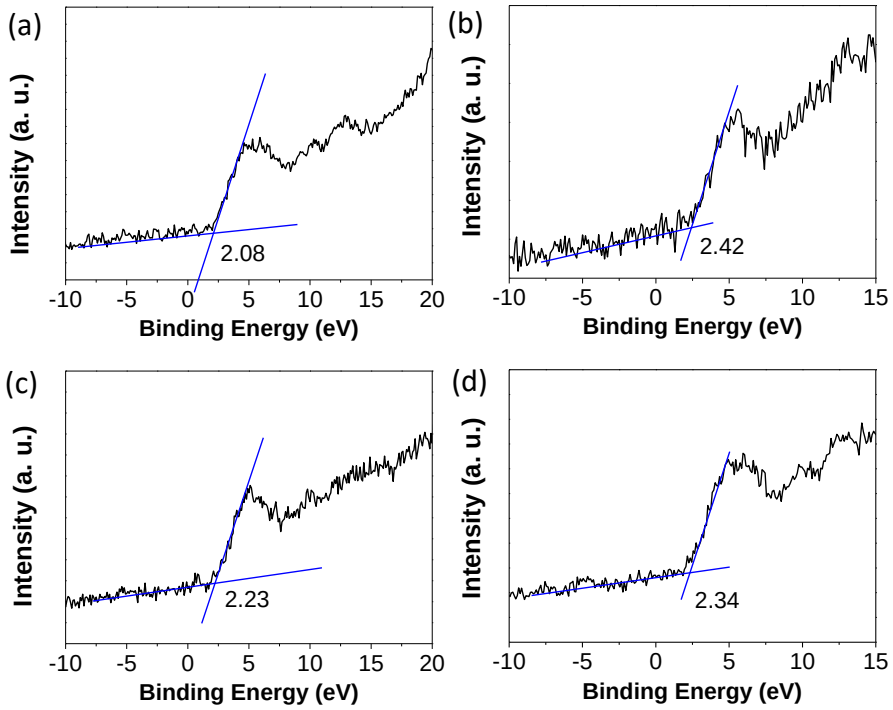

Figure S14. HOCO band of UiO-66(Zr) (a), UiO-66(Zr)-NO_2 (b), UiO-66(Zr)-NH_2 (c) and MIL-125(Ti)-NH_2 (d).

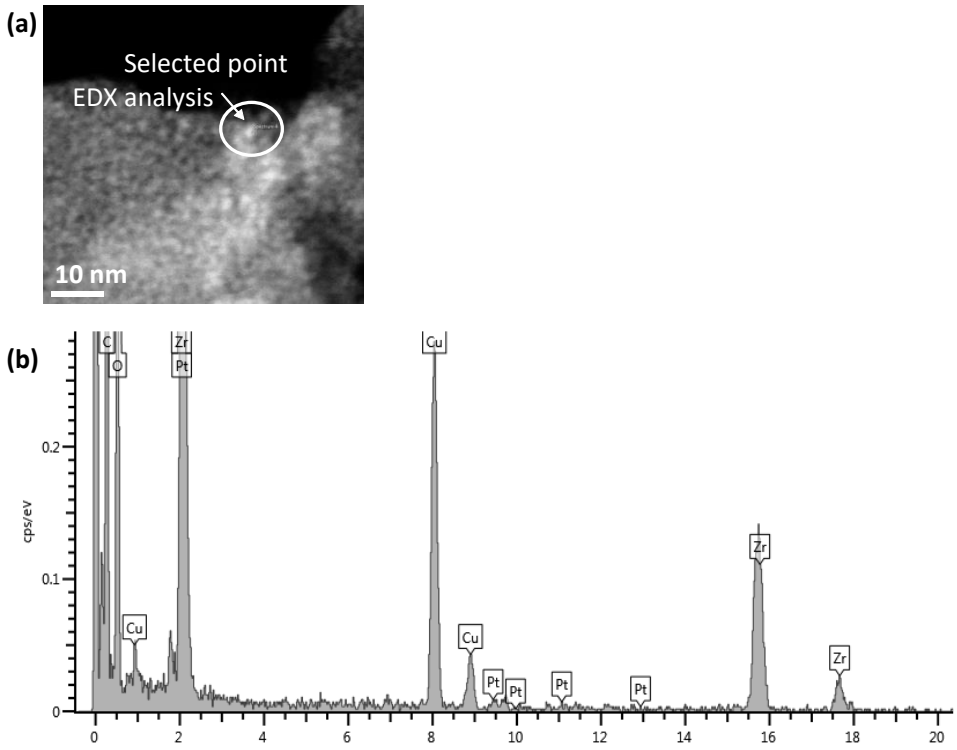

Figure S15. Representative DF-STEM image (a) and point EDX analysis of fresh Pt/UiO-66(Zr)-NH_2 (b).

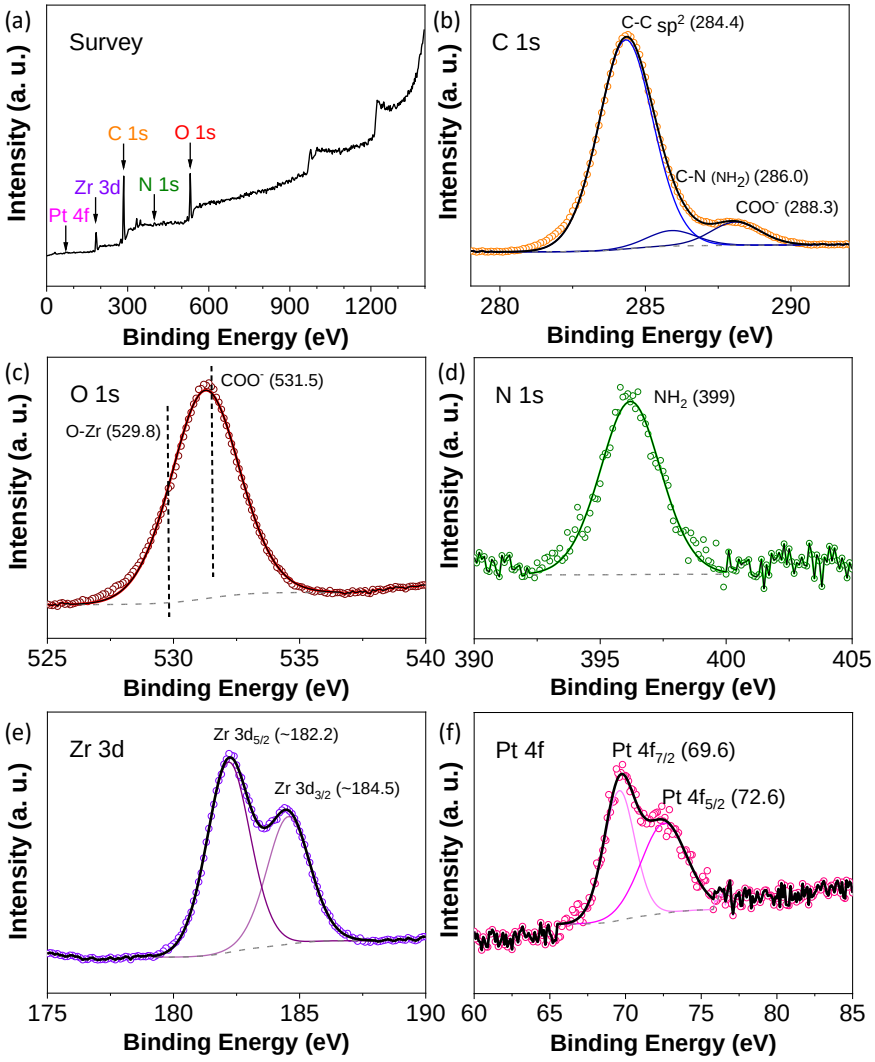

Figure S16. XPS C 1s (b), O 1s (c), N 1s (d), Zr 3d (e) and Pt 4f (f) of 1%wtPt@UiO-66(Zr)-NH_2.

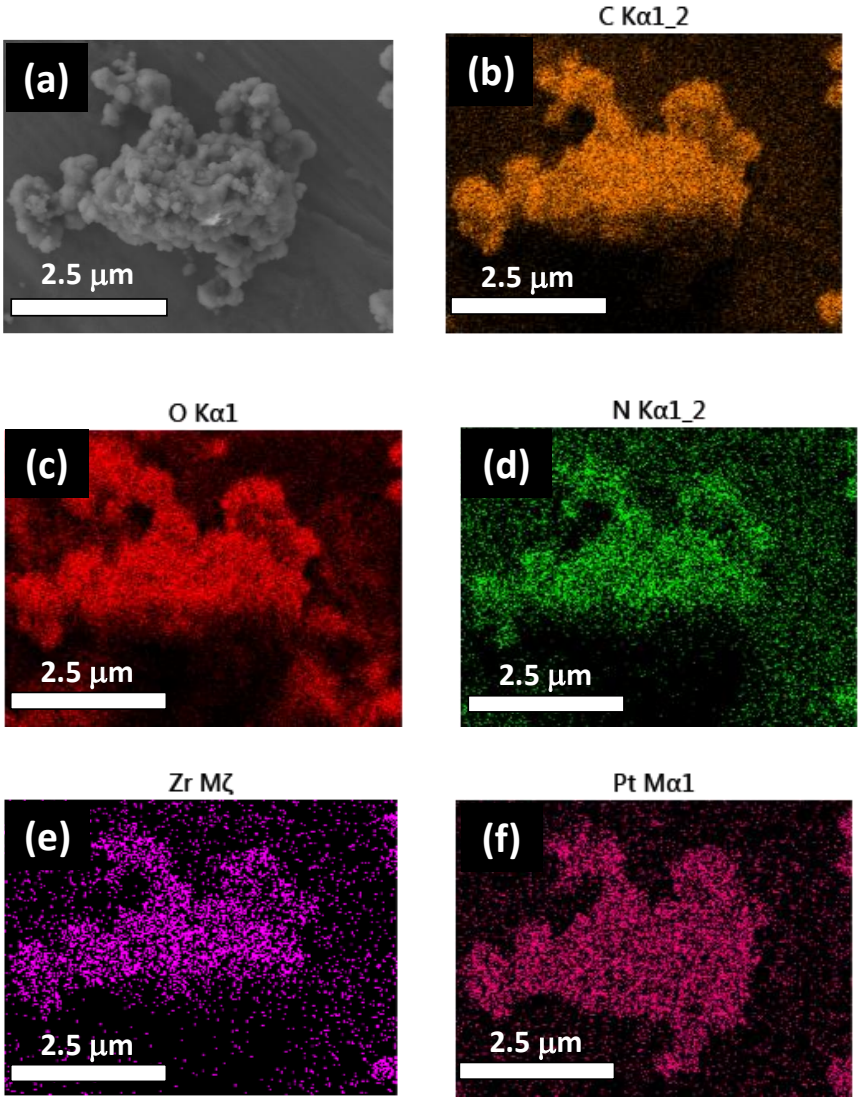

Figure S17. HR-SEM image of 1%wtPt@UiO-66(Zr)-NH_2. (a) and EDX mapping: carbon (b), oxygen(c), nitrogen (d), zirconium (e), platinum (f).

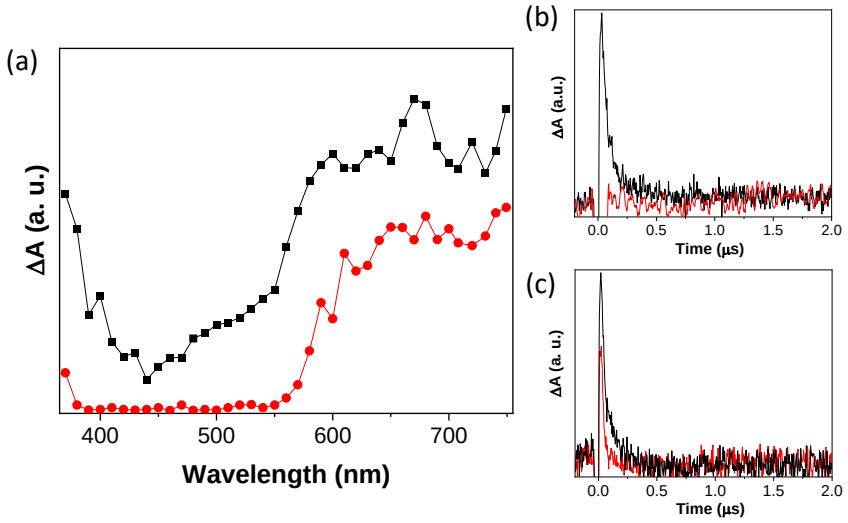

Figure S18. TAS spectra of Pt@UiO-66(Zr)-NH_2 purged with argon (■) and after adding CH_3OH (●) (a). Absorbance transition decay of Pt@UiO-66(Zr)-NH_2 before (black line) and after adding CH_3OH (red line) recorded at 380 nm (b) and 680 nm (c).

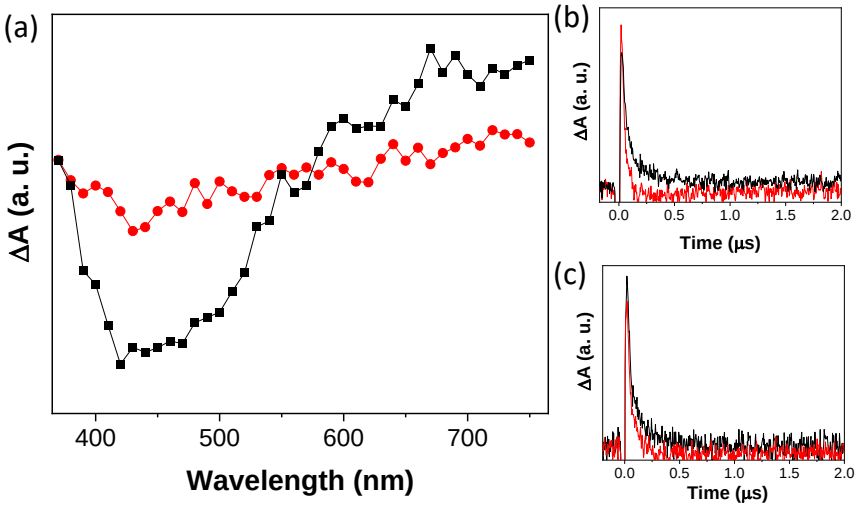

Figure S19. TAS spectra of Pt@UiO-66(Zr)-NH_2 purged with argon (■) and after adding molecular oxygen (●) (a). Absorbance transition decay of Pt@UiO- 66(Zr)- NH_2 before (black line) and after adding molecular oxygen (red line) recorded at 380 nm (b) and 680 nm (c).

3.8.3 References

(1). Melillo, A.; García-Vallés, C.; Ferrer, B.; Álvaro, M.; Navalón, S.; García, H., bifunctional metal-organic frameworks for hydrogenation of nitrophenol using methanol as hydrogen source. *Org. Biomol. Chem*. 2021, 19, 794-800.

(2). Shearer, G. C.; Chavan, S.; Bordiga, S.; Svelle, S.; Olsbye, U.; Lillerud, K. P., defect engineering: tuning the porosity and composition of the metal−organic framework UiO-66 via modulated synthesis. *Chem. Mater.* **2016,** *28*, 3749−3761.

Chapter 4. Solar-assisted photocatalytic water splitting using defective UiO-66 solids from modulated synthesis

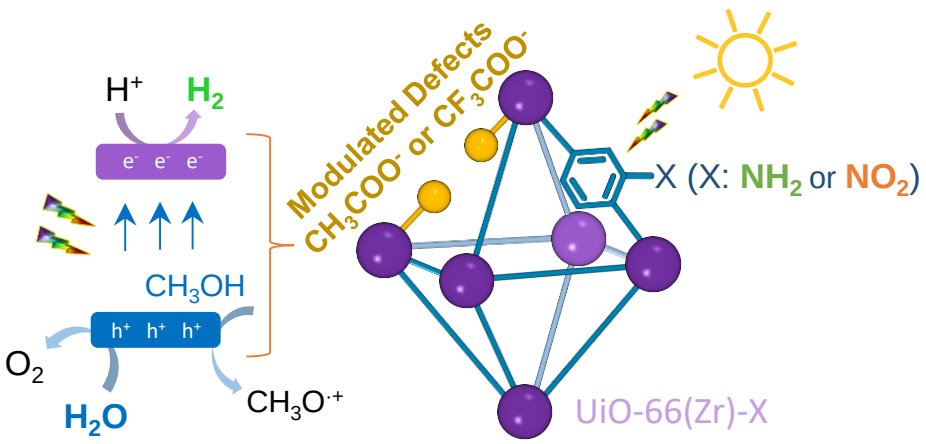

4.1 Abstract

MOFs are attracting increasing interest as photocatalysts for solar-driven hydrogen production from water. This chapter reports on a comparative study of using either acetic (AA) or trifluoroacetic acid (TFA) as the representative UiO-66 organic modulators for synthesizing visible light responsive UiO-66(Zr)-X (X: NH_2 or NO_2) photocatalysts for water splitting. The results show that photocatalytic hydrogen generation from a water/CH_3OH mixture can be improved by varying the nature and amount of the modulator employed to prepare the different UiO - 66(Zr)-X (X: NH_2 or NO_2) solid derivatives. UiO-66(Zr)-NH_2 was the most active photocatalyst, followed by UiO-66(Zr)-NO_2, both prepared with 12 equivalents (eq.) of acetic acid with respect to the organic ligand. This UiO-66(Zr)-NH_2 solid was more active than the parent MOF in photocatalytic OWS (H_2 and O_2 production of 450 and 160 μmol g^{-1}, respectively, in 5 h; AQY at 400 nm of 0.06 %) in the absence of CH_3OH and compares favorably with analogous reports. Information on the photocatalytic activity of the most active solids of both series was obtained by means of a series of techniques, including UV-Vis diffuse reflectance, XPS, LFP, EPR, PL and photoelectrochemical measurements together with DFT calculations. The results showed that organic acid modulators can be used to enhance the photocatalytic activity of missing linker UiO-66 defective materials in solar-powered water splitting.

4.2 Introduction

MOFs are a class of porous crystalline materials made up of multipodal organic ligands coordinated to metals ions, clusters or chains[1-6]. MOFs are among the most versatile and tuneable materials [7, 8] and can be used in a huge range of applications, including gas storage and separation[9,10], catalysis[11,12], photocatalysis[13,14] ,electrocatalysis[15], biomedicine[16], sensing[17] and many others[18,19].

In a seminal work in 2010, Garcia and co-workers reported the possibility of using UiO-66(Zr) and UiO-66(Zr)-NH_2 solids in the photocatalytic HER in the presence of CH_3OH as sacrificial electron donor under UV-Vis irradiation[20]. Later, in 2017 Huang, Liu and co-workers [21] used a MOF based on Ni(II) ions coordinated with the amino group of MIL-53(Al)-NH_2 as photocatalyst for OWS into H_2 and O_2 in the absence of sacrificial electron donor. Since then, the number of related studies especially for the HER [13, 22-25] and to a lesser extent for the more challenging OWS [13] has increased considerably. Some of the strategies reported to enhance MOFs photocatalytic activity for these reactions include [13, 22-26] deposition of metal NPs as co-catalysts, encapsulation of organic photosensitizers, preparation of MOFs with specific exposed-facets, development of heterojunctions based on MOF- on- MOF, MOF/inorganic semiconductors, MOF/carbon-based materials and tuning MOF-exposed facets, among others [13].

Another of the interesting possibilities of improving MOFs photocatalytic activity for hydrogen generation is the development of defective materials [27, 28]. In contrast to these few existing examples, MOF defect engineering has been shown as an appropriate approach to tune several of their physical, chemical and

textural properties[29-31] with applications in different areas, including heterogeneous catalysis[32-37]. In this context, there are several types of defective metal and/or organic ligand in MOFs that can be induced by PSM or in situ synthesis [29, 32-34, 38, 39]. For example, several studies have reported the introduction of structural defects in MOFs by PSM methods like thermal, chemical or plasma treatment [32, 38, 40, 41]. MOFs were reported as photocatalysts for water splitting in 2020, with the possibility of boosting the activity of MIL-125(Ti)-NH_2 by a PSM approach using an oxygen plasma treatment for both photocatalytic HER and OWS reactions [28]. The characterization data showed that this plasma treatment promotes the partial MOF decarboxylation and determines its energy level diagram. The most active defective sample had the most appropriate energy band diagram for both HER and OWS. Another method used to introduce defects in several MOFs, particularly in UiO-66 materials [42-44], is the so-called modulated synthesis [29, 32, 38, 40, 45]. This method consists of preparing the MOFs in the presence of organic (*ca.* formic, acetic, trifluoroacetic, benzoic acids) or inorganic (*ca.* HCl) compounds, sometimes simply referred to as modulators [29]. These modulators compete with the organic ligands during their coordination with the metal nodes, especially in MOFs with a high connectivity of SBU, i.e. UiO-66 based materials with 12-connected SBU [29, 46]. Some of the structural MOF defects are missing linkers or missing cluster defects [29, 46-48]. In this context, using formic acid as modulator during the preparation of UiO-66(Hf) produced UiO-66 missing-cluster defects in nanoregions with a *reo* topology [49]. Another study also reported that the modulated synthesis of UiO-66(Zr) using AA as modulator leads to the formation of missing linker defects [50]. In addition to the type of MOF structural defects [42], the nature and amount of the modulators can also determine their physical, chemical, morphological and textural properties [29]. A comprehensive investigation reported that monocarboxylic acid modulators with a growing acid

character, CH_3COOH < HCOOH < $Cl_2CHCOOH$ < F_3CCOOH, gradually increased some textural properties, such as the BET surface area[42]. About 20 eq. of the modulator had the strongest influence when using organic modulators, while larger amounts had less influence on these properties[42]. In this context, some theoretical[51] and experimental studies have shown that these organic modulators can modify MOF electronic properties such as UiO-66 solids and therefore their photocatalytic activity[27]. As a matter of fact, this former[51] and other theoretical works[36, 52-55] underlined the potential of theory to improve the photoactivity of functionalized UiO-66 defective materials via the setup of accurate structure-property relationships. Nonetheless, a complete theoretical picture addressing both the thermodynamics of the OWS reaction mechanisms, and the photophysics underlying these processes, has not been reported so far. It was also shown that HER photocatalytic activity under UV-Vis irradiation can be controlled by Pt NPs supported defective UiO-66(Zr)-NH_2 solids prepared with relatively high amounts of AA as modulator (50 to 200 eq.) with respect to the organic ligand[27]. A volcano relationship was found between the amount of AA and the photocatalytic activity for the series of Pt NPs supported UiO- 66(Zr)- NH_2 solids. The optimized photocatalyst prepared using 100 eq. of AA exhibited the highest charge separation efficiency and fastest relaxation kinetics, as revealed by ultrafast TAS. Based on the pertinent results achieved[27] and the reported possibilities to prepare defective MOFs from modulated synthesis[42], it would be of interest to further expand this line of research. For example, to achieve more evidence about the impact of defects generated by AA within UiO-66(Zr)-NH_2 during the photocatalytic HER it is planned to investigate the series of samples in the absence of Pt NPs as co- catalysts. In addition, the possibilities of visible-light responsive and defective MOFs having different energy band level diagrams like UiO-66(Zr)-NH_2 or UiO- 66(Zr)-NO_2 with other modulators to boost their

photocatalytic activities not only for HER but also for the challenging OWS with high interest for practical applications [13] are also explored.

With these precedents in mind, the present chapter describes a comparative study of the performance of UiO-66(Zr)-X (X: NH_2 or NO_2) solids prepared using relatively low proportions of AA and TFA as modulators during photocatalytic solar-driven overall water splitting reaction. The innovation of this investigation resides in the fact that for the first time here is reported the development of defective UiO-66(Zr)-X (X: NH_2 or NO_2) materials from modulated synthesis as an adequate strategy to enhance their photocatalytic activity for water splitting reactions in the absence of any co-catalyst. To the best of my knowledge, this is the first example describing the application of defective MOFs from modulated synthesis as photocatalysts for the OWS. Besides, the photocatalytic activity of the most active sample developed in this study namely UiO-66(Zr)-NH_2 from modulated synthesis with AA is higher than that achieved with other MOF-based photocatalysts having in some cases noble metals as co-catalysts (Section 3.2). In addition, the importance of this study associates with the fundamental understanding of the origin of the activity of the solids under study by experimental characterization using spectroscopic tools like LFP, PL, EPR, electrochemical impedance, transient photocurrent measurements together with DFT calculations.

4.3 Experimental section

4.3.1 Materials

All the materials employed in this study were supplied by Merck and were of analytical or HPLC grade.

4.3.2 Preparation procedures

UiO-66(Zr)-NH_2 materials. The UiO-66(Zr)-NH_2 solid was prepared by a solvothermal method previously reported[42]. Briefly, $ZrCl_4$ (0.862 g, 3.699 mmol), 2-aminoterephthalic acid (0.677 g, 3.701 mmol) and Mili-Q H_2O (0.200 mL, 11.10 mmol) were mixed with DMF (100 mL, 1291 mmol) in 250 ml volumetric flask. The system was heated at 70 °C and stirred during the preparation to ensure the complete dissolution of the reagents. Once all reagents were dissolved, the stirring magnet was removed from the system and the flask was closed. Then, it was placed in a pre-heated oven at 120 °C for 72 hours. The resulting precipitate was recovered by filtration. Then, it was washed 3 times with DMF and three more with CH_3OH. It was further washed in a Soxhlet for 4 h using CH_3OH as the solvent. And finally, the powder was dried under vacuum at 150 °C overnight. Similarly, a series of UiO-66(Zr)-NH_2 were prepared in the presence of different amounts of AA or TFA as modulators. The experimental procedure is the same as described for UiO-66(Zr)-NH_2 with the addition of different eq. of each modulator: 12 eq. of AA (2.542 mL), 36 eq. (7.626 mL), 100 eq. (21.183 mL) or TFA 12 eq. (3.425 mL) or 36 eq. (10.275 mL). Attempts to prepare UiO-66(Zr)-NH_2 with 100 eq. of TFA practically did not result in the formation of any solid. The samples were labelled as UiO-66(Zr)-NH_2-XAA or UiO-66(Zr)-NH_2-XTFA where “X” refers to the number of equivalents of modulator employed during the synthesis.

UiO-66(Zr)-NO_2 materials. The UiO-66(Zr)-NO_2 solid was synthesized using a solvothermal method reported[42]. Briefly, $ZrCl_4$ (0.862 g, 3.699 mmol), 2- nitroterephthalic acid (0.790 g, 3.701 mmol) and Mili-Q H_2O (0.200 mL, 11.10 mmol) were mixed with DMF (100 mL, 1291 mmol) in 250 ml volumetric flask. The system was heated at 70 °C while stirring to ensure the complete dissolution of the reagents. Once all reagents were well dissolved, the flask was placed in a pre-heated oven at 120 °C for 72 hours after removing the stirring magnet and closing the system. The resulting precipitate was recovered by filtration. Then, it was washed three times with DMF and subsequently, three times with CH_3OH. It was further washed in a Soxhlet for 4 h using CH_3OH as the solvent. Finally, the powder was recovered by drying under vacuum at 150 °C overnight. The series of modulated UiO-66(Zr)-NO_2 samples were similarly prepared with the addition of AA 12 eq. (2.542 mL), 36 eq. (7.626 mL), 100 eq. (21.183 mL) or TFA 12 eq. (3.425 mL) or 36 eq. (10.275 mL). Attempts to prepare UiO-66(Zr)-NO_2 with 100 eq. of TFA practically did not afford any formation of solid. Samples were labelled as UiO-66(Zr)-NO_2-XAA or UiO-66(Zr)-NO_2-XTFA where the "X" refers to the number of eq. of modulator employed during the synthesis.

Deposition of Pt NPs within UiO-66(Zr)-NH_2-12AA. Pt NPs were deposited within the UiO-66(Zr)-NH_2-12AA network using the photodeposition method[56]. As commented in Chapter 3 (Section 3.8.1) Briefly, 50 mg of the MOF was suspended in a mixture of H_2O (8 mL) and CH_3OH (13 mL) using a quartz tube. As platinum precursor, $H_2PtCl_6 \cdot (H_2O)_6$, previously dissolved in water (1 mL) was used and added to the solution. Then, the system was sonicated for 10 min (450 W) to get a good dispersion of the solid. Subsequently, the system was purged with an argon flow for 30 min to remove the presence of air. The system was maintained under

inert atmosphere using a balloon containing Ar. Finally, the system was irradiated with a Xe lamp (150 W) for 4 h. The resulting solid was obtained by filtration, washing it several times with Milli-Q water. The sample was placed in an oven at 100 °C for at least 24 h. Before use, the solid was activated under vacuum at 150 °C for 12 h.

4.3.3 Characterization

The samples were characterized by several techniques including PXRD, UV - Vis DRS, XPS, liquid- and solid-state ^{1}H- and ^{19}F-nuclear magnetic resonance spectroscopy (NMR), EIS, LFP spectroscopy, fluorescence spectroscopy, EPR spectroscopy, SEM and TEM electron microscopy techniques coupled to EDX, isothermal N_2 adsorption measurements, TGA, photoelectrochemical measurements (Figure S1) and computational calculations (Figures S2, S3 and Table S1), details can be found in Section 4.8.

4.3.4 Photocatalytic activity

The series of UiO-66(Zr)-X (X: NO_2 or NH_2) were tested as photocatalysts for water splitting. Briefly, the required amount of photocatalyst (10 mg) was dispersed in a mixture of H_2O (16 mL) and CH_3OH (4 mL) using a quartz reactor (50 mL). The system was sonicated for 20 min (450 W) to facilitate the solid suspension. In the case of the photocatalytic OWS, the liquid employed for the experiment was Mili-Q water (20 mL). The photoreactor was subsequently purged with an argon flow for 20 min to remove the presence of oxygen. The reaction started by irradiation the top of the reaction by simulated sunlight (LC-8 light guide lamp; 1.5 AM filter) with an irradiance power of 220 mW/cm^2.

4.4 Results and discussion

4.4.1 Photocatalyst characterization

The series of UiO-66(Zr)-X (X: NH_2 or NO_2) solids synthesized in the absence or presence of different eq. of AA or TFA as modulators with respect to the organic ligand were characterized by PXRD. Figure 1 shows that all the materials exhibited the expected UiO-66 topology according to the simulated pattern. Previous studies reported that the modulated synthesis of UiO-66 materials by AA can be used to introduce structural defects in the form of ordered missing linkers[41, 50]. In this work, the PXRD of the as-synthesized UiO-66 materials by either AA or TFA did not reveal the presence of diffraction peaks at around 4 and 6, associated with 100 and 110 reflections of the UiO-66 reo topology, respectively. The absence of these reflections indicates a relatively low proportion or absence of ordered missing cluster defects in the UiO-66 solids[42,49,57].

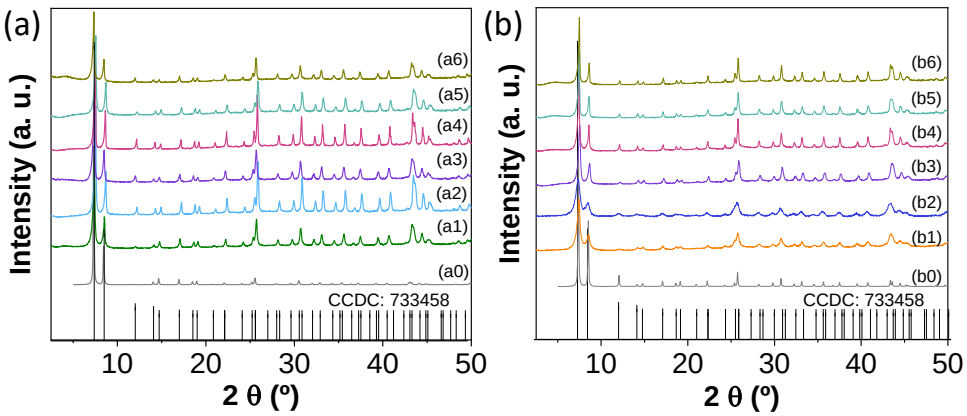

Figure 1. Simulated UiO-66 pattern (a0, b0) and PXRD of UiO-66(Zr)-NH_2 (a) or UiO-66(Zr)-NO_2 (b) solids prepared without (a1, b1) or with 12 (a2, b2), 36 (a3, b3) or 100 (a4, b4) eq. of AA or with 12 (a5, b5) or with 36 (a6, b6) eq. of TFA. PDF card was obtained from crystallographic data provided by K.P. Lillerud to the Cambridge Crystallographic Data Centre (CCDC), which deposition number is: 733458.

Based on related studies and the present UiO-66(Zr)-X (X: NH_2 or NO_2) solids characterization data, the presence of missing linker defects is likely[27,29,48,49,57-59].

Sample porosity was studied by isothermal N_2 adsorption measurements (Figures S4-S7 and Table 1 and S2). The modulated synthesis of UiO-66(Zr)-X (X: NH_2 or NO_2) solids by AA, and especially TFA, increases the porosity (BET and pore volume) in higher extent than the non-modulated materials, which is associated to the partial replacement of terephthalate-based ligands by monocarboxylic acid modulators in the SBU and, as a consequence, higher spaces are generated within the MOF structure [27]. The highest porosities were obtained for UiO-66(Zr)-X (X: NH_2 or NO_2) solids when using 12 eq. of TFA, followed by the samples prepared using the same AA eq. These results agree with previous reports that found the porosity of UiO-66(Zr) solid could be increased with TFA more than by AA [42]. Attempts to use higher eq. of modulators for TFA (*ca.* 36) or AA (*ca.* 36 or 100) as modulators did not increase the porosity or their photocatalytic activity for HER (Section 3.2). These results are similar to those obtained during UiO-66(Zr) synthesis by either TFA or AA in which the BET surface area rose by up to 30 % using less than 30 equivalents, while higher amounts produced a plateau of surface area values [42].

Table 1. List of UiO-66 materials prepared with indication of their BET [a], pore volume [a], average particle size[b] and standard deviation[b].

Eq.	Number	**UiO-66(Zr)-NH_2**			**UiO-66(Zr)-NO_2**		
		BET surface area (m^2/g)	Average particle size and standard deviation (nm)	Pore volume (cm^3/g)	BET surface area (m^2/g)	Average particle size and standard deviation (nm)	Pore volume (cm^3/g)
Without	0	827	278 ± 108	0.315	650	311 ± 248	0.260
AA	12	1201	62 ± 25	0.455	753	43 ± 18	0.290
	36	1141	344 ± 177	0.439	749	62 ± 20	0.283
	100	1083	468 ± 120	0.423	729	486 ± 60	0.280
TFA	12	1238	175 ± 63	0.496	816	134 ± 41	0.315
	36	739	191 ± 18	0.284	546	192 ± 22	0.224

[a] Estimated from isothermal N_2 adsorption measurements (Figures S1 and S2)
[b] Estimated from SEM measurements (Figure 3 and Figures S3-S7)

TGA of UiO-66(Zr)-NH_2 (Figures 2a and S8) and UiO-66(Zr)-NO_2 (Figures 2b and S8) solids were used to estimate the number of structural defects[42]. Based on previous studies, the number of linker defects per Zr_6 formula unit for UiO - 66(Zr) - X (X: NH_2 or NO_2) can be referred as $Zr_6O_{6+x}(BDC\text{-}NH_2)_{6-x}$ or $Zr_6O_{6+x}(BDC\text{-}NO_2)_{6-x}$ [42]. Weight losses at between room temperature and about 300 °C were attributable to the removal of water and the AA or TFA modulators. Higher temperatures caused the combustion of the 2-amino or 2-nitroterephthalate ligands and led to a residue above 700 °C associated with the formation of ZrO_2. For comparison, the TGA curves in Figure 2 are normalized to the residue obtained after calcination. The results indicate that using increasing amounts of AA from 12 to 100 equivalents as modulator when synthesizing UiO-

66(Zr)-NH_2 or UiO-66(Zr)-NO_2 solids reduces the proportion of 2-amino or 2-nitroterephthalate organic ligand below the metal content, respectively, as the number of defects (depicted as "x" in Figure 2) increases with the amount of modulator used to synthesize the UiO-66 solids (Figure 2 and S8), as other authors have found[42]. In other words, increasing the amount of AA in the synthesis produces a higher proportion of coordinated acetates than the 2-amino or 2-nitroterephthalates in the MOF network. In fact, liquid ^{1}H-NMR analysis of previously digested UiO - 66(Zr)-X (X: NH_2 or NO_2) solids prepared using AA show the presence of a singlet signal at 1.83 ppm associated with the -CH_3 group of the modulator (Figure S9). Additional characterization of the samples UiO-66(Zr)-X (X: NH_2 or NO_2) by solid-state ^{1}H-NMR revealed the appearance of broad signals associated due to the protons from the organic ligands together with Zr-OH signals that overlaps with methyl groups of acetates (Figure S11)[60]. Similarly, the UiO-66 samples prepared with TFA as modulator are characterized by a ^{19}F-NMR signal at -75.69 ppm (Figure S10). Solid-state ^{19}F-NMR characterization further confirms the more intense ^{19}F-NMR signal in the MOF structures prepared with 36 eq. of TFA as modulator (Figure S12)[54]. Figure 2 also shows that 12 equivalents of TFA produced more defective MOFs than even 100 AA equivalents. The UiO-66(Zr)-X (X: NH_2 or NO_2) samples prepared with AA or TFA as modulators were characterized by SEM-EDX analysis (Figures S13-24) and revealed the presence of the expected elements (C, O, N, Zr, F) in each case within the MOF particles.

In TGA analysis, the thermal stability of modulated UiO-66(Zr)-X (X: NH_2 or NO_2) generally decreases as the number of defects increases. These observations can be understood by considering the replacement of bipodal terephthalate to bridge the SBU of the MOF compared with the presence of monocarboxylate ligands in these SBU. Regardless of these comments it is pertinent to mention that to obtain

some insights about the nature of structural defects on MOFs advanced spectroscopic techniques such as positron annihilation lifetime spectroscopy, EPR spectroscopy, X-ray absorption near-edge structure, or extended X-ray absorption fine structure, among other possible can be used [34, 35, 61, 62].

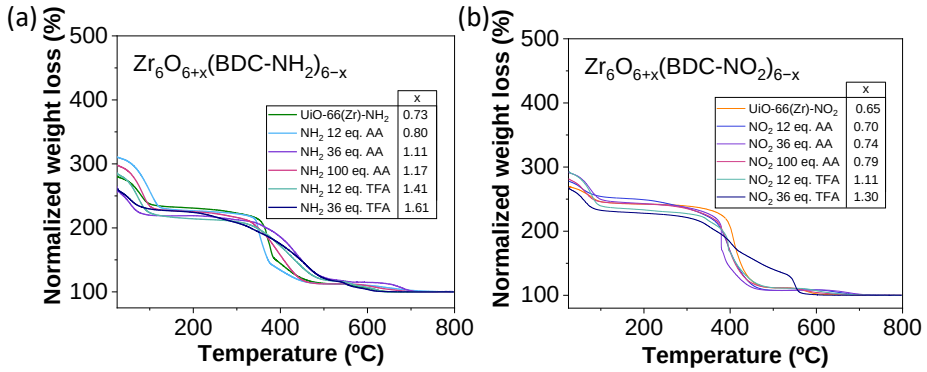

Figure 2. TGA analysis of UiO-66(Zr)-NH_2 (a) and UiO-66(Zr)-NO_2 (b) synthesized in the absence or in the presence of AA or TFA as indicated. The number of linker defects per Zr6 formula unit is indicated.

The particle size distribution and morphology of the series of UiO-66 solids were studied by SEM (Table 1, Figure 3 and S25-S29). Non-modulated UiO- 66(Zr)- NH_2 (Figure 3a and Figure S25) and UiO-66(Zr)-NO_2 (Figures S27a and S28a) samples were characterized by the presence of intergrown irregularly shaped particles with an estimated average particle size and standard deviations of about 278 ± 108 and 311 ± 248 nm, respectively. Using 12 equivalents of AA or TFA, the modulated synthesis of UiO-66(Zr)-X (X: NH_2 or NO_2) reduced the particle size distribution with respect to the parent MOFs (Table 1 and Figures 3, S25, S26). Increasing the amount of AA from 36 or 100 equivalents during the preparation of UiO-66(Zr)-X (X: NH_2 or NO_2) gradually increased the particle size distribution. In contrast to the non-modulated or modulated samples prepared with

36 equivalents of modulator or lower, the UiO-66(Zr)-X (X: NH_2 or NO_2) samples prepared with 100 equivalents of AA have a well-defined octahedral shape.

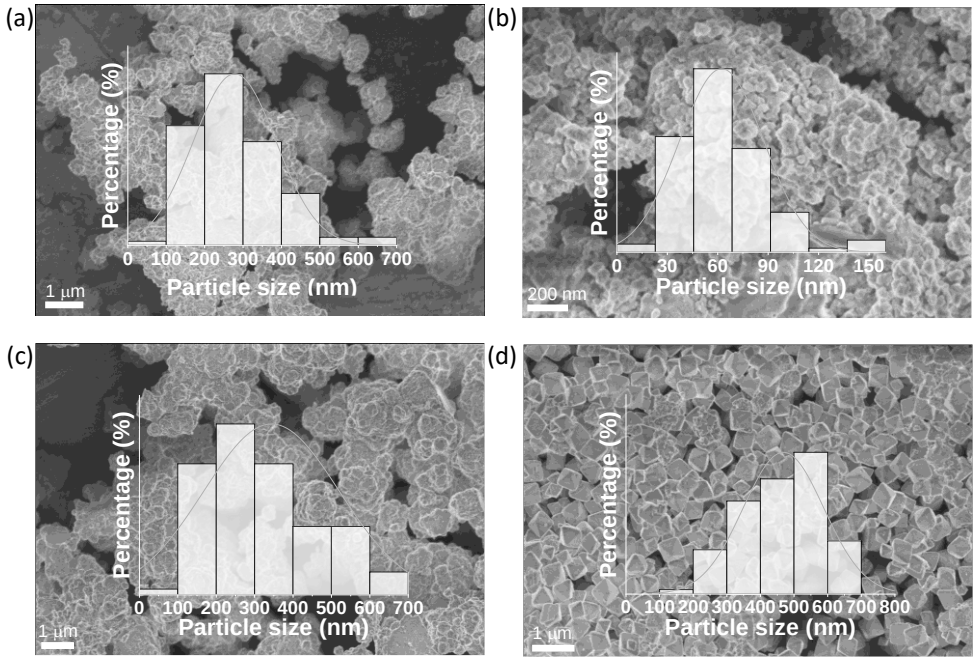

Figure 3. SEM images and particle size distribution of UiO-66(Zr)-NH_2 solids prepared in the absence (a) or in the presence of 12 (b), 36 (c) or 100 (d) equivalents of AA.

The most photocatalytically active UiO-66(Zr)-X (X: NH_2 or NO_2) samples prepared with 12 equivalents of AA and their parent MOFs were further characterized by XPS (Figure 4). The deconvolution of the individual elements present in the MOFs can be seen in Figures S30-S33. The XPS survey analysis of these samples showed the expected C 1 s, O 1 s, N 1 s and Zr 3p (Figure 4a). High resolution XPS was performed on the different elements. The expected general features of these MOFs are generally described as follows: C 1s spectra (Figure 4b) shows the presence of three deconvoluted bands centered at 284.4, 286.5 and 288.5 due to the presence of aromatic C-C sp^2 atoms, C-N bonds, and COO^- groups,

respectively. The broad band of O 1s spectra associated with the presence of oxygen atoms in the MOF as Zr-O bonds (529 eV) and COO^- (531 eV) (Figure 4c). The N 1s spectra of UiO-66(Zr)-NH_2 and UiO-66(Zr)-NO_2 is dominated by main bands at 399 and 405 eV due to the presence of amino and nitro groups, respectively (Figure 4c). Zr 2 p shows the expected bands for Zr(IV) ions at 182 and 185 eV due to the presence of Zr $2p_{1/2}$ and Zr $2p_{3/2}$, respectively (Figure 4c). C 1s XPS comparative analysis (Figure 4b) also reveal a small but significant difference between the modulated and non-modulated UiO-66 solids, which is the slightly higher proportion of -COO^- groups (288 eV) in the modulated samples, in agreement with previous characterization data on the incorporation of acetate groups within the SBU instead of terephthalate derivatives.

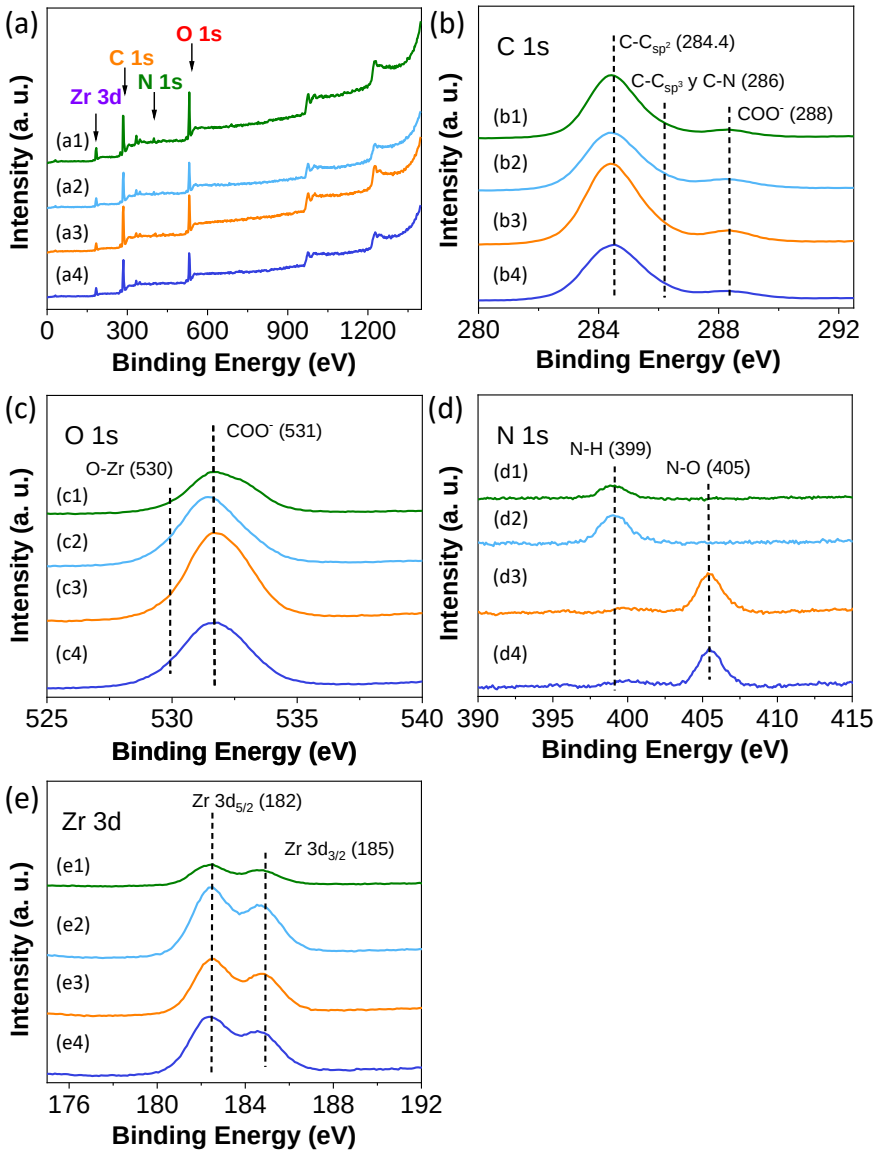

Figure 4. XPS (a) survey, C 1s (b), O 1s (c), N 1s (d) and Zr 3d (e) for UiO-66(Zr)-NH_2 (1, green), UiO-66(Zr)-NH_2-12AA (2, blue), UiO-66(Zr)-NO_2 (3, orange) and UiO-66(Zr)-NO_2-12AA (4, dark blue).

The optical properties of the modulated and non-modulated UiO-66(Zr)-X (X: NH_2 or NO_2) solids were analysed by UV-Vis diffuse reflectance spectroscopy (Figures S34 and S35). Figure 5 shows the absorption features of the most photocatalytically active UiO-66(Zr)-NH_2-12AA and UiO-66(Zr)-NO_2-12AA, together with their parent non-modulated solids. In good agreement with previous reports, the presence of the electron donor -NH_2 group in the terephthalate organic ligand favours the absorption of light up to about 450 nm compared to the white UiO-66(Zr) solid[56]. Although to a lesser extent, the presence of -NO_2 groups in the UiO-66(Zr) solid also favours a bathochromic shift of the absorption up to wavelengths of about 400 nm. The estimated optical band bap for UiO-66(Zr)-NH_2-12AA and UiO-66(Zr)-12AA by using the Tauc plot method was 2.85 and 3.10 eV, respectively. A comparative analysis of modulated and non-modulated UiO-66(Zr)-X (X: NH_2 or NO_2) using AA or TFA revealed the negligible influence of these modulators on their estimated optical band gaps (Figures S34- S35), indicating the important role of terephthalate organic ligands in determining the optical properties of these solids.

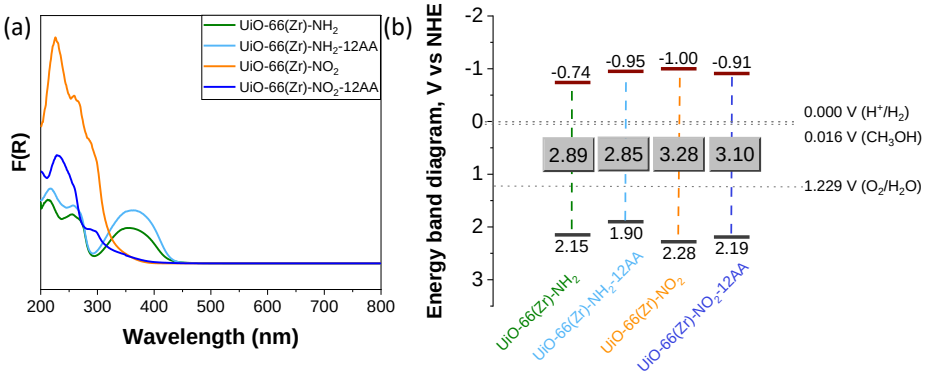

Figure 5. (a) UV-Vis diffuse reflectance and (b) energy band level diagram of UiO- 66 solids as indicated. The redox potentials required for water splitting and CH_3OH oxidation versus NHE are indicated [13,63].

XPS was further used to estimate the HOCO band of UiO-66(Zr)-X (X: NH_2 or NO_2)-12AA solids and compare it with their pristine MOFs (Figure S36). The results indicated a small but significant positive shift of the HOCO values measured for modulated samples compared to the parent MOFs. In a closely related precedent, theoretical calculations revealed that, compared to the ideal 12-fold coordinated nodes, in the UiO-66(Zr) structure the related structures with 10- or 9-fold coordinated linkers increases the charge transfer capabilities[51]. Photoinduced electrons are thus preferentially located on the lowest coordinated zirconium atoms of defective UiO-66 solids, a situation that is expected to increase the photocatalytic activity of defective solids. Other study using an optimized and partially decarboxylated MIL-125(Ti)-NH_2 solid showed that this material also exhibited a small shift towards positive HOCO values compared to the parent MOFs while having practically the same optical band gap[28]. These results show the possibility of fine-tuning the electronic properties of MOFs by missing-cluster strategies. The details of the calculations to estimate the energy band level of MOF shown in Figure 5 versus the NHE can be found in Section 4.8.1 Supporting Information. Together with other characterization techniques, these energy level diagrams will be employed later to explain the observed order of photocatalytic activity[13, 63].

4.4.2 Photocatalytic activity

The aim of this study was to investigate the influence of carboxylate organic modulators such as AA or TFA on UiO-66 photocatalysts in water splitting reactions. AA and TFA are common carboxylic acid modulators used to prepare UiO-66 solids with specific density of structural defects, physicochemical, textural and electronic properties compared to the ideal parent MOF. The photocatalytic activities of UiO-66(Zr)-X (X: NH_2 or NO_2) with or without organic modulators were

first evaluated for generating H_2 from water and CH_3OH mixtures under simulated sunlight irradiation. Pristine UiO-66(Zr)-NH_2 exhibits relatively higher activity than the UiO-66(Zr)-NO_2 photocatalyst (Figure 6). This could be associated with UiO-66(Zr)-NH_2's lower band gap, which provides a more efficient absorption of simulated solar light irradiation and favour the proton reduction reaction towards H_2 formation.

Interestingly, the UiO-66(Zr)-X (X: NH_2 or NO_2) solids synthesized with different equivalents of AA (12, 36 or 100 eq.) or TFA (12 or 36 eq.) as modulators are more active than the parent MOFs for HER under simulated sunlight irradiation (Figures 6a and 6b). The most active UiO-66(Zr)-X (X: NH_2 or NO_2) solids with respect to their parent MOFs are those prepared with 12 eq. of AA. In addition, Figures 6c and 6d show the H_2 production during the photocatalytic HER versus the number of linker defects per Zr_6 formula unit for UiO-66(Zr)-X (X: NH_2 or NO_2) referred as $Zr_6O_{6+x}(BDC\text{-}NH_2)_{6-x}$ or $Zr_6O_{6+x}(BDC\text{-}NO_2)_{6-x}$. These figures reveal a volcano-like relationship between the number of defects (x) introduced by using AA or TFA as modulators respect to the parent samples with the photocatalytic activities. The UiO-66 solids prepared with 12 eq. of AA exhibit the highest photocatalytic activities and are gradually decreased for the samples prepared with 36 or 100 eq of AA. Similarly, UiO-66 samples prepared with 12 eq. of TFA exhibit higher activity compared to those solids prepared with 36 eq.

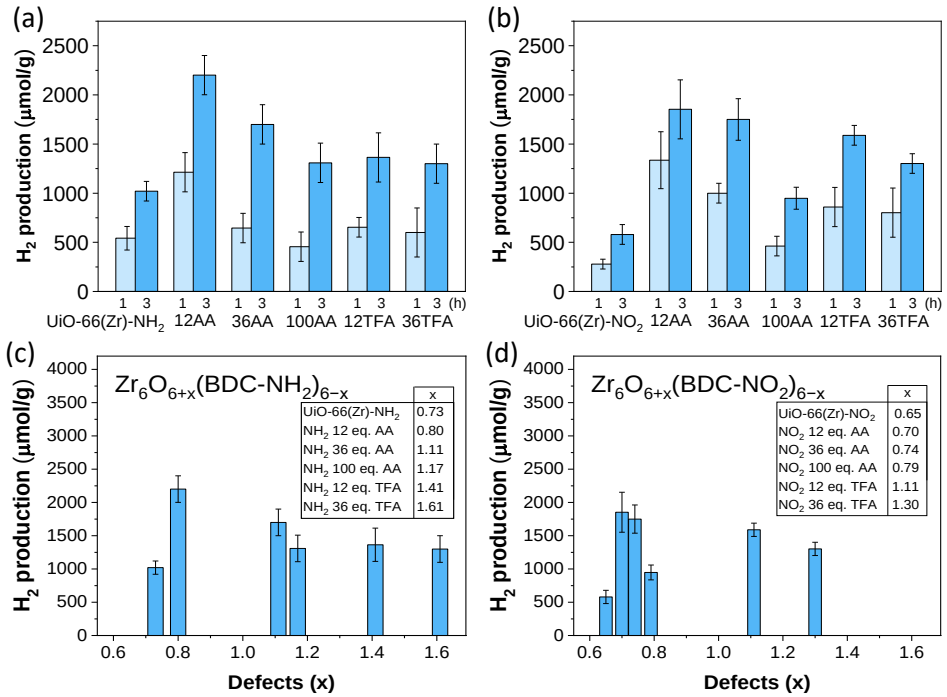

Figure 6. Photocatalytic HER under simulated sunlight irradiation using UiO- 66(Zr)-NH_2 (a) or UiO-66(Zr)-NO_2 (b) solids prepared with or without modulator as indicated. Relationship between the photocatalytic H_2 generation during HER at 3 h using UiO-66(Zr)-NH_2 (c) or UiO-66(Zr)-NO_2 solids as indicated and the number of defects (x) in each sample.

Initially the possible influence of the BET surface area or MOF particle size on the resulting photocatalytic activity was evaluated. Modulated synthesis of UiO- 66 solids prepared with AA (12, 36 or 100 eq.) or TFA (12 eq.) results in an increased BET surface areas respect to the parent samples (Table 1). However, the UiO-66(Zr)-X (X: NH_2 or NO_2) samples prepared with 12 eq. of TFA do not correspond to the highest photocatalytic activity (Figure 6). Additionally, UiO-66 solids prepared with 12, 36 or 100 eq of AA have almost similar BET values but exhibit different photocatalytic activities. Furthermore, UiO-66 solids prepared with 36 eq. of TFA exhibit a significant decrease in BET values compared to those

prepared with 12 eq. of TFA but, however, the differences in the activities are relatively lower. Therefore, the observed photocatalytic activities for the different UiO-66 defective solids suggest that the BET surface area is not a factor that determines the photocatalytic activity.

Additionally, UiO-66 solids prepared with 12 eq. of AA exhibit the smallest particle sizes of the series while maintaining high surface areas (Table 1) and this situation might favour their photocatalytic performances. However, some UiO-66 solids prepared with 36 or 100 eq. of AA have larger particle sizes than pristine solids but exhibiting higher activities compared to non-modulated MOFs. Moreover, even though the particle size of UiO-66(Zr)-NH_2-36AA is considerably higher (344 ± 177 nm) than UiO-66(Zr)-NH_2-12TFA (175 ± 63 nm), the photocatalytic activity of the former solid in the HER is almost similar. Thus, these results imply that besides particle size of UiO-66 solids some other factors should also contribute to the observed photocatalytic activities. In fact, it is anticipated that the increased activity of the defective UiO-66 solids is related to the efficient photoinduced charge separation and lower charge transfer resistance (Rct) as evidenced by transient photocurrent and EIS measurements, respectively (Section 3.3.1 Mechanistic evidence). Further, DFT calculations (Section 3.3.2) were also performed with UiO-66(Zr)-NH_2 solids prepared using AA or TFA as modulators and the observed data suggest that this is an appropriate strategy to decrease the energy barriers during both HER or OER respect to non-modulated solids.

UiO-66(Zr)-NH_2 prepared with 12 AA as the most active photocatalyst in the series was also found to be reusable without a significant loss of activity (Figure 7a). PXRD (Figure 7b) and ICP-OES measurements of the liquid phase after

the reaction showed that the three-times used solids retain their crystallinity with the absence of zirconium leaching, respectively. Additionally, ICP-OES analyses of acid digested used UiO-66(Zr)-NH_2-12AA solid reveal similar zirconium content compared to the fresh sample (32.5 wt%). In agreement with previous studies, the deposition of Pt NPs (2.48 ± 0.49 nm) as noble metal reference co-catalyst (Figure S29) for the photocatalytic HER within UiO-66(Zr)-NH_2-12AA solid further increases its photocatalytic activity to 2263 μmol g^{-1}.

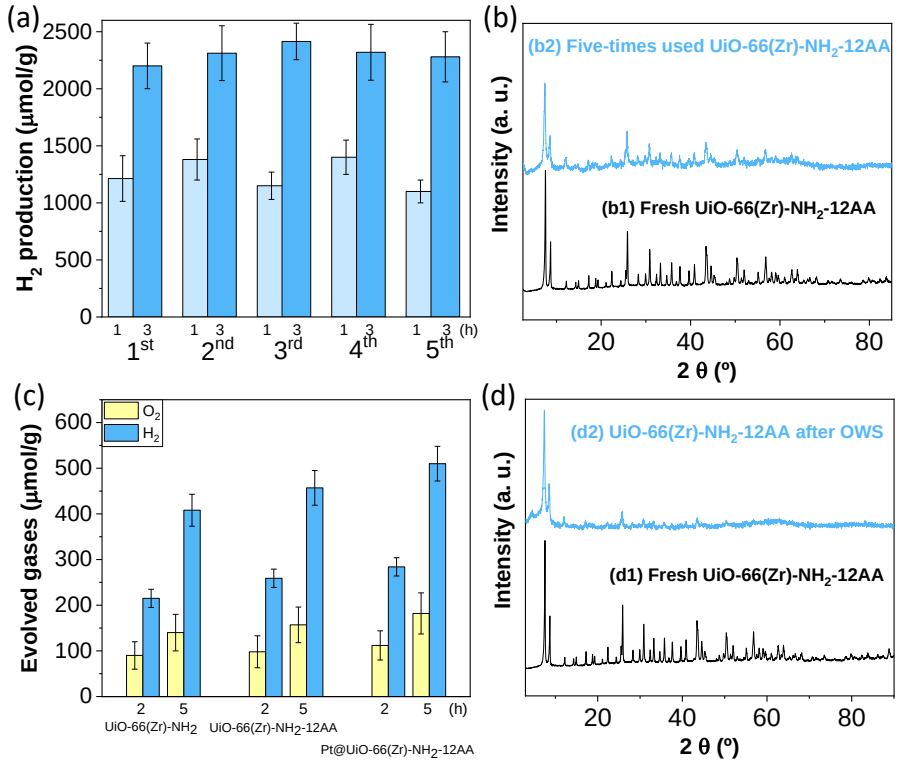

Figure 7. (a) Reusability of UiO-66(Zr)-NH_2-12AA during the photocatalytic HER under simulated sunlight irradiation. (b) PXRD of fresh (b1) and five-times used (b2) photocatalyst. (c) Photocatalytic OWS with UiO-66(Zr)-NH_2, UiO- 66(Zr)- NH_2- 12AA and Pt@UiO-66(Zr)-NH_2-12AA after 2 and 5 h reaction times. (d) XRD of fresh and used UiO-66(Zr)-NH_2-12AA after OWS.

The UiO-66(Zr)-NH_2 or UiO-66(Zr)-NO_2 materials prepared with 12 AA equivalents as modulator and their parent solids were further evaluated as photocatalysts for the OWS under simulated sunlight irradiation. For the sake of comparison, these experiments were performed under the same conditions used for photocatalytic HER but replacing CH_3OH by H_2O. The photocatalytic activity for OWS of UiO-66(Zr)-NH_2-12AA is higher compared to non-modulated UiO- 66(Zr)-NH_2 (Figure 7c). Similarly, the photocatalytic activity of UiO- 66(Zr)- NO_2-12AA shows 30 % more activity (233 and 89 μmol g^{-1} for H_2 and O_2, respectively, after 5 h) than pristine solid. The considerably lower activity of UiO- 66(Zr)-NO_2-12AA compared to UiO-66(Zr)-NH_2-12AA is associated with the higher band gap of the former. Importantly, photocatalytic OWS using UiO- 66(Zr)- NH_2-12AA sample with $H_2{}^{18}O$ and the subsequent analysis of the evolved gases by GC-MS showed m/z of 36 which confirms the formation of $^{18}O_2$ (Figure S37). This control experiment clearly proves the photocatalytic OWS oxidation pathway mediated by UiO-66(Zr)-NH_2-12AA. The use of UiO - 66(Zr) - NH_2- 12AA modified with Pt NPs (Figures S42 and S43) further increases the photocatalytic activity compared to UiO-66(Zr)-NH_2-12AA for the OWS (Figure 7c). In this case, ICP-OES analyses of the liquid phase after the OWS reaction show the presence of zirconium (1.7 mg/L) and platinum (0.094 mg/L) leaching that represent 1 and 1.9 wt% respect to the initial amounts of these metals in the fresh catalyst, respectively. Furthermore, ICP-OES analyses of acid- digested used Pt NPs supported UiO-66(Zr)-NH_2-12AA reveal the above conclusions on the occurrence of Pt or Zr leaching.

Figures 7c and S38 show that the ratio of H_2 production between 2 and 5 h is higher compared to O_2 production during the photocatalytic OWS. Based on previous related studies [13, 26, 64, 65], one possible explanation for this experimental

observation might be related with the in situ O_2 reduction reaction during the photocatalytic process leading to the formation of reactive oxygen species or H_2O_2. Thus, the possible formation of H_2O_2 during the photocatalytic OWS using UiO-66(Zr)-NH_2-12AA or UiO-66(Zr)-NO_2-12AA was proved by titration of reaction aliquots at different reaction times with titanyl oxalate as previously reported [26,66]. The obtained results do not show the presence of H_2O_2 during the OWS reaction. Therefore, the lower rate of O_2 production compared to H_2 might be related with the formation of non-measurable amounts of H_2O_2 by using the titanyl oxalate method and/or the occurrence of other side reactions that consume photogenerated O_2. Other possible reasons such as the saturation of MOF porosity by O_2 that is more soluble than H_2 may also be a reason of the different observed gas rates during the reaction[26].

XRD patterns of the used UiO-66(Zr)-NH_2-12AA sample show some changes compared to the fresh one after photocatalytic OWS (Figure 7d). Additionally, XPS comparisons of the fresh and used UiO-66(Zr)-NH_2-12AA show no significant differences between the spectra (Figures S39 and S40). Furthermore, SEM or SEM- EDX (Figure S41) characterization of the used UiO-66(Zr)-NH_2-12AA do not show significant changes of particle size distribution or elemental distributions. In contrast, analysis of the gas phase after the photocatalytic OWS reaction reveal the presence of CO_2 (87 μmol g^{-1} after 5 h). In this context, previous studies have shown that carboxylate-based MOFs can undergo partial decarboxylation under UV-Vis irradiation[14]. Therefore, it is proposed that UiO-66(Zr)-NH_2-12AA might undergo some partial decarboxylation during the reaction.

The photocatalytic activity of UiO-66(Zr)-NH_2-12AA was compared with that achieved in previous studies using related solids, and the results are summarised

in Table S2. As it can be seen in this table, UiO-66(Zr)-NH_2-12AA is the most active in H_2 and O_2, producing 450 and 160 μmol g^{-1}, respectively, after 5 h. Previously reported MOF-based catalysts under simulated or visible light irradiation, *ca* H_2 and O_2 productions in 22 h are below 400 and 200 μmol·g^{-1}, respectively, including UiO-66(Zr)-$NH_{2(core)}$@UiO-66(Ce)$_{(shell)}$[26], UiO-66(Ce)-NH_2 with Pt NPs (1 wt%) as co-catalyst[64], UiO-66(Zr/Ce/Ti)[67], MIL-125(Ti)-NH_2 treated with oxygen-plasma[68], Ti-MOF (IEF-11)[69] and comparable or higher to that of porphyrin-based MOFs like MIL-173(Zr/Ti)-40 (40 wt % of Ti content)[70], PCN-222(Zn)[65] or liposome-MOF built from Pt- porphyrin, [Ru(2,2′-bipyridine)$_3$]$^{2+}$ and Ir-bipyridine catalytic centers[71]. Besides, UiO-66(Zr)-NH_2-12AA achieved estimated AQY of 0.13, 0.06 and 0.04 % upon irradiations at 350, 400 and 450 nm, respectively. These AQY values are higher compared to a MOF-on-MOF composite built of UiO-66(Zr)-$NH_{2(core)}$@UiO-66(Ce)$_{(shell)}$ with the value of 0.034 % at 400 nm[26]. Not surprisingly, a couple of precedents using porphyrin-based MOFs such as MIL-173(Zr/Ti)-40 [70] (AQY at 450 nm of 0.11 %) or liposome-based MOF [71] containing Pt metalated porphyrin units together with [Ru(2,2′-bipyridine)$_3$]$^{2+}$ and Ir-bipyridine catalytic centers (AQY at 436 nm of 1.5 ± 1% at 436 nm) reported somehow higher AQY than UiO-66(Zr)-NH_2-12AA. In the present case, photodeposition of Pt NPs as the benchmark HER co-catalyst in UiO-66(Zr)-NH_2-12AA (Figures S42 and S43) solid further increases the resulting activity for the photocatalytic OWS (Figure 7c). Additionally, the estimated STH achieved with UiO-66(Zr)-NH_2-12AA sample during the photocatalytic OWS reaction is 0.022 %. This STH value is higher compared to Ni - based phosphonate MOF (0.0001 %) as photocatalyst[72]. Overall, these results indicate that the preparation of defective UiO-66 solids by modulated synthesis is a convenient strategy to boost the photocatalytic activity of the samples towards HER and the more challenging OWS under simulated sunlight irradiation.

4.4.3 Reaction mechanism

4.4.3.1 Spectroscopic and electrochemical study

Several spectroscopic and electrochemical analysis were carried out to analyse the observed photocatalytic activity using the series of modulated UiO- 66 samples. Figure 8a shows that the modulated synthesis of UiO-66(Zr)-NH_2 using either AA or TFA has an effect in their fluorescence properties, displaying much lower intensity than the parent solid. In this regard, the most photocatalytically active UiO-66(Zr)-NH_2-12AA displayed the lowest fluorescence of all derivatives. Moreover, in good agreement with these observations, the presence of Pt NPs (1 wt%) in UiO-66(Zr)-NH_2-12AA enhanced the photocatalytic activity for both HER and OWS and strongly reduced fluorescence intensity. Hence, the fluorescence results can thus be associated with the improvement of photoinduced charge separation in modulated samples with respect to pristine UiO-66(Zr)-NH_2. Similarly, lower fluorescence emission when using Pt NPs supported UiO-66(Zr)-NH_2-12AA further support the dual role of the co-catalyst in favouring both photoinduced charge separation and promoting the proton reduction reaction[13]. Similar fluorescence measurements were carried out using UiO-66(Zr)-NO_2 solids (Figure 8b). In this case, the lower emission of the UiO- 66(Zr)-NO_2 samples than UiO-66(Zr)-NH_2 samples is in line with their corresponding organic ligand emission in solution (Figure 8b inset). Further characterization of UiO-66 samples prepared with and without modulators by time-resolved fluorescence spectroscopy to get more information about electron-hole pair recombination indicates that these samples exhibit lifetimes below the quantification limit of the instrument used (< 2 ns) (Figure S44). Overall, it can also be concluded that the preparation of modulated UiO-66 solids resulted in a concomitant relative fluorescence quenching that agrees, to some extent,

with the volcano trend relationship between photocatalytic activity and number of defects shown above in Figure 6.

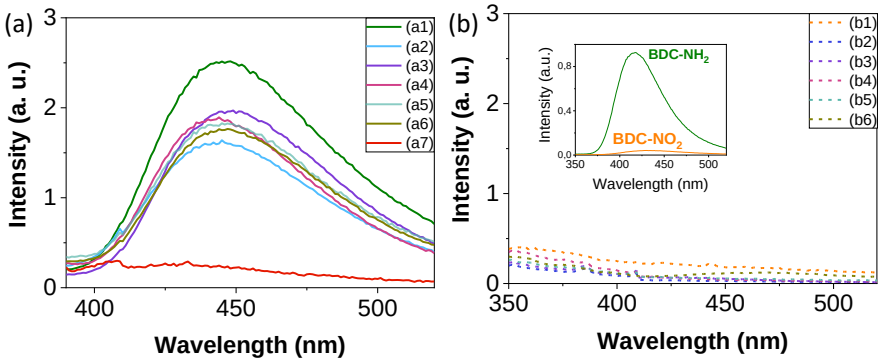

Figure 8. a) Fluorescence emission of UiO-66(Zr)-NH_2 solids prepared in the absence (a1) or in the presence of 12 (a2), 36 (a3), 100 (a4) eq. of AA or 12 (a5) or 36 (a6) eq. of TFA and Pt@UiO-66(Zr)-NH_2 (a7). (b) Fluorescence emission of UiO- 66(Zr)-NO_2 solids prepared in the absence (b1) or in the presence of 12 (b2), 36 (b3), 100 (b4) eq. of AA or 12 (b5) or 36 (b6) eq. of TFA. The inset in panel (b) shows the fluorescence emission spectra of 2-amino and 2-nitroterephthalic acid dissolved in CH_3CN containing Na_2CO_3 in H_2O (0.2 mL).

To study the photoinduced charge separation efficiency of the UiO-66 samples in depth, they were analysed by (photo)electrochemical techniques, and the results were compared with their corresponding non-modulated solids. Figures 9a and 9b shows the photocurrent results obtained using a working electrode of modulated and non-modulated UiO-66(Zr)-NH_2 (Figure 9a) or UiO-66(Zr)-NO_2 (Figure 9b) solids supported on a transparent FTO electrode submerged in an acetonitrile solution (0.1 M, NBu_4PF_6) and submitted to a polarization voltage of +0.9 V and several on/off cycles of simulated sunlight irradiation. As can be seen in these figures, the UiO-66(Zr)-NH_2 solids had much higher photocurrent intensities than the UiO-66(Zr)-NO_2 solids, possibly due to UiO-66(Zr)-NH_2's better ability to absorb simulated sunlight than UiO-66(Zr)-NO_2, as shown by UV-Vis DRS

(Figure S34 and S35). Previous studies found that the highest photocurrent intensities achieved with UiO-66(Zr)-NH_2 solids were due to their better charge carrier separation, since the amino group can stabilize the photogenerated holes[73]. Importantly, Figures 9a/9b show that modulated UiO-66(Zr)-X (X: NH_2 or NO_2) solids synthesized with AA (12, 36 or 100 eq.) or TFA (12 or 36 eq.) have enhanced photocurrent intensities respect to non-modulated MOFs. The highest photocurrent intensities achieved by UiO-66(Zr)-X (X: NH_2 or NO_2) solids prepared using 12 eq. of AA and gradually decrease for analogous samples prepared with 36 or 100 eq. of AA. The samples prepared with 12 or 36 eq. of TFA shows similar photocurrent responses. It is interesting to note that the order of photocurrent intensity agrees, to some extent, with the observed order of photocatalytic activity as a function of the number of defects (Figure 6). The highest photoinduced charge separation efficiency of modulated samples with 12 eq. of AA results in the photocatalysts with highest activities. It should be commented that the current intensity is due to the number of electrons extracted from the material and this measurement gives a quantification of the number of active sites in each solid [74].

Figures 9c and 9d show the photocurrent results obtained with a working electrode of modulated UiO-66(Zr)-NH_2-12AA (Figure 9c) or UiO-66(Zr)-NO_2 (Figure 9d) solids and parent MOFs supported on a transparent FTO electrode submerged in an acetonitrile solution (0.1 M, NBu_4PF_6), submitted to different polarization voltages (from 1.7 to -0.2 V) with several on/off cycles under simulated sunlight irradiation. These results indicate again that modulated UiO-66 solids have the highest photoinduced charge separation efficiencies, thus exhibiting higher photocatalytic activity. The influence of CH_3OH on the photocurrent measurements was studied to mimic the conditions during

photocatalytic HER with water/ CH_3OH mixtures as the reaction medium for the most active UiO-66(Zr)-NH_2-12AA and UiO-66(Zr)-NO_2-12AA samples. Figures 9a and 9b show that CH_3OH with the series of UiO-66 solids in all cases raises the photocurrent intensities higher than in experiments with acetonitrile as the solvent. The modulated UiO-66(Zr)-X (NO_2 or NH_2) samples again show a better photocurrent response than pristine MOFs. Firstly, the better photocurrent intensity in the presence of CH_3OH is in line with its role as sacrificial electron donor and partly reduces the electron/hole recombination. This facilitates the flow of electrons through the electrochemical cell and increases the photocurrent response, in agreement with greater photocatalytic hydrogen production using 12AA modulated and pristine UiO-66(Zr)-NH_2 solids in the presence of CH_3OH than in OWS experiments. Secondly, the highest photocurrent response of modulated UiO-66(Zr)-X (X: NH_2 or NO_2) samples in the presence of CH_3OH again reinforces their higher photoinduced charge carrier efficiencies, in accordance with their photocatalytic activities during HER. The comparison of Figures 9a and 9b shows that the influence of CH_3OH on the resulting photocurrent responses of modulated and non-modulated samples is higher in the case of the UiO- 66(Zr)- NO_2 solid. This is in good agreement with the relatively higher photocatalytic HER enhancement when using modulated and non-modulated UiO-66(Zr)-NO_2 than with the corresponding UiO-66(Zr)-NH_2 ones.

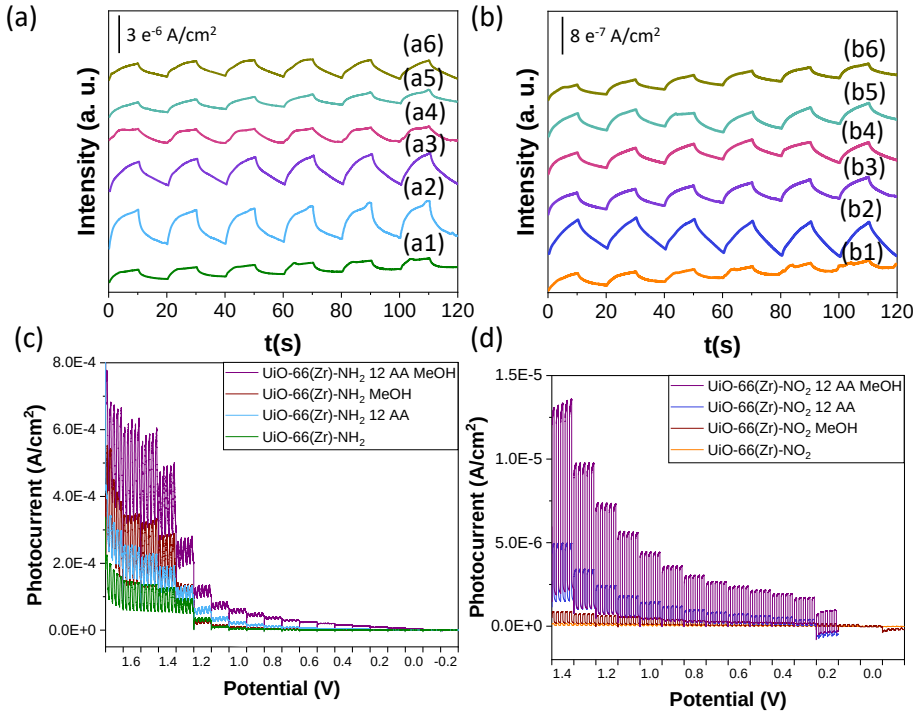

Figure 9. Current respond of modulated and pristine UiO-66(Zr)-NH_2 (a) or UiO- 66(Zr)-NO_2 solids (b) supported on a FTO electrode and immersed in acetonitrile (0.1 M, NBu_4PF_6) solution upon polarization at +0.9 V *vs.* Ag/AgCl during six consecutive on/off cycles with simulated sunlight (150 W Xe-He lamp equipped with an 1.5 AM filter). Legend: (1) 0 eq. modulator, (2) 12AA, (3) 36AA, (4) 100AA, (5) 12TFA, (6) 36TFA. Current respond of pristine or modulated UiO- 66(Zr)- NH_2 (c) or UiO-66(Zr)-NO_2 (d) solids as indicated supported on a FTO electrode in acetonitrile (0.1 M, NBu_4PF_6) or a mixture of acetonitrile and CH_3OH (0.3 mL CH_3OH) solution upon polarization from 1.7 to -0.2 V *vs.* Ag/AgCl during five consecutive on/off cycles with simulated sunlight.

EIS was used to evaluate the Rct of modulated and non-modulated UiO- 66(Zr)- X (X: NH_2 or NO_2) solids (Figure 10 and Table S4). Figures 10a and 10b show the Nyquist plots of the series of samples supported in a FTO electrode. An initial comparison shows that non-modulated UiO-66(Zr)-NH_2 has a smaller Nyquist plot arc radius than UiO-66(Zr)-NO_2, with Rct values of 3540 and 3775 Ω,

respectively. The modulated UiO-66(Zr)-X (X: NH_2 or NO_2) solids also exhibit a smaller arc radius than pristine UiO-66 ones, indicating a lower Rct of modulated UiO-66 solids versus non-modulated solids as well as UiO-66(Zr)-NH_2 versus UiO- 66(Zr)-NO_2 (Table S4). Interestingly, the Nyquist plot arc radius of UiO- 66(Zr)-X (X: NH_2 or NO_2) solids prepared with AA or TFA as modulators follows the increasing order 12 < 36 < 100 eq. and 12 < 36 eq., respectively. Furthermore, analogous EIS measurements performed using pristine UiO-66(Zr)-X (X: NH_2 or NO_2) solids or analogous prepared with 12 eq. of AA in sunlight, which promotes photoinduced charge carrier transfer, further reduces the charge resistance with respect to dark conditions (Figures 10c,d and Table S3).

In brief, the EIS and photocurrent results indicate that the higher photocurrent intensity and lower Rct of the modulated UiO-66 solids is in line with their enhanced photocatalytic activity and volcano trend relationship with the number of defects (Figure 6).

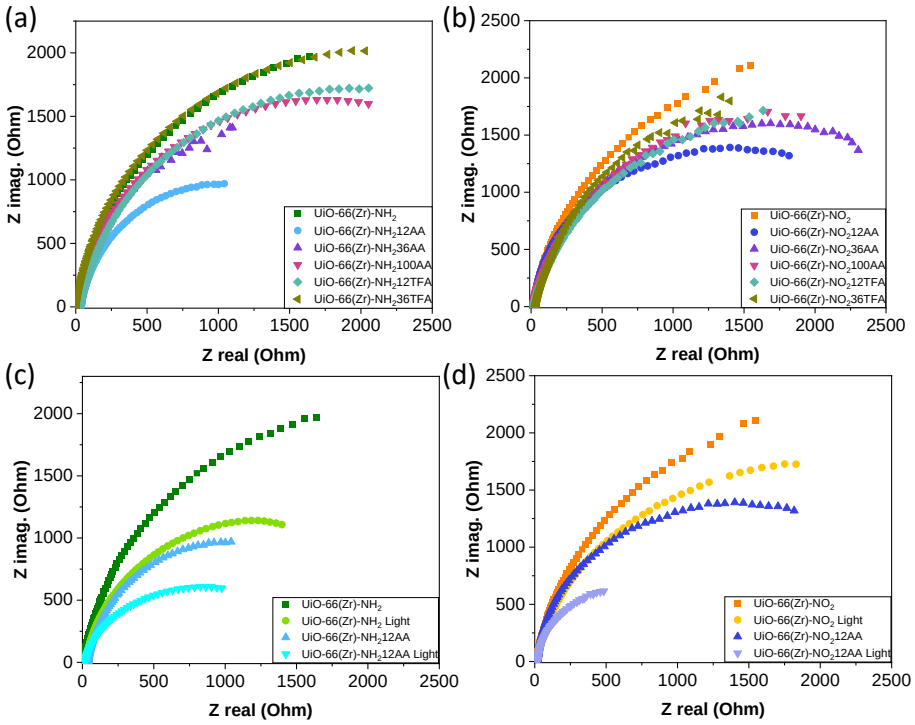

Figure 10. Nyquist plots of UiO-66(Zr)-NH_2 (a, c) and UiO-66(Zr)-NO_2 (b, d) solids under dark or simulated sunlight irradiation as indicated.

Modulated UiO-66(Zr)-X (NH_2 or NO_2) solids with 12AA and their parent MOFs were studied by TAS in the microsecond time scale using the LFP technique to study the photoinduced charge carrier dynamics in greater depth using the most active photocatalysts. Initially, Ar-purged acetonitrile suspensions of these solids were prepared with the same optical density (*ca*. 0.35) at the excitation wavelength of 266 nm. The TAS recorded for the UiO-66(Zr)-NH_2-12AA sample had a continuous absorption band ranging from 300 to 750 nm (Figure 11a). To evaluate the nature of the transient absorption species of this spectrum, an analogous measurement was carried out in the presence of a hole quencher such as CH_3OH. Thus, excitation of UiO-66(Zr)-NH_2-12AA in the presence of CH_3OH resulted in quenching of the TAS in the region of about 350 to 560 nm, while the

560-to-750 nm intensity signal was enhanced. As CH_3OH acts as a sacrificial electron donor in such a way that is oxidized by photogenerated holes and partially avoids the electron/hole pair recombination, the TAS results indicate that the quenching and enhancement of the absorption signals in the presence of CH_3OH can be attributed to the holes and electrons in these regions, respectively. Similar conclusions can be drawn when performing analogous LFP experiments using Pt@UiO-66(Zr)-NH_2-12AA (Figure S45) or non- modulated UiO-66(Zr)-NH_2 (Figure S46) solids. The TAS analysis of modulated UiO-66(Zr)-NO_2-12AA solid reveal that regions of holes and electron are located at about 300-500 nm and 550-700 nm, respectively (Figure 11b). Similar features were observed in the case of non-modulated UiO-66(Zr)-NO_2, except for two electron regions at 500-560 and 650-750 nm.

A comparative study of the kinetics of the samples at different wavelengths was performed to investigate the photochemical behaviour. Figures 11c,d show the transient absorption decay traces at 460 nm for the UiO-66 series after excitation at 266 nm. Quantitative information on these decays was obtained from trace adjustment by a mono- or bi-exponential law according to Eq. S1 and the results summarised in Table 2. Based on previous studies on MOF-based photocatalysts, the faster and more intense trace component can be associated with photoinduced charge separation, while the longer-lived and less intense second component is more closely related to charge delocalization [75]. Figure 11c shows that modulated UiO-66(Zr)-NH_2-12AA displays faster relaxation kinetics than pristine UiO-66(Zr)-NH_2.

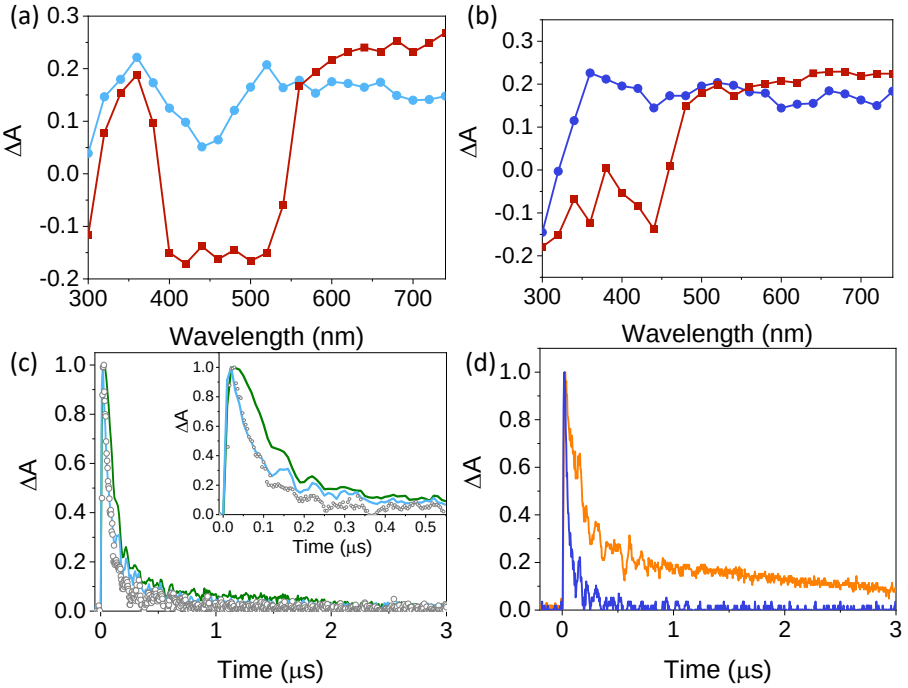

Figure 11. (a) Transient absorption spectra recorded 25 ns after the laser pulse for UiO-66(Zr)-NH_2-12AA in Ar-purged acetonitrile suspensions in the absence (blue circles) or in the presence (dark red squares) of CH_3OH. (b) Transient absorption spectra recorded 25 ns after the laser pulse for UiO-66(Zr)-NO_2-12AA in Ar-purged acetonitrile suspensions in the absence (dark blue circles) or in the presence (dark red squares) of CH_3OH. (c) Decay traces for Pt@UiO- 66(Zr)- NH_2- 12AA (grey open circles), UiO-66(Zr)-NH_2-12AA (blue line) and non-modulated UiO-66(Zr)-NH_2 (green line) at 460 nm after excitation at 266 nm. (d) Decay traces for UiO-66(Zr)-NO_2-12AA (dark blue line) and non- modulated UiO-66(Zr)-NO_2 (orange line) at 460 nm after excitation at 266 nm.

Deposition of Pt NPs in UiO-66(Zr)-NH_2-12AA accelerates slightly but significantly this process. In this context, related studies have proposed that the presence of Pt NPs in a photocatalyst can favour additional electron transfer channels that results in accelerating the kinetics[75]. Accordingly, this was observed for Pt@UiO-66(Zr)-NH_2-12AA, and it is associated with the opening of a new

channel mediated by the noble NPs. Interestingly, the fastest relaxation kinetics achieved with Pt@UiO-66(Zr)-NH_2-12AA versus UiO-66(Zr)-NH_2-12AA or UiO- 66(Zr)-NH_2-12AA versus UiO-66(Zr)-NH_2 correlates with their highest photocatalytic activities. In contrast, the lowest relaxation kinetics achieved, for example, non-modulated UiO-66(Zr)-X (X: NH_2 or NO_2), are related to trapping the photoinduced charge carriers in the MOF, which can hardly be used during the reactions [75]. In the case of modulated UiO-66(Zr)-NO_2-12AA compared to pristine MOF, the faster relaxation kinetics also agree with the higher photocatalytic activity. Similar conclusions can be drawn for the series of UiO-66(Zr)-X (X: NH_2 or NO_2) after excitation at 266 nm and recording the trace kinetics at 680 nm (Figures S47 and 48, Table S4).

Table 2. LFP lifetimes and weight of each component obtained for the series of UiO-66 solids under study recorded at 460 nm. The mean lifetime (<t>) is also shown.

	t_1(μs)	P_1(%)	t_2(μs)	P_2(%)	<t>(μs)
UiO-66(Zr)-NH_2	0.105	91	2.04	9	0.134
UiO-66(Zr)-NH_2-12AA	0.051	80	0.34	20	0.108
Pt@UiO-66(Zr)-NH_2-12AA	0.049	93	0.42	7	0.066
UiO-66(Zr)-NO_2	0.143	62	9.37	38	0.231
UiO-66(Zr)-NO_2-12AA	0.027	87	0.17	13	0.044

Previous studies using EPR spectroscopy have demonstrated that irradiation of UiO-66(Zr)-NH_2 based solids result in a photoinduced charge separation from the organic ligand to the metal node[76,77]. This process results in the transformation of Zr(IV) into Zr(III) species that has been proposed as reductive active sites[76,78]. To get some information about the reaction mechanism that takes place with UiO-66(Zr)-X (X: NH_2 or NO_2-AA) solids, solid-state EPR measurements have been carried out. Initially, EPR spectra of UiO-66 solids were recorded under dark reaction conditions. Figures 12a and S49a show that pristine and modulated UiO-66(Zr)-NH_2 solids show the presence of EPR signals that have

been previously ascribed to the presence of Zr(III) sites[76, 77, 79, 80]. In contrast, analogous measurements using UiO-66(Zr)-NO_2 based solids (Figures 12b and S49b) do not show the presence of any paramagnetic signal. Importantly, irradiation of UiO-66(Zr)-NH_2-12AA or UiO-66(Zr)-NO_2-12AA results in the formation of a new EPR signal at g 2.004 that can be associated with the generation of Zr(III) species via photoinduced electron transfer processes[76, 77, 79]. Regardless of the more intense signal intensities observed with UV-Vis, irradiations with simulated sunlight also allow the formation of these species but with less intensities. These EPR results agree with previous characterizations like fluorescence, TAS, electrochemical measurements by EIS and photocurrent measurements, thus indicating the formation of Zr(III) during the photocatalytic process.

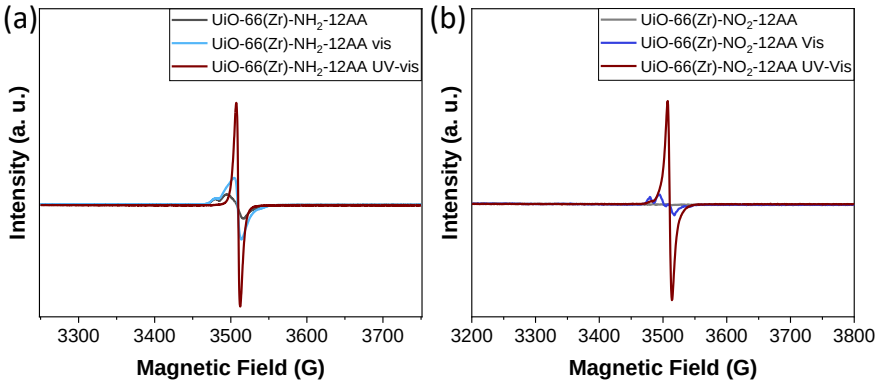

Figure 12. EPR spectra of UiO-66(Zr)-NH_2-12AA (a) or UiO-66(Zr)-NO_2-12AA (b) under dark or irradiation conditions as indicated.

4.4.3.2 DFT calculations

To shed light on the HER and OER mechanisms in the defective UiO-66(Zr)-NH_2, UiO-66(Zr)-NH_2-AA, and UiO-66(Zr)-NH_2-TFA, it is systematically investigated the thermodynamics of these processes for the three MOFs by means of DFT calculations. As a first stage, periodic defective MOF structure models

encompassing one defective linker per Zr_6 formula unit saturated by the terminal functions explored experimentally in the three scenarios were constructed as illustrated in Figure S2. Herein, the exposed Zr site is assumed to be the catalytic site of the reaction and the adjacent Zr site is grafted by AA and TFA in a monodentate fashion. Such assumption has been widely established and used in studies of defective MOF catalysis[81-84]. Gibbs free energy (ΔG) curves corresponding to the HER and OER intermediates were then calculated for each scenario. The corresponding data reported in Figures 13a-13b reveals that for HER, UiO-66(Zr)-NH_2-AA (ΔG=0.56 eV) and UiO-66(Zr)-NH_2-TFA (ΔG=0.62 eV) are associated with similar free energies that are much lower compared to the value obtained for UiO-66(Zr)-NH_2 (ΔG=2.47 eV). This thus emphasizes that the modulation of the terminal functions makes UiO-66(Zr)-NH_2 more effective for HER, UiO-66(Zr)-NH_2-AA being predicted to be the best candidate in line with the experimental trend shown in Figure 6a. In the meantime, the calculated free energy for UiO-66(Zr)-NH_2 is positive, indicating that the adsorption of the H species towards the Zr exposed sites in UiO- 66(Zr)- NH_2 is weaker than that in the other two defective forms. This is corroborated by the analysis of the DFT-optimized distance between the H and Zr sites, which demonstrated that the H-Zr distance in UiO-66(Zr)-NH_2 is the longest one (2.01 Å and 1.93 Å, for UiO-66(Zr)-NH_2-AA and UiO-66(Zr)-NH_2-TFA). Moving now to the OER process, Figure 13b illustrates for each elementary step the Gibbs free energy calculated for the four-electron reaction pathway as depicted in Figure 13c. For UiO-66(Zr)-NH_2 and UiO-66(Zr)-NH_2-TFA, $[OH]^* \rightarrow O^* + (H^+ + e^-)$ was determined to be the rate-determining step, while $[OOH]^* \rightarrow {}^* + O_2 + (H^+ + e^-)$ was found as the rate-determining step for UiO-66(Zr)-NH_2-AA (Figure S50). The corresponding $[\Delta G]_{maxOER}$ are 2.69, 2.46 and 2.45 eV for UiO-66(Zr)-NH_2, UiO-66(Zr)-NH_2-AA, and UiO-66(Zr)-NH_2-TFA, respectively. Therefore, the computed thermodynamic overpotential of the UiO-

66(Zr)-NH_2-AA and UiO-66(Zr)-NH_2-TFA (1.23 and 1.22 V) is clearly lower than the value obtained for the UiO-66(Zr)-NH_2 (1.46 V). As a result, the calculations confirmed the experimental observations that UiO- 66(Zr)- NH_2- AA outperform UiO-66(Zr)-NH_2 (Figures 6,7) and show that the improved catalytic activity of the exposed Zr site with AA functionalization MOF is responsible for their good performance.

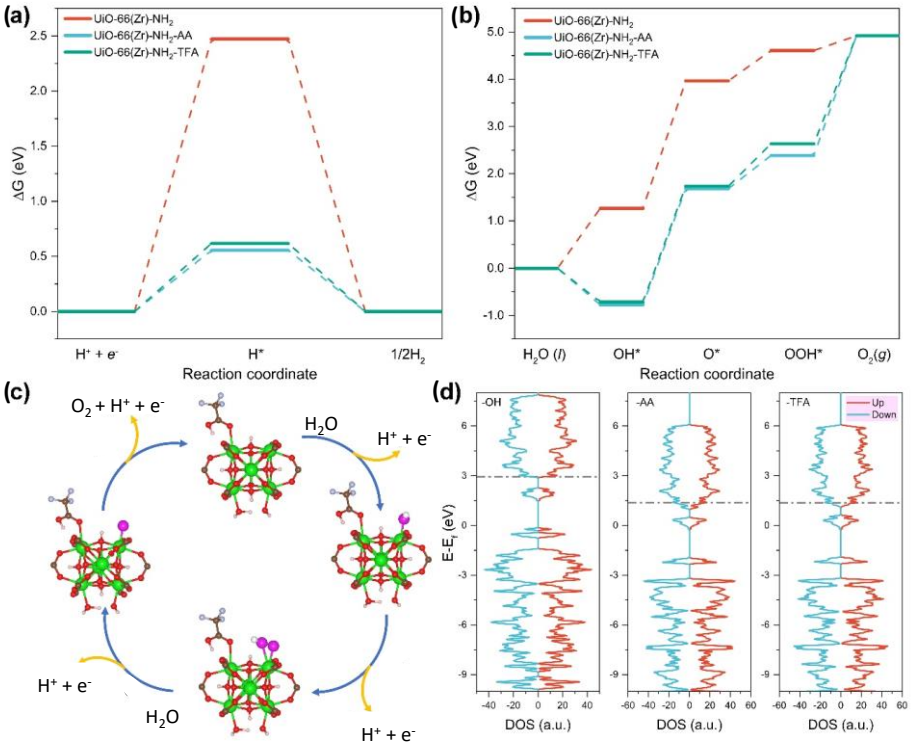

Figure 13. Gibbs free energy diagrams of the (a) HER and (b) OER on different UiO-66(Zr) series. (c) Reaction mechanisms for OER on UiO-66(Zr)-NH_2-TFA under alkaline conditions. All calculations are performed in a periodic system. The cluster model is used to highlight the reaction process. Color code: Zr, green; C, brown; O, red; H, pink; F, gray. Adsorbed intermediates are highlighted with different colors (magenta and white). (d) Total density of states of the UiO- 66(Zr)- NH_2 (left), UiO-66(Zr)-NH_2-AA (middle), and UiO-66(Zr)-NH_2-TFA (right), respectively. The d orbital of exposed Zr catalytic center is represented by the grey dotted line. The Fermi level position is set at 0 eV.

In a subsequent step, with the aim to gain an in-depth understanding of the underlying mechanisms for the intermediate's adsorption on the different UiO- 66-NH_2 forms, their electronic structure properties were further analyzed. In this context, d-band center of catalyst near to the Fermi level should yield in principle to strong adsorption, whereas a d-band center offsets which are too negative/positive hinder the adsorption process. As shown in Figure 13d, UiO- 66(Zr)-NH_2, UiO-66(Zr)-NH_2-AA, and UiO-66(Zr)-NH_2-TFA exhibit d-band center offsets amounting to 2.93, 1.37 and 1.36 eV, respectively due to the energy stabilization induced by the AA and TFA functional groups. On the same vein, according to the Bader charge population analysis and the charge density difference profiles (Figure S51), a more pronounced electron transfer from the Zr active site to H^* occurs for UiO-66(Zr)-NH_2-AA (0.53 e^-) when compared to UiO- 66(Zr)-NH_2 (0.42 e^-). This indicates that the charge transfer from Zr to the H^* intermediate enhances the adsorption of H^* on UiO-66(Zr)-NH_2-AA, and results in an enhanced HER activity. Notably, compared to the structure models used for the exploration of the catalytic reaction with 1 Zr exposed site and 1 neighbouring Zr site saturated by AA and TFA, here when focusing only on the modification of the opto-electronic properties due to the presence of the modulators, this spatial constraint is not anymore required and both oxygen atoms from the carboxylic anchoring groups can be coordinated to the Zr sites. In this viewpoint, with the aim of rationalizing the impact of the modulators (AA and TFA) in the optical response of the defective materials, it has been investigated the excited state properties of the UiO-66(Zr)-NH_2 cluster models bearing AA and TFA moieties coordinated in a bidentate manner on the Zr sites by means of Time-Dependent DFT (TD-DFT) calculations (Section 4.8.3). The absorption spectra of the pristine defective (OH) and the AA and TFA coordinated clusters are displayed in Figure 14a. Notably, the simulated spectra nicely reproduced the absorption features

from the UV-Vis diffuse reflectance plots represented in Figures 5 and S34, bearing three main bands in these energy regions: one in the near Vis centered at 370 nm and the two others in the UV peaked at 265 and 225 nm (Table S5). Regarding the AA and TFA spectra, only a slight increase in the intensity of the lowest energy absorption bands was observed when compared to the reference OH system, which is fully consistent with the similar absorption characteristics measured for all set of samples analyzed experimentally (Figure S34). Furthermore, identical trends followed by the absorption features of the AA/TFA *vs.* OH systems were obtained for the simulated spectra of the periodic materials, as they are represented in Figure S53 (see also Table S6 for the properties of the main excited states of the spectra). In this viewpoint, in order to get a deeper understanding of the nature of these absorption bands, two types of excitation analysis were carried out: the Natural Transition Orbital (NTO) [84] plots which provided us a spatial representation of the distribution of the photogenerated charges (holes and electrons), and the charge transfer (CT) analysis which allowed us to get a quantitative estimation of the delocalization of both particles along the ligands and the metallic nodes, as well as the extent of the CT induced by this excitation. Interestingly, the NTOs plotted in Figure 14b and Figure S53 demonstrated that both holes and electrons are mostly localized on the BDC-NH_2 ligands, being holes especially confined in one of the BDC moieties, while electrons remained localized on both ligands with a certain extent of delocalization around the ZrO metal nodes. Indeed, a similar electronic density delocalization was found for the energy levels involved in the main transitions of the simulated spectra of the periodic systems, as it can be observed in the frontier crystalline orbitals shape plots depicted in Figure S54. On the same footing, the CT analysis revealed that the hole delocalization along the ligands amounted to 90-100 %, whereas for electrons the extent of delocalization around the ZrO metal cluster was equal to

10-40 %. As a result, these states acquire a given ligand-to-metal CT (LMCT) character which amounted to ~0.1 for the Vis region band, and ~0.3-0.4 for the UV bands. Interestingly, the observation of such LMCT processes in defective UiO-66 materials are congruent with previous theoretical works [50], and it evidences the role played by Zr metal nodes as reductive active sites, as it has been confirmed by the transformation of Zr(IV) into Zr(III) measured via spectroscopic measurements[76,77,79]. The spatial distribution of the generated particles was indeed found independent of the terminal functions coordinated to the metal node, which goes in line with the fact that the most important absorption features of these MOFs arise from the ligand states. To sum up, it can be concluded that light harvesting capacity of these porous materials is weakly affected by the modulator employed to prepare the materials, which clearly corroborates that the OWS activity enhancement induced by the presence of AA and TFA coordinated groups is mainly attributed to the lowering of the energy barriers for both HER and OER intermediates simulated above by DFT calculations.

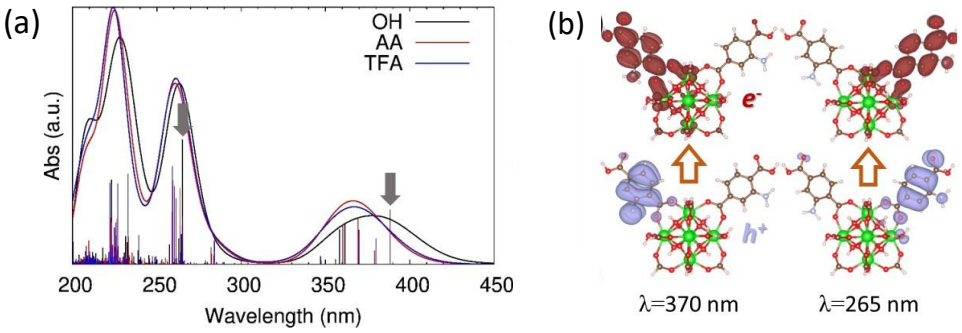

Figure 14. (a) TD-DFT simulated absorption spectra for the OH (black), AA (red) and TFA (blue) cluster models. Vertical bars represent the intensity of the transitions conforming the spectra. The excited state properties for the main vertical transition composing these spectra are collected in Table S5; (b) NTO shapes for the occupied/virtual (purple/red) orbitals for the states of the OH cluster model highlighted with vertical arrows in Figure 14a. The rest of relevant NTOs for the states composing the spectra are collected in Figure S53. The isovalue used for the isodensity plots was set to 0.02 a.u.

Figure 15 summarizes the proposed photocatalytic mechanism during HER or OWS. Briefly, simulated sunlight irradiation of UiO-66(Zr)-NH_2-12AA promotes the photoinduced electron transfer from the organic ligand to the metal node. Then, a one-electron reduction process results in the transformation of Zr(IV) species into Zr(III) ones that act as reductive active sites. It is proposed that the holes are stabilized in the organic ligand and are responsible for the oxidation of CH_3OH or H_2O to the oxidized products or O_2 during the HER or OWS, respectively.

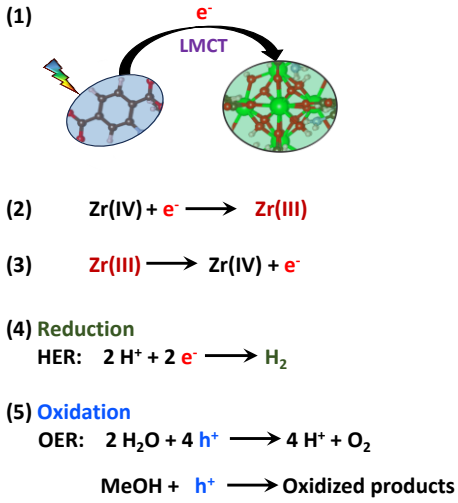

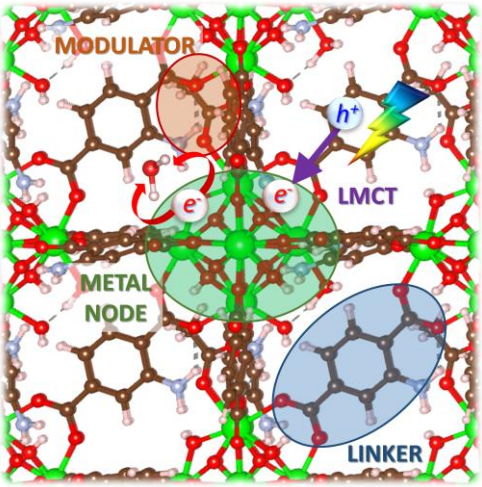

Figure 15. Plausible photocatalytic reaction mechanism during HER and OWS using UiO-66(Zr)-NH_2-12AA under simulated sunlight irradiation.

4.5 Conclusions

This study has shown the influence of the synthesis of UiO-66(Zr)-X (X: NH_2 or NO_2) solids with common AA or TFA organic modulators on their resulting photocatalytic activity for the HER and OWS under simulated sunlight irradiation. The UiO-66(Zr)-NH_2 solids showed higher catalytic activity than UiO-66(Zr)-NO_2, associated with the lower band gap values and more negative LUCO values of the former solids than their analogous UiO-66(Zr)-NO_2 materials. The UiO-66 solids modulated by either AA or TFA prepared in this study showed greater

photocatalytic activity for HER than their corresponding pristine materials. The most active samples of each series were prepared using 12 AA equivalents. The most active UiO-66(Zr)-NH_2 modulated sample also enhanced OWS photoactivity with respect to pristine UiO-66(Zr)-NH_2. The characterization of modulated UiO-66(Zr)-NH_2 and UiO-66(Zr)-NO_2 by means of photocurrent and EIS revealed that these samples had a better charge transfer ability than their pattern solids. Additional LFP and PL measurements confirmed that the optimized modulated samples improved e^-/h^+ charge separation with respect to non-modulated samples. Furthermore, theoretical calculations revealed that, whereas the presence of modulators barely modified the absorption features of and the extent of LMCT towards the metal node in the defective UiO-66 materials, they had a major impact in the thermodynamics of the OWS reactions via a significant lowering of energy barriers for reaction for both HER and OER processes. Importantly, the optimized UiO-66(Zr)-NH_2 prepared with 12 eq. of AA and further modified with Pt NPs (1 wt%) as co-catalyst exhibited better photocatalytic activity than analogous MOF-based materials for OWS under simulated sunlight irradiation.

4.6 Author contribution

Celia María Rueda Navarro synthesized all the materials under study and conducted all the photocatalytic tests. For the characterization of the solids, she measured XRD, FT-IR, NMR and SEM, and participated in TEM analyses. Additionally, she handled the data analysis for other characterizations performed by technicians, including BET, TGA, XPS, and UV. She also conducted the photocurrent and EIS experiments while as well participated in the EPR and PL experiments. She participated in several technical meetings with the researchers in charge of the computational studies.

4.7 References

(1) Férey, G. Hybrid porous solids: past, present, future. *Chem. Soc. Rev.* **2008**, *37*, 191-214.

(2) Kitagawa, S.; Kitaura, R.; Noro, S.-I. Functional porous coordination polymers. *Angew. Chem. Int. Ed.* **2004**, *43*, 2334-2375.

(3) Freund, R. C., S.; Cohen, S.M.; Wei Yan, Y.; Deng, H.; Guillerm, V.; Eddaoudi, M.; Madden, D.G.; Fairen-Jimenez, D.; Lyu, H.; Macreadie, L.K.; Ji, Z.; Zhang, Y.; Wang, B.; Haase, F.; Wöll, C.; Zaremba, O.; Andreo, J.; Wuttke, S.; Diercks, C.S. 25 Years of reticular chemistry. *Angew. Chem., Int. Ed.* **2021**, *60*, 23946–23974.

(4) Jiang, H. A., D.; Eddaoudi, M. A reticular chemistry guide for the design of periodic solids. *Nat. Rev. Mater.* **2021**, *6*, 466-487.

(5) Férey, G.; Mellot-Draznieks, C.; Serre, C.; Millange, F.; Dutour, J.; Surblé, S.; Margiolaki, I. A chromium terephthalate-based solid with unusually large pore volumes and surface area. *Science* **2005**, *23*, 2040-2042.

(6) Li, H.; Eddaoudi, M.; O'Keeffe, M.; Yaghi, O. M. Design and synthesis of an exceptionally stable and highly porous metal- organic framework. *Nature.* **1999**, *402*, 276-279.

(7) Feng, L. D., G.S.; Wang, K.-Y.; Yuan, S.; Zhou, H.-C. Strategies for pore engineering in zirconium metal-organic frameworks. *Chem* **2020**, *6*, 2902–2923.

(8) Xu, W. T., B.; Liu, Q.; Shu, Y.; Liang, C.C.; Diercks, C.S.; Yaghi, O.M.; Zhang, Y.-B.; Deng, H.; Li, Q. Anisotropic reticular chemistry. *Nat. Rev. Mater.* **2020**, *5*, 764-779.

(9) Li, J. B., P.M.; Li, J.; Eddaoudi, M.; Liu, Y. Recent progress on microfine design of metal–organic frameworks: structure regulation and gas sorption and separation. *Adv. Mater.* **2020**, *32*, 2002563.

(10) Li, J.-R.; Sculley, J.; Zhou, H.-C. Metal-organic frameworks for separations. *Chem. Rev.* **2012**, *112*, 869-932.

(11) Bavykina, A.; Kolobov, N.; Khan, S.; Bau, J. A.; Ramirez, A.; Gascon, J. Metal–organic frameworks in heterogeneous catalysis: Recent progress, new trends, and future perspectives. *Chem. Rev.* **2020**, *16*, 8468–8535.

(12) Wei, Y.-S. Z., M.; Zou, R.; Xu, Q. Metal-organic framework-based catalysts withsingle metal sites. *Chem. Rev.* **2020**, *120*, 12089–12174.

(13) Navalon, S.; Dhakshinamoorthy, A.; Alvaro, M.; Ferrer, B.; Garcia, H. Metal–organic frameworks as photocatalysts for solar-driven overall water splitting. *Chem. Rev.* **2023**, *123*, 445-490.

(14) Mateo, D., Cerrillo, J.L., Durini, S., Gascon, J. Fundamentals and applications of photo-thermal catalysis. *Chem. Soc. Rev.* **2021**, *50*, 2173-2210.

(15) Downes, C. A. M., S.C. Electrocatalytic metal–organic frameworks for energy applications. *ChemSusChem* **2017**, *10*, 4374-4392.

(16) Horcajada, P. G., R.; Baati, T.; Allan, P.K.; Maurin, G.; Couvreur, P.; Férey, G.; Morris, R.E.; Serre, C. Metal-organic frameworks in biomedicine. *Chem. Rev.* **2012**, *112*, 1232–1268.

(17) Kreno, L. E. L., K.; Farha, O.K.; Allendorf, M.; Van Duyne, R.P.; Hupp, J.T. Metal-organic framework materials as chemical sensors. *Chem. Rev.* **2012**, *112*, 1105-1125.

(18) Cai, G. Y., P.; Zhang, L.; Zhou, H.-C.; Jiang, H.-L. Metal-organic framework-based hierarchically porous materials: synthesis and applications. *Chem. Rev.* **2021**, *121*, 12278–12326.

(19) Furukawa, H.; Cordova, K. E.; O'Keeffe, M.; Yaghi, O. M. The chemistry and applications of metal-organic frameworks. *Science* **2013**, *341*, 1230444.

(20) Gomes Silva, C.; Luz, I.; Llabres i Xamena, F. X.; Corma, A.; Garcia, H. Water stable Zr–benzenedicarboxylate metal–organic frameworks as photocatalysts for hydrogen generation. *Chem. Eur. J.* **2010**, *16*, 11133-11138.

(21) An, Y.; Liu, Y.; An, P.; Dong, J.; Xu, B.; Dai, Y.; Qin, X.; Zhang, X.; Whangbo, M.-H.; Huang, B. NiII coordination to Al-based metal–organic framework made from 2-aminoterephthalate for photocatalytic overall water splitting. *Angew. Chem. Int. Ed.* **2017**, *56*, 3036 –3040.

(22) Jaryal, R.; Kumar, R.; Khullar, S. Mixed metal-metal organic frameworks (MM-MOFs) and their use as efficient photocatalysts for hydrogen evolution from water splitting reactions. *Coord. Chem. Rev.* **2022**, *464*, 214542.

(23) Reddy, D. A.; Kim, Y.; Gopannagari, M.; Kumar, D. P.; Kim, T. K. Recent advances in metal-organic framework-based photocatalysts for hydrogen production. *Sust. Energ. Fuels* **2021**, *5*, 1597-1618.

(24) Luo, H.; Zeng, Z.; Zeng, G.; Zhang, C.; Xiao, R.; Huang, D.; Lai, C.; Cheng, M.; Wang, W.; Xiong, W.; et al. Recent progress on metal-organic frameworks based- and derivedphotocatalysts for water splitting. *Chem. Eng. J.* **2020**, *383*, 123196.

(25) Meyer, K.; Ranocchiari, M.; van Bokhoven, J. A. Metal organic frameworks for photo-catalytic water splitting. *Energy Environ. Sci.* **2015**, *8*, 1923-1937.

(26) Melillo, A. C.-A., M.; Ferrer, B.; Dhakshinamoorthy, A.; Baldoví, H.G.; Navalón, S. MOF-on-MOF composites with UiO-66-based materials as photocatalysts for the overall water splitting under sunlight Irradiation. *Energy Fuels* **2023**, *37*, 5457–5468.

(27) Ma, X.; Wang, L.; Zhang, Q.; Jiang, H.-L. Switching on the photocatalysis of metal–organic frameworks by engineering structural defects. *Angew. Chem. Int. Ed.* **2019**, *58*, 12175 –12179.

(28) Cabrero-Antonino, M.; Albero, J.; García-Vallés, C.; Álvaro, M.; Navalón, S.; García, H. Plasma-induced defects enhance the visible-light photocatalytic activity of MIL-125(Ti)-NH2 for overall water splitting. *Chem. Eur. J.* **2020**, *26*, 15682-15689.

(29) Forgan, R. S. Modulated self-assembly of metal–organic frameworks. *Chem. Sci.* **2020**, *11*, 4546-4562.

(30) Kirchon, A.; Feng, L.; Drake, H. F.; Joseph, E. A.; Zhou, H.-C. From fundamentals to applications: a toolbox for robust and multifunctional MOF materials. *Chem. Soc. Rev.* **2018**, *47*, 8611-8638.

(31) Taddei, M. When defects turn into virtues: The curious case of zirconium-based metal-organic frameworks. *Coord. Chem. Rev.* **2017**, *343*, 1–24.

(32) Xiang, W. Z., Y.; Chen, Y.; Liu, C.-J.; Tu, X. Synthesis, characterization and application of defective metal-organic frameworks: Current status and perspectives. *J. Mater. Chem. A* **2020**, *8*, 21526–21546.

(33) Bagheri, M. M., M.Y. Quasi-metal organic frameworks: Preparation, applications and future perspectives. *Coord. Chem. Rev.* **2022**, *468*, 214643.

(34) Ren, J. L., M.; Musyoka, N.M.; Langmi, H.W.; Mathe, M.; Liao, S.; Pang, W. Structural defects in metal–organic frameworks (MOFs): Formation, detection and control towards practices of interests. *Coord. Chem. Rev.* **2017**, *349*, 169–197.

(35) Feng, X. J., H.S.; Krishnaraj, C.; Leus, K.; Wang, G.; Chen, H.; Jia, C.; Van Der Voort, P. Generating catalytic sites in UiO-66 through defect engineering. *ACS Appl. Mater. Interf.* **2021**, *13*, 60715–60735.

(36) Feng, X. H., J.; Jena, H.S.; Wang, G.; Veerapandian, S.K.P.; Morent, R.; De Geyter, N.; Leyssens, K.; Hoffman, A.E.J.; Meynen, V.; Marquez, C.; De Vos, D.E.; Van Speybroeck, V.; Leus, K.; Van Der Voort, P. Engineering a highly defective stable

UiO-66 with tunable Lewis-Brønsted acidity: The role of the hemilabile linker. *J. Am. Chem. Soc.* **2020**, *142*, 3174–3318.

(37) Kholdeeva, O. M., N. Metal-organic frameworks in oxidation catalysis with hydrogen peroxide. *Catalysts* **2021**, *11*, 1-23.

(38) Yuan, S. F., L.; Wang, K.; Bosch, M.; Lollar, C.; Sun, Y.; Qin, J.; Yang, X.; Zhang, P.; Wang, Q.; Zou, L.; Zhang, Y.; Zhang, L.; Fang, Y.; Li, J.; Zhou, H.-C. Stable metal–organic frameworks: design, synthesis, and applications. *Adv. Mater.* **2018**, *30*, 1704303.

(39) Bueken, B. V., N.V.; Krajnc, A.; Smolders, S.; Taulelle, F.; Mellot-Draznieks, C.; Mali, G.; Bennett, T.D.; De Vos, D. Tackling the defect conundrum in UiO-66: a mixed-linker approach to engineering missing linker defects. *Chem. Mater.* **2017**, *29*, 10478–10486.

(40) Hou, X. W., J.; Mousavi, B.; Klomkliang, N.; Chaemchuen, S. Strategies for induced defects in metal-organic frameworks for enhancing adsorption and catalytic performance. *Dalton Trans.* **2022**, *51*, 8133–8159.

(41) Vermoortele, F. B., B.; Le Bars, G.; Van de Voorde, B.; Vandichel, M.; Houthoofd, K.; Vimont, A.; Daturi, M.; Waroquier, M.; Van Speybroeck, V.; Kirschhock, C.; De Vos, D. . Synthesis modulation as a tool to increase the catalytic activity of metal-organic frameworks: the unique case of UiO-66(Zr). *J. Am. Chem. Soc.* **2013**, *135*, 11465−11468.

(42) Shearer, G. C.; Chavan, S.; Bordiga, S.; Svelle, S.; Olsbye, U.; Lillerud, K. P. Defect engineering: tuning the porosity and composition of the metal−organic framework UiO-66 via modulated synthesis. *Chem. Mater.* **2016**, *28*, 3749−3761.

(43) Cavka, J. H.; Jakobsen, S.; Olsbye, U.; Guillou, N.; Lamberti, C.; Bordiga, S.; Lillerud, K. A new zirconium inorganic building brick forming metal organic frameworks with exceptional stability. . *J. Am. Chem. Soc.* **2008**, *130*, 13850-13851.

(44) Tatay, S. M.-G., S.; Rubio-Gaspar, A.; Gómez-Oliveira, E.; Castells-Gil, J.; Dong, Z.; Mayoral, A.; Almora-Barrios, N.; Padial, N.M.; Martí-Gastaldo, C. Synthetic control of correlated disorder in UiO-66 frameworks. *Nat. Commun.* **2023**, *14*, 6962.

(45) Lázaro, I. A.; Almora-Barrios, N.; Tatay, S.; Popescu, C.; Martí-Gastaldo, C. Linker depletion for missing cluster defects in non-UiO metal-organic frameworks. *Chem. Sci.* **2021**, *12*, 11839-11844.

(46) Shearer, G. C.; Vitillo, J. G.; Bordiga, S.; Svelle, S.; Olsbye, U.; Lillerud, K. P. Functionalizing the defects: Ppstsynthetic ligand exchange in the metal organic framework UiO-66. *Chem. Mater.* **2016**, *28*, 7190-7193.

(47) Islamov, M. B., P.; Babaei, H.; McGaughey, A.J.H.; Wilmer, C.E. Correlated missing linker defects increase thermal conductivity in metal–organic framework UiO-66. *Chem. Sci.* **2023**, *14*, 6592-6600.

(48) Liu, L. C., Z.; Wang, J.; Zhang, D.; Zhu, Y.; Ling, S.; Huang, K.-W.; Belmabkhout, Y.; Adil, K.; Zhang, Y.; Slater, B.; Eddaoudi, M.; Han, Y. Imaging defects and their evolution in a metal-organic framework at sub-unit-cell resolution. *Nat. Chem.* **2019**, *11*, 622-628.

(49) Cliffe, M. J. W., W.; Zou, X.; Chater, P. A.; Kleppe, A. K.; Tucker, M. G.; Wilhelm, H.; Funnell, N. P.; Coudert, F. X.; Goodwin, A. L., . Correlated defect nanoregions in a metal-organic framework. *Nat. Commun.* **2014**, *5*, 4176.

(50) Wu, H. C., Y.; Krungleviciute, V.; Tyagi, M.; Chen, P.; Yildirim, T.; Zhou, W. . Unusual and highly tunable missing-linker defects in zirconium metal-organic framework UiO-66 and their important effects on gas adsorption. *J. Am. Chem. Soc.* **2013**, *135*, 10525−10532.

(51) De Vos, A. H., K.; Van Der Voort, P.; Van Speybroeck, V.; Lejaeghere, K. Missing linkers: an alternative pathway to UiO-66 electronic structure engineering. *Chem. Mater.* **2017**, *29*, 3006-3019.

(52) Vandichel, M.; Hajek, J.; Vermoortele, F.; Waroquier, M.; De Vos, D. E.; Speybroeck, V. V. Active site engineering in UiO-66 type metal–organic frameworks by intentional creation of defects: a theoretical rationalization. *CrystEngComm* **2015**, *17*, 395-406.

(53) Vandichel, M. H., J.; Ghysels, A.; De Vos, A.; Waroquier, M.; Van Speybroeck, V. Water coordination and dehydration processes in defective UiO-66 type metal organic frameworks. *CrystEngComm* **2016**, *18*, 7056-7069.

(54) Jiao, Y. L., Y.; Zhu, G.; Hungerford, J.T.; Bhattacharyya, S.; Lively, R.P.; Sholl, D.S.; Walton, K.S. Heat-treatment of defective UiO-66 from modulated synthesis: Adsorption and stability studies. *J. Phys. Chem. C* **2017**, *121*, 23471–23479.

(55) Yang, K.; Jiang, J. Computational design of a metal-based frustrated Lewis pair on defective UiO-66 for CO_2 hydrogenation to methanol. *J. Mater. Chem. A* **2020**, *8*, 22802-22815.

(56) Rueda-Navarro, C. M. F., B.; Baldoví, H.G.; Navalón, S. Photocatalytic hydrogen production from glycerol aqueous solutions as sustainable feedstocks using

Zr-based UiO-66 materials under simulated sunlight irradiation. *Nanomaterials.* **2022**, *12*, 3808.

(57) Nørskov, J. K. R., J.; Logadottir, A.; Lindqvist, L.; Kitchin, J. R.; Bligaard, T.; Jónsson, H. . Origin of the Overpotential for Oxygen Reduction at a Fuel-Cell Cathode. J. *Phys. Chem. B* **2004**, *108*, 17886–17892.

(58) Feng, X. J., H.S.; Krishnaraj, C.; Arenas-Esteban, D.; Leus, K.; Wang, G.; Sun, J.; Rüscher, M.; Timoshenko, J.; Cuenya, B.R.; Bals, S.; Van Der Voor, P. Creation of exclusive artificial cluster defects by selective metal removal in the (Zn, Zr) mixed-metal UiO-66. *J. Am. Chem. Soc.* **2021**, *143*, 21511−21518.

(59) Wei, R. G., C. A.; Li, G; Islamoglu, T.; Zhang, Z.; Yu, P.; Farha, O. K.; Cramer, C. J.; Gagliardi, L.; Yang, D.; Gates, B. C. . Tuning the properties of Zr6O8 nodes in the metal organic framework UiO-66 by selection of node-bound ligands and linkers. *Chem. Mater.* **2019**, *31*, 1655–1663.

(60) Svane, K. L.; Bristow, J. K.; Gale, J. D.; Walsh, A. Vacancy defect configurations in the metal–organic framework UiO-66: energetics and electronic structure. *J. Mater. Chem.* **2018**, *6*, 8507-8513.

(61) Devautour-Vinot, S. M., G.; Serre, C.; Horcajada, P.; da Cunha, P.; Guillerm, V.; de Souza Costa, A.; Taulelle, F.; Martineau, C. Structure and dynamics of the functionalized MOF type UiO-66(Zr): NMR and dielectric relaxation spectroscopies coupled with DFT calculations. *Chem. Mater.* **2012**, *24*, 2168−2177.

(62) Fang, Z. B., B.; De Vos, D. E.; Fischer, R. A. . Defect-engineered metal-organic frameworks. *Angew. Chem. Int. Ed. Eng.* **2015**, *54*, 7234-7254,

(63) Dissegna, S. E., K.; Heinz, W. R.; Kieslich, G.; Fischer, R. A. . Defective metal-organic frameworks. *Adv. Mater.* **2018**, *30* 1704501.

(64) Dai, S. M.-L., E.; Tissot, A.; Baldoví, H. G.; García, H.; Navalón, S.; Serre, C. . Room temperature design of Ce(IV)-MOFs: from photocatalytic HER and OER to overall water splitting under simulated sunlight irradiation. *Chem. Sci.* **2023**, *14*, 3451–3461.

(65) Semerci, T. G. M., A.; Mutlu, Y.C.; Garcia, H. . Band alignment of PCN-222 via selection of the metal porphyrin linker for sunlight driven photocatalytic overall water splitting. *Catal. Today.* **2023**, *22*, 113931.

(66) Manickam-Periyaraman, P. E., J. C.; Ferrer, B.; Subramanian, S.; Álvaro, M.; García, H.; Navalón, S. Bimetallic iron-copper oxide nanoparticles supported on nanometric diamond as efficient and stable sunlight-assisted Fenton photocatalyst. *Chem. Eng. J.* **2020**, *393*, 124770.

(67) Melillo, A.; Cabrero-Antonino, M.; Navalón, S.; Alvaro, M.; Ferrer, B.; García, H. Enhancing visible light photocatalytic activity for overall water splitting in UiO-66 by controlling metal node composition. *Appl. Catal. B. Environ.* **2020**, *278*, 119345.

(68) Cabrero-Antonino, M.; Albero, J.; García-Vallés, C.; Álvaro, M.; Navalón, S.; García, H. Plasma-induced defects enhance the visible-light photocatalytic activity of MIL-125(Ti)-NH2 for overall water splitting. *Chem. Eur. J.* **2020**.

(69) Salcedo-Abraira, P.; Babaryk, A. A.; Montero-Lanzuel, E.; Contreras-Almengor, O. R.; Cabrero-Antonino, M.; Svensson Grape, E. S.; Willhammar, T.; Navalón, S.; elkäim, E.; García, H.; et al. A novel porous Ti-squarate as efficient photocatalyst in the overall water splitting reaction under simulated sunlight irradiation. *Adv. Mater.* **2021**, *33*, 2106627.

(70) Gikonyo, B. M.-L., E.; Baldovi, H.G.; De, S.; Journet, C.; Devic, T.; Guillou, N.; Tiana, D.; Navalon, S.; Fateeva, A. . Mixed-metal Zr/Ti MIL-173 porphyrinic metal-organic frameworks as efficient photocatalysts towards solar-driven overall water splitting. *J. Mater. Chem. A* **2022**, *10*, 24938-24950.

(71) Hu, H. W., Z.; Cao, L.; Zeng, L.; Zhang, C.; Lin, W.; Wang, C. . Metal-organic frameworks embedded in a liposome facilitate overall photocatalytic water splitting. *Nat. Chem.* **2021**, *13*, 358.

(72) Salcedo-Abraira, P.; Vilela, S. M. F.; Babaryk, A. A.; Cabrero-Antonino, M.; Gregorio, P.; Salles, F.; Navalón, S.; García, H.; Horcajada, P. Nickel phosphonate MOF as efficient water splitting photocatalyst. *Nano Res.* **2021**, *14*, 450–457.

(73) Santiago-Portillo, A.; Baldoví, H. G.; Fernandez, M. T. G.; Navalón, S.; Atienzar, P.; Ferrer, B.; Alvaro, M.; Garcia, H.; Li, Z. Ti as mediator in the photoinduced electron transfer of mixed-metal NH_2–UiO-66(Zr/Ti): transient absorption spectroscopy study and application in photovoltaic cell. *J. Phys. Chem. C* **2017**, *121*, 7015-7024.

(74) García-Baldoví, A. D. A., R.; Mouchaham, G.; Liu, S.; Fan, D.; Maurin, G.; Navalon, S.; Serre, C.; Garcia, H. Active site imprinting on Ti oxocluster metal–organic frameworks for photocatalytic hydrogen release from formic acid. *Energy Environ. Sci.* **2023**, *16*, 167–177.

(75) Fang, X. S., Q.; Wang, Y.; Jiao, L.; Yao, T.; Li, Y.; Zhang, Q.; Luo, Y.; Jiang, H.-L. Single Pt atoms confined into a metal–organic framework for efficient photocatalysis. *Adv. Mater.* **2018**, *30*, 1705112.

(76) Sun, D. F., Y.; Liu, W.,; Ye, L.; Wang, D.; Yang, L.; Fu, X.; Li, Z. Studies on photocatalytic CO_2 reduction over NH_2-UiO-66(Zr) and its derivatives: Towards

a better understanding of photocatalysis on metal–organic frameworks. *Chem. Eur. J.* **2013**, *19*, 14279 – 14285.

(77) Xiao, J.-D.; Shang, Q.; Xiong, Y.; Zhang, Q.; Luo, Y.; Yu, S.-H.; Jiang, H.-L. Boosting photocatalytic hydrogen production of a metal–organic framework decorated with platinum nanoparticles: The platinum location matters. *Angew. Chem. Int. Ed.* **2016**, *55*, 9389 –9393.

(78) Yu, X. L., J.; Du, M.; Song, X.; Huang, H.; Nie, L. Adaptive lattice-matched MOF and COF coreshell heterostructure for carbon dioxide photoreduction. *Cell Rep. Phys. Sci.* **2023**,

(79) He, Y. L., C.; Chen, X.-B.; Shi, Z.; Feng, S. Visible-light-responsive UiO-66(Zr) with defects efficiently promoting photocatalytic CO_2 reduction. *ACS Appl. Mater. Interfaces.* **2022**, *14*, 28977−28984.

(80) Long, J.; Wang, S.; Ding, Z.; Wang, S.; Zhou, Y.; Huang, L.; Wang, X. Amine-functionalized zirconium metal–organic framework as efficient visible-light photocatalyst for aerobic organic transformations. *Chem. Commun.* **2012**, *48*, 11656-11658.

(81) Zhao, S. W., Y.; Dong, J.; He, C. T.; Yin, H.; An, P.; Zhao, K.; Zhang, X.; Gao, C.; Zhang, L.; Lv, J.; Wang, J.; Zhang, J.; Khattak, A. M.; Khan, N. A.; Wei, Z.; Zhang, J.; Liu, S.; Zhao, H.; Tang, Z. . Ultrathin metal-organic framework nanosheets for electrocatalytic oxygen evolution. *Nat. Energy* **2016**, *1*, 1–10.

(82) Wei, Y. S. Z., M.; Zou, R.; Xu, Q. . Metal-organic framework-based catalysts with single metal sites. *Chem. Rev.* **2020**, *120*, 12089–12174.

(83) Zhou, G. W., P.; Li, H.; Hu, B.; Sun, Y.; Huang, R.; Liu, L. Spin-sate reconfiguration induced by alternating magnetic field for efficient oxygen evolution reaction. *Nat. Commun.* **2021**, *12*, 1–9.

(84) Martin, R. L. Natural transition orbitals. *J. Chem. Phys.* **2003**, *118*, 4775–4777.

4.8 Supporting Information

4.8.1 Characterization techniques

Most of the characterization techniques (PXRD, UV-Vis, TGA, XPS, SEM, TEM, Isothermal N_2 adsorption and photoelectrochemical analysis) have already been discussed in the preceding chapter in Section 3.8.2. Thus, the techniques that have been varied or the techniques used for this chapter not used for the materials of Chapter 3, are described here.

Liquid-state ^{1}H- and ^{19}F-NMR measurements were acquired on a Bruker AVANCE III 400 equipment (400 MHz).

Solid-state ^{1}H- and ^{19}F-MAS-NMR spectra were recorded in a Bruker AVANCE III HD spectrometer, spinning the sample at 20 kHz and using a recycle delay of 5 s.

EPR measurements were performed in a Bruker ER 200 D spectrometer under ambient conditions.

The photocurrent generated by the electrodes was measured by chopped Linear sweep voltammetry (LSV) with an applied potential from 1.7 to -0.2 V. A 0.1 M NBu_4PF_6 acetonitrile solution was used as electrolyte. CH_3OH (0.3 mL) was added as hole scavenger for LSV measurements.

EIS was carried out with frequencies ranging from 0.1 Hz to 100 kHz at +0.9 V. Prior to the measurements, the electrolyte solutions were purged with argon for 10 minutes. UV-Vis irradiation of the working electrodes was carried out with a

spot light Hamamatzu Xe lamp (Lightnincure LC8 model, 800–200 nm, 1000 W/m^2, fiber optic light guide with a spot size of 0.5 cm).

The Simplified Randles equivalent circuit (Figure S1) has been used to fit the EIS spectra for calculating the Rct, series resistance (Rs), and double layer capacitance (Cdl), as depicted in the following equivalent circuit:

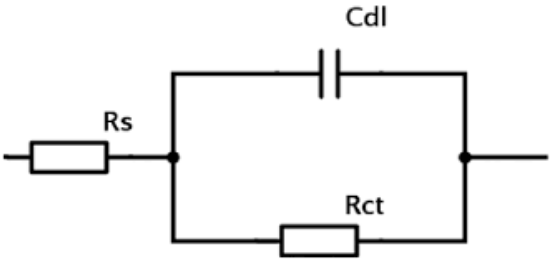

Figure S1. Illustration of simplified Randles equivalent circuit.

Transient absorption spectroscopy in the microsecond time-scale was measured by means of the LFP technique using a pulsed Nd:YAG L52137 V LOTIS TII upon excitation at 266 nm. The single pulses were *ca*. 10 ns duration, and the energy was ~12 mJ/pulse. The LFP system consisted of the pulsed laser, a 77250 Oriel monochromator, and an oscilloscope DP04054 Tektronix. The output signal from the oscilloscope was transferred to a personal computer. Absorbances of all solutions were adjusted at ~0.20 at 266 nm in acetonitrile (HPLC grade). All measurements were done using 10 × 10 mm^2 quartz cuvettes at room temperature under different conditions: deaerated atmosphere (10 min Ar bubbling), oxygen saturated atmosphere (10 min O_2 bubbling) and in deaerated atmosphere in the presence of 25 % of CH_3OH. Control experiments indicated that the degree of decomposition of the samples after photolysis was lower than 2 %.

The LFP decay traces were fitted using a multi-exponential function following the Levenberg-Marquardt iteration algorithm:

$$F(t,\lambda) = \sum_{i=1}^{n} a_i(\lambda) e^{\left(-\frac{t}{\tau_i}\right)} + y_0 \qquad (Eq.\ S1)$$

$$n: 2\ or\ 3$$

Fluorescence spectroscopy. Steady-state fluorescence measurements (λ_{exc} = 266 nm) were performed on an Edinburgh FS5 spectrofluorometer, provided with a monochromator in the wavelength range of 200-900 nm. The absorbance of the samples was identical (*ca*. 0.1) at the excitation wavelength. Time-resolved fluorescence measurements were done using an EasyLife X system containing a sample compartment composed of an automated Peltier cuvette holder to control the temperature at 24 ºC, a pulsed LED excitation source and a lifetime detector. The employed LED excitation source was 265 nm, with emission filter of WG305. The absorbance of the samples was identical (*ca*. 0.1) at the excitation wavelength. Fluorescence measurements were done using 10 × 10 mm^2 quartz cuvettes at room temperature under deaerated acetonitrile atmosphere (10 min Ar bubbling). The fluorescence lifetimes were obtained upon fitting the decay traces by a non-linear fitting/deconvolution procedure using a one- exponential function $F(t) = \sum a_i \cdot exp(-t/\tau_i)$.

4.8.2 Estimation of UiO-66 missing ligands

Quantification of the defects were obtained though TGA data following a general procedure based on previous related report [2]. To estimate the defectivity of the UiO-66(Zr)-X (X: NH_2 or NO_2) materials prepared in this study, the number

of ligand deficiencies per Zr_6 formula unit (i.e., the value of x in composition Zr_6O_{6+x} (BDC ligand)$_{6-x}$) was calculated as explained below:

The complete combustion of a defect-free UiO-66 involves the formation of 6 moles of ZrO_2. Therefore, assuming the TGA residue as pure ZrO_2, the end weight of the measurement was normalized to 100 % to find the experimental TGA plateau where dehydroxylation of the MOF has already occurred. Theoretical TGA plateau for the ideal MOF was calculated considering the molar mass of both the residue and the defect-free MOF, being 123.22 g·mol^{-1} for ZrO_2 (6·123.22=739.34 g·mol^{-1}), 1754.10 g·mol^{-1} for Zr_6O_6(BDC-NH_2)$_6$ and 1934.05 g·mol^{-1} for Zr_6O_6(BDC-NO_2)$_6$. Thus, the ideal TGA plateau can be calculated as the percentage of the division of the MOF's molar mass between the molar mass of the 6 ZrO_2, being 237.3 % in the case of UiO-66(Zr)-NH_2 and 261.6 % for UiO- 66(Zr)- NO_2 as it can be seen in Figure 2 and Figure S8, represented by the horizontal dashed line. Assuming the average composition of the defective MOFs as: Zr_6O_{6+x}(BDC-NH_2)$_{6-x}$, Zr_6O_{6+x}(BDC-NO_2)$_{6-x}$, an experimental plateau where the only molecule that is remaining is the linker, was chosen for each material. The temperature chosen for the plateau can be observed as the vertical dashed line in Figure 2 and S8: being 337 ºC for the MOFs containing the BDC-NH_2 ligand, and 278 ºC for the UiO-66(Zr)-NO_2 series. With this data, the experimental number of ligands present in the framework could be obtained as follows:

$$W_{end} = MW_{ZrO_2} \cdot n_{ZrO_2} \qquad \text{(Eq. S2)}$$

$$n_{MOF} = \frac{n_{ZrO_2}}{NL_{Id.}} \quad \text{(Eq. S3)}$$

To calculate n_{MOF} eq. (S2) is substituted in eq. (S3):

$$n_{MOF} = \frac{n_{ZrO_2}}{NL_{Id.}} = \frac{\frac{W_{end}}{MW_{ZrO_2}}}{NL_{Id.}} \qquad \text{(Eq. S4)}$$

The experimental plateau weight is obtained using Eq. S5:

$$W_{Pexp.} = MW_{Pexp.} \cdot n_{MOF} \quad \text{(Eq. S5)}$$

Equation (S4) is substituted in eq. (S5) to obtain the experimental MW:

$$MW_{Pexp.} = \frac{W_{Pexp.} \cdot MW_{ZrO_2}}{W_{end} \cdot NL_{Id.}} \quad \text{(Eq. S6)}$$

$$MW_{Pexp.} = 6 \cdot AW_{Zr} \cdot (6 + x) \cdot AW_O + (6 - x) \cdot MW_{(BDC-X)} \qquad \text{(E. S7)}$$

The global formula for the defect calculation is:

$$x = \frac{MW_{Pexp.} - NL_{Id.}(AW_{Zr} + AW_O + MW_{(BDC-X)})}{AW_O - MW_{(BDC-X)}} \qquad (Eq. S8)$$

W_{end}: *End weight of the TGA curve*

MW_{ZrO_2}: *Molecular weight of* ZrO_2

$NL_{Id.}$: *Ideal number of linkers*

$W_{Pexp.}$: *Experimental plateau weight*

AW_Y: *Atomic weight of* Y $(Y: Zr, O)$

$MW_{Pexp.}$: *Molecular weight of the MOF at the experimental plateau*

$MW_{(BDC-X)}$: *Molecular weight of* $BDC - X$ $(X: NH_2, NO_2)$

An example of the defects' calculation for UiO-66(Zr)-NH_2-12AA, is described:

$W_{end} = 100\,g$

$MW_{ZrO_2} = 123.2228\ g/mol$

$NL_{Id.} = 6$

$W_{Pexp.} = 216.2\,g\ at\ T{=}337\ ºC$

$AW_{Zr} = 91.224\ g/mol$

$AW_O = 15.99\ g/mol$

$MW_{(BDC-NH_2)} = 181.15\ g/mol$

$$n_{MOF} = \frac{n_{ZrO_2}}{NL_{Id.}} = \frac{\frac{W_{end}}{MW_{ZrO_2}}}{NL_{Id.}} = \frac{\frac{100\ g}{123.2228\frac{g}{mol}}}{6} = 0.135\ mol$$

$$W_{Pexp.} = MW_{Pexp.} \cdot n_{MOF}$$

$$MW_{Pexp.} = \frac{W_{Pexp.} \cdot\ MW_{ZrO_2}}{W_{end} \cdot\ NL_{Id.}} = \frac{216.20\ g}{0.1352\ mol} = 1598.446\ g/mol$$

$$x = \frac{MW_{Pexp.} - NL_{Id.}\left(AW_{Zr} + AW_O + MW_{(BDC-NH_2)}\right)}{AW_O - MW_{(BDC-NH_2)}}$$

$$x = \frac{1598.446\frac{g}{mol} - 6 \cdot (91.224\ g/mol + 15.99\ g/mol + 181.15\ g/mol)}{15.99\ g/mol - 181.15\ g/mol}$$

$$x = 0.798$$

Once the parameter “x” is obtained, it could be substituted in the equation as shown:

$$Zr_6O_{6-x}(BDC-NH_2)_{6-x} = Zr_6O_{(6-0.80)}(BDC-NH_2)_{(6-0.80)}$$

$$Zr_6O_{5.2}(BDC-NH_2)_{5.2}$$

4.8.3 Computational details

Ground state periodic calculations

All ground state calculations were conducted within the Vienna Ab initio Simulation Package (version 5.4.4) [3] in the DFT framework, by using the Perdew-Burke-Ernzerhof (PBE) functional in the Generalized Gradient Approximation (GGA) [4-6]. A plane wave energy cutoff of 650 eV was used with a precision of 10^{-5} eV. The atomic positions of the defective unit cells described in Figure S2 were fully relaxed until the maximum force on each atom reached an energy threshold equal to 10^{-3} eV/Å. The Brillouin zone was sampled by using a 2×2×2 Monkhorst- Pack k-mesh grid[7]. Periodic boundary conditions were enforced in all directions. The long-range interactions were taken into account by introducing the van der Waals dispersion correction within the Grimme’s DFT-D3 method [8]. Gaussian smearing with a width of 0.05 eV was used to assist the DFT convergence.

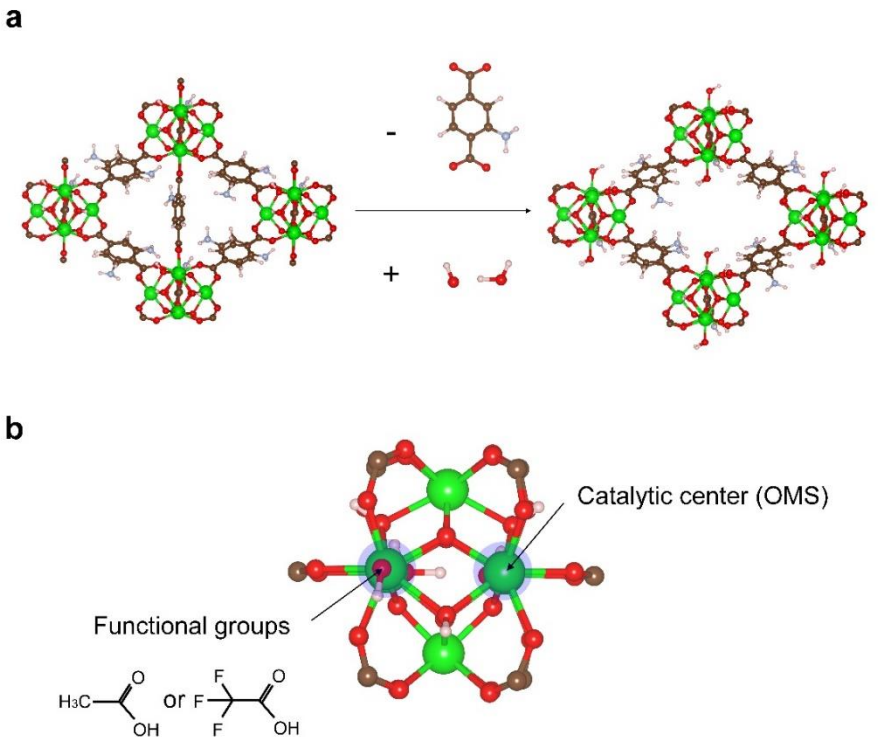

Figure S2. (a) A schematic of the generation of a defect model of UiO-66(Zr)-NH_2, where the defect concentration is 1 missing-linker per Zr_6 unit cell formula to be consistent with the experimental value (0.88 missing linker per Zr_6 formula unit, as shown in Figure 14 of the main text). The resulting exposed Zr sites were terminated with -OH and H_2O[9]. The representative UiO-66(Zr)-NH_2 structure was extracted from a previous work[10] and finally the functionalized model was constructed based on this structural prototype. All atom positions were fully relaxed during the structure optimization process. (b) Schematic representation of the model during the calculation of catalytic reactions. Here it is assumed that the removal of H_2O creates exposed metal sites that serve as active centers for all subsequent catalytic reactions. The neighbouring -OH can be functionalized with AA and TFA.

For each elementary step of HER and OER, the free-energy calculations are based on the approach proposed by Nørskov et al. [11]. The free energy difference between the initial and final reaction states was defined as follows

$$\Delta G = \Delta \mathrm{E} + \Delta \mathrm{ZPE} - \mathrm{T}\Delta \mathrm{S} - eU$$

where ΔE is the total energy difference between reactants and products; ΔZPE is the zero-point energy; ΔS is the vibrational entropy change at the temperature T (298 K in this work); *e* is the elementary charge; U is the electrode potential.

The calculated T×S and ZPE are presented in the Table S1.

Table S1. Values used for the entropy and zero-point energy corrections in determining the free energy of reactants, products, and intermediate species adsorbed on catalysts.

Species	**T×S (eV) (298.15 K)**	**ZPE (eV)**
$H_2(g)$	0.4209	0.2712
$H_2O(g)$	0.6040	0.5714
OH^* [OH/AA/TFA]	0.00/0.00/0.00	0.353/0.354/0.353
O^* [OH/AA/TFA]	0.00/0.00/0.00	0.073/0.047/0.047
OOH^* [OH/AA/TFA]	0.00/0.00/0.00	0.432/0.469/0.461
H* [OH/AA/TFA]	0.00/0.00/0.00	0.136/0.164/0.164

Cluster models

The calculations done for the cluster models have been conducted by following the procedure reported in ref. [12]. Within this approach finite clusters were built by cutting one ZrO based metal node and two BDC based ligands from the relaxed periodic structure, and by capping the unsaturated sites with protons (Figure S3). Then the geometries of the added hydrogens were optimized in a simulation box of large dimensions (>20Å) to avoid the interaction between

neighbouring clusters, meanwhile keeping the rest of the atoms frozen. For the sake of consistency, these energy optimizations were done within the same methodology as the one employed for the cell relaxations. The excited state properties of the resulting structures were estimated at the TD-DFT level within the standard Heyd–Scuseria–Ernzerhof functional[13] and by employing a 6-311+G(d) basis set[13,14] for H, C, N, O, F atoms, and the Stuttgart–Dresden–Dunning (MWB28) basis set [15] and effective core potential for Zr. All cluster calculations were done in the gas phase since the effect of the implicit water solvent, which was taken into account by means of the Conductive Polarizable Continuum Model[16], only yielded to small red-shifts and a slight increase in the bands absorption, and more importantly, this did not affect the trends in the absorption observed when modifying the coordination groups, as it can be appreciated in the spectra depicted in Figure S2. The CT analysis between ligand and metal node was performed via the transition density matrix analysis method implemented in TheoDORE program[17]. More in detail, two main exciton localization characteristics were evaluated: the participation ratio (PR) along the two moieties which spam from 1 to 2, and the CT character coefficient, owing values between 0 and 1. Finally, all set of cluster model calculations were carried out within the Gaussian16 package [18].

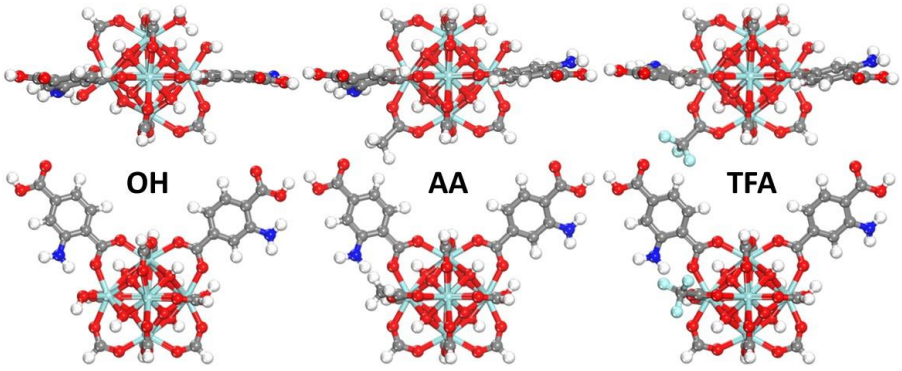

Figure S3. Top and lateral views of the OH, AA and TFA-coordinated cluster models employed for the TD-DFT calculations.

Excited state properties periodic structures

The excited state properties of the periodic systems were computed by relying on the Time-dependent density functional perturbation theory (TD-DFPT) linear response approach [19], as it is implemented in the CP2K package [20]. We adopted the same computational set up as the one reported in refs [21, 22]. where TD-DFPT calculations were performed within the PBE functional [5], and by employing a DZVP MOLOPT basis set [23] to represent the HOCO electrons, whereas Goedecker–Teter–Hutter pseudopotentials [24] were used for the core electrons. Semiempirical Grimme's D3 method [8] was used to consider the van der Waals interactions. We relied on a 600 Ry cut-off for computing the electron density of the ground state, while for the excited state calculations it was set a 200 Ry cut- off and a 10^{-5} eV convergence energy threshold. The whole series of excited state periodic calculations were run on Γ point. All computed absorption spectra were generated via the convolution of Gaussian functions with a half-width at full- length of σ=0.15 eV.

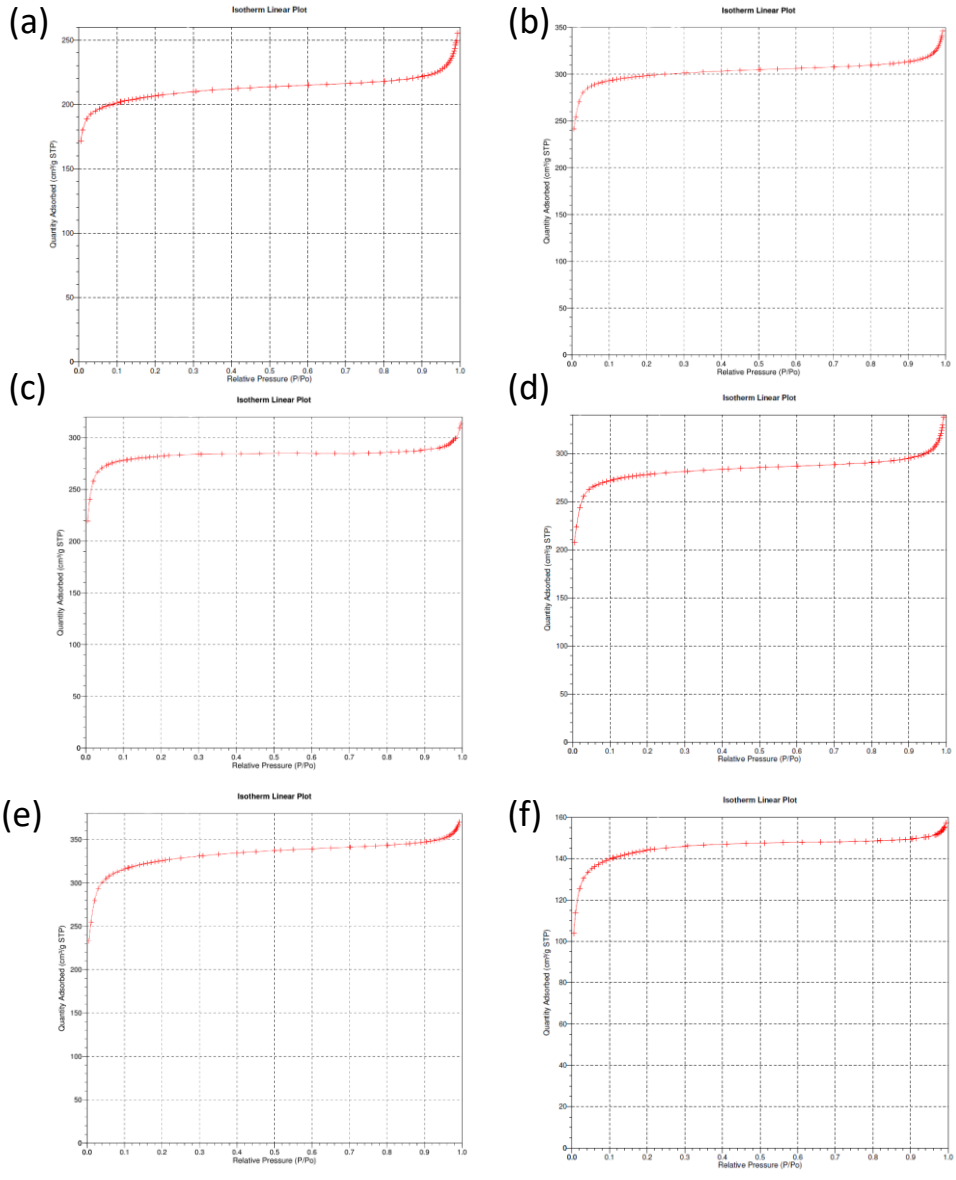

Figure S4. Isothermal N_2 adsorption curve of (a) UiO-66(Zr)-NH_2, (b) UiO- 66(Zr)- NH_2-12AA, (c) UiO-66(Zr)-NH_2-36AA, (d) UiO-66(Zr)-NH_2-100AA, (e) UiO-66(Zr)-NH_2-12TFA, (f) UiO-66(Zr)-NH_2-36TFA.

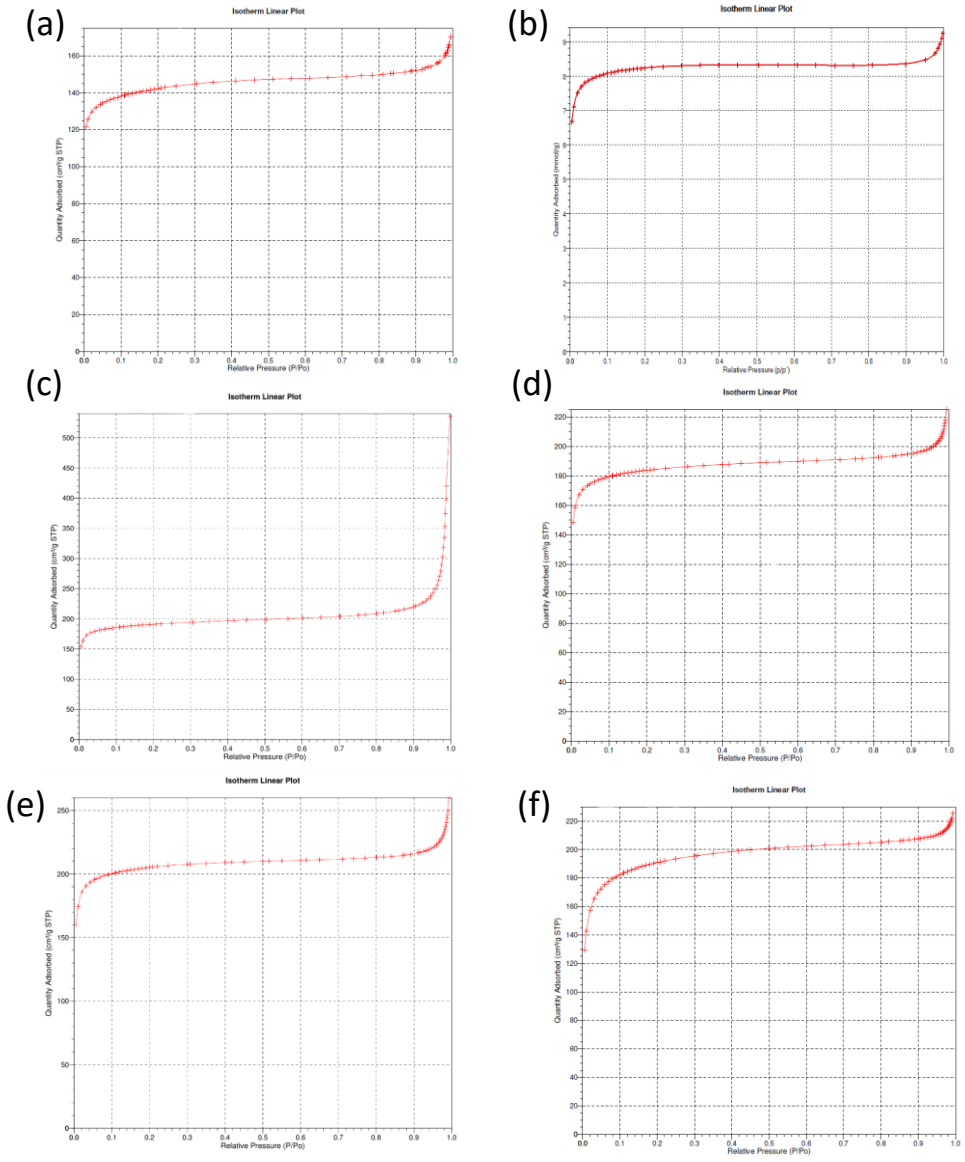

Figure S5. Isothermal N_2 adsorption curve of(a) UiO-66(Zr)-NO_2, (b) UiO- 66(Zr)- NO_2-12AA, (c) UiO-66(Zr)-NO_2-36AA, (d) UiO-66(Zr)-NO_2-100AA, (e) UiO-66(Zr)-NO_2-12TFA, (f) UiO-66(Zr)-NO_2-36TFA.

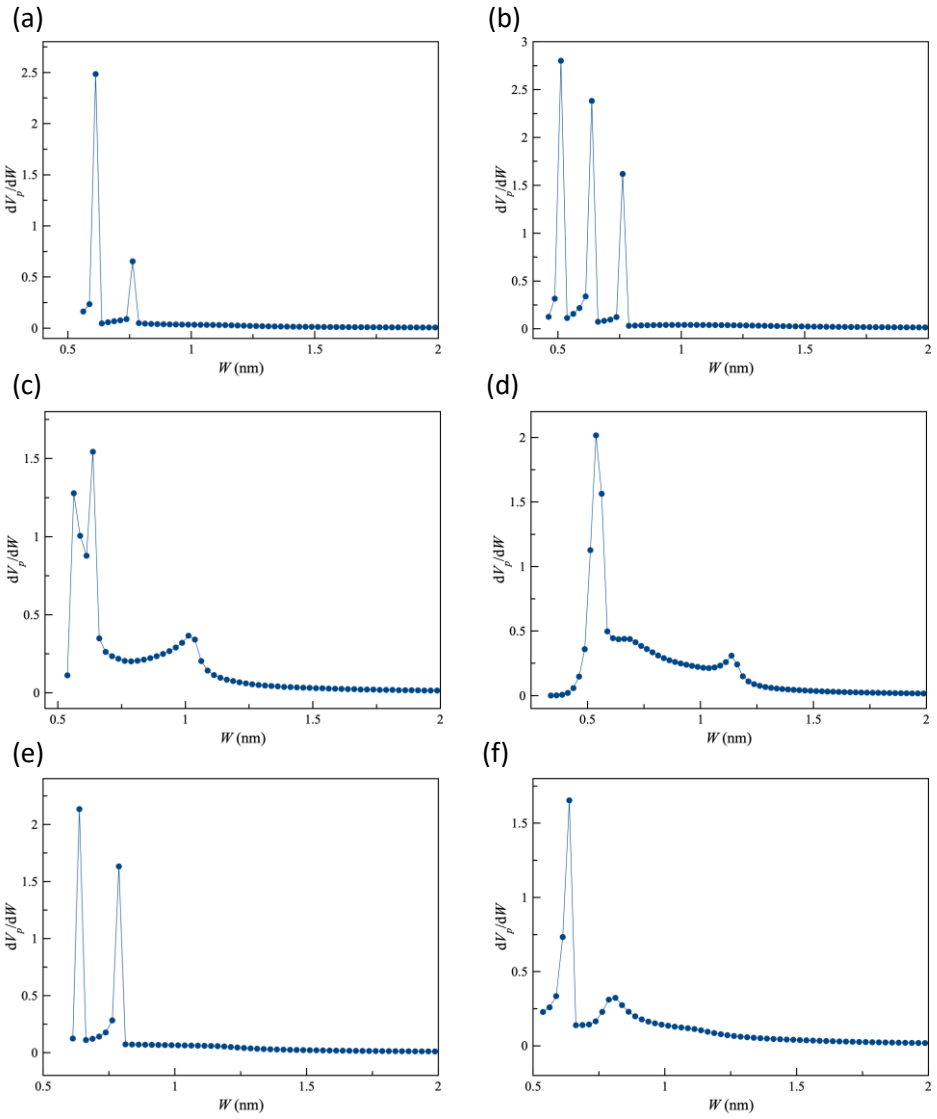

Figure S6. Pore size distribution of (a) UiO-66(Zr)-NH_2, (b) UiO-66(Zr)-NH_2-12AA, (c) UiO-66(Zr)-NH_2-36AA, (d) UiO-66(Zr)-NH_2-100AA, (e) UiO-66(Zr)-NH_2-12TFA, (f) UiO-66(Zr)-NH_2-36TFA.

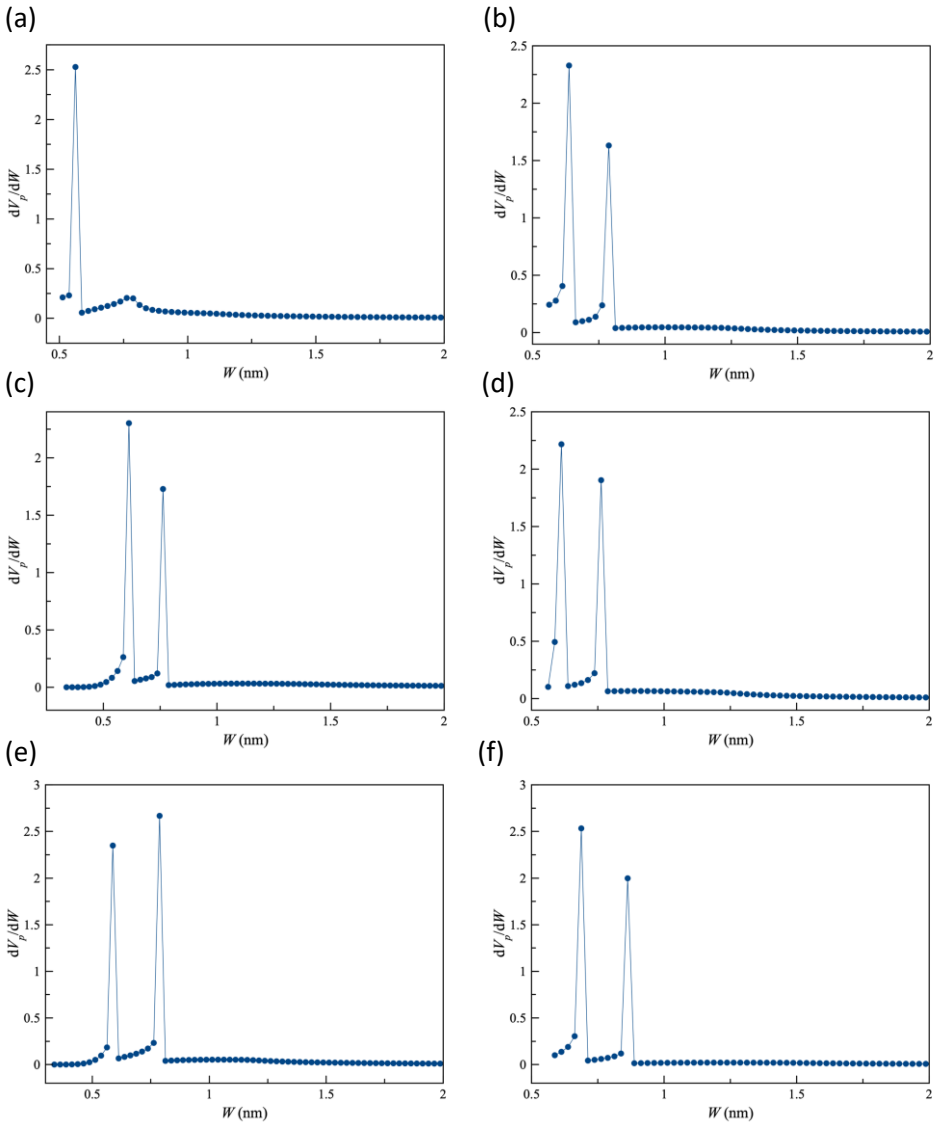

Figure S7. Pore size distribution of (a) UiO-66(Zr)-NO_2, (b) UiO-66(Zr)-NO_2-12AA, (c) UiO-66(Zr)-NO_2-36AA, (d) UiO-66(Zr)-NO_2-100AA, (e) UiO-66(Zr)-NO_2-12TFA, (f) UiO-66(Zr)-NO_2-36TFA.

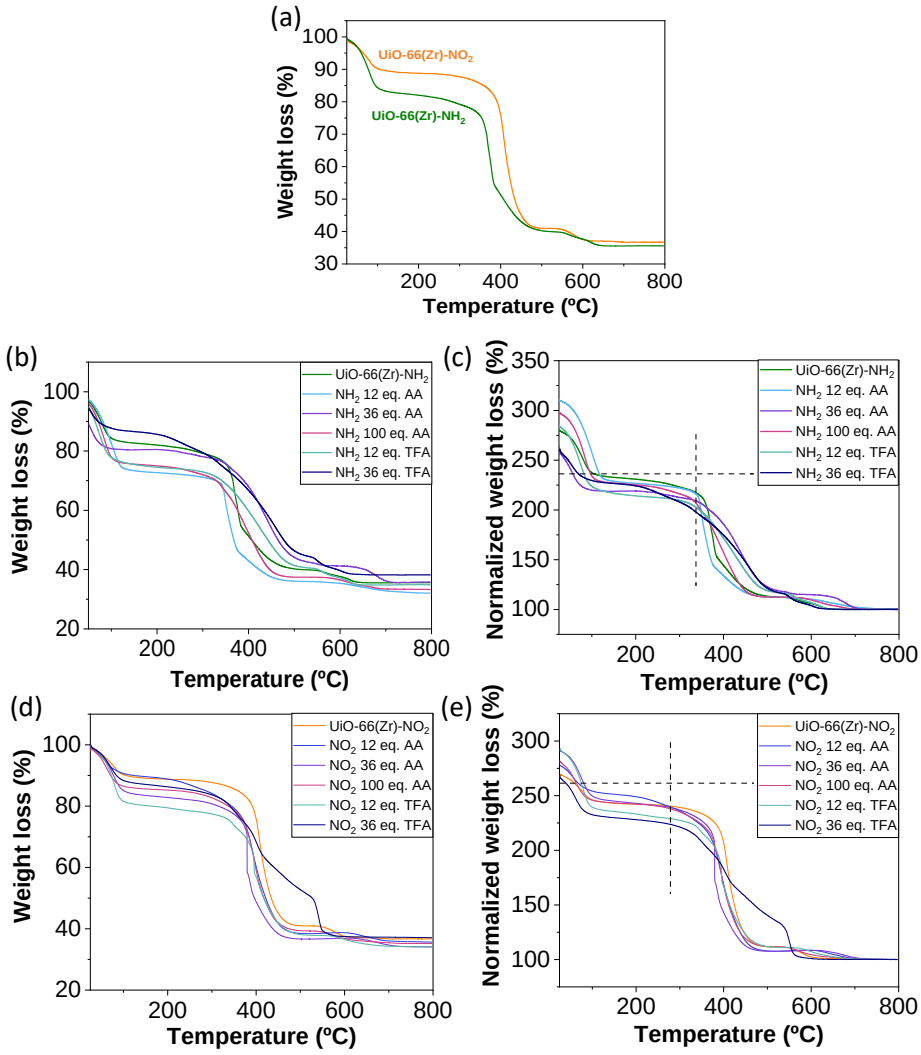

Figure S8. TGA analysis of UiO-66(Zr)-NH_2 and UiO-66(Zr)-NO_2 (a); and synthesized in the absence or in the presence of AA or TFA as indicated for each of the series (b, d); and the TGA analysis normalized to the residue (c, e).

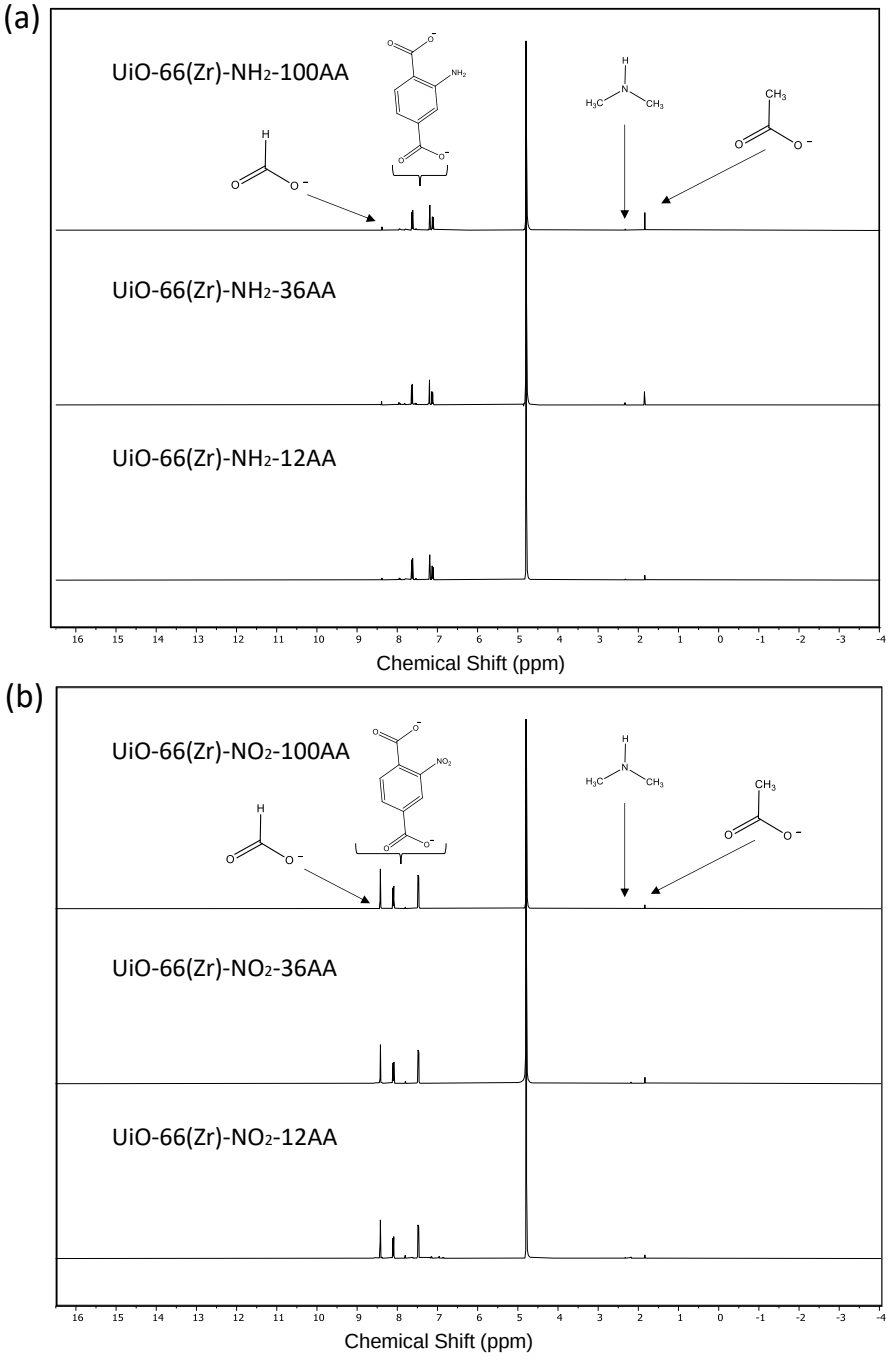

Figure S9. ^{1}H-NMR of digested UiO-66(Zr)-NH_2 (a) and UiO-66(Zr)-NO_2 (b) solids prepared using different equivalents of AA as indicated.

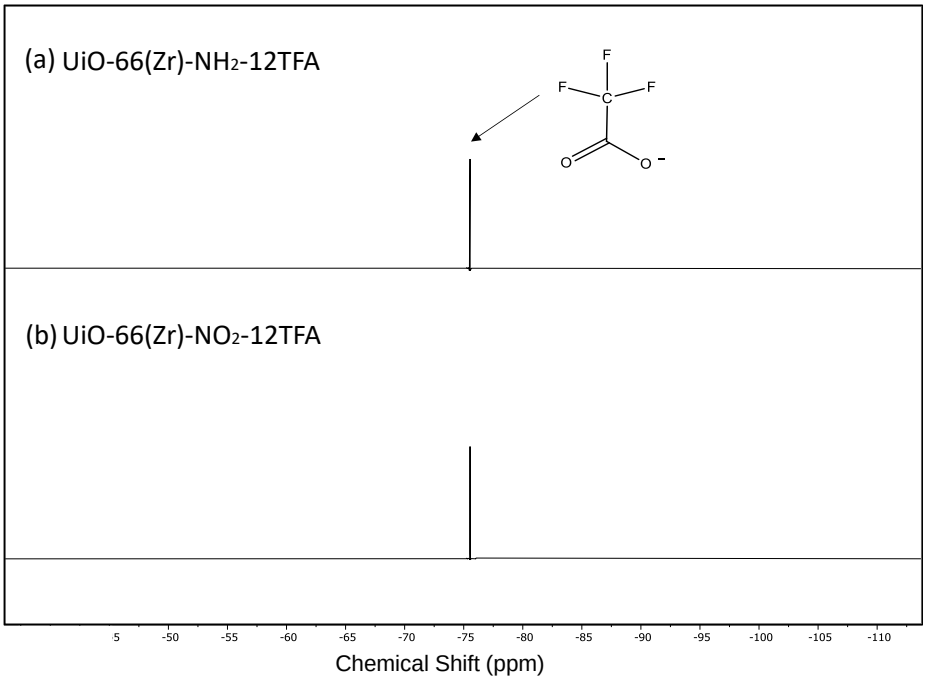

Figure S10. ^{19}F-NMR of digested (a) UiO-66(Zr)-NH_2 and (b) UiO-66(Zr)-NO_2 solids prepared using 12 equivalents of TFA.

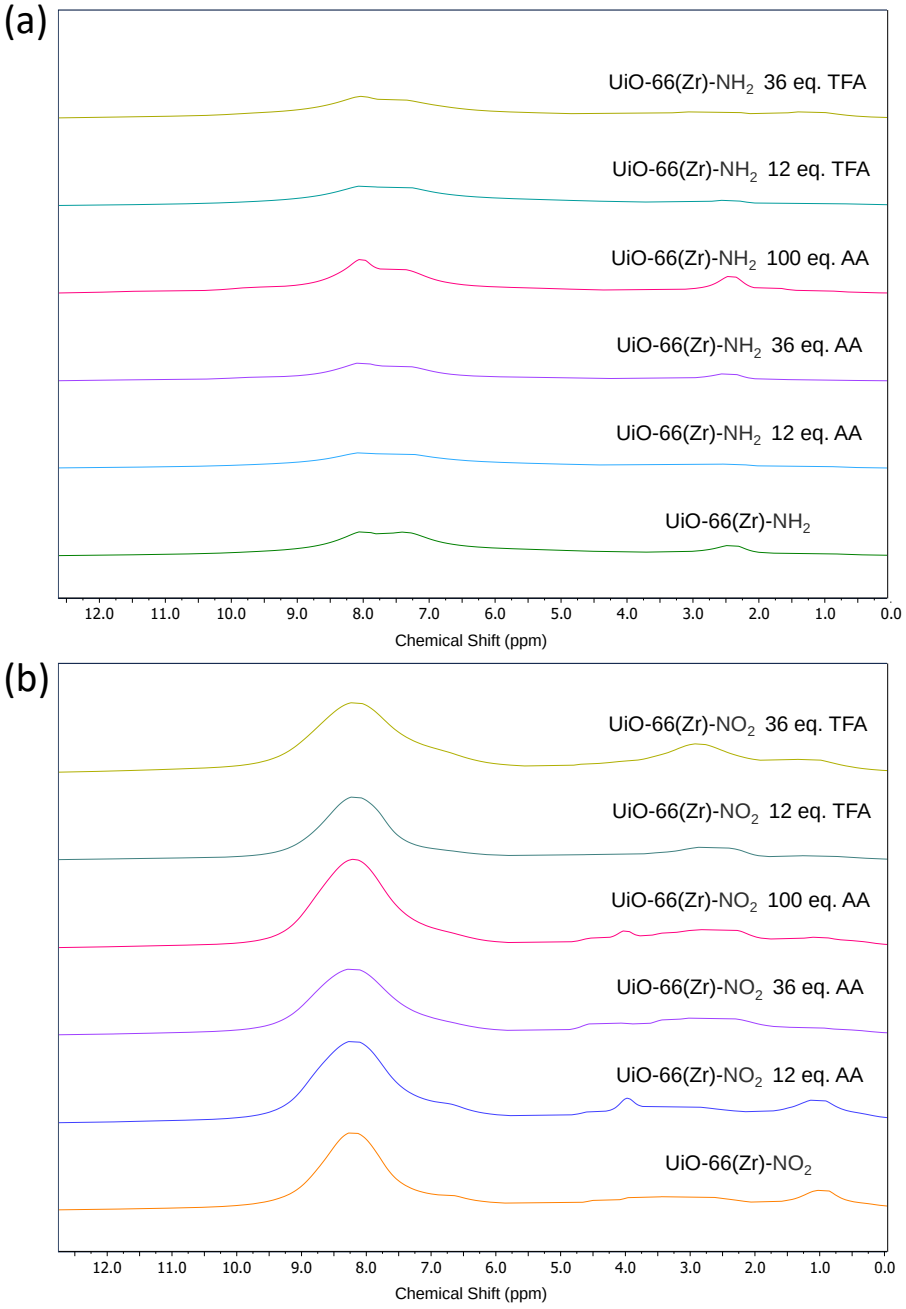

Figure S11. Solid-state ^{1}H-NMR UiO-66(Zr)-NH_2 (a) and UiO-66(Zr)-NO_2 (b) solids as indicated.

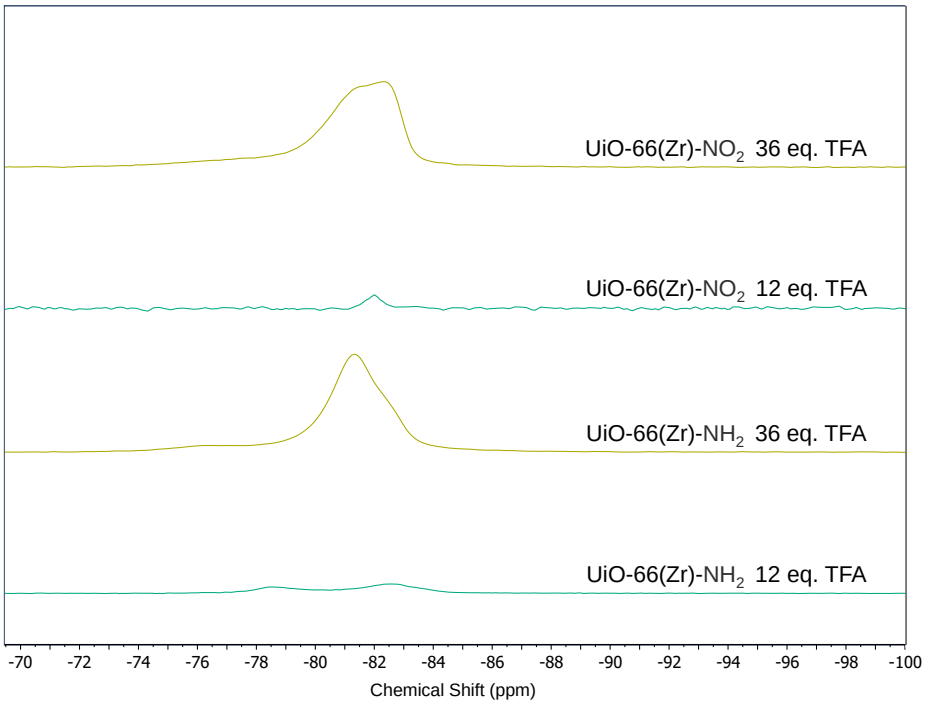

Figure S12. Solid-state ^{19}F-NMR of UiO-66(Zr)-NH_2 (a) and UiO-66(Zr)-NO_2 (b) prepared using TFA as indicated.

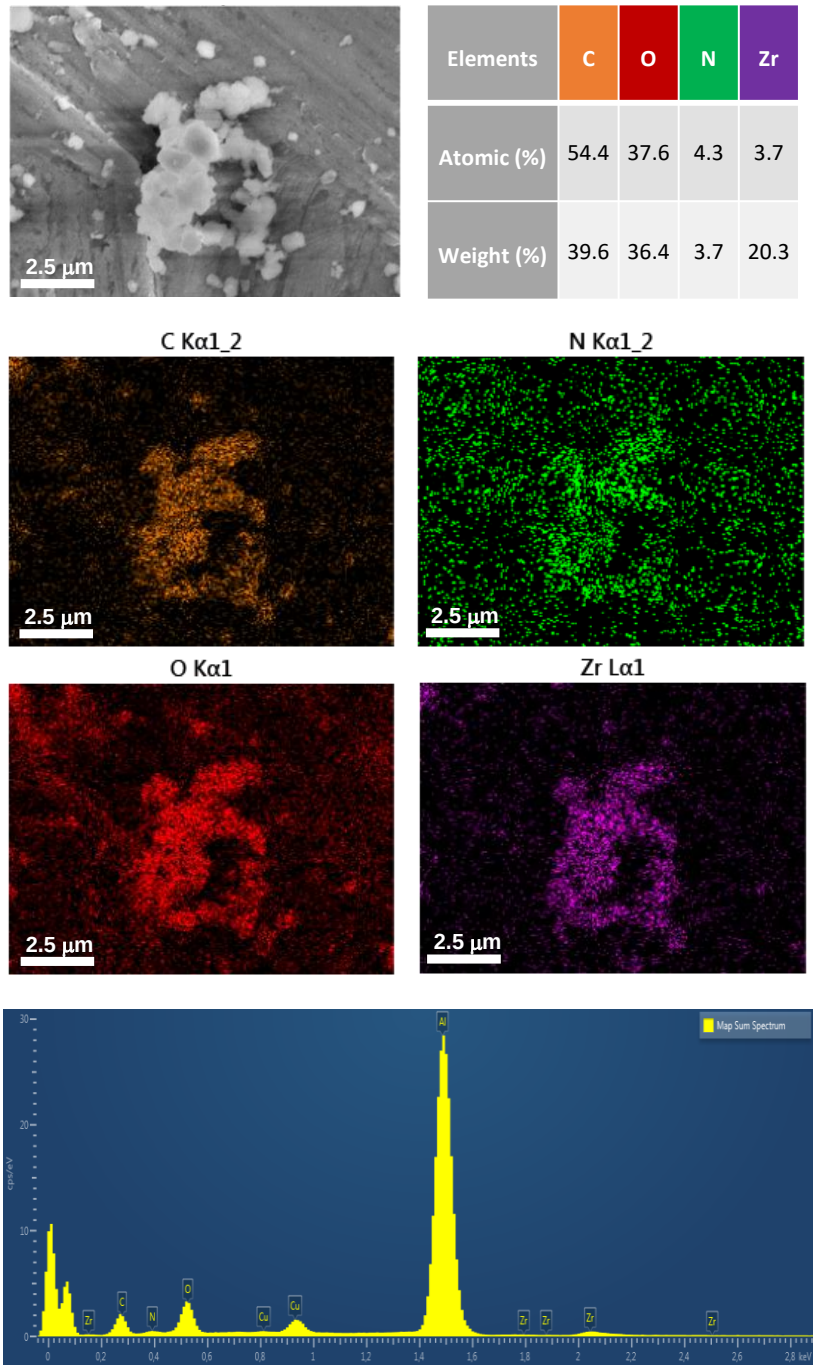

Figure S13. SEM-EDX of non-modulated UiO-66(Zr)-NH_2.

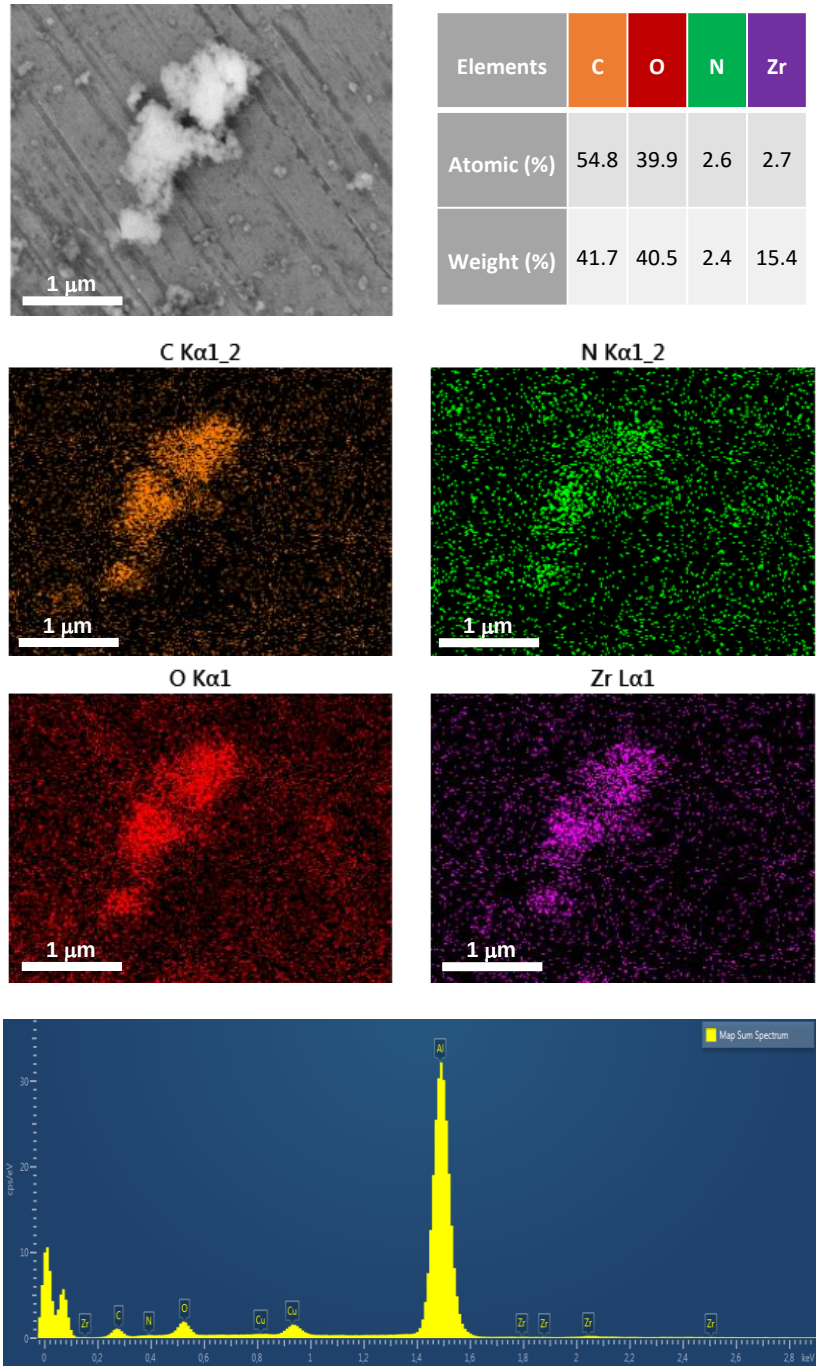

Elements	C	O	N	Zr
Atomic (%)	54.8	39.9	2.6	2.7
Weight (%)	41.7	40.5	2.4	15.4

Figure S14. SEM-EDX of modulated UiO-66(Zr)-NH_2-12AA.

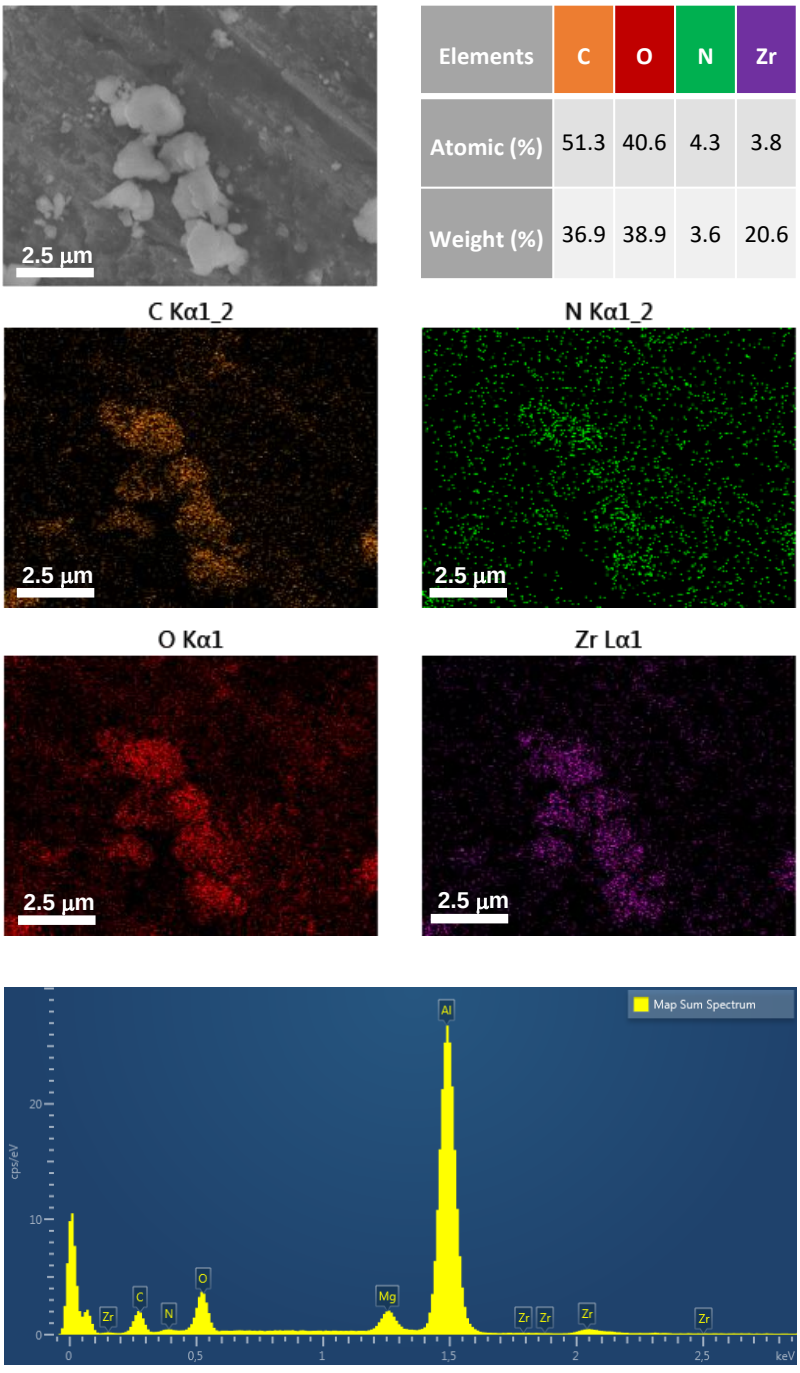

Figure S15. SEM-EDX of modulated UiO-66(Zr)-NH_2-36AA.

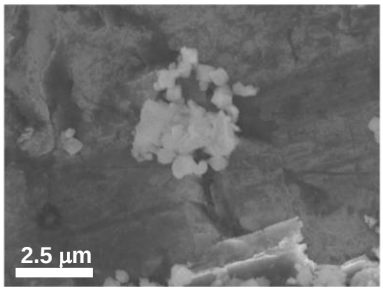

Elements	C	O	N	Zr
Atomic (%)	41.3	53.9	2.4	2.4
Weight (%)	30.8	53.5	2.1	13.5

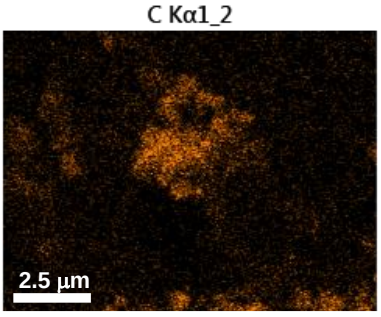

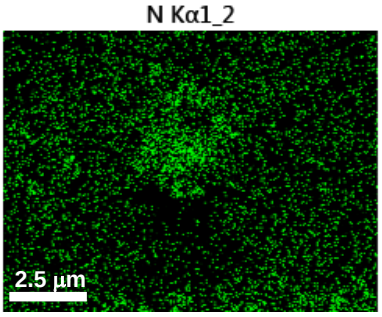

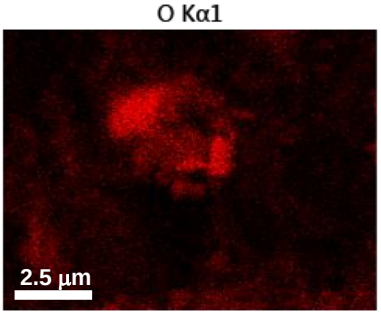

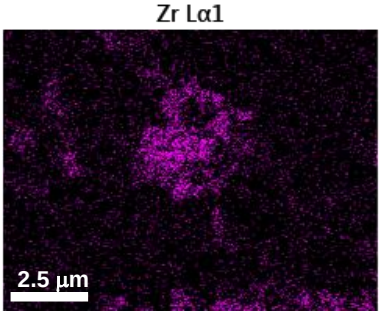

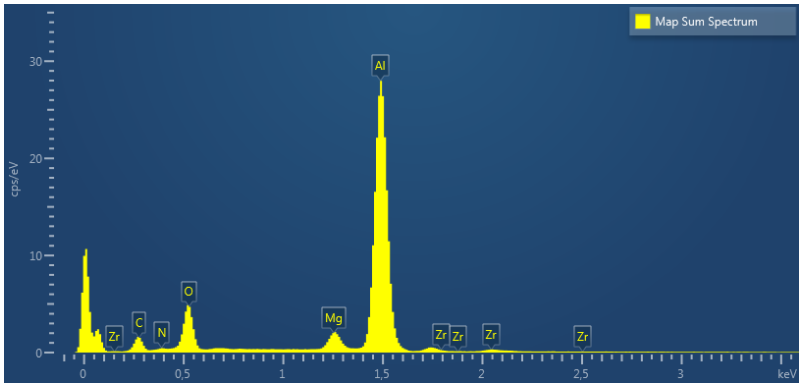

Figure S16. SEM-EDX of modulated UiO-66(Zr)-NH_2-100AA.

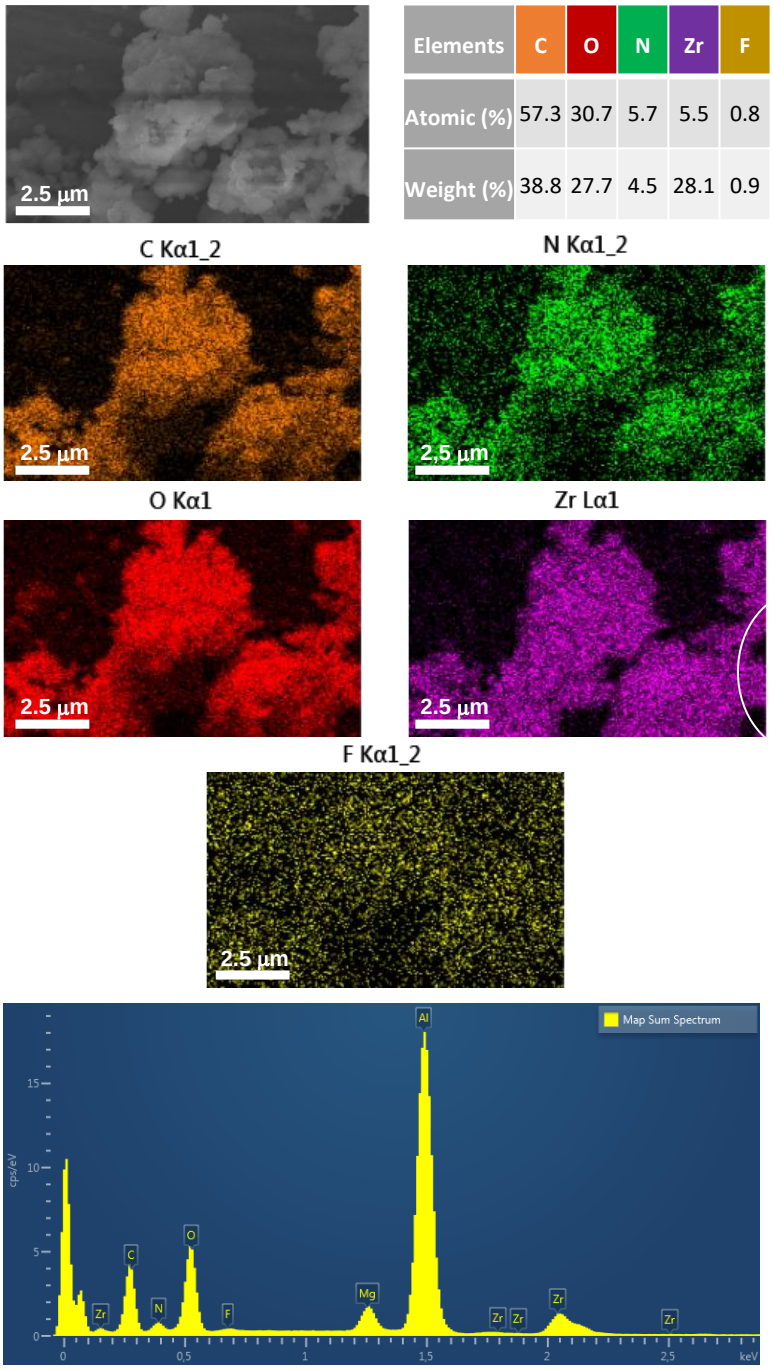

Figure S17. SEM-EDX of modulated UiO-66(Zr)-NH_2-12TFA.

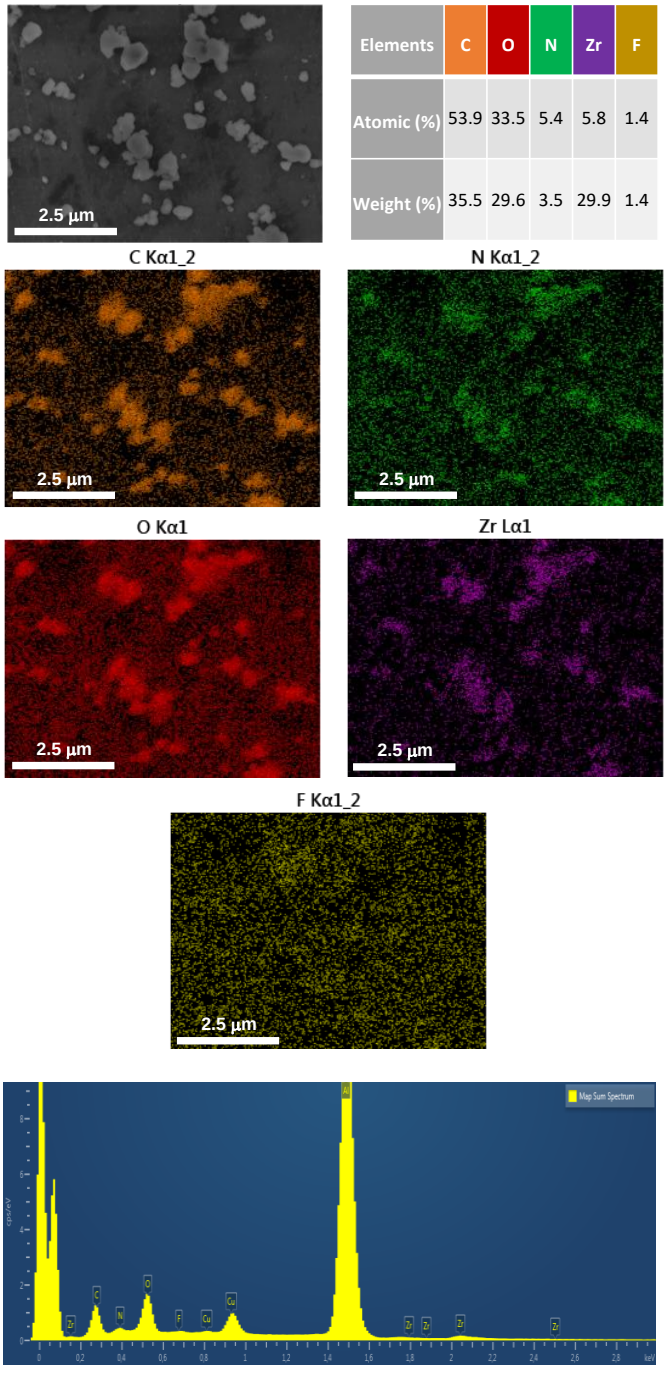

Figure S18. SEM-EDX of modulated UiO-66(Zr)-NH_2-36TFA.

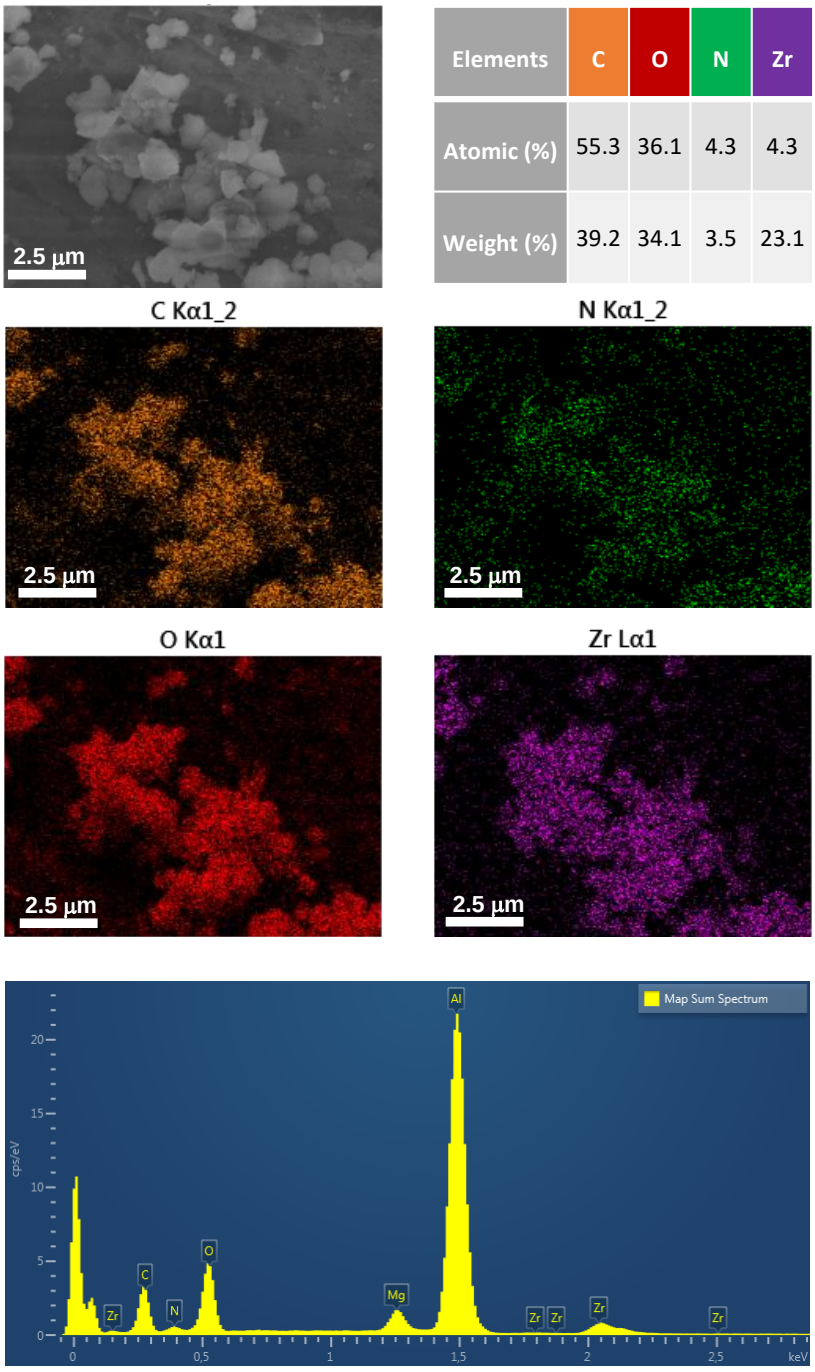

Figure S19. SEM-EDX of non-modulated UiO-66(Zr)-NO_2.

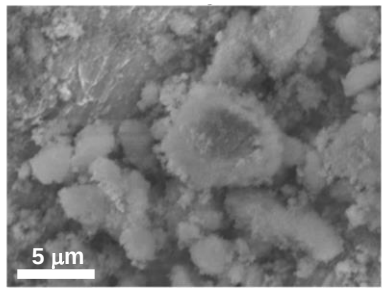

Elements	C	O	N	Zr
Atomic (%)	54.4	34.8	5.8	5.0
Weight (%)	37.4	31.9	4.7	26.0

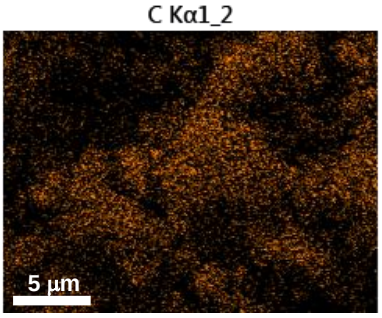

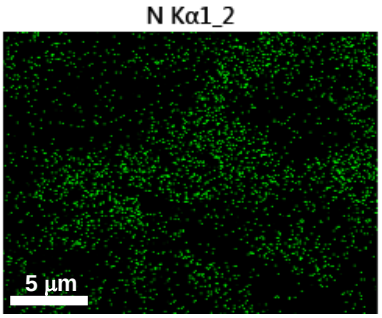

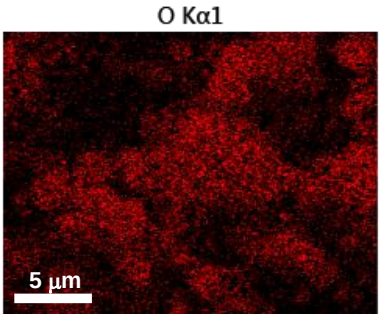

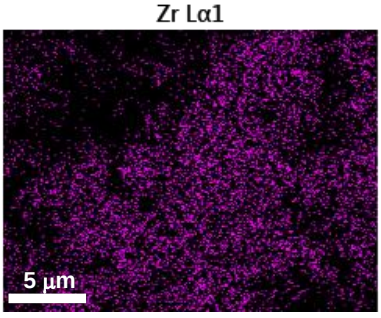

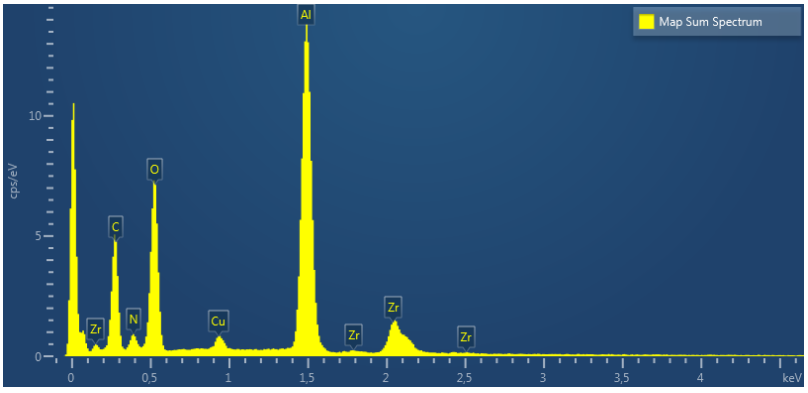

Figure S20. SEM-EDX of modulated UiO-66(Zr)-NO_2-12AA.

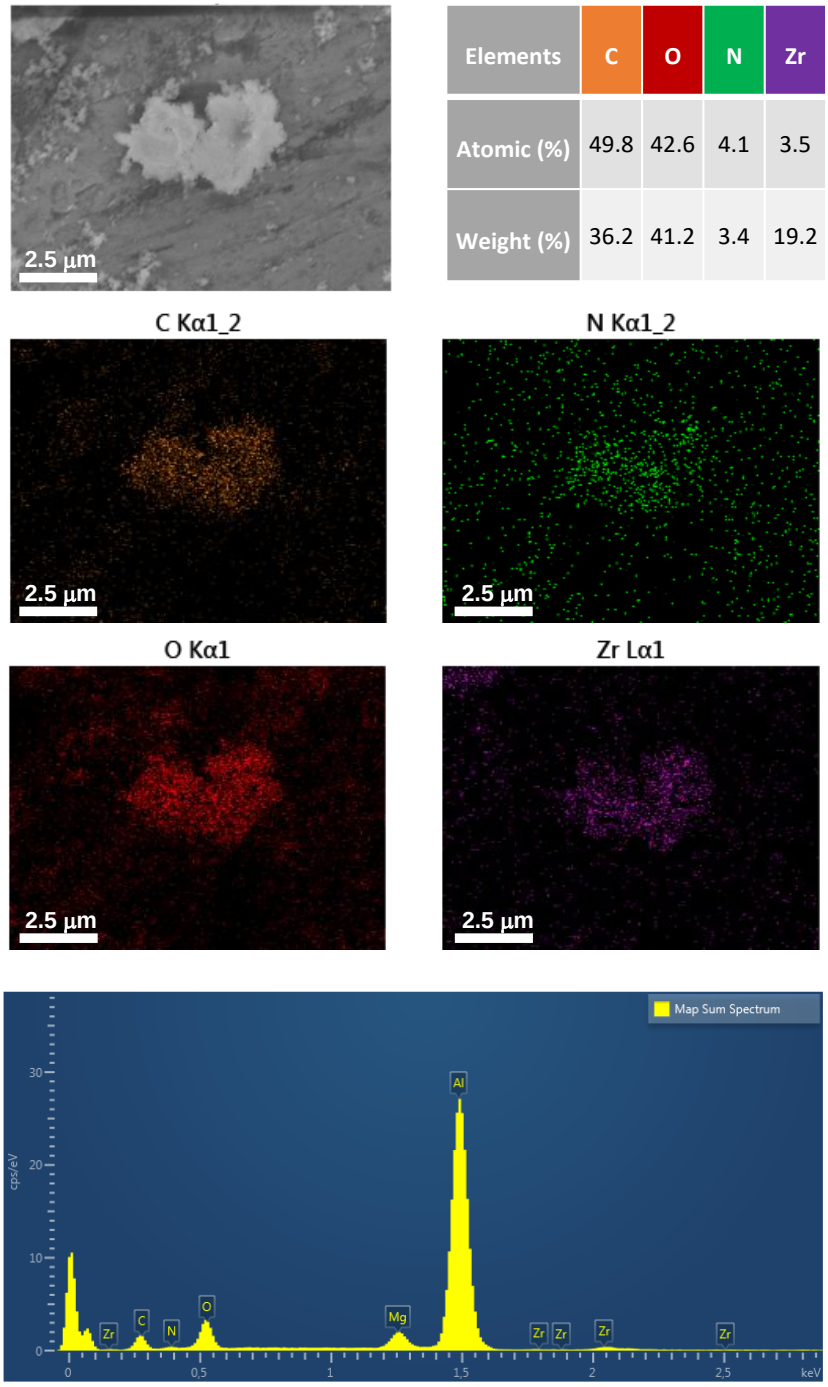

Figure S21. SEM-EDX of modulated UiO-66(Zr)-NO_2-36AA.

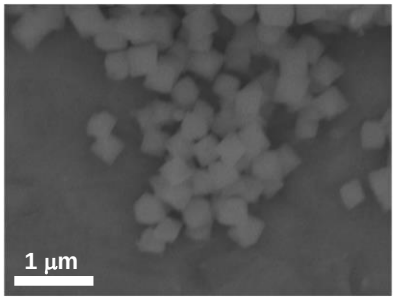

Elements	C	O	N	Zr
Atomic (%)	52.2	35.0	2.6	10.2
Weight (%)	29.1	26.0	1.7	43.3

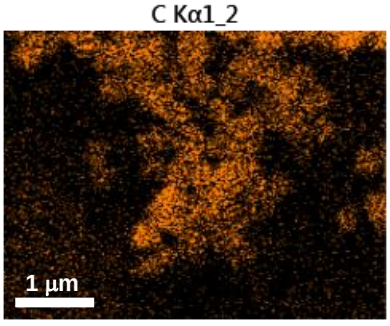

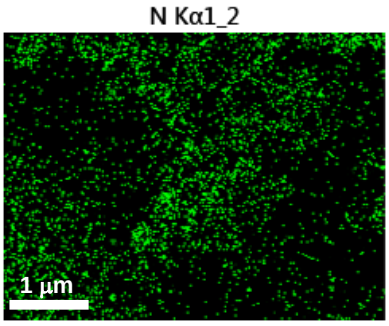

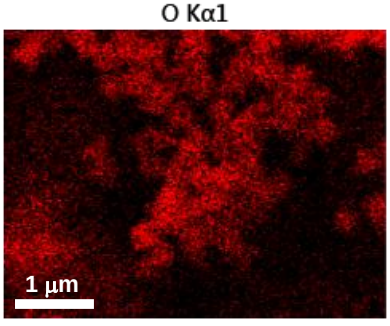

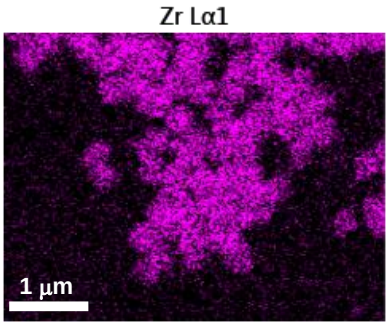

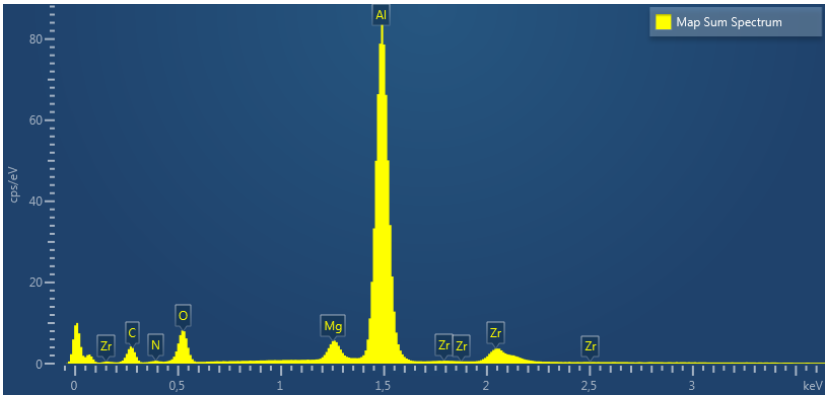

Figure S22. SEM-EDX of modulated UiO-66(Zr)-NO_2-100AA.

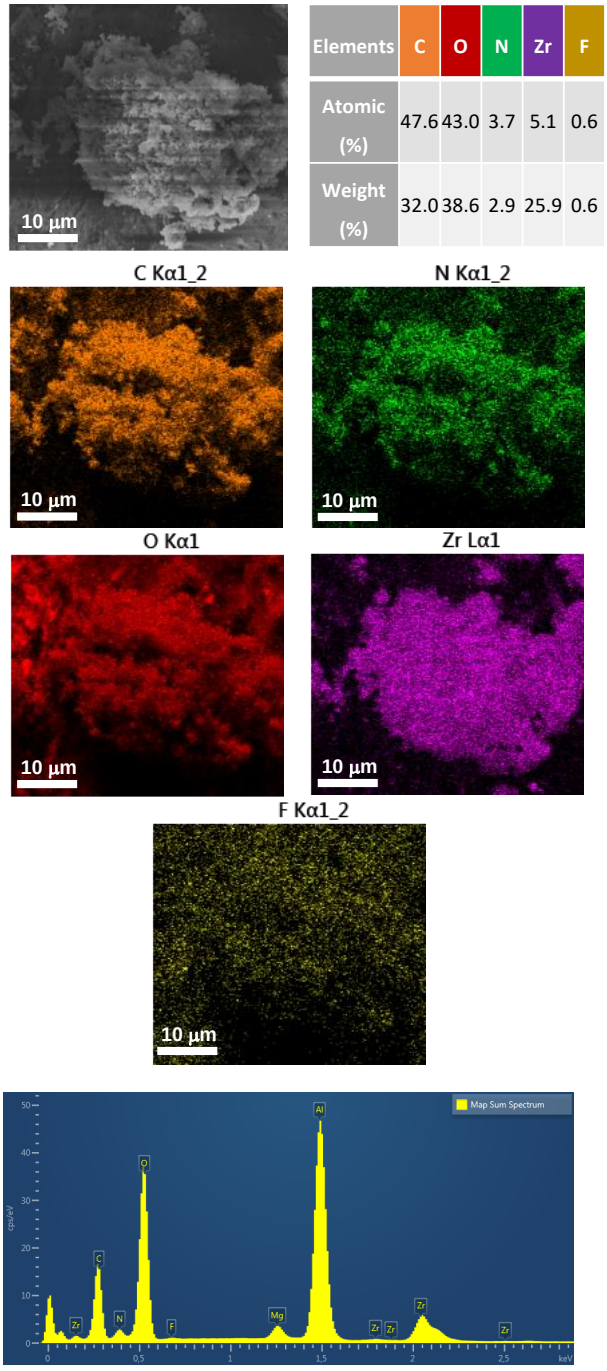

Elements	C	O	N	Zr	F
Atomic (%)	47.6	43.0	3.7	5.1	0.6
Weight (%)	32.0	38.6	2.9	25.9	0.6

Figure S23. SEM-EDX of modulated UiO-66(Zr)-NO_2-12TFA.

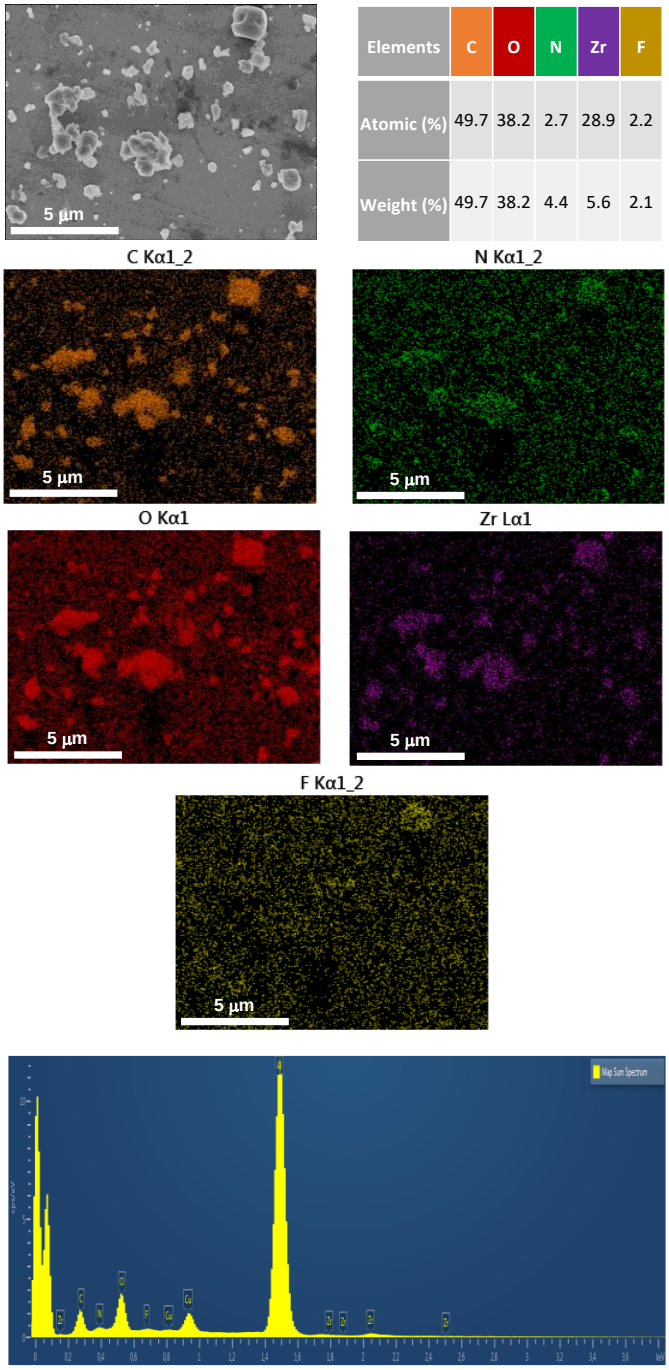

Elements	C	O	N	Zr	F
Atomic (%)	49.7	38.2	2.7	28.9	2.2
Weight (%)	49.7	38.2	4.4	5.6	2.1

Figure S24. SEM-EDX of modulated UiO-66(Zr)-$NO_{2;}$

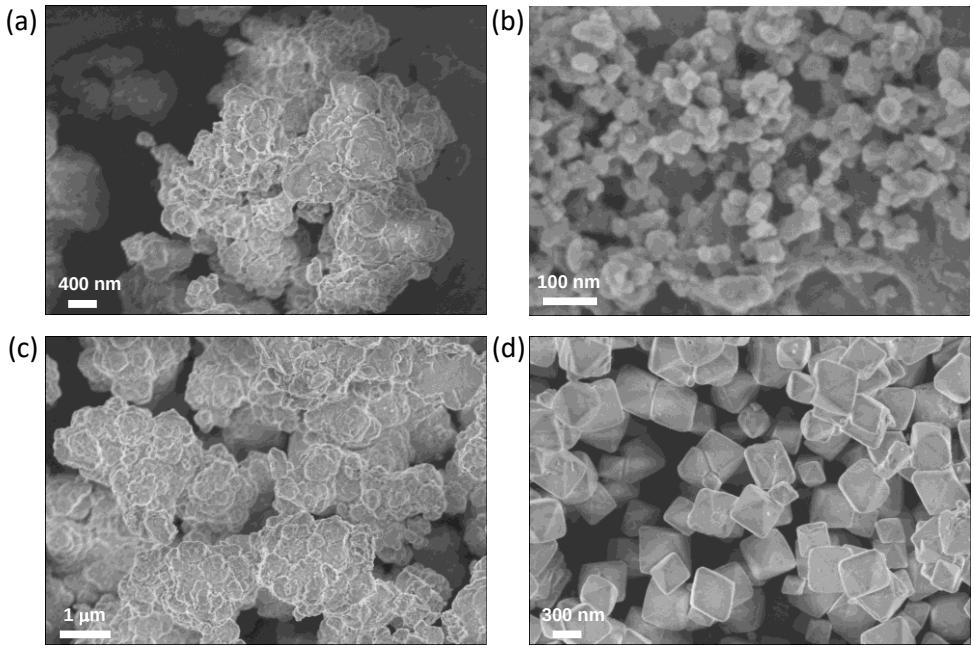

Figure S25. SEM images of UiO-66(Zr)-NH_2 solids prepared in the absence (a) or in the presence of 12 (b), 36 (c) or 100 (d) equivalents of AA as modulator.

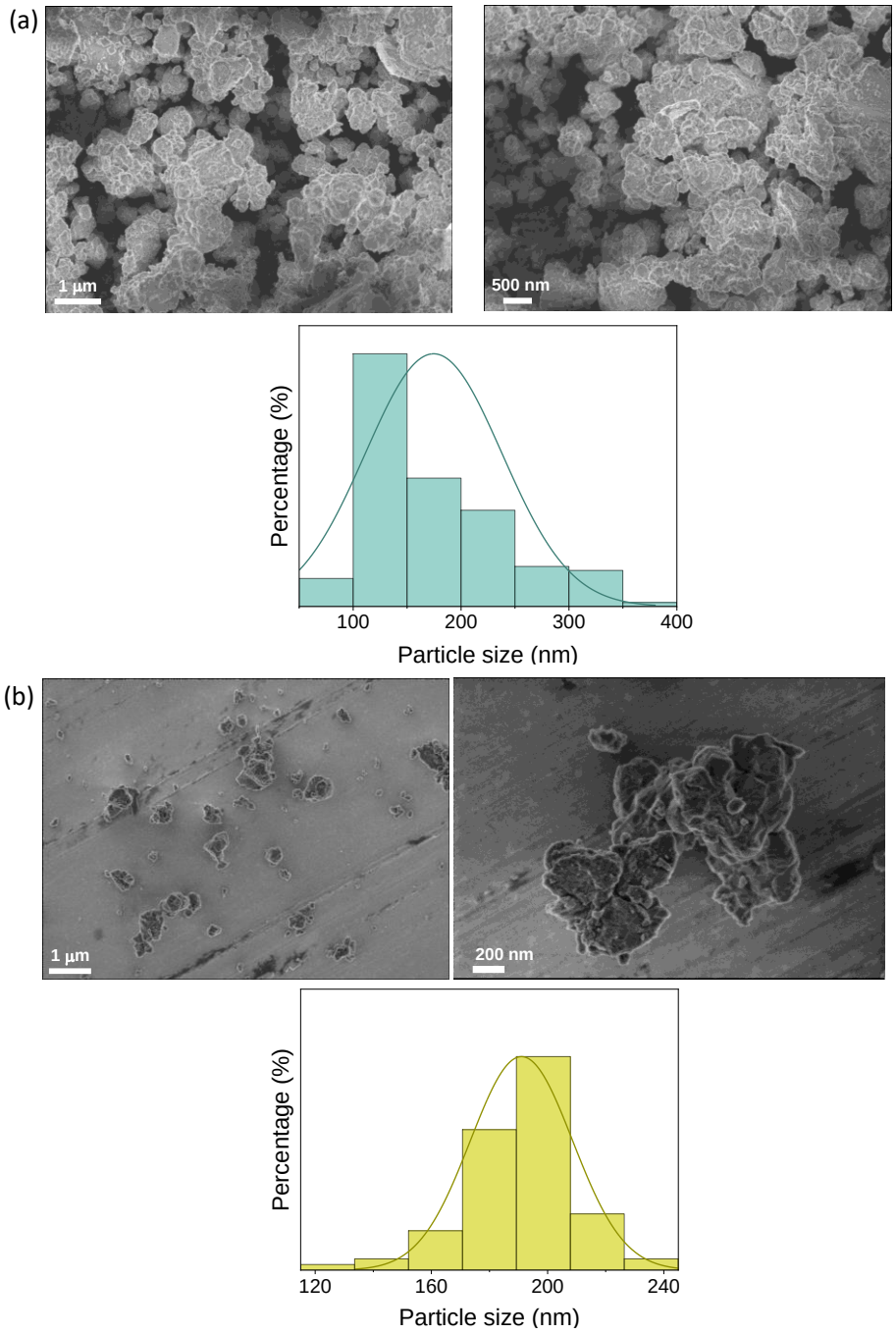

Figure S26. SEM images and particle size distribution of UiO-66(Zr)-NH_2 solid prepared in the presence of 12 (a) and 36 (b) equivalents of TFA as modulator.

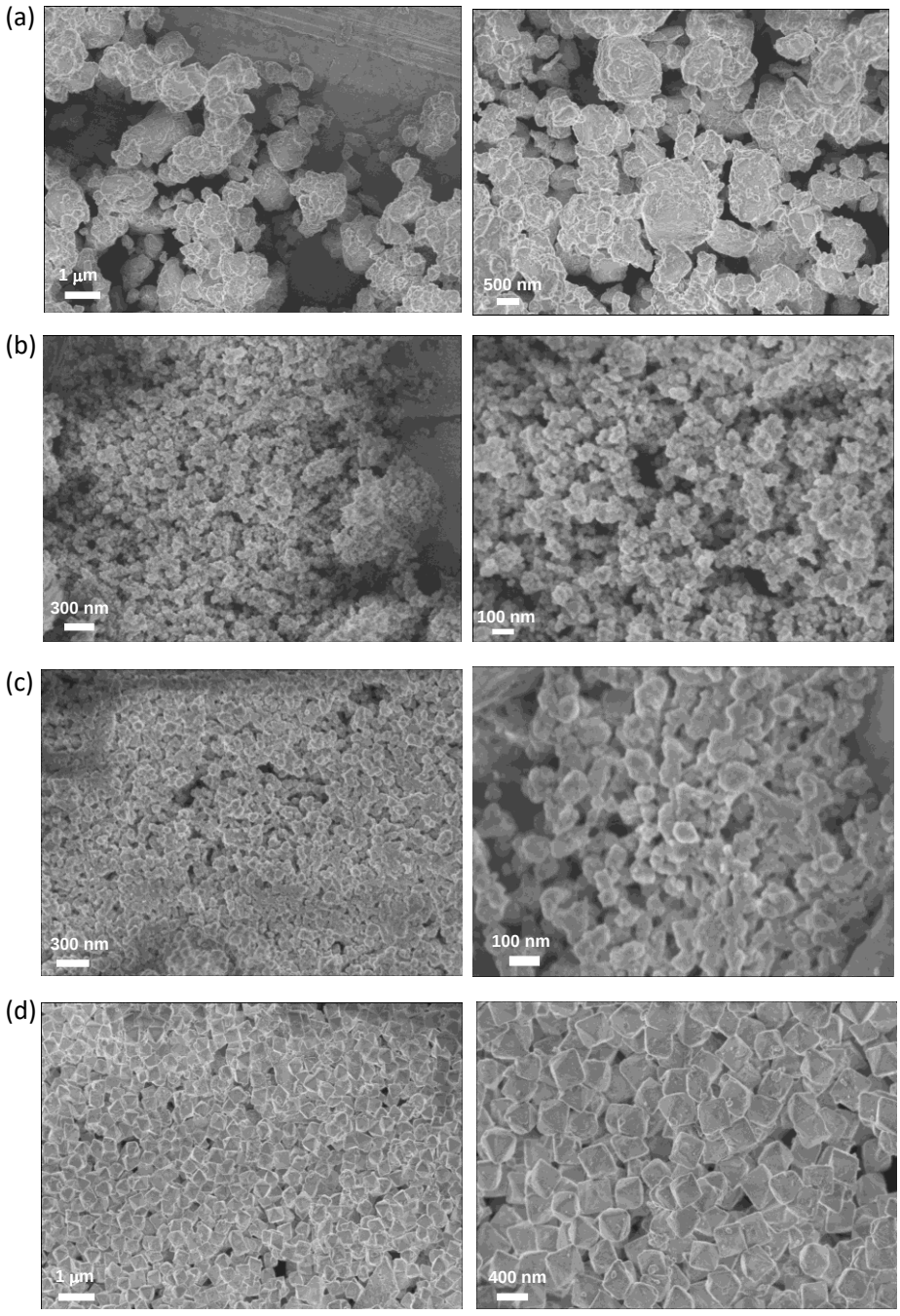

Figure S27. SEM images of UiO-66(Zr)-NO_2 solids prepared in the absence (a) or in the presence of 12 (b), 36 (c) or 100 (d) equivalents of AA as modulator.

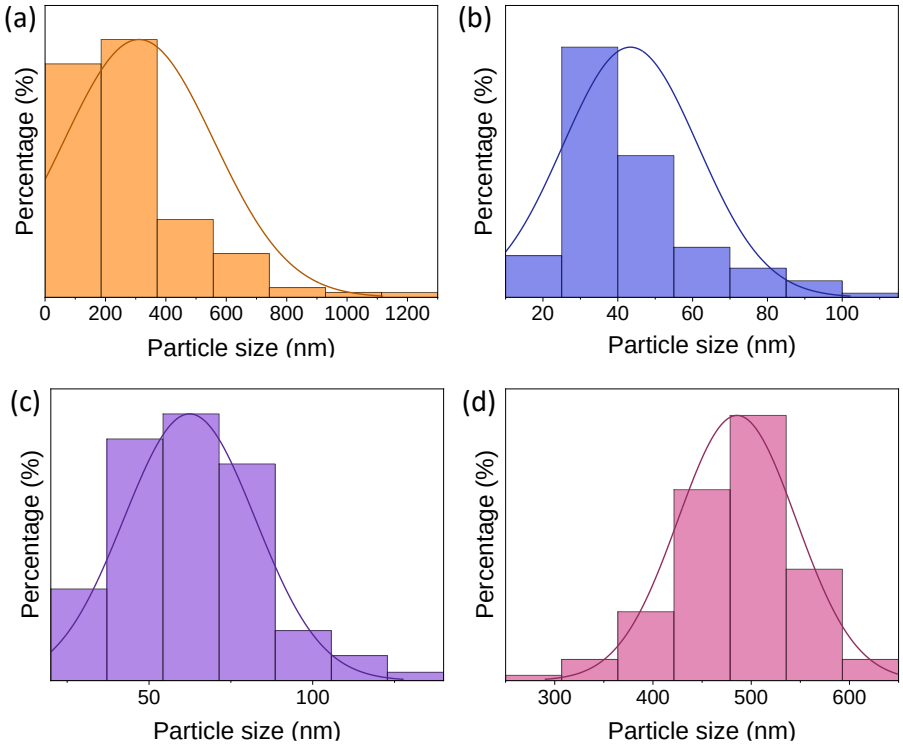

Figure S28. Particle size distribution of UiO-66(Zr)-NO_2 solids prepared in the absence (a) or in the presence of 12 (b), 36 (c) or 100 (d) equivalents of AA as modulator.

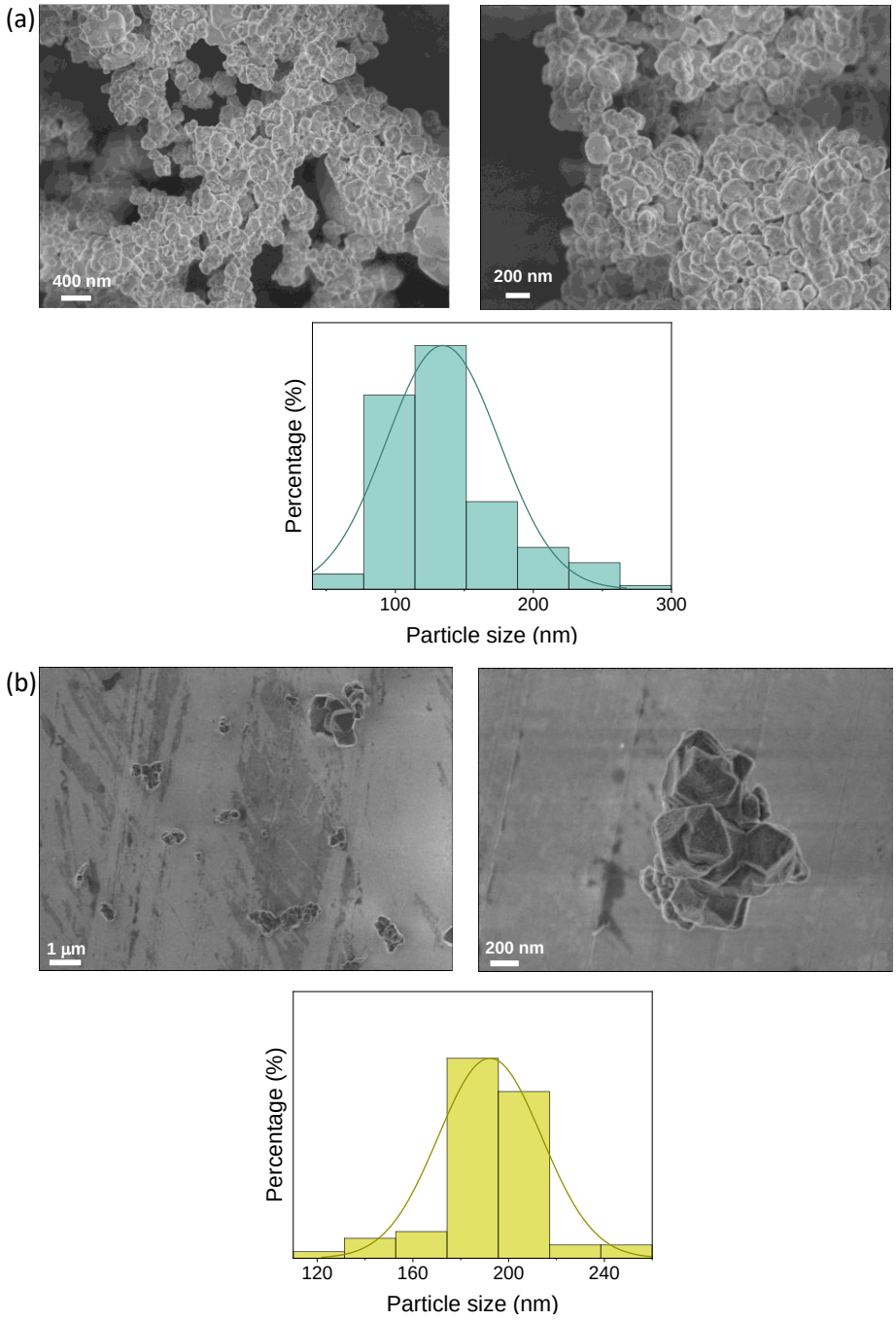

Figure S29. SEM images and particle size distribution of UiO-66(Zr)-NO_2 solid prepared in the presence of 12 (a) or 36 (b) equivalents of TFA as modulator.

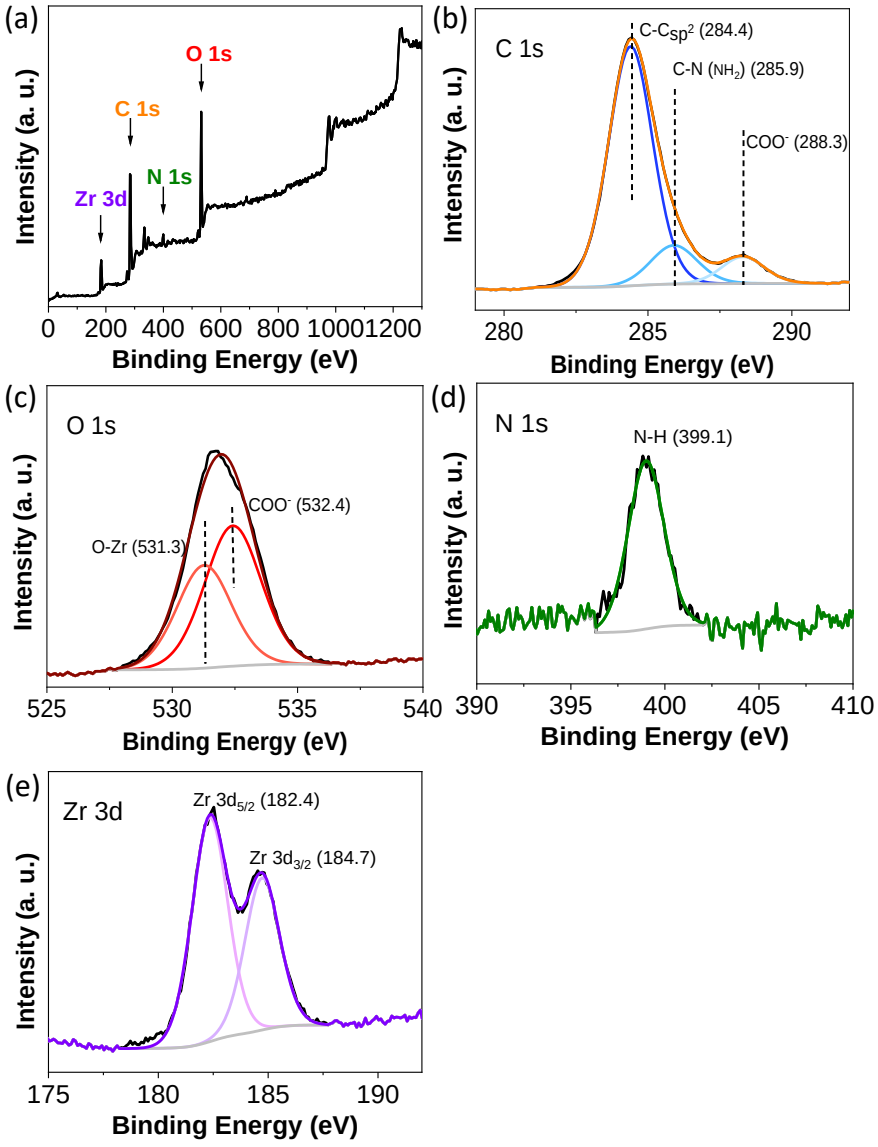

Figure S30. XPS Survey (a), C 1s (b), O 1s (c), N 1s (d) and Zr 3d (e) for UiO-66(Zr)-NH_2.

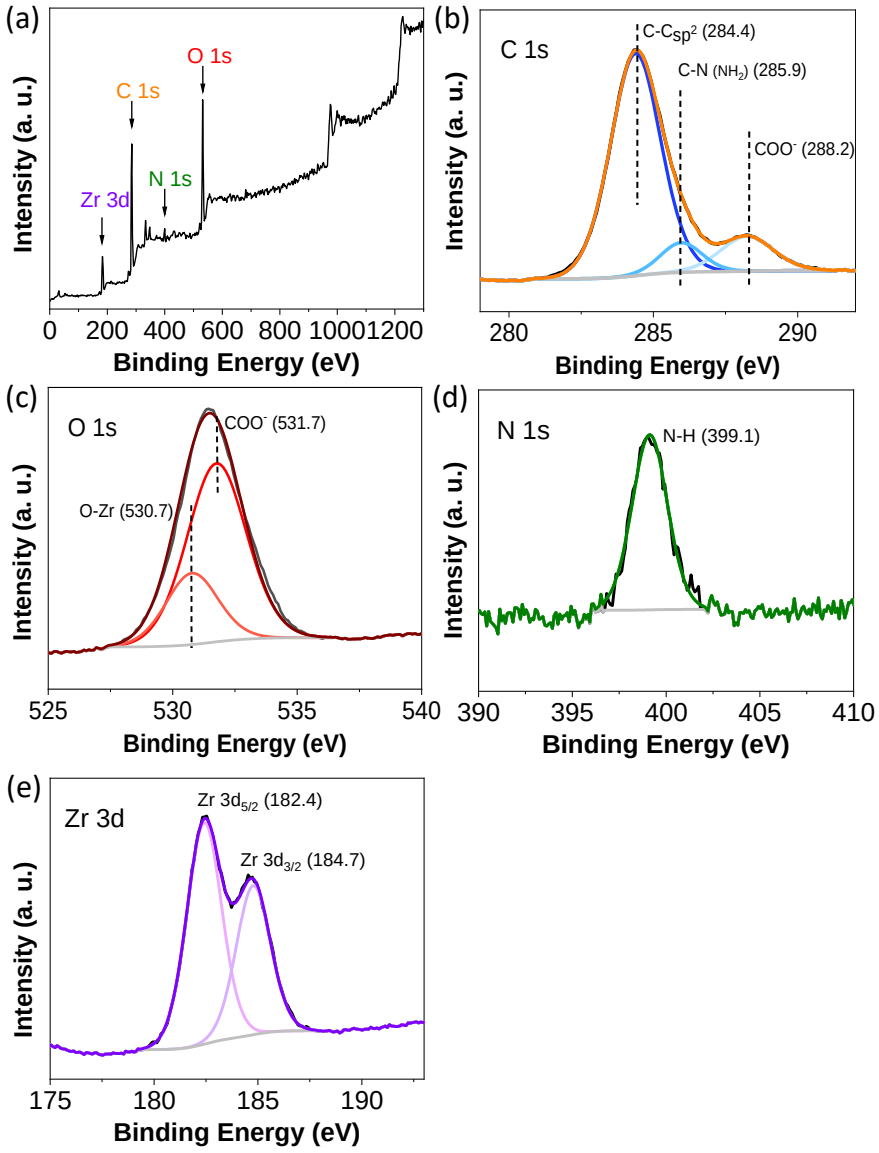

Figure S31. XPS Survey (a), C 1s (b), O 1s (c), N 1s (d) and Zr 3d (e) for UiO-66(Zr)-NH_2-12AA.

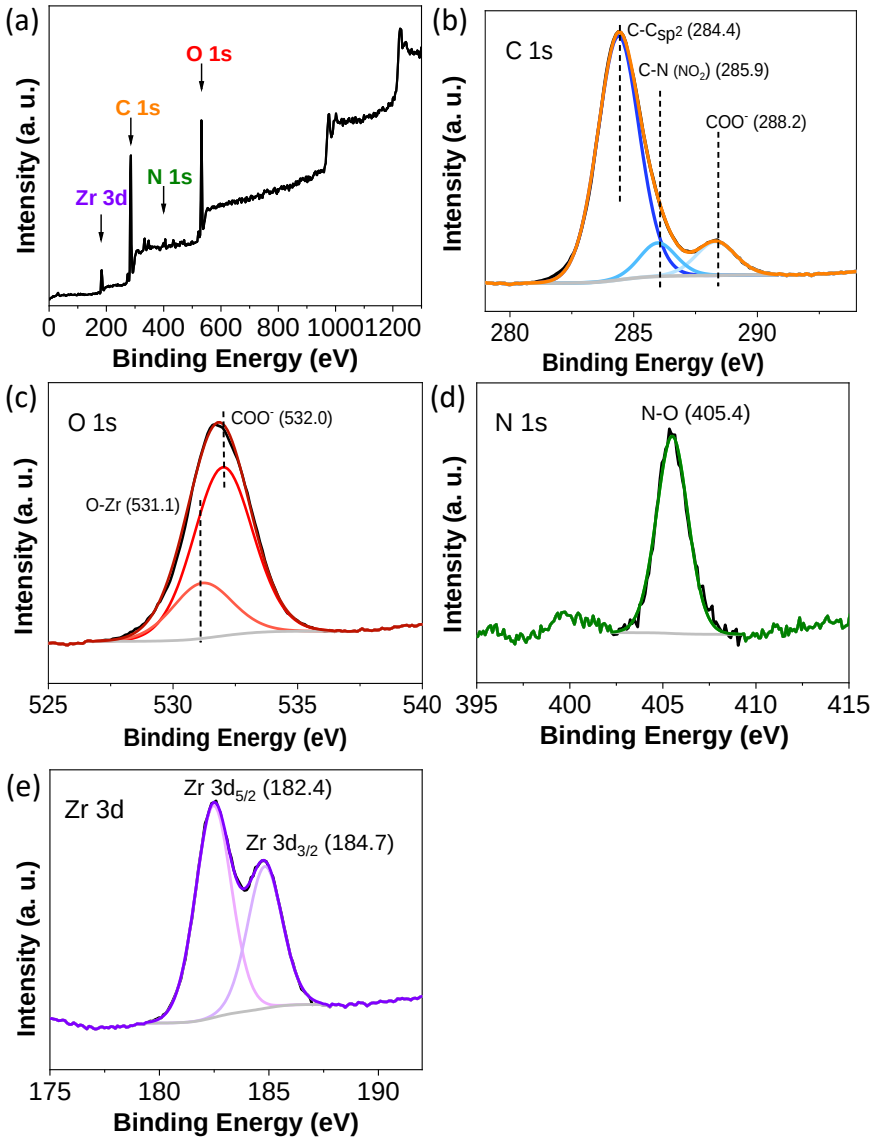

Figure S32. XPS Survey (a), C 1s (b), O 1s (c), N 1s (d) and Zr 3d (e) for UiO-66(Zr)-NO_2.

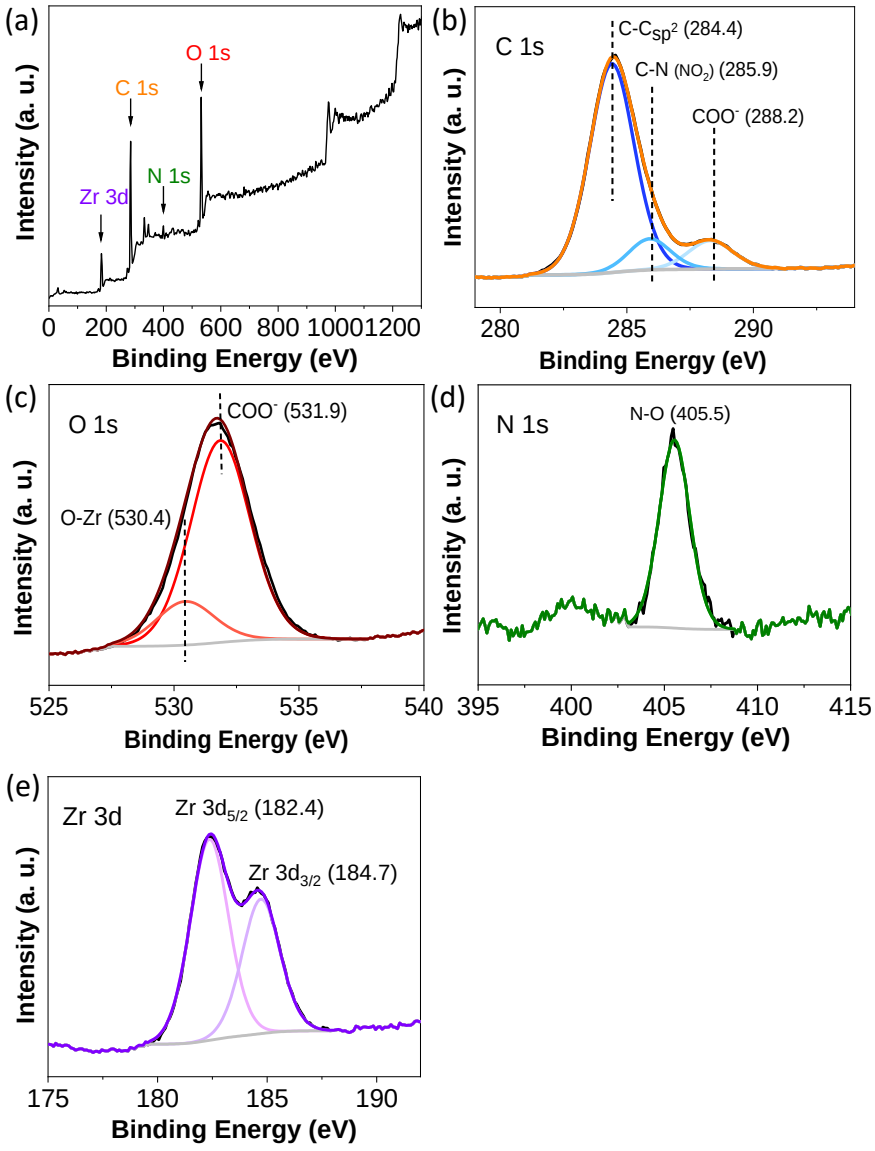

Figure S33. XPS Survey (a), C 1s (b), O 1s (c), N 1s (d) and Zr 3d (e) for UiO-66(Zr)-NO_2-12AA.

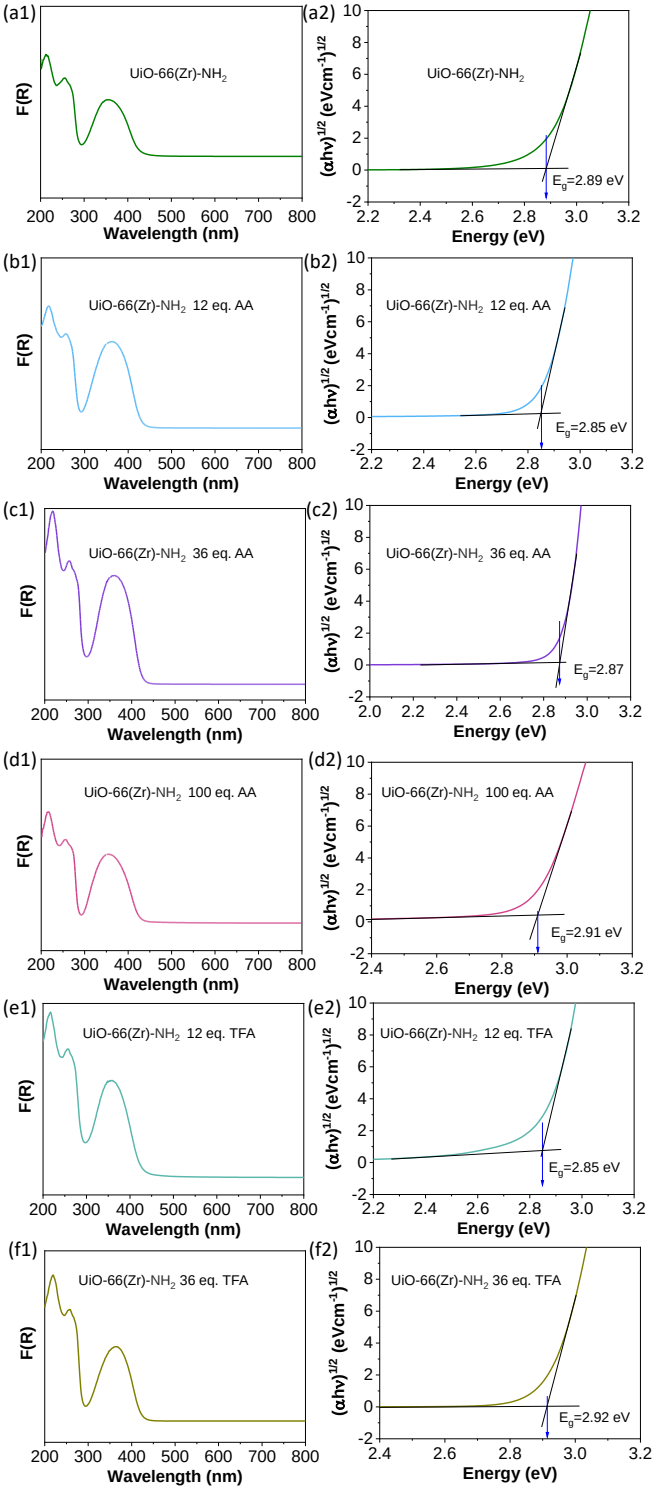

Figure S34. UV-Vis diffuse reflectance (left side) and Tauc plot (right side) of UiO-66(Zr)-NH_2 solids prepared in the absence (a1, a2) or in the presence of 12 (b1, b2), 36 (c1, c2) or 100 (d1, d2) equivalents of AA or 12 (e1, e2) or 36 (f1, f2) equivalents of TFA.

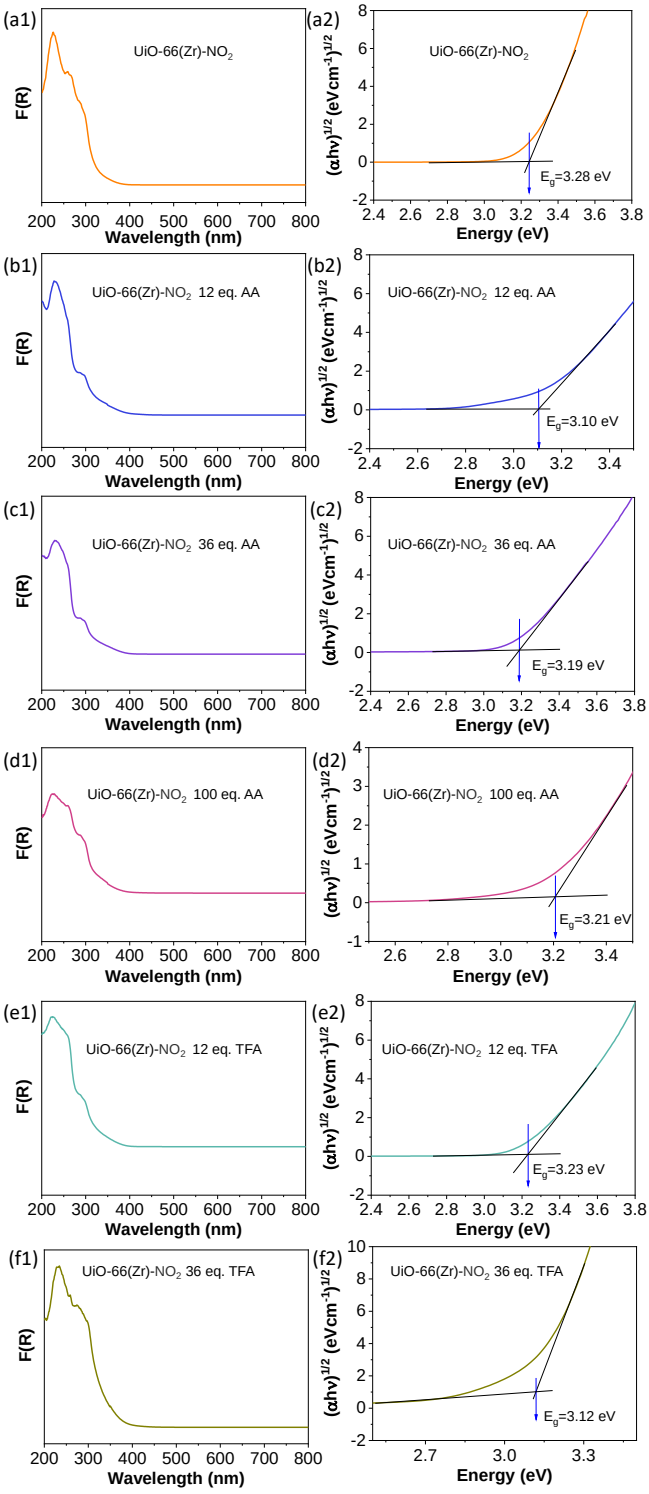

Figure S35. UV-Vis diffuse reflectance (left side) and Tauc plot (right side) of UiO- 66(Zr)-NO_2 solids prepared in the absence (a1, a2) or in the presence of 12 (b1, b2), 36 (c1, c2) or 100 (d1, d2) equivalents of AA or 12 (e1, e2) or 36 (f1, f2) equivalents of TFA.

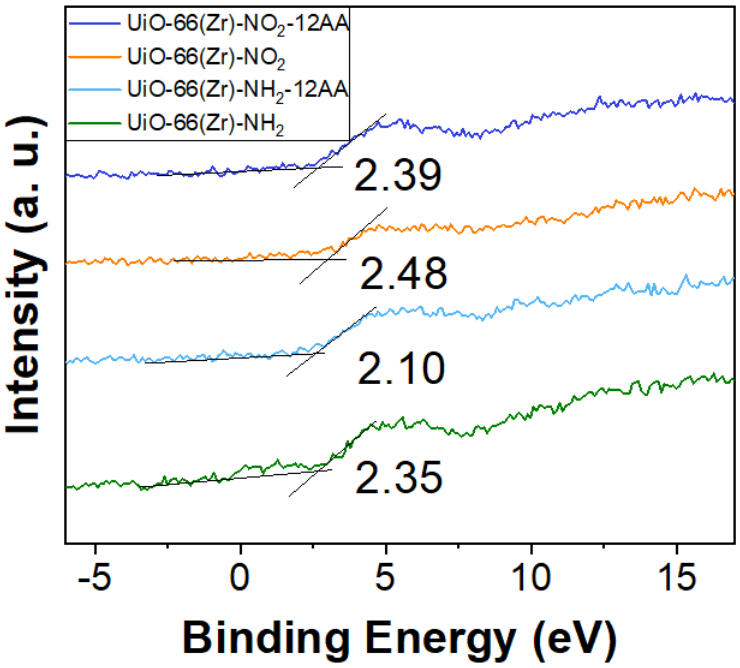

Figure S36. HOCO band XPS for UiO-66(Zr)-NH_2 (a), UiO-66(Zr)-NH_2-12AA (b), UiO- 66(Zr)-NO_2 (c) and UiO-66(Zr)-NO_2-12AA (d).

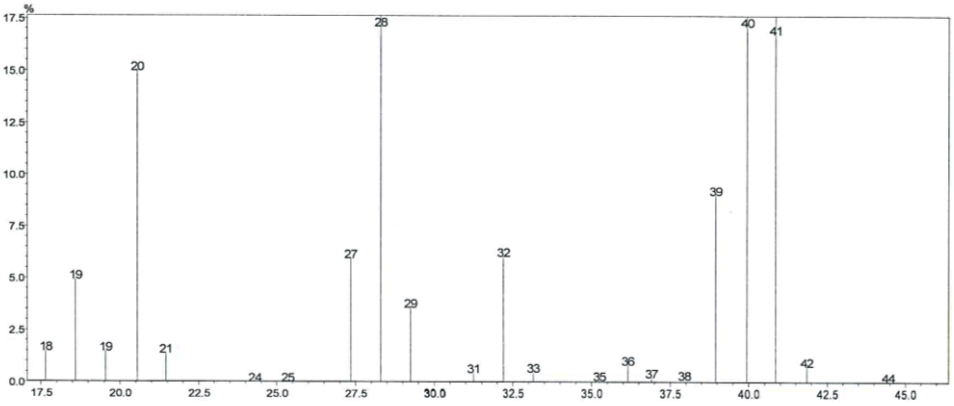

Figure S37. GC-MS obtained after the photocatalytic reaction using $H_2{}^{18}O$ and UiO-66(Zr)-NH_2-12AA.

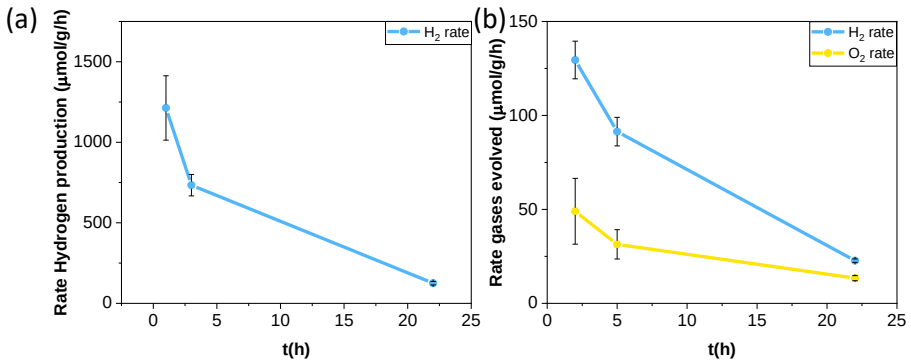

Figure S38. Gas reaction rate achieved during the photocatatytic HER (a) or OWS (b) using UiO-66(Zr)-NH_2-12AA. Data extracted from Figure 6a and 7c in the main text.

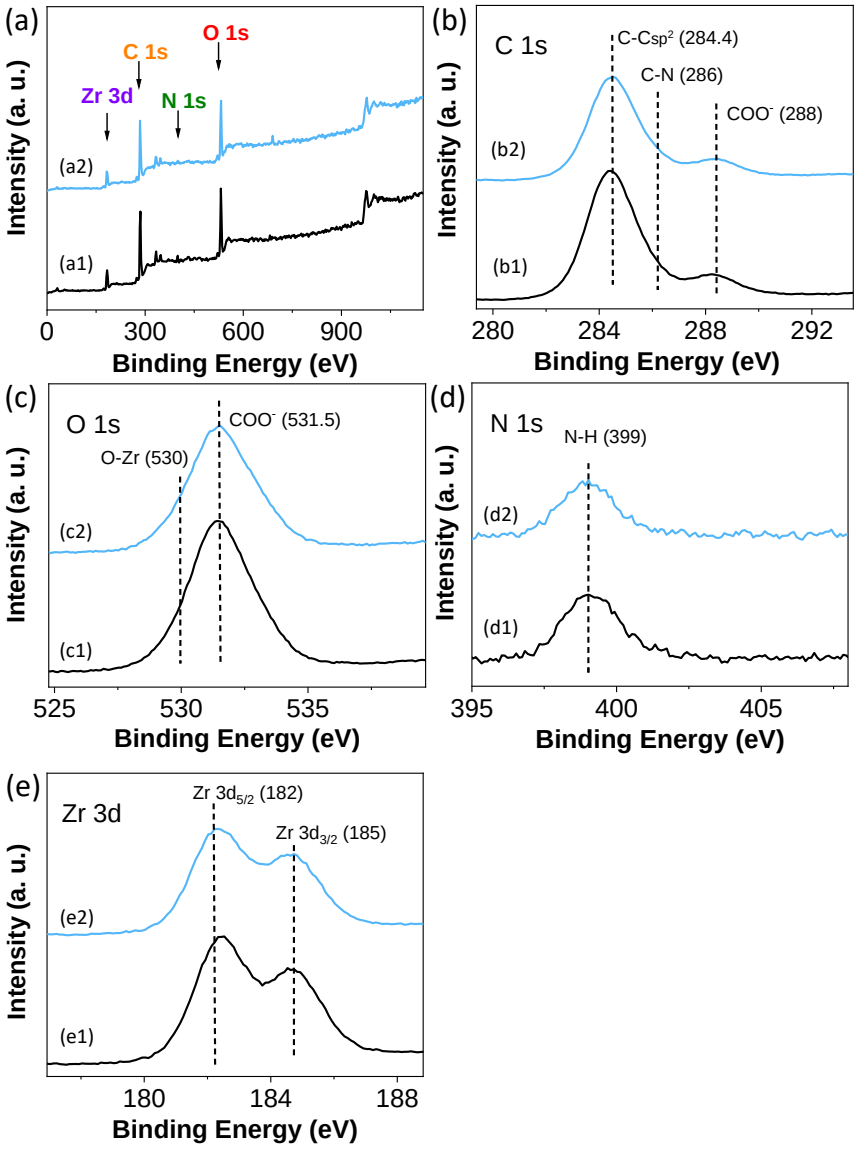

Figure S39. Comparison of XPS (a) survey, C 1s (b), O 1s (c), N 1s (d) and Zr 3d (e) for fresh (1, black) and used (2, blue) UiO-66(Zr)-NH_2-12AA after the photocatalytic OWS.

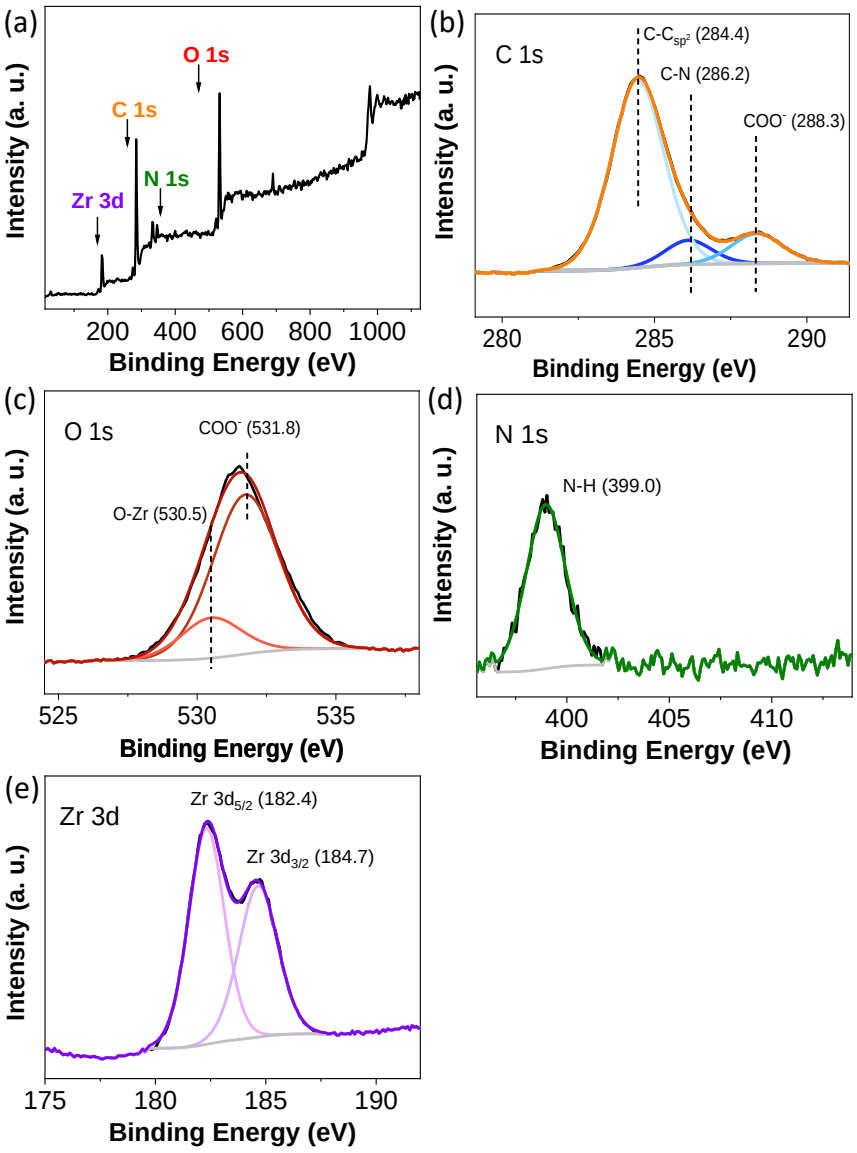

Figure S40. XPS Survey (a), C 1s (b), O 1s (c), N 1s (d) and Zr 3d (e) for UiO- 66(Zr)- NH_2-12AA sample after used as photocatalyst during the OWS.

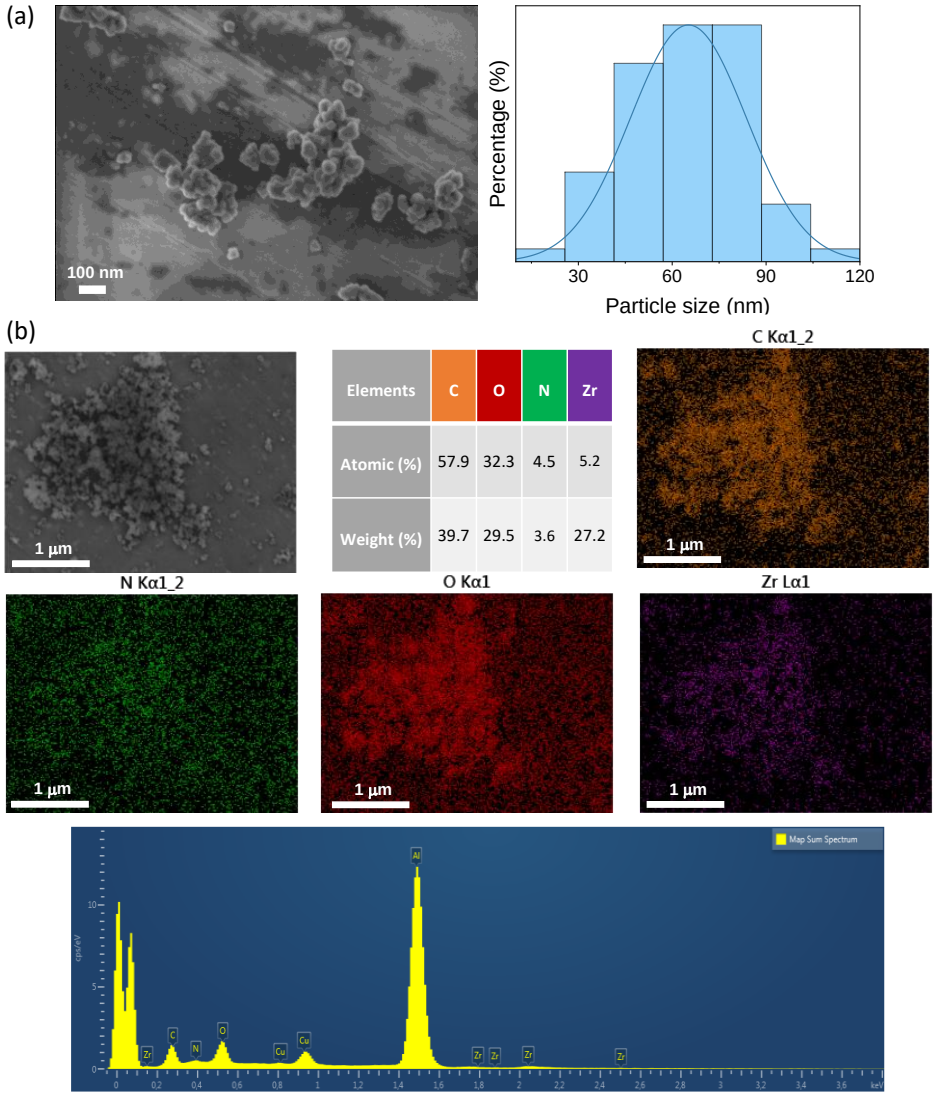

Figure S41. SEM image and particle size distribution (a) and SEM-EDX mapping (b) of UiO-66(Zr)-NH_2-12AA after used during the photocatalytic OWS. Note: Average particle size and standard deviation: 65 ± 18 nm.

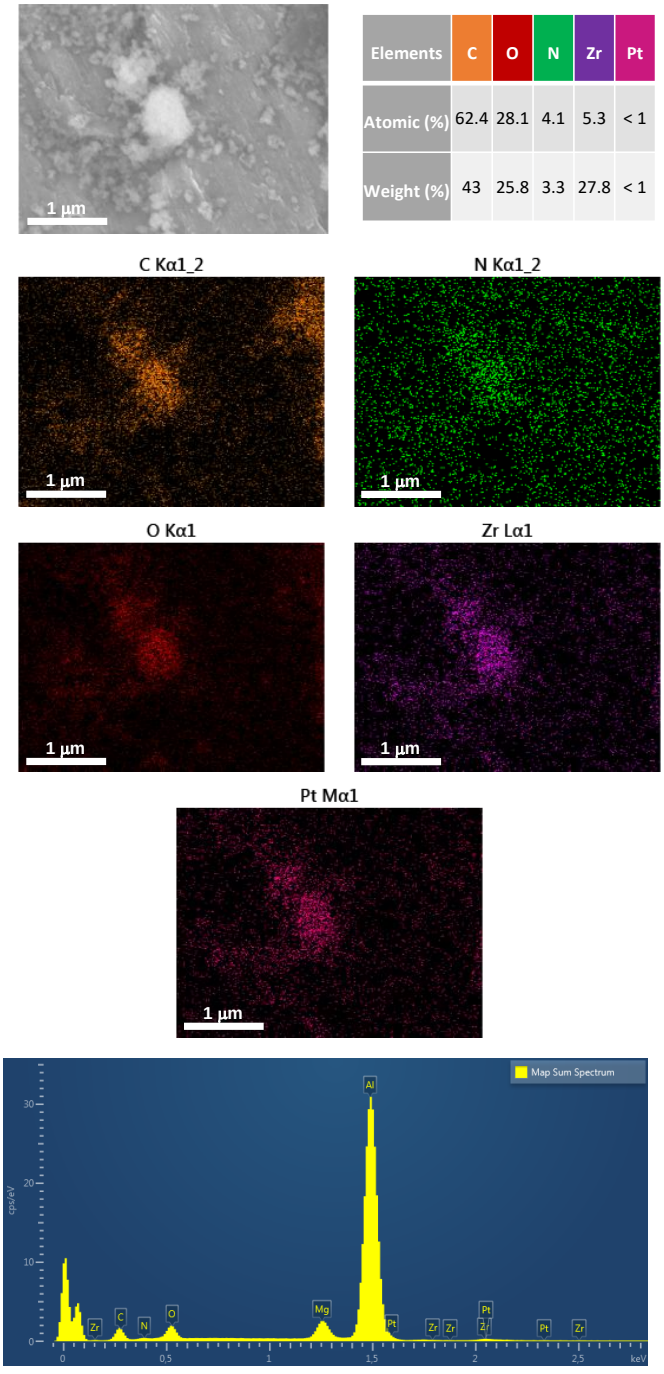

Figure S42. SEM-EDX of Pt@UiO-66(Zr)-NH_2-12AA.

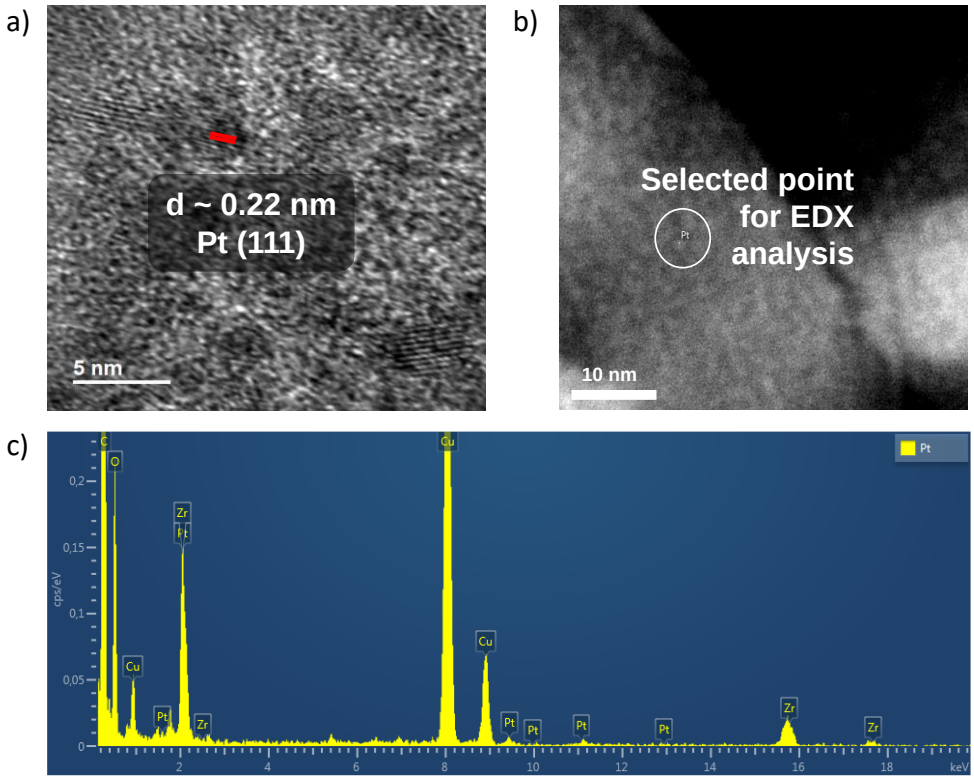

Figure S43. (a) HR-TEM and (b) DF-STEM images of Pt@UiO-66(Zr)-NH_2-12AA. Panel (c) shows the EDX spectrum from selected point in panel (b).

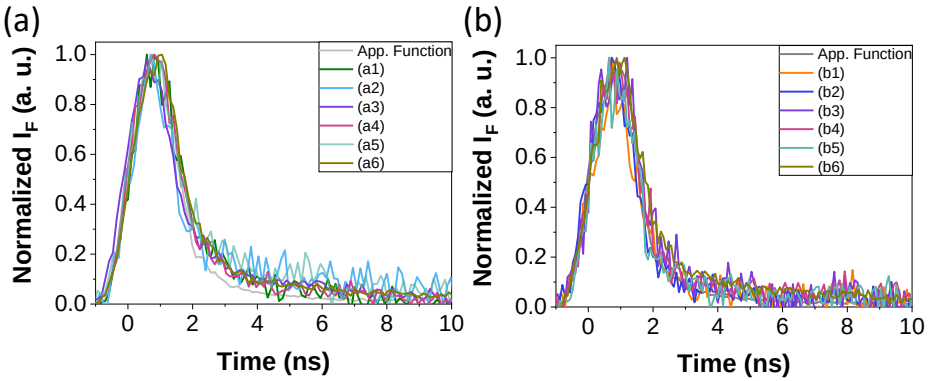

Figure S44. (a) Fluorescence decay traces for UiO-66(Zr)-NH_2 solids prepared in the absence (a1) or in the presence of 12 (a2), 36 (a3), 100 (a4) eq. of AA or 12 (a5) and 36 (a6) eq. of TFA. (b) Fluorescence decay traces for UiO-66(Zr)-NO_2 solids prepared in the absence (b1) or in the presence of 12 (b2), 36 (b3), 100 (b4) eq. of AA or 12 (b5) and 36 (b6) eq. of TFA. The apparatus function is shown in grey. All measurements were performed in deaerated acetonitrile at λ_{exc} = 265 nm.

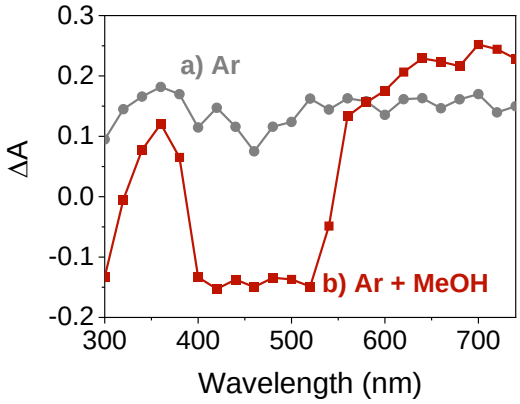

Figure S45. (a) TAS spectra of Pt NPs supported UiO-66(Zr)-NH_2-12AA suspensions in acetonitrile under Ar atmosphere in the absence (grey circles) or in the presence (dark red squares) of CH_3OH.

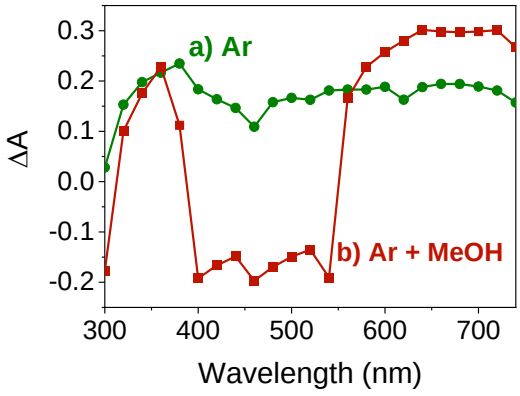

Figure S46. (a) TAS spectra of non-modulated UiO-66(Zr)-NH_2 suspensions in acetonitrile under Ar atmosphere in the absence (green circles) or in the presence (dark red squares) of CH_3OH.

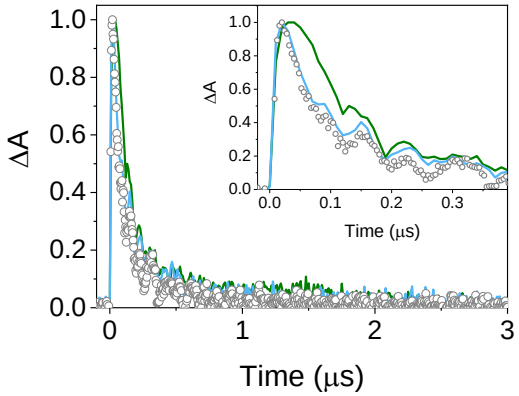

Figure S47. Absorbance transition decay of Pt@UiO-66(Zr)-NH_2-12AA (grey open circles), UiO-66(Zr)-NH_2-12AA (blue line) and non-modulated UiO-66(Zr)-NH_2 (green line) after excitation at 266 nm and recorded 680 nm.

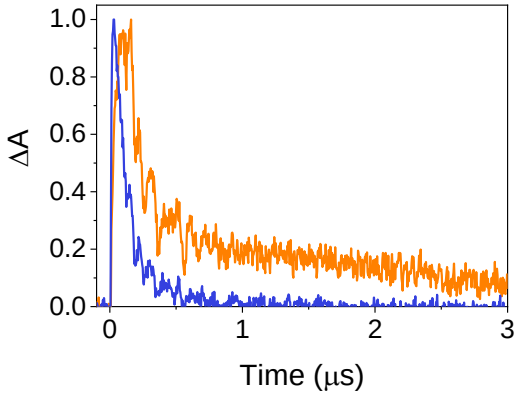

Figure S48. Absorbance transition decay of UiO-66(Zr)-NO_2-12AA (dark blue line) and non-modulated UiO-66(Zr)-NO_2 (orange line) after excitation at 266 nm and recorded 680 nm.

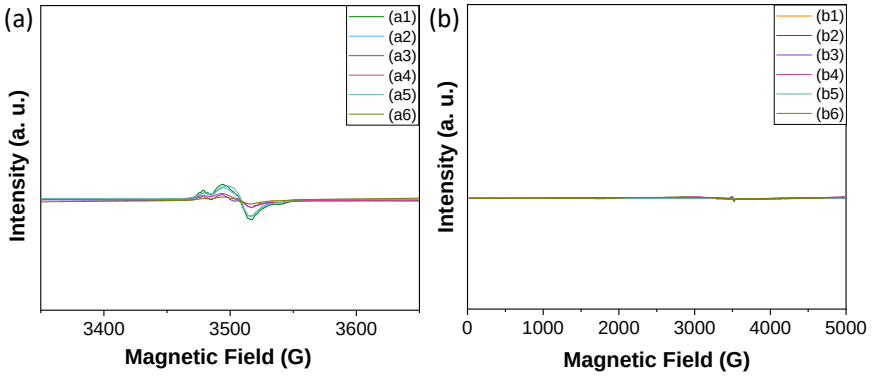

Figure S49. Solid-state EPR spectra of UiO-66(Zr)-NH_2 (a) and UiO-66(Zr)-NO_2 (b) samples as indicated.

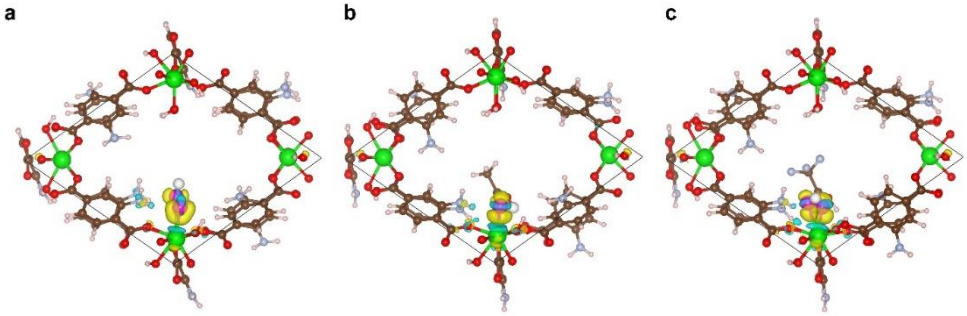

Figure S50. Calculated charge density difference between OOH^* and Zr metal site for (a) UiO-66(Zr)-NH_2, (b) UiO-66(Zr)-NH_2, and (c) UiO-66(Zr)-NH_2-TFA, respectively. The electron accumulation/decomposition isodensity surfaces with ±0.005 *e* $Å^{-3}$ are shown in yellow/blue (positive/negative density) respectively. The color code is the same as used in the main text (Figure 13c).

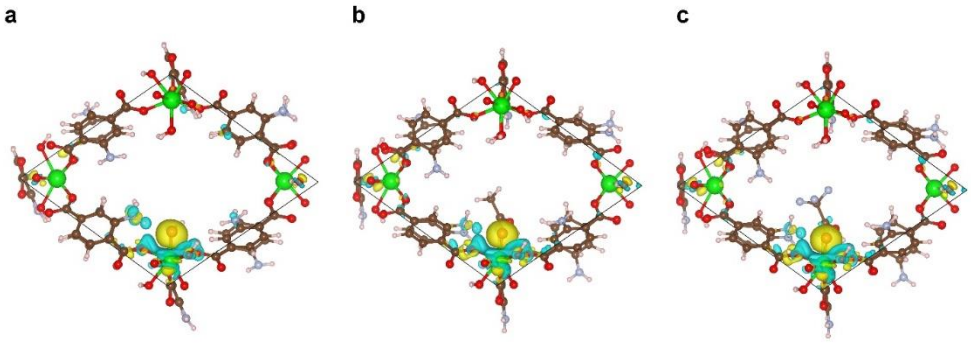

Figure S51. Calculated charge density difference between H^* and Zr metal site for (a) UiO-66(Zr)-NH_2, (b) UiO-66(Zr)-NH_2, and (c) UiO-66(Zr)-NH_2-TFA, respectively. The electron accumulation/ decomposition isodensity surfaces with ±0.002 *e* $Å^{-3}$ are shown in yellow/blue (positive/negative density) respectively. The color code is the same as used in the main text (Figure 13c).

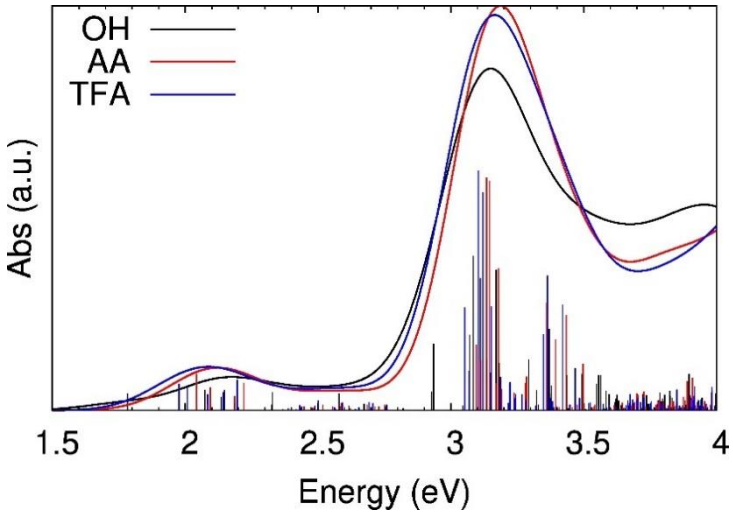

Figure S52. TD-DFPT Simulated absorption spectra for the OH (black), AA (red) and TFA (blue) periodic structures. Vertical bars represent the intensity of the transitions conforming the spectra. The excited state properties for the main vertical transition composing these spectra are collected in Table S5.

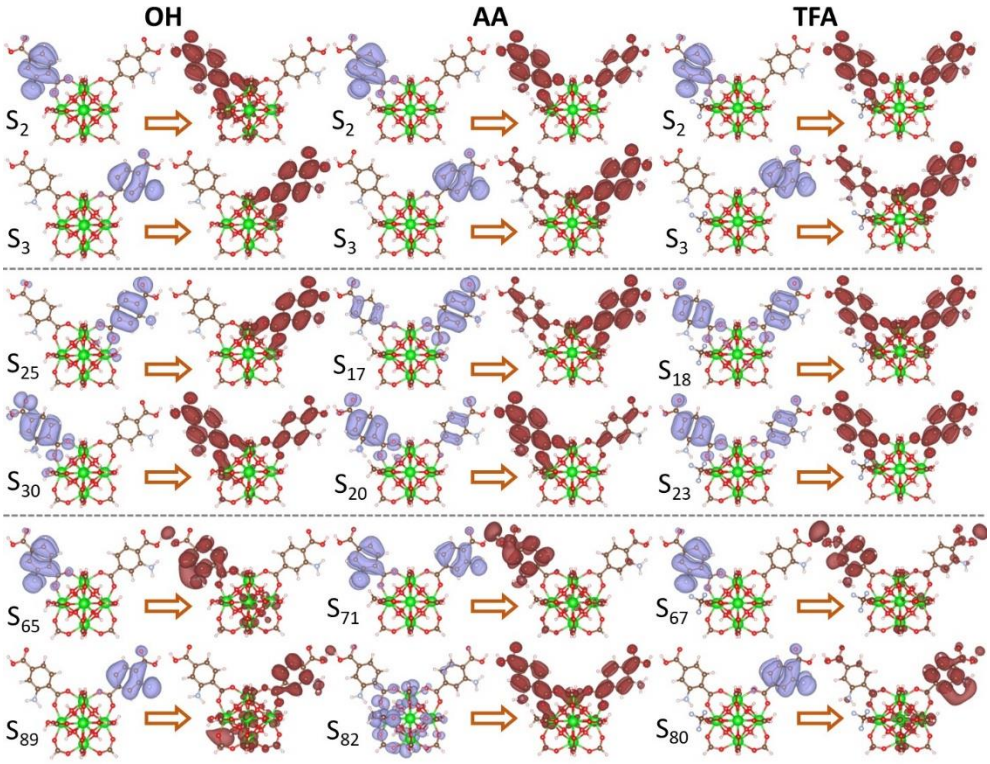

Figure S53. Natural Transition Orbitals (NTOs) shapes for the occupied/virtual (purple/red) states of the OH, AA, and TFA cluster models, whose characteristics are summarized in Table S6. The isovalue used for the isodensity plots was set to 0.02 a.u.

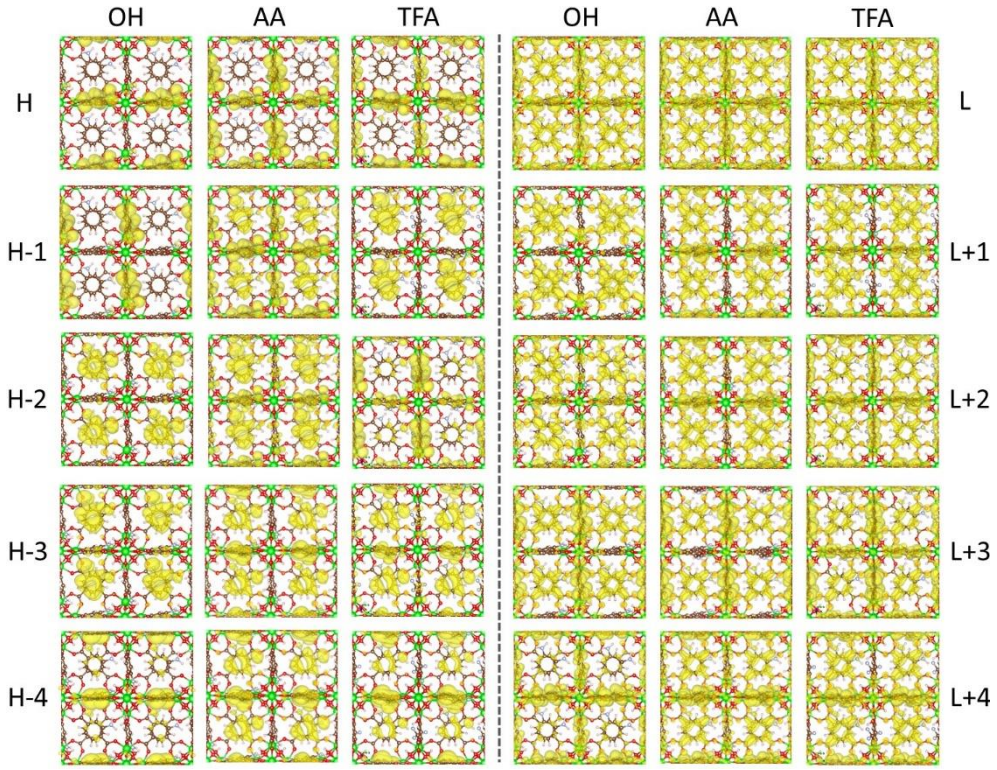

Figure S54. Crystal orbital isodensity plots for the five highest/lowest (right/left) occupied/unoccupied energy levels of the periodic OH, AA, and TFA structures (from the right to the left). The isovalue used for the isodensity plots was set to 0.02 a.u.

Table S2. Photocatalytic overall water splitting using MOF-based materials under visible or simulated sunlight irradiation.

	Reaction conditions	**H_2 and O_2 production**	**AQY (%)**	**Ref**
UiO-66(Zr)-NH_2-12AA	Photocatalyst (10 mg), H_2O (20 mL), simulated sunlight irradiation (Hg−Xe lamp 150 W equipped with an AM 1.5G filter), and 35 °C	450 and 160 μmol g^{-1} in 5 h	0.13, 0.06 and 0.04 % at 350, 400 and 450, respectively	This work
UiO-66(Zr)-$NH_{2(core)}$@UiO-66(Ce)$_{(shell)}$	Photocatalyst (10 mg), H_2O (20 mL), simulated sunlight irradiation (Hg−Xe lamp 150 W equipped with an AM 1.5G filter), and 35 °C	375 and 170 μmol g^{-1} in 22 h	0.034% at 400 nm	25
UiO-66(Ce)-NH_2 with Pt NPs (1 wt%) as co- catalyst	Photocatalyst (20 mg), H_2O (20 mL), simulated sunlight irradiation (150 W Hg-Xe lamp equipped with an AM 1.5G filter), 35 °C	208 and 80 μmol g^{-1} in 22 h	-	26
UiO-66(Zr)-NH_2 with Pt and MnO_x NPs as co- catalyst	Photocatalyst (10 mg), H_2O (100 mL), 5 °C, irradiation source (Xe lamp λ > 400 nm)	19.6 and 10.1 μmol g^{-1} h^{-1}	-	27
UiO-66(Zr/Ce/Ti)	Photocatalyst (20 mg), H_2O (20 mL), visible light irradiation (Hg-Xe lamp 150 W with a l> 450 nm cut-off filter)	210 and 70 μmol g^{-1} in 22 h	-	28
MIL-125(Ti)-NH_2 treated with oxygen- plasma	Photocatalyst (20 mg), H_2O (20 mL), 35 °C, solar simulator (1 sun)	83 and 29 μmol g^{-1} in 22 h	-	29
Ti-MOF: IEF-11	Photocatalyst (10 mg), H_2O (20 mL), simulated sunlight irradiation (Xe_Hg lamp 150 W, 1.5 AM filter), 35 °C	260 and 107 μmol g^{-1} in 22 h	-	30
Ni-MOF: IEF-13	Photocatalyst (5 mg), H_2O (20 mL), simulated sunlight irradiation (solar simulator; Oriel, 1 sun) 20 °C	160 and 14 μmol g-1 in 22 h	-	31
Porphyrin-based MOF: Liposome- MOF built from Pt-porphyrin, $[Ru(2,2'\text{-bipyridine})_3]^{2+}$, and Ir-bipyridine catalytic centers.	Photocatalyst solution (10 mL) and redox relays [tetrachlorobenzoquinone/tetrachlorobenzohydrosemiquinone; Fe^{3+}/Fe^{2+}, H_2O (20 mL),LED light	836 and 418 μmol g^{-1} in 72 h	1.5 ± 1% at 436 nm	32
Porphyrin-based MOF: MIL-173(Zr/Ti)-40 (40 wt% of Ti content)	Photocatalyst (10 mg), H_2O (20 mL), simulated sunlight irradiation (Xe-Hg lamp 150 W, 1.5 AM filter), 35 °C	381 and 145 μmol g^{-1} in 22 h	0.11% at 450 nm	33
PMOF: PCN-222(Zn)	Photocatalyst (20 mg), H_2O (20 mL), simulated sunlight irradiation (1 sun), 22 h	~340 and ~30 μmol g^{-1} in 22 h	-	34

Table S3. Calculated model parameters for the simplified Randles equivalent circuit for the series of UiO-66 solids.

Material	**Solution resistance Rs (Ω)**	**Charge Transfer resistance Rct (Ω)**	**Double layer capacitance Cdl (mF)**
UiO-66(Zr)-NH_2	21.22	3540	$116.8 \cdot e^{-6}$
UiO-66(Zr)-NH_2 (Irradiated)	23.45	2042	$136.6 \cdot e^{-6}$
UiO-66(Zr)-NH_2-12AA	28.32	1803	$112.4 \cdot e^{-6}$
UiO-66(Zr)-NH_2-12AA (Irradiated)	28.03	1690	$158.4 \cdot e^{-6}$
UiO-66(Zr)-NH_2-36AA	13.93	2521	$118.9 \cdot e^{-6}$
UiO-66(Zr)-NH_2-100AA	16.74	2973	$107.8 \cdot e^{-6}$
UiO-66(Zr)-NH_2-12TFA	26.16	3059	$84.12 \cdot e^{-6}$
UiO-66(Zr)-NH_2-36TFA	26.19	3480	$84.86 \cdot e^{-6}$
UiO-66(Zr)-NO_2	15.60	3775	$141.5 \cdot e^{-6}$
UiO-66(Zr)-NO_2 (Irradiated)	17.75	3052	$128.3 \cdot e^{-6}$
UiO-66(Zr)-NO_2-12AA	19.02	2661	$156.3 \cdot e^{-6}$
UiO-66(Zr)-NO_2-12AA (Irradiated)	19.10	1324	$119.7 \cdot e^{-6}$
UiO-66(Zr)-NO_2-36AA	14.99	3210	$125.0 \cdot e^{-6}$
UiO-66(Zr)-NO_2-100AA	17.46	3255	$124.3 \cdot e^{-6}$
UiO-66(Zr)-NO_2-12TFA	17.46	3347	$94.71 \cdot e^{-6}$
UiO-66(Zr)-NO_2-36TFA	28.30	3427	$96.83 \cdot e^{-6}$

Table S4. LFP lifetimes and weight of each component obtained for the series of UiO-66 solids under study recorded at 680 nm. The mean lifetime (<t>) is also shown.

	t_1 (μs)	**P1 (%)**	**t_2 (μs)**	**P2 (%)**	**<t> (μs)**
UiO-66(Zr)-NH_2	0.093	90	1.59	10	0.142
UiO-66(Zr)-NH_2-12AA	0.069	83	0.52	17	0.133
Pt/UiO-66(Zr)-NH_2-12AA	0.044	71	0.21	29	0.1
UiO-66(Zr)-NO_2	0.178	90	3.41	10	0.362
UiO-66(Zr)-NO_2-12AA	0.096	93	0.65	7	0.112

Table S5. Main vertical excitation and Charge Transfer (CT) properties for the main states composing the three lowest energy absorption bands from the OH, AA and TFA cluster model spectra depicted in Figure 14a: state number (*n*), absorption wavelengths (λ) in nm, oscillator strengths (*f*), main occupied/virtual orbital transitions (o→v) with their correspondent weight coefficient (C_i) in parenthesis, hole/electron (h^+/e^-) fraction localized along the ligand and metal node fragments, participation ratio (PR) and CT coefficients.

					Ligand		*Metal*			
	n	λ(nm)	*f*	o→v (C_i)	h^+	e^-	h^+	e^-	PR	CT
OH	2	370	0.13	H→L+1 (0.70)	1.00	0.00	0.78	0.22	1.27	0.23
	3	362	0.10	H-1→L (0.70)	1.00	0.00	0.92	0.08	1.08	0.08
	25	265	0.29	H-3→L (0.55)	0.98	0.02	0.70	0.30	1.39	0.32
	30	261	0.16	H-2→L+1 (0.45)	0.96	0.04	0.76	0.24	1.33	0.27
	65	233	0.21	H→L+30 (0.31)	0.74	0.26	0.55	0.45	1.80	0.37
	89	223	0.20	H-1→L+17 (0.43)	0.95	0.05	0.51	0.49	1.56	0.51
AA	2	369	0.11	H→L+1 (0.70)	1.00	0.00	0.95	0.05	1.06	0.06
	3	360	0.09	H-1→L (0.70)	1.00	0.00	0.91	0.09	1.10	0.09
	17	264	0.18	H-2→L (0.44)	0.97	0.03	0.74	0.26	1.34	0.28
	20	260	0.20	H-3→L+1 (0.54)	0.97	0.03	0.80	0.20	1.26	0.22
	71	226	0.11	H→L+17 (0.34)	0.90	0.10	0.62	0.38	1.55	0.42
	82	223	0.11	H-16→L (0.32)	0.42	0.58	0.69	0.31	1.85	0.55
TFA	2	370	0.08	H→L+1 (0.70)	1.00	0.01	0.95	0.05	1.06	0.06
	3	358	0.08	H-1→L (0.69)	1.00	0.00	0.88	0.12	1.14	0.13
	18	265	0.11	H-3→L (0.40)	0.98	0.02	0.61	0.39	1.47	0.40
	23	260	0.18	H-3→L+1 (0.54)	0.98	0.02	0.84	0.16	1.20	0.17
	67	227	0.19	H→L+22 (0.31)	0.84	0.16	0.70	0.30	1.55	0.37
	80	220	0.19	H-1→L+21 (0.43)	0.90	0.10	0.60	0.40	1.57	0.43

Table S6. Main vertical transition properties for the main states composing the two lowest absorption energy bands from OH, AA and TFA periodic structure spectra depicted in Figure S53: state number (*n*) excitation energies (E_x) in eV, oscillator strengths (*f*) and main occupied/virtual orbital transitions (o→v) with their correspondent weight coefficient (C_i) in parenthesis.

OH				AA				TFA			
n	*Ex (eV)*	*f*	*o→v (Ci)*	*n*	*Ex (eV)*	*f*	*o→v (Ci)*	*n*	*Ex (eV)*	*f*	*o→v (Ci)*
1	1.78	0.02	H→L (0.99)	1	2.04	0.04	H→L (0.97)	1	1.98	0.03	H→L (0.97)
2	2.07	0.02	H-1→L (0.97)	3	2.09	0.03	H-2→L (0.97)	2	2.01	0.03	H-1→L (0.97)
5	2.15	0.02	H-3→L (0.91)	4	2.19	0.02	H-3→L (0.96)	4	2.14	0.02	H-3→L (0.97)
8	2.33	0.02	H-4→L (0.92)	5	2.22	0.03	H-4→L (0.96)	5	2.20	0.03	H-4→L (0.96)
24	3.08	0.17	H-2→L+1 (0.59)	23	3.13	0.25	H-2→L+2 (0.45)	23	3.10	0.26	H-2→L+3 (0.67)
25	3.11	0.14	H-1→L+3 (0.72)	24	3.15	0.25	H-3→L+4 (0.52)	24	3.12	0.24	H-3→L+1 (0.48)
28	3.17	0.15	H-4→L+2 (0.62)	26	3.18	0.16	H-4→L+1 (0.41)	26	3.18	0.11	H-4→L+1 (0.49)

4.8.4 References

(1) Cabrero-Antonino, M.; Ferrer, B.; Baldoví, H. G.; Navalón, S. Toward solar-driven photocatalytic CO_2 methanation under continuous flow operation using benchmark MIL-125(Ti)-NH_2 supported ruthenium nanoparticles. *Chem. Eng. J.* **2022**, *445*, 136426.

(2) Shearer, G. C.; Chavan, S.; Bordiga, S.; Svelle, S.; Olsbye, U.; Lillerud, K. P. Defect engineering: tuning the porosity and composition of the metal−organic framework UiO-66 via modulated synthesis. *Chem. Mater.* **2016**, *28*, 3749−3761.

(3) Kresse, G. J., D. From ultrasoft pseudopotentials to the projector augmented-wave method. *Phys. Rev. B - Condens. Matter Mater. Phys.* **1999**, *59*, 1758–1775.

(4) Blöchl, P. E. Projector Augmented-Wave Method. *Phys. Rev. B - Condens. Matter Mater. Phys.* **1994**, *50*, 17953–17979.

(5) Perdew, J. P. B., K.; Ernzerhof, M. Generalized gradient approximation made simple. *Phys. Rev. Lett.* **1996**, *77*, 3865–3868.

(6) Perdew, J. P. E., M.; Burke, K. Rationale for mixing exact exchange with density functional approximations. *J. Chem. Phys.* **1996**, *105*, 9982–9985.

(7) Pack, J. D. M., H. J. Special Points for Brillonin-Zone Integrations. . *Phys. Rev. B* **1976**, *16*, 1748–1749.

(8) Stefan, G. Semiempirical GGA-type density functional constructed with a long-range dispersion correction. . *J. Comput. Chem.* **2006**, *27*, 1787–1799.

(9) Mileo, P. G. M. C., K. H.; Chang, J. S.; Maurin, G. . Water adsorption fingerprinting of structural defects/capping functions in Zr-Fumarate MOFs: a hybrid computational-experimental approach. *Dalt. Trans.* **2021**, *50*, 1324–1333.

(10) Soares, C. V. L., A. A.; Maurin, G. Computational evaluation of the chemical warfare agents capture performances of robust MOFs. *Microporous Mesoporous Mater.* **2019**, *280*, 97–104.

(11) Nørskov, J. K. R., J.; Logadottir, A.; Lindqvist, L.; Kitchin, J. R.; Bligaard, T.; Jónsson, H. . Origin of the Overpotential for Oxygen Reduction at a Fuel-Cell Cathode. J. . *Phys. Chem. B* **2004**, *108*, 17886–17892.

(12) Wu, X.-P.; Gagliardi, L.; Truhlar, D. G. Cerium metal–organic framework for photocatalysis. *J. Am. Chem. Soc.* **2018**, *140*, 7904-7912.

(13) Heyd, J. S., G. E.; Ernzerhof, M. Hybrid functionals based on a screened coulomb potential. *J. Chem. Phys.* **2003**, *118*, 8207–8215.

(14) Krishnan, R. B., J. S.; Seeger, R.; Pople, J. A. Self-Consistent Molecular Orbital Methods. XX. A Basis Set for Correlated Wave Functions. *J. Chem. Phys.* **1980**, *72*, 650–654.

(15) Andrae, D. H., U.; Dolg, M.; Stoll, H.; Preuß, H. . Energy-Adjusted Ab Initio Pseudopotentials for the Second and Third Row Transition Elements. *Theor. Chim. Acta* **1990**, *77*, 123–141.

(16) Tomasi, J. M., B.; Cammi, R. Quantum Mechanical Continuum Solvation Models. . *Chem. Rev.* **2005**, *105*, 2999–3093.

(17) Plasser, F. T. A. A Toolbox for a Detailed and Automated Analysis of Electronic Excited State Computations. *J. Chem. Phys.* **2020**, *152*, 084108.

(18) Frisch, M. e.; Trucks, G.; Schlegel, H. B.; Scuseria, G.; Robb, M.; Cheeseman, J.; Scalmani, G.; Barone, V.; Petersson, G.; Nakatsuji, H. Gaussian 16. Gaussian, Inc. Wallingford, CT: **2016**.

(19) Iannuzzi, M. C., T.; Wallman, T.; Hutter, J. . Ground and excited state density functional calculations with the gaussian and augmented-plane-wave method. *Chimia (Aarau)* **2005**, *59*, 499–503.

(20) Hutter, J. I., M.; Schiffmann, F.; Vandevondele, J. Cp2k: Atomistic Simulations of Condensed Matter Systems. . *Wiley Interdiscip. Rev. Comput. Mol. Sci.* **2014**, *4*, 15–25.

(21) Syzgantseva, M. A. S., N. F.; Syzgantseva, O. A. Carrier lifetimes and recombination pathways in Metal-Organic Frameworks. *J. Phys. Chem. Lett.* **2019**, *10*, 5041–5046.

(22) Syzgantseva, M. A. S., N. F.; Syzgantseva, O. A. . Computing the Effect of Metal Substitution in Metal-Organic Frameworks on the Recombination Times of Charge Carriers. . *J. Phys. Chem. C* **2020**, *124*, 24372–24378.

(23) VandeVondele, J. H., J. Gaussian basis sets for accurate calculations on molecular systems in gas and condensed phases. *J. Chem. Phys.* **2007**, *127*,

(24) Goedecker, S. T., M. Separable dual-space gaussian pseudopotentials. *Phys. Rev. B - Condens. Matter Mater. Phys.* **1996**, *54*, 1703–1710.

(25) Melillo, A. C.-A., M.; Ferrer, B.; Dhakshinamoorthy, A.; Baldoví, H.G.; Navalón, S. . MOF-on-MOF composites with UiO-66-based materials as photocatalysts for the overall water splitting under sunlight Irradiation. *Energy Fuels* **2023**, *37*, 5457–5468.

(26) Dai, S. M.-L., E.; Tissot, A.; Baldoví, H. G.; García, H.; Navalón, S.; Serre, C. . Room temperature design of Ce(IV)-MOFs: from photocatalytic HER and OER to overall water splitting under simulated sunlight irradiation. *Chem. Sci.* **2023**, *14*, 3451–3461.

(27) Zhang, J. B., T.; Huang, H.; Yu, M.-H.; Fan, X.; Chang, Z.; Bu, X.-H. Metal-organic-framework-based photocatalysts optimized by spatially separated co-catalysts for overall water splitting. *Adv. Mater.* **2020**, *32*, 2004747.

(28) Melillo, A.; Cabrero-Antonino, M.; Navalón, S.; Alvaro, M.; Ferrer, B.; García, H. Enhancing visible light photocatalytic activity for overall water splitting in UiO-66 by controlling metal node composition. *Appl. Catal. B. Environ.* **2020**, *278*, 119345.

(29) Cabrero-Antonino, M.; Albero, J.; García-Vallés, C.; Álvaro, M.; Navalón, S.; García, H. Plasma-induced defects enhance the visible-light photocatalytic activity of MIL-125(Ti)-NH2 for overall water splitting. *Chem. Eur. J.* **2020**.

(30) Salcedo-Abraira, P.; Babaryk, A. A.; Montero-Lanzuel, E.; Contreras-Almengor, O. R.; Cabrero-Antonino, M.; Svensson Grape, E. S.; Willhammar, T.; Navalón, S.; Elkäim, E.; García, H.; et al. A novel porous Ti-squarate as efficient photocatalyst in the overall water splitting reaction under simulated sunlight irradiation. *Adv. Mater.* **2021**, *33*, 2106627.

(31) Salcedo-Abraira, P.; Vilela, S. M. F.; Babaryk, A. A.; Cabrero-Antonino, M.; Gregorio, P.; Salles, F.; Navalón, S.; García, H.; Horcajada, P. Nickel phosphonate MOF as efficient water splitting photocatalyst. *Nano Res.* **2021**, *14*, 450–457.

(32) Hu, H. W., Z.; Cao, L.; Zeng, L.; Zhang, C.; Lin, W.; Wang, C. . Metal-organic frameworks embedded in a liposome facilitate overall photocatalytic water splitting. *Nat. Chem.* **2021**, *13*, 358.

(33) Gikonyo, B. M.-L., E.; Baldovi, H.G.; De, S.; Journet, C.; Devic, T.; Guillou, N.; Tiana, D.; Navalon, S.; Fateeva, A. . Mixed-metal Zr/Ti MIL-173 porphyrinic metal-organic frameworks as efficient photocatalysts towards solar-driven overall water splitting. *J. Mater. Chem. A* **2022**, *10*, 24938-24950.

(34) Semerci, T. G. M., A.; Mutlu, Y.C.; Garcia, H. . Band alignment of PCN-222 via selection of the metal porphyrin linker for sunlight driven photocatalytic overall water splitting. *Catal. Today* **2022**, *22*, 113931.

Chapter 5. Solar gas-phase CO_2 hydrogenation by multifunctional UiO-66 photocatalysts

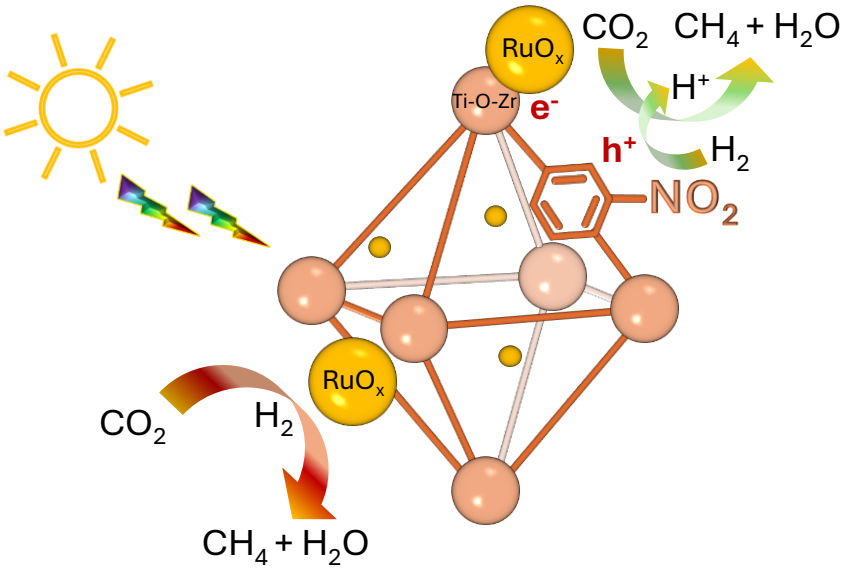

5.1 Abstract

Solar-assisted CO_2 conversion into fuels and chemical products involves a range of technologies aimed at driving industrial decarbonization methods. In this chapter it is shown the development of a series of multifunctional MOFs based on nitro- or amino-functionalized UiO-66(M) (M: Zr or Zr/Ti) supported RuO_x NPs as photocatalysts, having different energy band level diagrams, for CO_2 hydrogenation under simulated concentrated sunlight irradiation. RuO_x(1 wt %; 2.2 ± 0.9 nm)@UiO-66(Zr/Ti)-NO_2 was found to be a reusable photocatalyst and selective for CO_2 methanation (5.03 mmol g^{-1} after 22 h, AQY at 350, 400 and 600 nm of 1.67, 0.25 and 0.01%, respectively) and shows about 3-6 times activity compared with previous investigations. The photocatalysts were characterized by advanced spectroscopic techniques like femto- and nanosecond transient absorption, spin electron resonance and photoluminescence spectroscopies together with (photo)electrochemical measurements. The photocatalytic CO_2 methanation mechanism was assessed by *operando* FT-IR spectroscopy. The results indicate that the most active photocatalyst operates under a dual photochemical and photothermal mechanism. This investigation shows the potential of multifunctional MOFs as photocatalysts for solar-driven CO_2 recycling.

5.2 Introduction

The present level of burning fossil fuels to meet the world's energy requirements is steadily raising the CO_2 emissions released into the atmosphere and is responsible for global warming and climate change [1, 2]. There is thus an urgent need to shift from these fuels to renewable energy obtained from natural resources like the sun, wind, water or biomass[3, 4]. The development of

technologies based on carbon-free energy carriers like green H_2 is considered vital to help decarbonize the world's economies [5,6], while carbon capture, storage and utilization (CCSU) are some processes that can minimize the negative effects of CO_2 emissions [7, 8]. Even though certain CCSU processes have achieved relative success, most of the technologies used to convert CO_2 into valuable products or fuels are still under development [7-13], including solar- assisted photocatalysis, which is considered to be a promising cost- efficient and sustainable process for recycling CO_2 [14-19]. In 1978 a pioneering study reported on the possibility of reducing CO_2 using GaP as the photocatalyst[20]. Since then, many other inorganic semiconductors[18, 21-24] and more recently perovskites [23, 25], carbon-based materials similar to graphenes[23, 26, 27] or carbon nitrides[23, 28] among others [23, 29] have been used for this purpose. H_2 as the reducing agent seems to be more suitable for achieving better performance than H_2O[30]. Since it is expected that green H_2 will be economically feasible in the medium- and long-term, this innovation will boost the large scale production of compounds and fuels from CO_2 hydrogenation [31]. Of these, the photocatalytic solar-driven reduction of CO_2 by H_2 to CH_4, a process also termed as the photocatalytic Sabatier reaction, is attracting increasing interest for the transition to zero net emissions[32-34]. This process considerably improves the efficiency of the thermo-catalytic reaction even when working under mild reaction conditions[32]. For example, photocatalytic CO_2 methanation can be carried out at much lower reaction temperatures (~ 200 °C)[25] than the thermo-catalytic version (300-350 °C) while achieving similar results[25, 32]. The synthetic CH_4 thus obtained can then be directed to the existing natural gas infrastructures to minimize its implementation costs[33]. In less extent, other related studies have also shown the possibility of performing the photocatalytic CO_2[30] or CO[35] hydrogenation into C_{2+} and even C_{5+} value-added chemicals and fuels.

MOFs, a relatively new research field for a solar-driven photocatalytic Sabatier reaction, is now under development[36]. MOFs are porous crystalline materials built from multitopic organic ligands coordinated to metal ions, metal clusters or metal-oxo chains[37-39]. For about 20 years MOFs have been considered as highly tunable photocatalysts for many organic and inorganic reactions[31, 40-42]. In the field of CO_2 photoreduction, most of the knowledge achieved so far has come from the liquid-phase reaction using organic solvents in the presence of sacrificial electron donors under UV-Vis or visible light irradiation[40]. Acetonitrile is frequently used as a solvent to favor CO_2 dissolution, while TEOA is employed as the electron donor to recover photogenerated holes, minimize electron-hole recombination and thus increase the efficiency of the reduction process[40]. These studies on MOFs represent an interesting area of research in understanding the theoretical and practical aspects of CO_2 conversion.

A series of recent studies have reported on using MOFs as photocatalysts for gas-phase CO_2 reduction by H_2 under interesting reaction conditions for large scale processes. The possibility of using MOF-based materials for the photocatalytic gas-phase Sabatier reaction under UV-Vis at 215 °C [36] was reported for the first time in 2019. Since then, other studies have described a process with MOF-based photocatalysts modified with RuO_x NPs for solar-assisted CO_2 methanation at 200 °C. RuO_x NPs are the benchmark co-catalyst in achieving high efficiency during CO_2 (photo)methanation[32]. Some of these photocatalysts include Ti-MOFs, such as MIP-208(Ti)[43] or MIL-125(Ti)-NH_2[44] functionalized with NH_2 groups. The presence of amino groups determines the MOF energy band level, i.e. a band gap reduction and a negative shift of LUCO with respect to the non-functionalized parent MOF and favors the thermodynamics of the reduction processes[45, 46]. Other studies have reported that amino groups in MOFs favor the

stabilization of photogenerated holes and, in turn, the photoinduced charge separation efficiency[47, 48]. Amino-MOFs like UiO-66(Zr)-NH_2 have a higher CO_2 adsorption capacity than the analogous UiO-66(Zr)-NO_2 due to the bonding capacity of the amino groups[49]. Despite the research on the possibility of tuning the energy band diagram of MOFs with functional groups other than amino groups, such as nitro, bromo or methyl groups and their resulting photocatalytic activity, few studies have to date addressed its influence on photocatalytic CO_2 hydrogenation[45, 50, 51]. Other related studies have shown that mixed-metal MOFs involve higher photocatalytic activity in CO_2 reduction[45, 52]. For example, the better performance of the UiO-66(Zr/Ti)-based photocatalyst than UiO-66(Zr) is associated with the role of Ti(IV) as the electron mediator that favors photoinduced LMCT processes from the organic ligand to the metal node[52, 53]. Despite these important findings, as far as it is known, no studies have yet explored the possibility of developing multifunctional MOF-based materials with a unique energy band diagram determined by the presence of specific functional groups, e.g. the amino or nitro groups, simultaneously containing mixed-metal nodes for more effective photoinduced charge separation and co-catalysts to boost the solar-assisted photocatalytic Sabatier reaction.

In this context, it is reported here the development of multifunctional nitro- or amino functionalized Zr(IV)- or Zr(IV)/Ti(IV)-based-MOFs with a UiO-66 topology- supported RuO_x NPs for the solar-driven solid-gas phase Sabatier reaction. The materials were characterized by PXRD, analytical, spectroscopic and electron microscopy techniques and their photocatalytic activities were tested under simulated concentrated sunlight irradiation. Femto- and nanosecond TAS, PL, EPR and electrochemical impedance (EIS) spectroscopies together with transient photocurrent measurements and additional specific

photocatalytic experiments were used to determine the role of MOF counterparts during CO_2 photomethanation via a likely dual photochemical and photothermal mechanism. The photocatalytic CO_2 hydrogenation pathway was studied by *operando* FT-IR spectroscopy.

5.3 Experimental section

Details of the materials, preparation, characterization, and photocatalytic procedures used in the study can be found in the section 5.8 Supporting information (5.8.1 Synthesis of the MOF-based materials; 5.8.2. Characterization techniques; 5.8.3. Photocatalytic activity).

5.3.1 Materials, preparation methods and characterization

All the materials employed in this study were of analytical or HPLC grade and supplied by Merck. UiO-66(Zr)-NH_2 and UiO-66(Zr)-NO_2 were prepared according to previous procedures[54-56] and were post-synthetically modified by titanium(IV) chloride tetrahydrofuran complex [$TiCl_4(THF)_2$] to obtain UiO-66(Zr/Ti)-NH_2 and UiO-66(Zr/Ti)-NO_2 as reported[57, 58]. RuO_x NPs were supported on these four UiO-66 solids using the photodeposition method[44] described specifically in Section 5.8.1.

The solids were characterized by PXRD, UV-Vis DRS, XPS, EPR, steady-state PL, EIS, femto- and microsecond transient spectroscopies and electron microscopy, including such as TEM and SEM coupled with EDX detector. Isothermal N_2 adsorption, thermogravimetric and photoelectrochemical measurements were also used.

5.3.2 Photocatalytic activity

Photocatalytic reactions were carried out under batch reaction conditions (Section 5.8.3. Photocatalytic activity) and the data given are the average of at least three separate experiments.

5.4 Results and discussion

5.4.1 Photocatalyst characterization

The MOF-based materials prepared, i.e. UiO-66(M)-X (M: Zr and/or Ti; X: NH_2 or NO_2), both loaded or unloaded with RuO_x NPs, were characterized by different techniques. PXRD analyses revealed that these solids had the expected UiO-66 topology (Figure 1) [56]. The ICP-OES analyses of acid-digested MOFs were used to quantify the zirconium and/or titanium elements, either loaded or not loaded with RuO_x NPs at 1 wt% of ruthenium. UiO-66(Zr/Ti)-NH_2 and UiO-66(Zr/Ti)-NO_2 have a titanium content of 0.9 and 1.3 wt%, respectively. In this regard, previous studies reported that PSM of UiO-66(Zr) based materials with $TiCl_4(THF)_2$ complex results in the incorporation of Ti(IV) in the solid by metal exchange and/or grafting onto the metal node at the linker vacancy[59]. Partial replacement of Zr(IV) by Ti(IV) ions with smaller ionic radii contract the unit cell reflected in PXRD by a small negative shift of the position of the diffraction peaks. In the present work, UiO-66(Zr/Ti)-X (X: NH_2 or NO_2) solids showed similar PXRD peak positions to those in zirconium, indicating that Ti(IV) ions are mostly grafted onto the MOF metal nodes [57, 59]. The PXRD of UiO-66 solids loaded with RuO_x NPs have similar features to those of the parent MOFs. The absence of RuO_x diffraction peaks was attributed to the low ruthenium loading (1 wt%) in the MOF and/or good dispersion of small NPs [44].

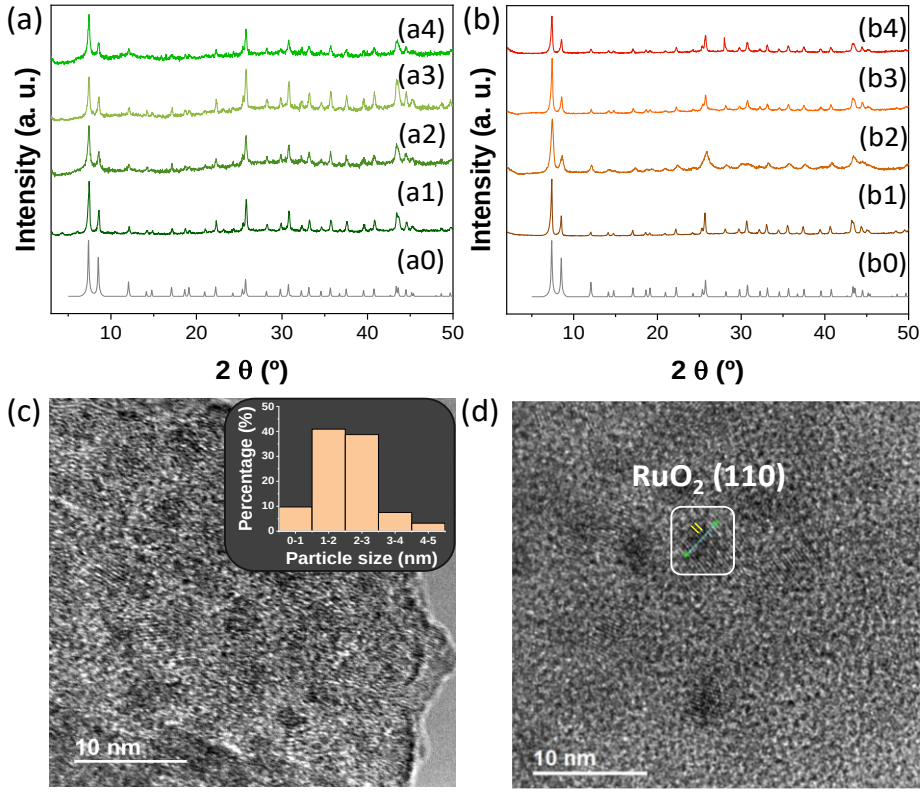

Figure 1. XRD of simulated UiO-66 (a0, b0) or PXRD of UiO-66(Zr)-NH_2 (a) or UiO-66(Zr)-NO_2 (b) materials. Legend panel (a): UiO-66(Zr)-NH_2 (a1), RuO_x@UiO-66(Zr)-NH_2 (a2), UiO-66(Zr/Ti)-NH_2 (a3), RuO_x@UiO-66(Zr/Ti)-NH_2 (a4). Legend panel (b): UiO-66(Zr)-NO_2 (b1), RuO_x@UiO-66(Zr)-NO_2 (b2), UiO-66(Zr/Ti)-NO_2 (b3), RuO_x@UiO-66(Zr/Ti)-NO_2 (b4). (c) HRTEM image and RuO_x particle size distribution of RuO_x@UiO-66(Zr/Ti)-NO_2; RuO_x average particle size and standard deviation of 2.08 ± 0.82 nm. (d) d-spacing is determined (0.32 nm) from HRTEM image of RuO_x@UiO-66(Zr/Ti)-NO_2.

The HR-SEM analyses showed that UiO-66 crystals are characterized by the agglomeration of small cubes with average particle sizes and standard deviations of 118 ± 57 nm (Figure S1). HR-SEM in combination with EDX analyses (Figures S2- S10) showed a good distribution of MOF elements within the particles. The relatively low intensity of ruthenium due to its low loading

(1 wt% Ru) was within the instrument's detection limit. DF-STEM coupled with EDX and HR-TEM measurements characterized RuO_x NPs (2.14 ± 0.86 nm) supported on UiO-66 particles. HRTEM measurements (Figures S11-S14) indicated the presence of 0.32 nm lattice spacings (Figure S15-S17), characteristic of (110) facet of RuO_2 [60].

The UiO-66 samples were also characterized by XPS (Figure 2 and Figures S18- S21) to determine the oxidation state of the elements within the solids. The XPS spectra of the C 1s region is associated with the presence of the 2- amino or 2-nitroterephthalates ligands of the MOFs: C-C sp^2 bonds (284.4 eV), COO^- groups (288 eV) and C-N bonds of amino or nitro (~285 eV) groups. The N 1s XPS of amino-functionalized UiO-66 solids shows the expected C-N signal at about 399 eV. In the case of nitro-functionalized UiO-66 materials, N 1s XPS spectra are dominated by a main band at 405 eV, due to the nitro group, while a signal associated with the presence of an amino group can also be detected. This situation, i.e. the presence of a small band assigned to the amino group when preparing nitro-functionalized UiO-66 solids, has previously been reported [51]. For the series of RuO_x NPs supported UiO-66 solids, the XPS Ru 3d spectra showed a weak band centered at about 282 eV (Figures S22 and S25), partially overlapping with C-C sp^2 bond signals (284.4 eV), which can be assigned to the presence of RuO_2 NPs [44]. Supported RuO_2 NPs were further characterized by Ru 3p XPS, where the expected two bands could be seen at about 462.5 and 485 eV characteristic of Ru $3p_{3/2}$ and Ru $3p_{1/2}$, respectively. The O 1s XPS signal was assigned to the presence of COO^- groups (532 eV) and M-O bonds (M: Zr, Ti or Ru) (530 eV). Zr 3d and Ti 2p XPS spectra showed the expected signals of Zr(IV) and Ti(IV) ions in the UiO-66 structure. Zr 3d XPS spectra had two bands centered at about 182 and 185 eV due to Zr $3d_{5/2}$ and Zr $3d_{3/2}$, respectively. The XPS spectra of the Ti 2p region

for mixed-metal UiO-66(Zr/Ti)-X (X: NH_2 or NO_2) confirmed the presence of Ti(IV) indicated by two bands at 459 and 464 eV due to Ti $2p_{3/2}$ and Ti $2p_{1/2}$, respectively.

The UiO-66 solids were analyzed by FT-IR spectroscopy (Figure S26). In all cases, COO^- groups were characterized by stretching vibrations at about 1574 and 1423 cm^{-1}, respectively. Amino-functionalized UiO-66 solids showed two bands at 3488 and 3374 cm^{-1} due to the asymmetric and symmetric vibrations of $-NH_2$, respectively, together with another band at 1255 cm^{-1} due to C-N stretching vibration. In the case of nitro-functionalized UiO-66 solids, two bands could be seen at about 1543 and 1496 cm^{-1} due to the characteristic asymmetric and symmetric vibration bands of this group, respectively. These spectra also showed small bands attributable to the presence of amino groups, in good agreement with the XPS analyses. These XPS and FT-IR results indicate a need for the development of new synthetic methodologies to prepare UiO-66 solids with only 2-nitroterephthalate ligands in their structure.

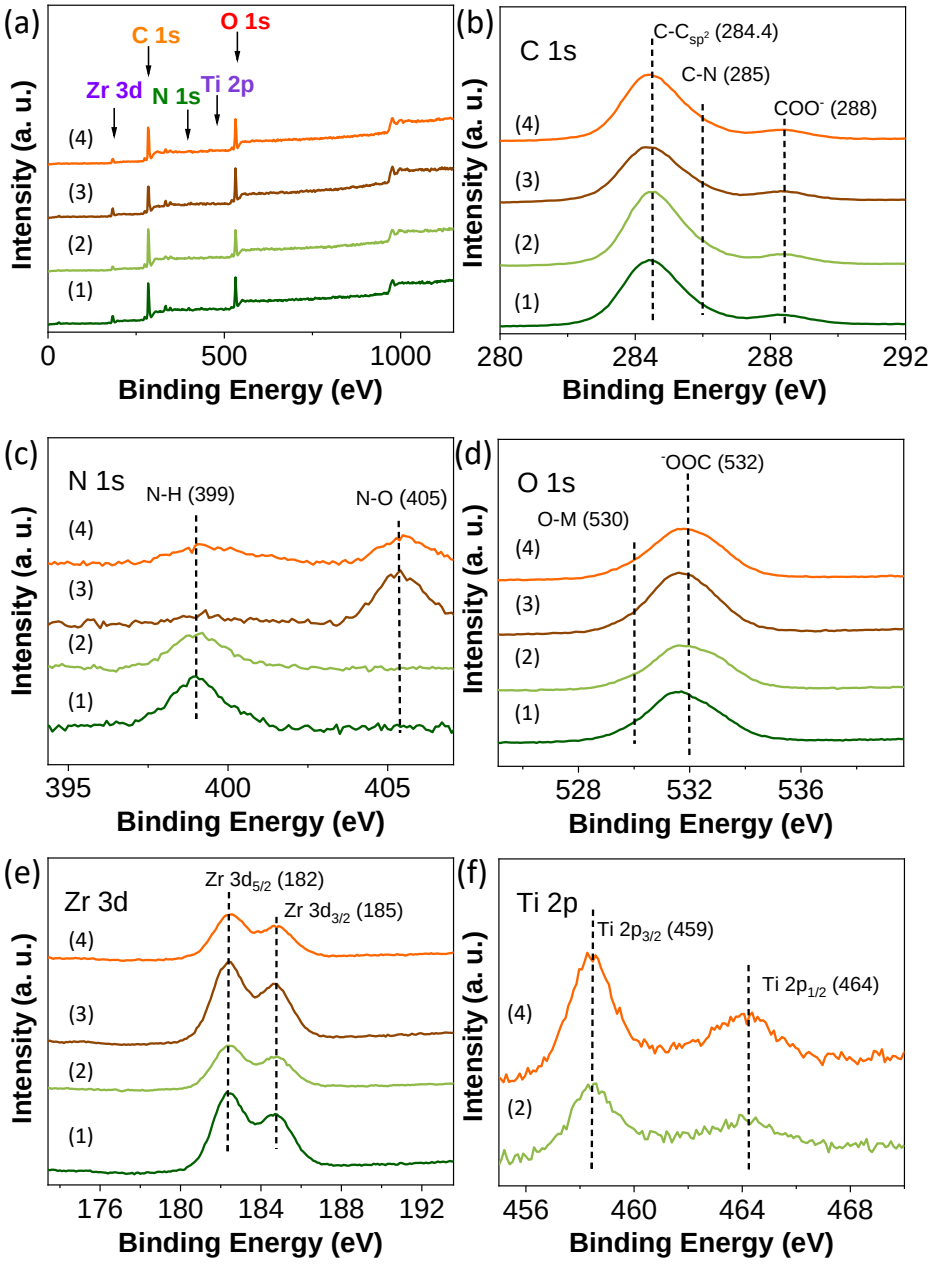

Figure 2. XPS survey (a), C 1s (b), O 1s (c), N 1s (d), Zr 3d (e) and Ti 3p (f) of UiO- 66(Zr)-NH_2 (1), UiO-66(Zr/Ti)-NH_2 (2), UiO-66(Zr)-NO_2 (3), UiO- 66(Zr/Ti)- NO_2 (4).

Isothermal N_2 adsorption measurements were used to estimate the BET surface areas (Figure S27) and pore volumes of pristine mono- and bimetallic UiO - 66 solids with values ranging from 600 to 700 m^2/g and 0.23 to 0.26 cm^3/g, respectively, in agreement with previous studies [57]. TGA analyses under oxidant (air) or inert (nitrogen) atmospheres further confirmed that these UiO-66 samples are thermally stable at temperatures of about 300 ºC and these observations are in agreement with previous reports (Figure S28) [57, 61, 62]. It should be commented that the stability observed below 300 ºC under these atmospheres might differ somehow the stability under the reaction conditions of photocatalytic CO_2 hydrogenation (H_2:CO_2 molar ratio 4:1 at 200 ºC). Additionally, a control experiment revealed that the TGA of UiO-66(Zr/Ti)-NO_2 solid previously submitted to these reaction conditions exhibited a very similar TGA profile under air than the fresh sample and, thus, confirming its relative stability under studied reaction conditions.

The optical properties of the UiO-66 materials were studied by UV-Vis DRS measurements. Figure 3 shows that the presence of NO_2, and especially NH_2, groups in the MOF organic ligand favors visible light absorption with absorption onsets at about 400 and 450 nm, respectively. In the case of amino-functionalized UiO-66 solids the band centred about 365 nm is due to the interaction of the lone pair of electrons of amino group with the π*-orbital of aromatic ring and this situation results in a new higher HOCO level that favours visible light absorption[63]. Tauc plot analyses using the UV-Vis DRS data (Figure S29) confirmed that the optical band gaps of amino-functionalized UiO-66 solids were lower than the nitro-functionalized UiO-66 solids [64]. Besides, mixed-metal UiO-66 solids exhibit somehow lower optical band gaps associated with the role of Ti(IV) ions as electron mediators in agreement with previous experimental [48, 58] and theoretical

studies [65]. XPS HOCO band measurements (Figure S30) were used to estimate the UiO-66 energy band diagrams together with the optical band gaps. In general, all the solids possessed the thermodynamic requirements for photocatalytic CO_2 hydrogenation under sunlight irradiation, while the UV-Vis DRS of RuO_x NPs on UiO-66 solids showed an extra weak absorption band in the visible region associated with the resonance plasmon band of these NPs (Figure S31).

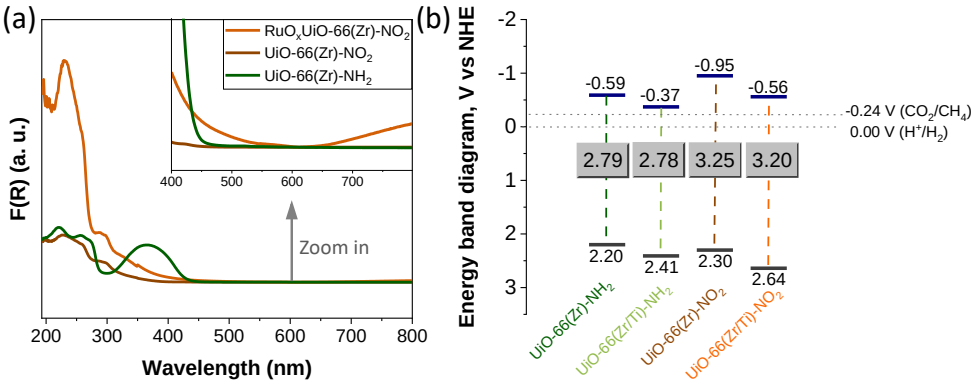

Figure 3. (a) UV-Vis DRS and (b) energy band level diagram of UiO-66 solids as indicated.

5.4.2 Photocatalytic CO_2 hydrogenation

UiO-66-based solids were first tested as photocatalysts for CO_2 hydrogenation at 200 °C under simulated concentrated sunlight irradiation (200 mW/cm^2). For this purpose, the quart reactor is heated with a mantle, then, the system irradiated. It should be remembered that one sun is defined as 100 mW/cm^2 of irradiance. From the point of view of practical applications, solar concentrators could be used to reach the simulated concentrated sunlight irradiations used in this study. Pristine UiO-66 solids showed little activity and CH_4 was the only product detected (< 30 μmol g^{-1}). Specifically, to illustrate the importance of

supported RuO_x NPs in enhancing the photocatalytic activity in the performance of UiO-66(Zr)-NH_2, UiO-66(Zr/Ti)-NH_2, UiO-66(Zr)-NO_2 and UiO-66(Zr/Ti)-NO_2 were carried out and the results indicate a production of only 2, 13, 3 and 4 $\mu mol \cdot g^{-1}$ after 22 h, respectively. However, RuO_x NPs supported UiO-66 materials boosted activities toward CH_4 generation by various degrees, in agreement with the role of RuO_x NPs as benchmark co-catalyst for selective CO_2 (photo)catalytic methanation [32]. RuO_x NPs have the ability to favor chemisorption CO_2 and its reaction intermediates like CO or H_2CO with sufficient strength to be completely hydrogenated to CH_4 [34]. Even though the analyses allow identification and quantification of several carbon products such as CO or short-chain hydrocarbons (Section 5.8.3), CH_4 was the main product together with small amounts of ethane detected for all tested photocatalysts. In other words, all (photo)catalytic tests carried out in this study resulted in CH_4 selectivities higher than 99 %. Control experiments in which CO_2 was replaced by Ar did not indicate the formation of CH_4 or any other product. Due to the similar particle size distribution of RuO_x NPs supported on UiO-66 solids, i.e. a mean average particle size and standard deviations of 2.14 ± 0.04 nm, it is considered that the composition of the UiO-66 photocatalysts determines the resulting activities. Furthermore, it was found that product selectivity is not influenced by the use of UiO-66 composition loaded or not with RuO_x NPs. As an example, the product selectivity distribution of the most active RuO_x@UiO-66(Zr/Ti)-NO_2 indicates a CH_4 selectivity higher than 99 % accompanied with ethane. Figure 4 shows that nitro-functionalized UiO-66 photocatalysts are more active than amino-functionalized UiO-66 photocatalysts. This is an important finding since, as commented in the introduction's section, amino-functionalized MOFs like UiO-66 are among the preferred solids for photocatalytic applications, including CO_2 reduction. Regardless of UiO-66(Zr)-NO_2's higher optical band gap than UiO-66(Zr)-NH_2

(3.16 *vs.* 2.79 eV), its better reduction and oxidation capacity than those of the amino group seems to determine its photocatalytic activity (Figure 3). Figure 4 also shows that the photocatalytic activities of RuO_x NPs supported UiO-66(Zr)-X (X: NH_2 or NO_2) are further increased by the preparation of analogous mixed-metal Zr/Ti materials. Previous studies have demonstrated the role of Ti(IV) ions in the metal node of UiO-66(Zr/Ti)-NH_2 as photoinduced electron transfer mediators[48,58].

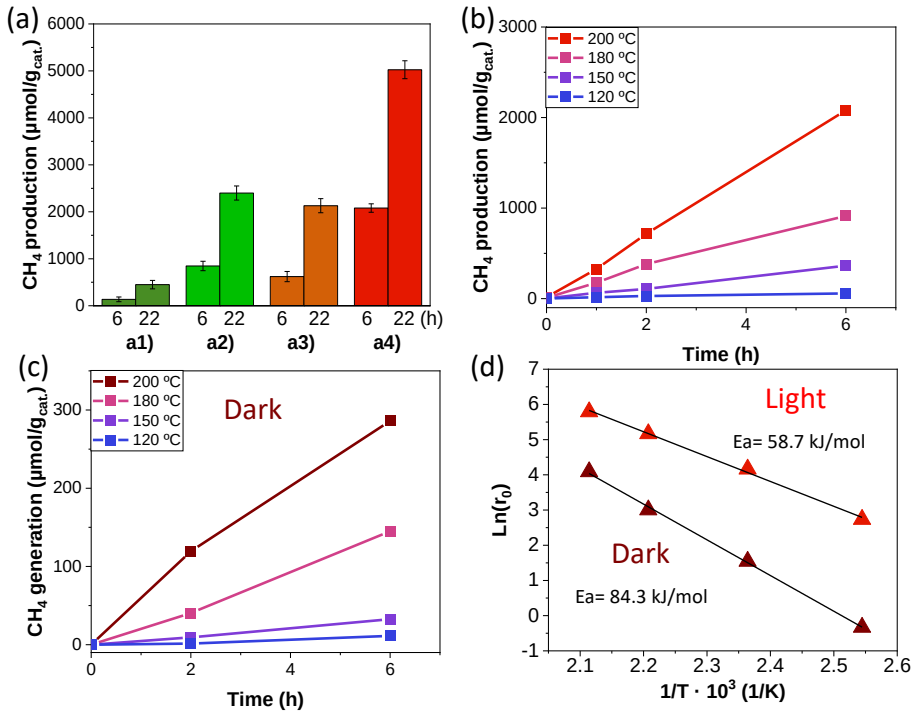

Figure 4. (a) Photocatalytic CO_2 methanation using RuO_x@UiO-66 solids under simulated concentrated sunlight irradiation. Legend: (a1) UiO-66(Zr)-NH_2, (a2) UiO-66(Zr/Ti)-NH_2, (a3) UiO-66(Zr)-NO_2, (a4) UiO-66(Zr/Ti)-NO_2. Influence of reaction temperature on CH_4 generation during photocatalytic CO_2 reduction in light (b) or dark (c) conditions. (d)The Arrhenius plot obtained from initial reaction rates of CH_4 generation as a function of the reaction temperature. Reaction conditions: photocatalyst (15 mg), CO_2:H_2 (1:4), 200 ºC, simulated concentrated sunlight (200 mW/cm^2) irradiation.

As will be shown below, the better performance of mixed-metal UiO-66 photocatalysts supported by RuO_x NPs than those analogous monometallic ones, can be attributed to increased photoinduced charge separation efficiency, as shown by the spectroscopic and electrochemical characterization.

To further verify the role of nitro or amino groups in UiO-66(Zr)-X (X: NO_2 or NH_2) on the resulting photocatalytic activity, an analogous photocatalyst termed as UiO-66(Zr) was prepared using terephthalic acid as organic ligand and further modified with RuO_x NPs by photodeposition method. The samples were characterized by PXRD, spectroscopic (UV-Vis, XPS), analytical (TGA), textural (isothermal N_2 adsorption) and electron microscopic techniques (Figures S32-S37). PXRD confirmed that RuO_x@UiO-66(Zr) and UiO-66(Zr) samples are isostructural crystalline materials with UiO-66 topology (Figure S32). XPS analyses revealed the general expected features of XPS C 1s, O 1s, Zr Ru 3d and 3p (Figure S33). These solids are constituted by particles of 98 ± 63 nm as revealed by SEM analyses (Figure S34). TEM measurements revealed the presence of supported RuO_x NPs with sizes of 2.4 ± 0.8 nm (Figure S35). The sample exhibited good porosity (1008 m^2/g and 0.38 cm^3/g) and thermal stability under air atmosphere (> 400 °C) (Figure S36). The energy band level diagram of UiO-66(Zr) is characterized by a wide optical band gap (3.7 eV) with HOCO and LUCO positions of +1.81 and -2.15 V, respectively (Figure S37). The use of RuO_x@UiO-66(Zr) and pristine UiO-66(Zr) as photocatalysts under conditions described in Figure 4 showed a selective CH_4 production of respectively 500 and 2 μmol g^{-1} after 22 h. The activity of this RuO_x@UiO-66(Zr) photocatalyst is slightly lower to that of RuO_x@UiO-66(Zr)-NH_2 and about three times lower than that achieved using RuO_x@UiO-66(Zr)-NO_2 photocatalyst. Regardless the lower CO_2 adsorption capacity and higher optical band gap of UiO-66(Zr) compared to UiO-66(Zr)-NH_2

their photocatalytic activities are similar to each other. In contrast, as previously commented RuO_x@UiO-66(Zr)-NO_2 exhibits the higher activity and associated to its unique structure due to the presence of nitro functional groups. The performance of the most active RuO_x@UiO-66(Zr/Ti)-NO_2 sample (~13% CO_2 conversion; 5.03 $mmol_{CH4}{\cdot}g^{-1}$ after 22 h) during photocatalytic CO_2 hydrogenation to CH_4 was further studied. A photocatalytic experiment using labelled $^{13}CO_2$ and gas-phase aliquot analysis by gas chromatograph coupled to mass spectrometer (GC-MS) using an electron ionization method confirmed the formation of $^{13}CH_4$ (m/z 17) after 22 h of reaction at 200 ºC (Figure S38). It should be noted, however, that the characteristic ionization profile of CH_4 differs in some extent to the one obtained and associated to the contribution of other molecules like H_2O and air from ambient during the injection that are not chromatographically separated in the system used. As it will be shown later in Section 5.4.3 the transformation of CO_2 into CH_4 has been further confirmed by using *operando* FT-IR analyses. A control experiment under dark reaction conditions at 200 ºC also revealed lower CH_4 production (1.9 mmol g^{-1} after 22 h) than that achieved under simulated concentrated sunlight irradiation. The observation of some activity under dark reaction conditions was not unexpected, since previous studies have reported that RuO_x NPs are an active and selective co-catalyst during thermal catalytic processes[32]. Quantitative information on the performance of RuO_x@UiO- 66(Zr/Ti)-NO_2 as photocatalyst at 200 ºC was obtained by estimating the AQY at specific wavelengths. After deducting the activity observed under dark reaction conditions, the AQYs achieved by irradiation at 350, 400 and 600 nm were 1.67, 0.25 and 0.01, respectively. The influence of the reaction temperature on the photocatalytic activity of RuO_x@UiO-66(Zr/Ti)-NO_2 was then studied (results in Figure 4b). As can be seen, photocatalytic CH_4 generation as a function of the reaction temperature follows the Arrhenius law, making it possible to estimate an

apparent Ea of 58.7 kJ/mol. In a series of analogous experiments carried out in the absence of irradiation (thermal catalysis), the estimated Ea resulted to be 90 kJ/mol. Based on analogous studies [66-68] and as it will be further studied in Section 3.3, this significant decrease in Ea can be attributed to the operation of a photothermal reaction pathway.

The photocatalytic activity of RuO_x@UiO-66(Zr/Ti)-NO_2 was compared with those MOF-based photocatalysts reported in previous studies and the results are summarized in Table S1. The use of the same reaction conditions than most of the studies in Table S1, i.e. P_{H2}=1.05 bar, P_{CO2}=0.25 bar instead the previous P_{H2}=1.2 bar, P_{CO2}=0.3 bar, resulted in a CH_4 production decrease of about 5 % in agreement with Chatelier's principle. RuO_x NPs supported trimetallic UiO- 66(Zr/Ce/Ti) was recently reported as one of the most active MOF-based photocatalysts for CO_2 methanation under simulated concentrated sunlight irradiation (1.8 mmol g^{-1}_{CH4} after 22 h at 200 ºC) (Table S1, entry 2), showing that the activity of RuO_x@UiO-66(Zr/Ti)-NO_2 is about 3 times higher than this photocatalyst under similar reaction conditions. Furthermore, RuO_x@UiO- 66(Zr/Ti)-NO_2 exhibits an activity 3-6 times higher than that achieved using analogous solids based on RuO_x NPs supported on Ti-based MOFs, such as MIL-125(Ti)-NH_2 (Table S1, entries 3 and 4) or MIP-208(Ti) (Table S1, entry 5). It is remarkable that the activity of RuO_x@UiO-66(Zr/Ti)-NO_2 (Table S1, entry 1) is more than two times compared with RuO_x@MIL-125(Ti)-NH_2 (Table S1, entry 4) having the doble amount of ruthenium (2 wt%). It should be noted that all these photocatalysts have a similar RuO_x NP loading (1 wt % of ruthenium) and an average particle size (~ 2 nm). The higher activity of RuO_x@UiO-66(Zr/Ti)-NO_2 thus appears to be related to the energy band diagram level of the photocatalyst determined by the combination of 2-nitroterephthalates ligands and

mixed- metal Zr(IV)/Ti(IV) metal nodes, which boosts the efficiency of the reaction. Regardless of these comments, it is pertinent to mention that the state-of-the-art in current photocatalytic gaseous methanation has reported activities, in some cases, greater than 100 mmol·$g^{1}h^{1}$. In one of these examples, a ultrathin Mg-Al layered double hydroxide nanosheet supported Ru NPs was found to achieve efficient photothermal CO_2 methanation (277 mmol h^{-1} g^{-1}; 300 W Xe lamp) under continuous flow operation[69].

The activity and stability of RuO_x@UiO-66(Zr/Ti)-NO_2 were studied by performing consecutive reuse experiments. Figure 5 shows that the photocatalyst can be reused without significant loss of activity for four consecutive times with an accumulated reaction time of 90 h. According to PXRD analysis, the crystallinity of the four-times used photocatalyst is preserved. TEM analyses of the reused photocatalyst confirmed that RuO_x average particle size and standard deviation (2.32 ± 0.90 nm) are similar compared to the fresh sample (2.08 ± 0.82 nm). Besides, HR-TEM characterization of the used photocatalyst revealed the presence of lattice fringes with spacings of about 0.203 and 0.32 nm, which were ascribed to the crystal planes (101) and (110) of Ru(0) and RuO_2, respectively (Figure S39).

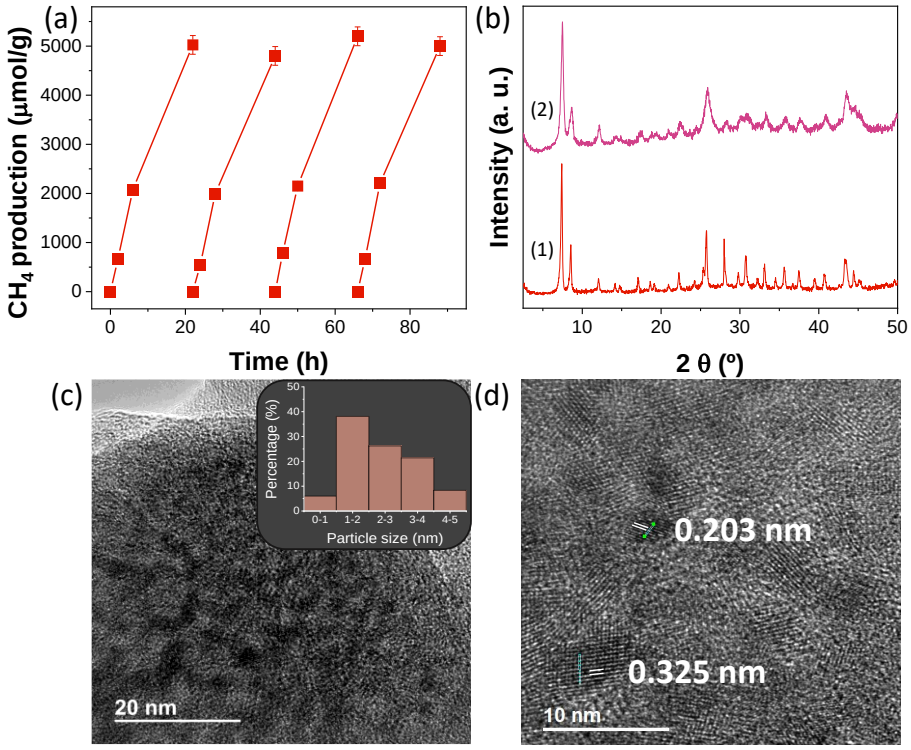

Figure 5. (a) Reusability of RuO_x@UiO-66(Zr/Ti)-NO_2 during photocatalytic CO_2 methanation. (b) PXRD of RuO_x@UiO-66(Zr/Ti)-NO_2 fresh (1) and used (2). (c) TEM image and particle size distribution of used photocatalyst; (d) HRTEM for interplanar distance.

C 1s, O 1s, Zr 3d and Ti 2p XPS analyses of the four-times used photocatalyst (Figure S40) showed similar features to those of the fresh material, while N 1s and Ru 3d XPS showed small but appreciable differences with respect to the fresh sample (Figure 6 and S41). N 1s XPS of the used photocatalyst revealed slight hydrogenation of the nitro group to the amino group (Figure 5). Specifically, the fresh and used RuO_x@UiO-66(Zr/Ti)-NO_2 photocatalysts have a proportion in weight percent of NO_2 versus NH_2 of 55.2/44.8 and 46.8/53.2, respectively. Although partial reduction of NO_2 to NH_2 is observed in the used RuO_x@UiO- 66(Zr/Ti)-NO_2 photocatalyst by XPS, the structural integrity of the

used photocatalyst still contains enough NO_2 groups (46.8 at%) to promote the photocatalyst activity without much significant difference (Figure 6). Furthermore, UV-Vis DRS of the used sample showed an extra absorption band with onset absorption at about 430 nm, which agrees with partial nitro hydrogenation to the amino group (Figure 5). In the case of Ru 3d XPS, a small shift of the Ru 3 $d_{5/2}$ was seen toward lower binding energies with respect to the fresh sample (281.9 *vs.* 280.8 eV). These results agree with previous studies that also showed the supported RuO_x NPs employed as co-catalysts during (photo)catalytic hydrogenations at temperatures of about 200 °C that can be converted in some extent to metallic phase [44, 69-72].

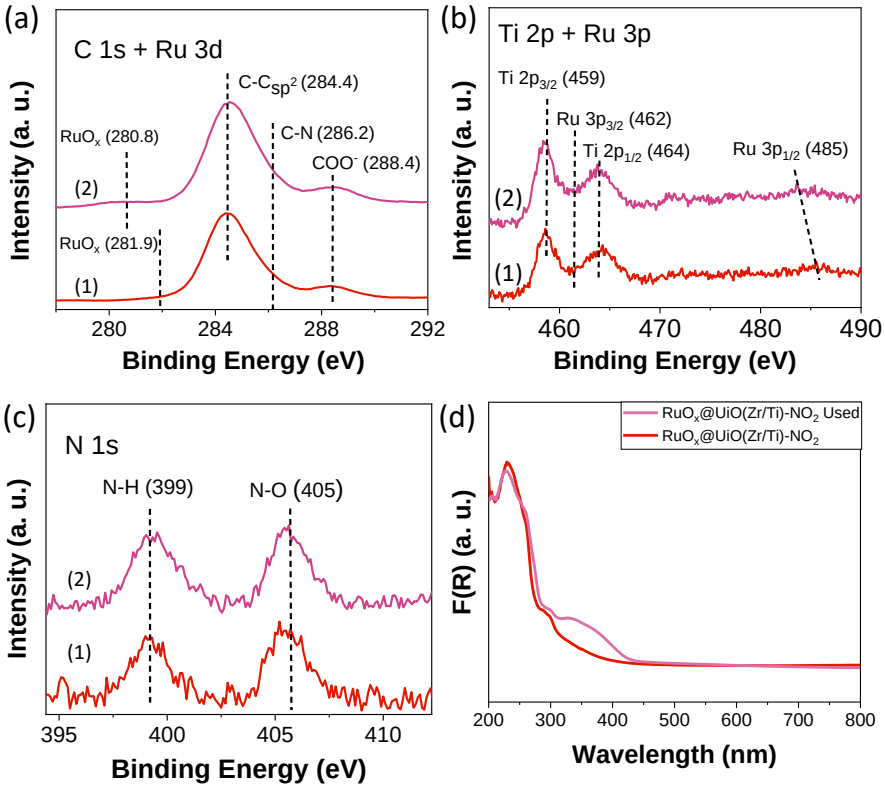

Figure 6. (a) C1s + Ru 3d, (b) Ti 2p + Ru 3p, (c) N 1s XPS of fresh (1) and used (2) photocatalyst and (d) UV-Vis of fresh and used RuO_x@UiO-66(Zr/Ti)-NO_2.

In the present study, additional *in situ* XPS experiments with the fresh RuO_x@UiO-66(Zr/Ti)-NO_2 sample is submitted to a H_2 thermal treatment at 200 ºC, revealing that supported RuO_x NPs are susceptible to be partially reduced to metallic NPs under the studied reaction conditions (Figure S42). It should be noted that metallic ruthenium species have been proposed as responsible species to activate molecular H_2 and initiate CO_2 hydrogenation[69, 70, 72, 73]. Besides, as it will be shown latter RuO_x and Ru species also favor CO_2 and CO chemisorption as evidenced by FT-IR spectroscopy. Overall, these results demonstrate that RuO_x NPs supported on UiO-66(Zr/Ti)-NO_2 are partially reduced during the photocatalytic CO_2 hydrogenation process leading to co-existence of supported RuO_x and Ru(0) species within the photocatalyst.

In the area of photocatalysis using MOFs, some studies have reported UV-Vis irradiation of carboxylate-based MOFs at 200 ºC that resulted in partial decarboxylation[74]. To address this issue, a photocatalytic control experiment in which CO_2 was replaced by Ar revealed the presence of CO_2, attributed to the partial decarboxylation of the terephthalate MOF ligand during the reaction (1.8 wt% respect to the amount of the initial carboxylate). These results indicate a need to develop active MOF-based photocatalysts that can operate under milder reaction conditions with operational stabilities.

5.4.3 Photocatalytic reaction pathways

5.4.3.1 Photochemical and photothermal reaction mechanisms

Based on previous reports, photocatalytic CO_2 reduction using metal/metal oxide NPs supported on MOFs or other materials can occur via a photochemical[24,34] and/or photothermal reaction mechanisms [24,34,75-77]. During the

photochemical pathway, the irradiation of the photocatalysts results in the formation of reducing and oxidizing electron and hole pairs, respectively. This is a common reaction mechanism found when using MOFs as photocatalysts, when their irradiation by appropriate wavelengths produces photoinduced electron transfer from the organic ligand to the metal node [43]. The presence of metal NPs like RuO_x as co-catalysts can also favor photochemical pathway efficiency by opening new channels for charge carrier separation and enhancing photocatalytic activity[44]. RuO_x NPs have also been reported to promote the photothermal reaction pathway in which light energy is transformed into heat, which favors CO_2 methanation[75].

Several characterization techniques were used to further study these possible reaction pathways using RuO_x NPs supported UiO-66(Zr and/or Ti)-X (X: NH_2 or NO_2). It should be noted that, as shown in Figure 6, the RuO_x@UiO-66(Zr/Ti)-NO_2 photocatalyst used exhibits a partial reduction of supported RuO_x NPs with respect to the fresh sample. To consider the possible influence of the RuO_x oxidation state on the subsequent characterization data, some comparative measurements were carried out using both fresh and used photocatalysts.

To evaluate the photoinduced processes arising from excitation of the different UiO-66(Zr/Ti)-X (X: NH_2 or NO_2) photocatalysts at 267 nm[30, 75] were first studied by femtosecond transient absorption spectroscopy (fs-TAS). This technique has been shown to be sensitive and precise for investigating processes occurring at a very early stage after excitation, including ultrafast electron transfer or charge separation [78]. The recorded transient absorption spectra (Figure S43) and kinetics (Figures S44) of UiO-66(Zr)–NH_2 showed good agreement with previously reported observations [79], while notable differences

were found in the transient absorption spectra when using NO_2 (Figures S45). Transient absorbance of the latter samples covers the entire visible spectrum and does not exhibit any remarkable band/feature (Figures S45). A set of the kinetic traces ranging from 550 to 750 nm were analyzed by means of a global fit, including two-time constants, to describe the dynamics during the first ns after photoexcitation. Table S2 includes the resulting time constants for all the species studied. The fastest components (of the order of a few tens of ps) were associated with electron transfer processes from HOCO to LUCO of MOFs [79], while the longer-lived components, which remained up to the nanosecond time scale, were assigned to a deep trap state [80]. Figures 7a shows for nitro-functionalized UiO-66 solids a comparison of the transients together with the average lifetimes calculated for each probe wavelength on the basis of the time constants derived from the global fit. The data reveal that the fastest relaxation dynamics are those of RuO_x@UiO-66(Zr/Ti)-NO_2, followed by an analogous mixed-metal UiO - 66(Zr/Ti)-NO_2 parent sample, while monometallic UiO-66(Zr)-NO_2 exhibited longer-lived components. Similar conclusions can be drawn for amino-functionalized UiO-66 materials (Figure S44). In this regard, kinetic traces have been used as indicators to evaluate electron-hole separation efficiency of the photocatalysts. It is therefore proposed, by means of comparisons with previous ultrafast results from related MOFs,[79] that the faster the relaxation dynamics, the higher the charge-separation efficiency. In fact, the order of photocatalytic activity in this case agrees, to some extent, with the relaxation trace kinetics using ultrafast TAS measurements.

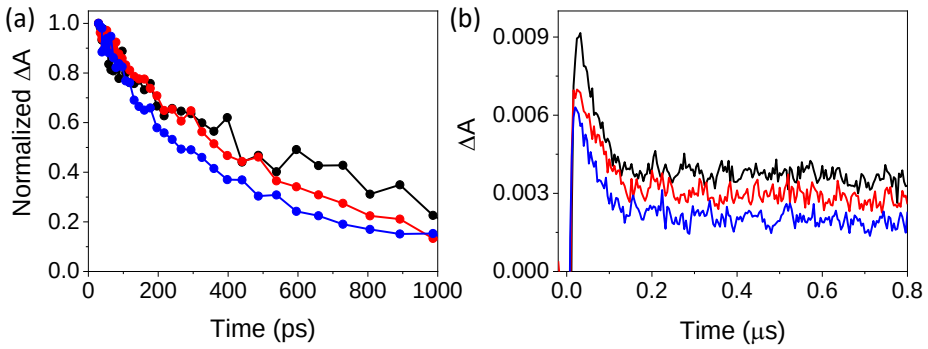

Figure 7. (a) Femtosecond transient absorption recorded at 586 nm and (b) LFP decay traces recorded at 520 nm for UiO-66(Zr)-NO_2 (black), UiO-66(Zr/Ti)-NO_2 (red) and RuO_xUiO-66(Zr/Ti)-NO_2 (blue). FTA measurements were performed at λ_{exc} = 267 nm in aerated MeCN, whereas those of LFP were done at λ_{exc} = 266 nm in MeCN under Ar atmosphere.

Long-lived trap states for UiO-66 photocatalysts were further investigated on longer timescales by the LFP technique at λ_{exc} = 266 nm. The spectra obtained for the different nitro- (Figures 7b and S46) and amino- (Figures S47), functionalized UiO-66 photocatalysts in an Ar atmosphere on the nanosecond timescale and characterized by a continuous absorption band from 300 to 750 nm. Previous TAS studies by some of us using UiO-66(Zr)-X (X: NH_2 or NO_2) assigned these transient absorption bands to photogenerated electron and holes based on selective quenching experiments [51, 54]. Similar conclusions have been obtained in the present case using CH_3OH as hole quencher for the series of amino-functionalized UiO-66 solids. Figure S48 shows that CH_3OH quenches the region from 300 to 400 nm, resulting in a parallel increase of the transient signals around 600 nm, which indicates that hole deactivation enhances the yield of photogenerated electrons, an effect previously found in other related MOF- based photocatalysts [81, 82]. These results agree with those obtained from ultrafast TAS and demonstrate the photogeneration of charge separation species as electrons and holes. In line with the ultrafast results, LFP decay traces at 400 and 680 nm show that the faster the

decay components (Table S2), the higher the photocatalytic activity of all the studied RuO_x NPs supported UiO-66(Zr/Ti)-X (X: NH_2 or NO_2) in their series. In short, in terms of photocatalyst decay relaxation dynamics both fs- and ns-TAS serve as indicators of charge separation efficiency and agree with the order observed in their photocatalytic activity.

To further evaluate the photoinduced charge separation efficiency of UiO-66 solids and their relationship with their photocatalytic activities, photocatalysts were characterized by PL spectroscopy, transient photocurrent and EIS measurements. PL spectroscopy is commonly used in heterogeneous photocatalysis, including MOFs, to evaluate the photoexcited charge transfer and recombination processes [83,84]. Amino functionalized UiO-66 solids have a different degree of fluorescence while negligible emission was found when using the nitro functionalized solids. These results agree with some of previous results showing that acetonitrile solutions of 2-aminoterephthalate emit much more on excitation at 266 nm than the analogous 2-nitroterephthalate acetonitrile solutions[54]. Figure 8a shows that the UiO-66(Zr/Ti)-NH_2 suspension has lower emissions than UiO-66(Zr)-NH_2, which agrees with similar studies that highlighted the higher efficiency of photoinduced charge separation of mixed-metal UiO- 66(Zr/Ti)-NH_2 solids, in which Ti(IV) atoms act as the electron mediator during the process[48]. Similar measurements using fresh or used RuO_x NPs supported UiO-66(Zr)-NH_2, and especially UiO-66(Zr/Ti)-NH_2 solids, produced considerably less fluorescence emission intensity. Regardless the much lower fluorescence emission intensity observed when using nitro-functionalized UiO- 66-based solids compared to amino ones, analogous conclusions about the fluorescence quenching in mixed-metal solids with or without fresh and used RuO_x respect to the parent sample can be drawn (Figure 8b). These results

indicate that the presence of RuO_x NPs in the UiO-66 solids reduces the recombination rate of photogenerated electron-hole pairs and thus increases the efficiency of photoinduced charge separation.

The transient photocurrent results using UiO-66 solids under several on/off illumination cycles are shown in Figure 8c,d. For these measurements, UiO-based photocatalysts were supported on a carbon substrate electrode and used in a standard three-electrode electrochemical cell as a working electrode previously polarized at + 0.9 V. The results show that mixed-metal UiO-66 solids have higher photocurrent intensities than monometallic ones (Figure 8c,d). Analogous measurements using used and fresh RuO_x@UiO-66(Zr/Ti)-NO_2 photocatalysts found higher current intensities in simulated concentrated sunlight illumination and indicated an improvement in charge separation efficiency. An additional experiment using fresh RuO_x@UiO-66(Zr/Ti)-NO_2 in the presence of CH_3OH gave a 5-fold enhancement of current intensity (Figure S49). This was due to the oxidation of CH_3OH in the photogenerated holes that partially avoided electron recombination, so that a higher current intensity was measured than in the experiment with pure acetonitrile as solvent.

PL and transient photocurrent conclusions were complemented by EIS measurements (Figure 8e,f). The smallest Nyquist arc radii were obtained from the most active samples of the series with the lowest Rct. PL, transient photocurrent and EIS measurements showed that titanium ions in the metal nodes of UiO-66(Zr/Ti) and/or RuO_x@UiO-66 solids acted as electron mediators during the photoinduced electron transfer from the organic ligand to the metal node and increased the process efficiency [48, 84].

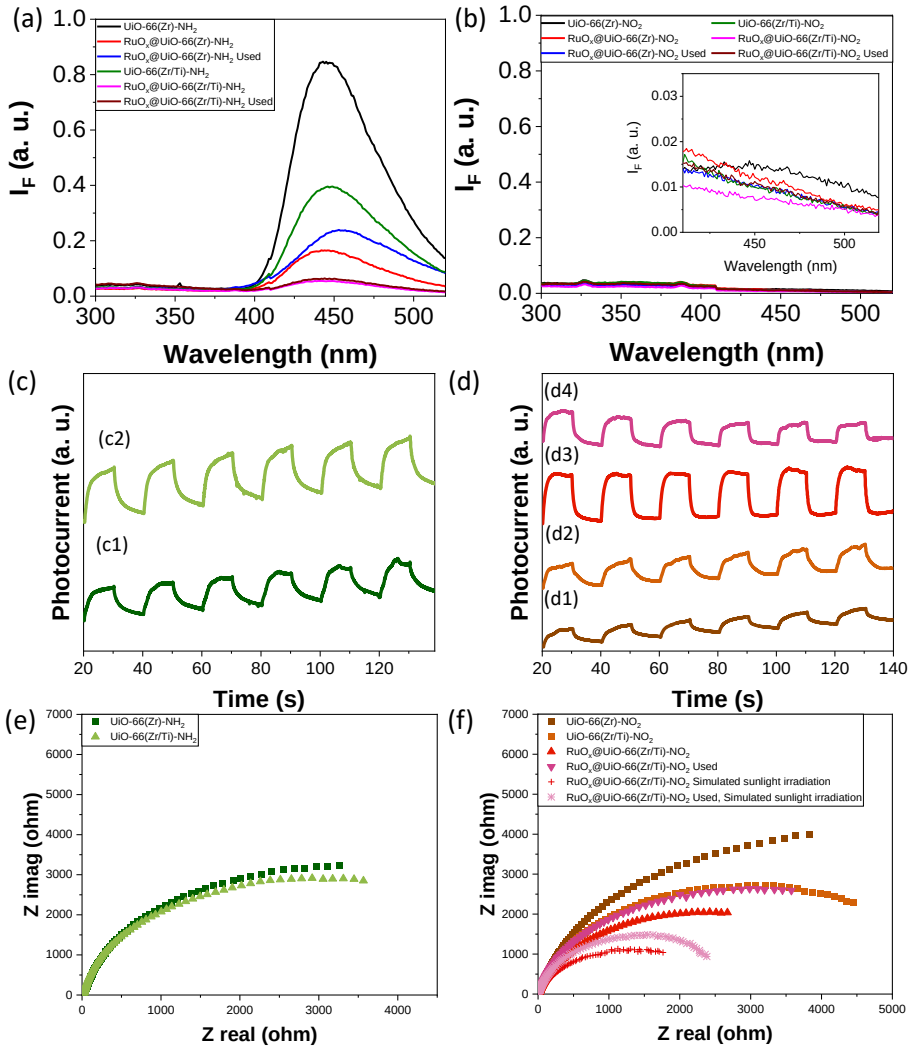

Figure 8. (a) PL measurements performed in acetonitrile MOF suspension having the same optical absorption (*ca.* 35 a.u.) at 266 nm corresponding with the monochromatic excitation wavelength of the MOF organic ligand. (b) Current intensity response of amino- (c) or nitro-based (d) UiO-66 solids. Nyquist plots of amino- (e) or nitro-based (f) UiO-66 solids under dark or simulated concentrated sunlight irradiation as indicated. Legend: (c1) UiO-66(Zr)-NH_2, (c2) UiO-66(Zr/Ti)-NH_2, (d1) UiO-66(Zr)-NO_2, (d2) UiO-66(Zr/Ti)-NO_2, (d3) RuO_x@UiO-66(Zr/Ti)-NO_2 fresh, (d4) RuO_x@UiO-66(Zr/Ti)-NO_2 used.

Previous studies reported the use of solid-state EPR spectroscopy to characterize the formation of photoactive reductive sites in MOFs like UiO- 66(Zr)- NH_2 [54, 58] or MIL-125(Ti)-NH_2. For example, it has been reported that irradiation of UiO-66(Zr)-NH_2 results in photoinduced charge separation from the organic ligand to the metal node and the transformation of Zr(IV) species into Zr(III) species while the holes are located in the organic ligand[54, 58, 85]. Other studies have proposed that the irradiation of mixed-metal UiO-66(Zr/Ti)-NH_2 produces an LMCT mechanism with the initial reduction of Ti(IV) to Ti(III) in Ti(III)-O-Zr(IV) metal nodes, which are later transformed into Ti(IV)-O-Zr(III) [48]. These studies highlight the role of Ti(IV) species in mixed-metal UiO-66 solids act as electron mediators from excited organic ligands that favor charge separation. In the present study, solid-state EPR experiments were carried out using UiO-66(Zr)-X (X: NH_2 or NO_2) and the analogous mixed-metals UiO-66(Zr/Ti)-X (X: NH_2 or NO_2) (Figures 9a and S50). Control solid-state EPR experiments in dark conditions revealed the presence of some paramagnetic signals in amino-functionalized UiO-66, associated with the presence of Zr(III) species that, however, are absent in analogous nitro solids, in agreement with previous related studies[54]. Irradiation of mono- or bimetallic UiO-66 solids functionalized with either amino or nitro groups in all cases produce the formation of an EPR band with g value of 2.004, characteristic of the Zr(III) species. These experiments indicate the occurrence of LMCT mechanisms in MOFs, while the absence of EPR Ti(III) signals could be associated with the previously proposed fast kinetics of metal electron transfer from Ti(III) as electron mediator to geminal Zr(IV)[48].

Based on previous studies and due to the use of RuO_x NPs as co-catalysts during photocatalytic CO_2 reduction, the occurrence of a photothermal pathway can be hypothesized in which light energy is transformed into heat energy[75-77]. An

indirect experiment to determine this possible pathway was conducted by evaluating photocatalytic CO_2 methanation as a function of the simulated sunlight intensity. Figure 9b shows that photocatalytic CH_4 production increases linearly as a function of irradiance intensity up to about 125 mW/cm^2 and then an exponential relationship can be seen. These results are interpreted as the occurrence of a photothermal reaction pathway, especially at high irradiance intensities, in which light irradiation is transformed into local heat in RuO_x NPs, promoting CO_2 hydrogenation to CH_4.

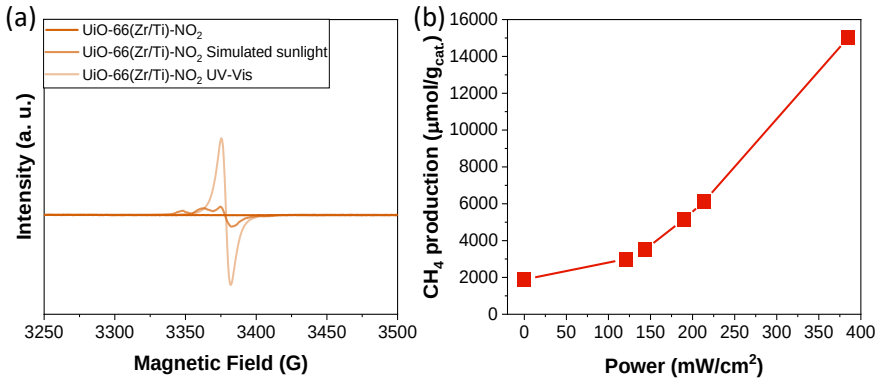

Figure 9. (a) EPR of solid UiO-66(Zr/Ti)-NO_2 after different irradiation conditions as indicated; (b) Influence of simulated light intensity into photocatalytic CH_4 formation.

The measurement of catalyst temperature during the photothermal reaction is of great importance to understand the thermal- and non-thermal contributions of the whole process[86]. To address this challenging measurement, several techniques have been reported like direct measurement with a thermocouple, or non-contact techniques with infrared sensors or thermal cameras[86]. Other common method to assess catalyst local heating is based on the use of supported inorganic QDs as temperature sensor with optical readout[26, 87]. Specifically, the measurement of PL emission decrease of supported QDs on a photocatalyst is a

function of the local temperature[26, 43]. In this work, commercially available CdSe- ZnS QDs were employed as local nanothermometers. The series of PL experiments upon CdSe-ZnS QDs excitation at 450 nm were performed at temperatures from 200 to 280 ºC under dark or upon simulated sunlight irradiation intensities from 85 to 385 mW/cm^2. Figure S51 shows that the characteristic PL emission band of CdSe-ZnS QDs centered about 540 nm gradually decreases as the temperature increases. These experiments confirmed the possibility of using these CdSe-ZnS QDs as local nanothermometers in agreement with previous reports [26, 43]. Additionally, the PL emission intensity of CdSe-ZnS QDs recorded at 200 ºC also decreased upon irradiation, the highest the irradiation intensity the highest the PL quenching and associated to the local heating of CdSe-ZnS QDs upon irradiation. Analogous PL results were obtained in the case of used RuO_x@UiO-66(Zr/Ti)-NO_2 photocatalyst supported CdSe/ZnS QDs deposited on a quartz holder as a function of either the temperature or the simulated sunlight irradiation at different irradiances. It should be noted that during these PL experiments negligible temperature changes of the sample upon different irradiations were measured using an infrared thermometer. Therefore, it is likely to propose that the observed PL quenching upon irradiation might be associated with a photocatalyst local heating (*ca.* to about 220 or 280 ºC as a function of the irradiance; Figure S52) due to irradiation. Overall, these PL results together with those ones shown in Figure 9 about the influence of simulated light intensity into photocatalytic CH_4 formation would agree with the occurrence of a photothermal reaction pathway during CO_2 reduction.

Further investigation of the photothermal behavior was conducted by monitoring the IR bands shift of the structural bands using *operando* FT-IR experiment under different temperatures, given the fact as temperature

increases the molecular vibration of the different species increases resulting a shift in IR bands [88, 89]. Results confirm this behavior with RuO_x@UiO-66(Zr/Ti)-NO_2 showing a structural band shift from 3668 to 3665 cm^{-1} (assigned to OH vibration) as temperature increased from 100 to 200 °C under dark conditions (inset of Figure 10a). This effect was then investigated for the reaction under irradiation at room temperature. Interestingly, a significant band shift from 3369 to 3360 cm^{-1} (Figure 10b) is observed indicating a potential localized temperature increase (estimated of around 145 °C). However, at elevated temperature (200 °C) this effect was diminished whereby a lower band shift is observed (Figure 10c). This result is consistent with that of the PL quenching with QDs.

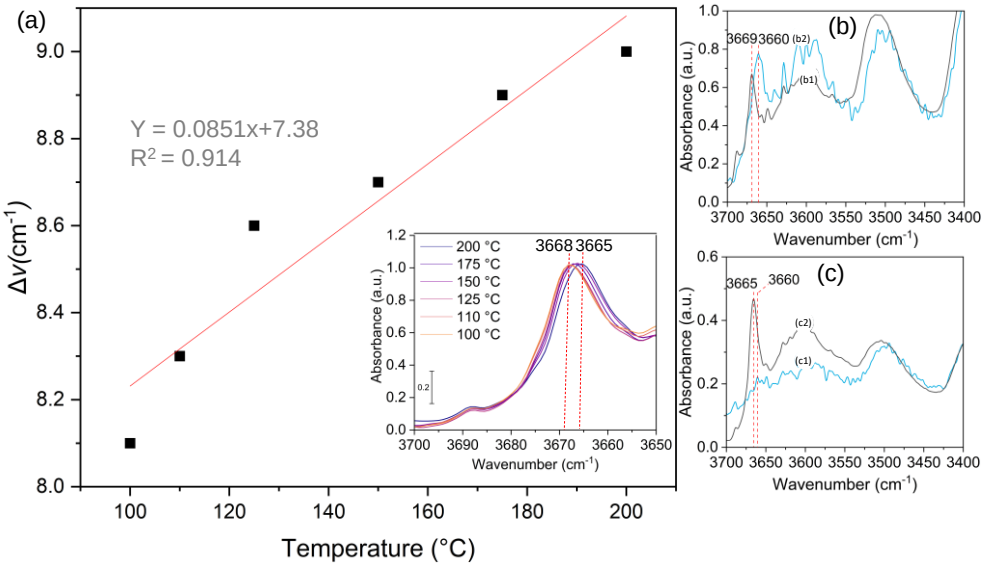

Figure 10. (a) Evolution of the structural band shift as a function of temperature (inset: Direct surface FT-IR spectra of RuO_x@UiO-66(Zr/Ti)-NO_2 in the 3700- 3650 cm^{-1} region at different temperatures in dark), (b) and (c) FT-IR spectra in the same region (1) in dark and (2) under irradiation at 30 °C and 200 °C respectively. Spectra collected under continuous flow of Ar (20 cm^3/min).

Overall, RuO_x NPs supported UiO-66(Zr/Ti)-NO_2 generally act as a multifunctional photocatalyst during CO_2 methanation under simulated concentrated sunlight irradiation (Figure 11). During the photochemical pathway irradiation of the photocatalyst, it can be considered that a photoinduced electron transfer from the organic ligand to the metal-oxo cluster takes place. These electrons can be further transferred to RuO_x NPs, where CO_2 methanation occurs. Irradiation can also promote the heating of RuO_x NPs CO_2 hydrogenation to CH_4.

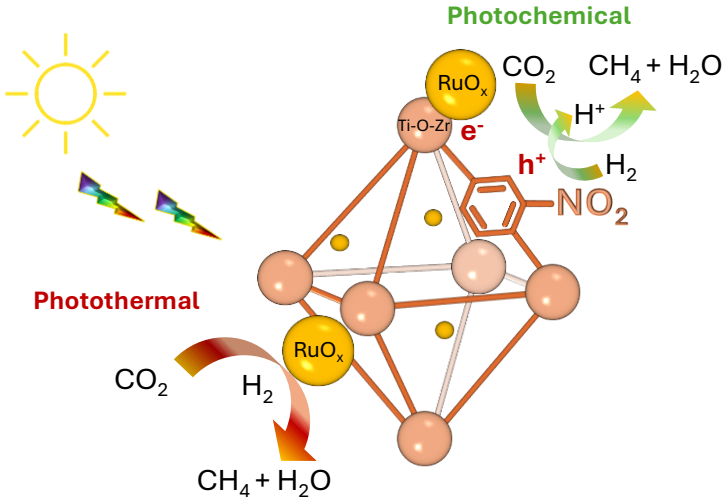

Figure 11. Proposed reaction mechanism during CO_2 methanation using RuO_x@UiO-66(Zr/Ti)-NO_2 as multifunctional photocatalyst.

5.4.4 Evaluation of photocatalytic CO_2 hydrogenation to CH_4

The previous photocatalytic results using UiO-66-based materials have shown a selective CO_2 hydrogenation to CH_4. These results agree with analogous studies reporting that the use of supported RuO_x NPs facilitates chemisorption of CO_2 and their reaction intermediates and promote the (photo)catalytic hydrogenation to CH_4[90-92]. To shed some light on the CO_2 and CO adsorption capacity over RuO_x@UiO-66(Zr/Ti)-NO_2 topic, CO_2 and CO adsorption experiments were conducted under continuous flow of CO_2/Ar and CO/Ar under *operando* conditions and the results were analyzed through IR[93, 94]. Initially, different concentrations of CO_2 were introduced in Ar with a total flow rate of 20 $cm^3 \cdot min^{-1}$. It is witnessed that as the concentration of CO_2 increases, the band centered at 2238 cm^{-1} characteristic of chemisorbed CO_2 increases in a linear way, as illustrated in Figure 12a. The results are presented after subtraction of gaseous CO_2 phase. Direct spectra can be found in the Figure S54a. Upon reaching saturation, CO_2 adsorption was investigated as a function of the temperature (as depicted in Figure 12b). These results demonstrated an exponential decrease in chemisorbed CO_2 concentration as the temperature increases, until reaching 200 °C. Subsequently, the enthalpy and entropy of this reaction were calculated based on the linear relationship of $\mathrm{Ln}\left[\frac{nCO_2\,(T=T_n)}{nCO_2(T=298)-nCO_2(T=T_n)} \times \frac{P}{P_0}\right]$ (where nCO_2 represents the number of moles of chemisorbed CO_2, T_n is the temperature reached at each point, and P/P_0 is the relative pressure of CO_2 in Ar) as a function of the inverse of temperature (-1/T), as shown in Figure 12c. The enthalpy of the reaction was determined from the slope of the line and equal to -22.5 kJ/mol, indicating relatively weak and reversible adsorption of CO_2 on the catalyst surface. The investigation of CO adsorption on supported ruthenium catalysts

holds significance not only for understanding the mechanism of CO_2 methanation reaction (considering that CO is one of the potential intermediates of this reaction) but also for the characterization of their surface properties. CO serves as a prominent probe molecule, unveiling both the oxidation state and coordination environment of the sites to which it binds. Figure 12d shows the evolution of the FT-IR spectra of the RuO_x@UiO-66(Zr/Ti)-NO_2, in the CO vibration spectral region (2200-1800 cm^{-1}), upon the introduction of 0.05 % CO in Ar to the sample preactivated under H_2 at 200 °C. The results are subtracted from the spectrum after activation at room temperature and the direct spectra can be found in the Figure S54b. Different bands appeared on the surface, however, their assignment to specific adsorption sites is not straightforward, as witnessed by the different interpretations found in the literature. This variability likely arises from multiple factors influencing exact band positions, such as the coverage of CO, as well as the oxidation state of the adsorbant. According to literature findings, carbonyl species can predominantly be categorized into two distinct surface complexes: the spectral peaks at 2124 cm^{-1}, coupled with a component at 2055 cm^{-1}, are attributed to the asymmetric and symmetric stretching vibrations of an $Ru^{3+}(CO)_2$ species on the proximity of ZrO_2[95]. Meanwhile, the spectral peaks at 2070 cm^{-1} and 2004 cm^{-1} are associated to those of $Ru^{2+}(CO)_2$ species[89]. Furthermore, peaks at lower wavenumbers (1995, 1987 and 1955 cm^{-1}) may be attributed to monocarbonyls adsorbed on less oxidized $Ru^{\delta+}$ supported on TiO_2. Furthermore, a less intense peak at 2023 cm^{-1} may be attributed to CO linearly bound to metallic Ru^0. The approximative assignments of the spectral bands are summarized in Table S3.

The performance of the most active RuO_x@UiO-66(Zr/Ti)-NO_2 sample during photocatalytic CO_2 hydrogenation to CH_4 was further investigated through

operando FT-IR experiments where both the gas phase products and the surface of the catalyst are analyzed simultaneously in real time under similar irradiation conditions used previously in batch [96-98]. The setup is equipped with online GC-MS whereby online injections are taken throughout the reaction. A "Sandwich" cell reactor (Figure 13a) was used to carry out these experiments where the catalyst is fixed in the cell as a self-supported pellet (20 mg). The sample was first activated under H_2 at 200 °C then its activity for the CO_2 methanation was assessed with a molar ratio of 4:1 of H_2 to CO_2 with a total flow rate of 10 $cm^3 \cdot min^{-1}$.

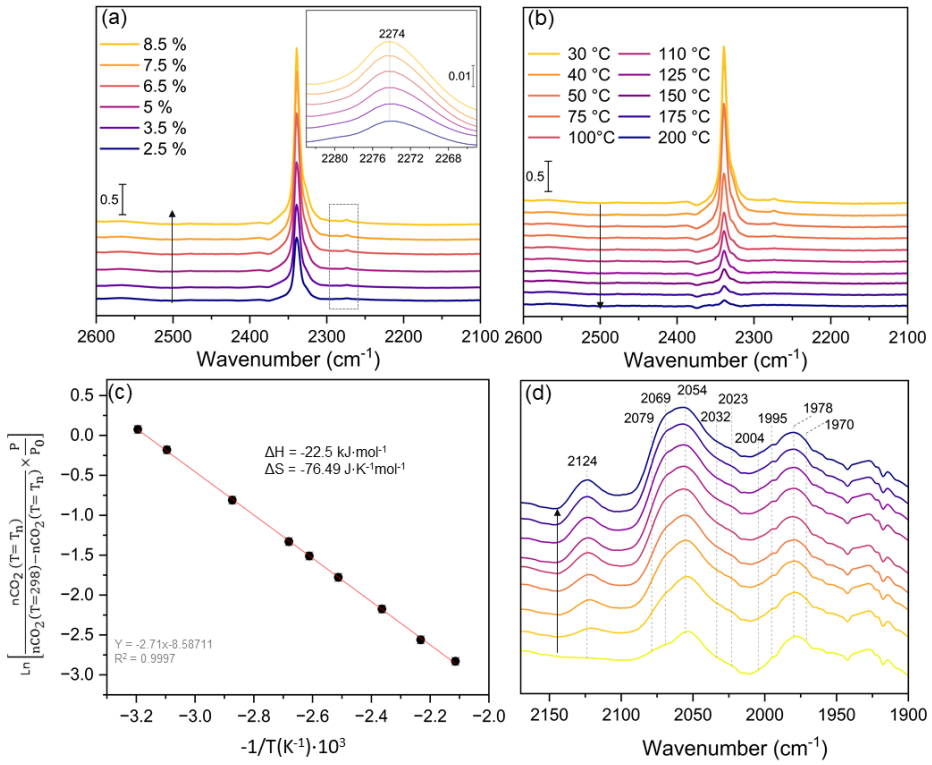

Figure 12. (a, b) FT-IR spectra of chemisorbed CO_2 on RuO_x@UiO-66(Zr/Ti)-NO_2 versus different concentration of CO_2 in Argon and temperature; respectively (total flow rate = 20 $cm^3 \cdot min^{-1}$), (c) the corresponding enthalpy and the entropy of the CO_2 chemisorption, and (d) Evolution of FT-IR spectra of adsorbed CO on RuO_x@UiO-66(Zr/Ti)-NO_2 in the 2150-1900 cm^{-1}.

The photo-thermal CO_2 methanation activity of RuO_x@UiO-66(Zr/Ti)-NO_2 was tested under different temperatures (Figure 13b,c). No CH_4 production was detected at 30 °C, either in darkness or under visible light irradiation, as evidenced by the analysis of the gas phase at the steady-state. However, upon reaching 75 °C, CH_4 production increased with rising temperature in the absence of light. Interestingly, under irradiation, CH_4 production exhibited a significant increase with increasing temperature, reaching 8 $mmol \cdot g^{-1} \cdot h^{-1}$ at 200 °C, with a selectivity of 98.3 %. This observation was further confirmed by FT-IR analysis, which revealed only CH_4 and H_2O as gas phase products (Figure 13b). Complementary results of the GC analysis showed, in addition to CH_4, the production of ethane (under the detection limit of the used FT-IR-gas analysis) as side product with a selectivity of 1.7 % respectively (inset of Figure 13c). Subsequently, an investigation into the impact of lamp intensity on the activity of RuO_x@UiO-66(Zr/Ti)-NO_2 was carried out at 200 °C, as illustrated in Figure 13d. The sample's activity decreased in quasi-linear manner from 8.7 to 3.5 $mmol \cdot g^{-1} \cdot h^{-1}$ as the relative intensity of the lamp decreased from 100 to 20 % I_0. No significant deactivation was observed in agreement with the previous experiments that were conducted in batch conditions at different simulated sunlight irradiation intensities. The decline in the sample's activity with decreasing lamp intensity suggests a diminished prominence of plasmonic effects during the reaction under irradiation. This indicates that the catalytic behavior may be governed by factors beyond predominant plasmonic-mediated mechanisms.

In an attempt to gain more information of the underlying mechanism of the CO_2 hydrogenation over the RuO_x@UiO-66(Zr/Ti)-NO_2, the surface of the catalyst was simultaneously monitored by FT-IR during the reaction. The IR spectra of the

surface, at steady state, between 30 and 200 °C are shown in Figure 13e. Results are subtracted from the spectrum at 30 °C of the preactivated sample. It is essential to note that the spectral regions corresponding to stretching vibration of formates and carbonates, specifically between 1600 and 1300 cm^{-1}, are saturated. Therefore, for assigning the different possible reaction intermediates, both the CO vibrational region and the unobstructed region between 1200 and 1000 cm^{-1} are taken into consideration. Different bands emerged as temperature increased in the CO region mainly at 2088 and 1985 cm^{-1} possibly attributed to adsorbed CO on $Ru^{\delta+}$ on the proximity of TiO_2 [89]. Furthermore, a band emerged as temperature increased from 30 to 75 °C at 2016 cm^{-1} after which it diminished. This decrease was accompanied with the start of the CH_4 production at 75 °C (Figure 13b curve b4). This band could be attributed to CO linearly adsorbed on Ru^0. These results indicates that the formation of CO on the surface is promoted at lower temperatures even if no CH_4 is produced yet. No detection of CO in gas phase at high temperature, emphasizes its key role as an intermediate in the CO_2 methanation reaction over RuO_x@UiO-66(Zr/Ti)-NO_2. At higher temperatures, the formation of formyl as an intermediate was suggested by the presence of the band at 1175 cm^{-1}.[99] Furthermore, various bands corresponding to methoxy species are observed in the spectra at 1160 (on-top) and 1060 (doubly bridging) cm^{-1} owing to the stretching vibrations of methoxys[100]. Also, a band at 1130 cm^{-1} elevated as temperature increased that probably attributed to dioxymethylene adsorbed on the surface[101]. It is important to mention that increasing the temperature causes a shift in the vibrational bands of species present on the surface[88], justifying the negative signals on the subtracted spectra.

To confirm involvement of the various species in the reaction mechanism and their intermediates role a steady state isotopic transient kinetic analysis (SSITKA)

experiment using *operando* FT-IR spectroscopy was performed at 200°C [102]. It corresponds to replacing $^{12}CO_2$ by its isotope $^{13}CO_2$ at steady state under the same reaction conditions. The isotopic transient leads to shift of the IR bands of the surface intermediates as well as their corresponding final. Additionally, this approach ensures that any observed shift would solely result from isotopic exchange between $^{13}CO_2$ and $^{12}CO_2$ and not due to the change of temperature and structural band's shift. However, due to the fact that pure $^{13}CO_2$ is very expensive, this experiment was carried out under diluted conditions (1 % of $^{12}CO_2$ in Argon then exchange to 1% of $^{13}CO_2$ in Argon). Interestingly $^{13}CH_4$ was produced selectively with $^{13}CO_2$ with a similar quantity to that produced with $^{12}CO_2$ (Figure 13g). This was accompanied with the shift (3 or 4 cm^{-1}; Table S4) in IR bands of different species previously attributed to CO, formyl, methoxy, and dioxymethylene with $^{13}CO_2$, as depicted in Figure 13f. Therefore, these confirms the role of these species as reaction intermediates. It should be noted that due to the overlap with the CO vibration, it was difficult to distinguish the band related to the hydride bond formed by H_2 dissociation on reduced RuO_x.

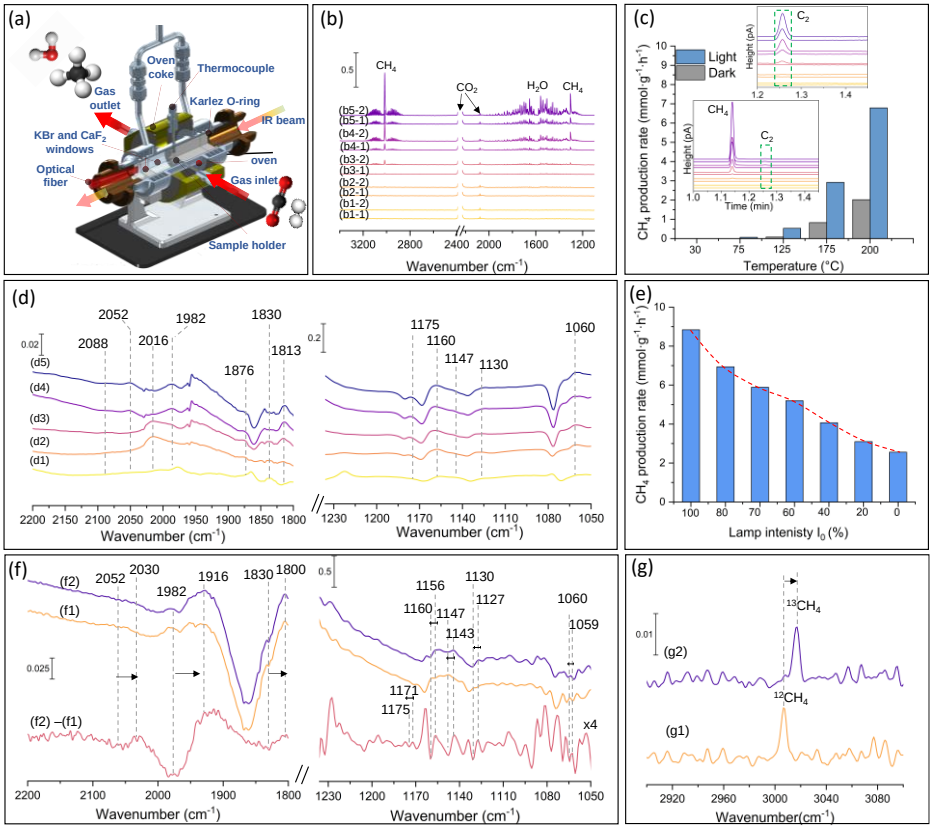

Figure 13. (a) Sandwich IR reactor-cell used for studying the CO_2 methanation reaction under visible light in continuous flow. (b) the FT-IR spectra of the reaction gas phase: (b1) 30, (b2) 75, (b3) 125, (b4) 175 and (b5) 200 °C with (-1) in dark and (-2) after irradiation at steady state, (c) activity of RuO_x@UiO-66(Zr/Ti)-NO_2 as function of temperature in dark and under visible light irradiation (inset: GC chromatograms of the reaction gas phase under same conditions). (d) *Operando* FT-IR spectra of RuO_x@UiO-66(Zr/Ti)-NO_2 versus temperature: (d1) 30, (d2) 75, (d3) 125, (d4) 175 and (d5) 200 °C in the 2200-1800 and the 1200-1000 cm^{-1} vibrational regions. (e) Activity of RuO_x@UiO-66(Zr/Ti)-NO_2 as function of lamp intensity. (f) FT-IR spectra of the catalyst during the photoassisted methanation at 200°C of (1) $^{13}CO_2$ and (2) $^{12}CO_2$ and the corresponding subtracted spectrum ($^{13}CO_2$ - $^{12}CO_2$) is presented in (d3) (intensity was multiplied by four for clarity. (g) FT-IR gas phase spectra of gaseous CH_4 produced during the photoassisted methanation of (1) $^{12}CO_2$ and (2) $^{13}CO_2$ at 200°C. The arrow corresponds to shift of the IR bands due to the isotopic exchange from $^{12}CO_2$ to $^{13}CO_2$. The assignments of the different IR bands are summarized in Tables S3 and S4.

Based on the spectral investigations mentioned above, an overall mechanism is proposed for the reaction unfolds as illustrated in Figure 14. Initially, CO_2 is adsorbed on the surface, primarily on RuO_x species, accompanied with a hydride formation of reduced RuO_x. Subsequently, CO is generated as the primary intermediate of CO_2 reduction, which exhibits strong surface adsorption. This is evident from the absence of CO as final product in the gas phase, as confirmed by FT-IR and GC analyses (Figure 13b, c).

As temperature increases, the photoassisted reduction of CO to formyl is promoted, followed by its conversion to dioxymethylene through interaction with surface oxygen. Then, the photoassisted reduction of dioxymethylene produces methoxy as the final intermediate species before generating CH_4 and water as final products through further reduction. This mechanism emphasizes the dual role of RuO_x and reduced Ru in the production of CH_4 from CO_2 and H_2.

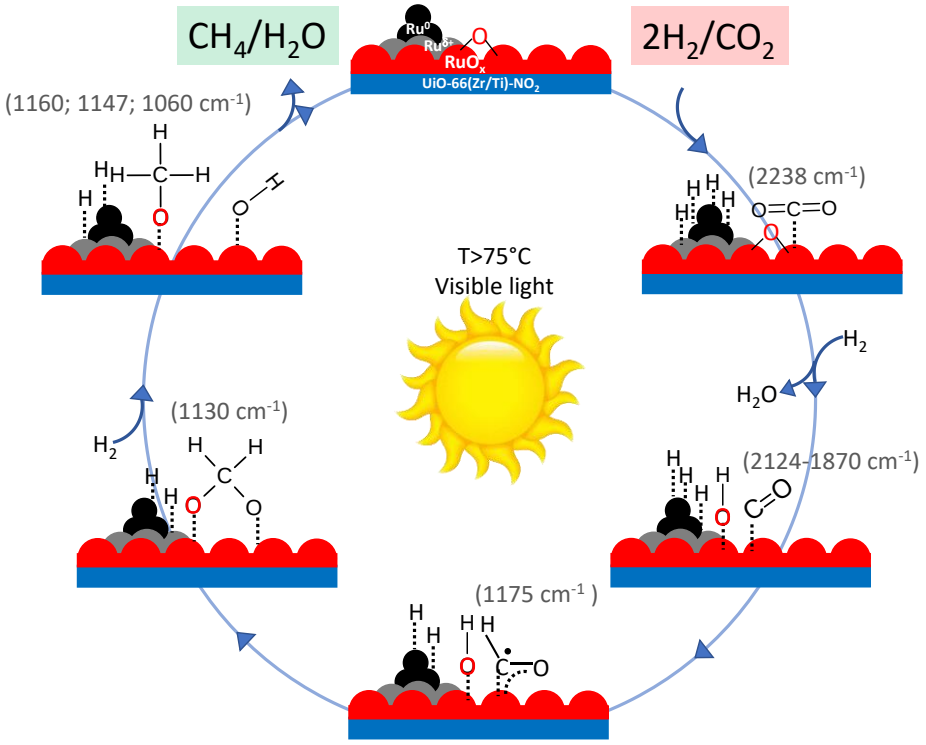

Figure 14. The proposed mechanism of the photo-assisted CO_2 methanation over RuO_x@UiO-66(Zr/Ti)-NO_2 based on the assignment of the characteristic IR bands of the various species.

5.5 Conclusions

This study describes the development of multifunctional and photocatalytically active UiO-66 solids supported RuO_x NPs (2 ± 0.1 nm) for CO_2 methanation at 200 ºC under simulated concentrated sunlight irradiation. The photocatalytic activity of the samples followed the order UiO-66(Zr/Ti)-NO_2 > UiO -66(Zr/Ti)-NH_2 ~ UiO-66(Zr)-NO_2 > UiO-66(Zr)-NH_2. In contrast to most reports involving UiO-66 photocatalysts based on the use of the 2-aminoterephthalate ligand, the present study highlights the importance of using 2-nitroterephthalate ligands to achieve high activity with Zr(IV) or mixed-metal Zr(IV)/Ti(IV) nodes within UiO-66 based materials and associated with the unique energy band level diagram of these solids. It should be noted that UiO-66(Zr/Ti)-NO_2 is a reusable photocatalyst that exhibits record activity (5.03 mmol g^{-1} after 22 h; AQY at 350, 400 and 600 nm of 1.67, 0.25 and 0.01, respectively) compared to previous analogous reports on MOF-based materials. Based on the results of several spectroscopic, electrochemical and photocatalytic experiments, it could be considered that RuO_x@UiO-66(Zr/Ti)-NO_2 operates in a dual photochemical and photothermal reaction pathway. The photocatalytic CO_2 hydrogenation pathway was further investigated in flow condition using *operando* FT-IR spectroscopy. The results are in very good agreement with that obtained under batch conditions. Basing on the surface analysis and SSITKA experiment, a mechanism involving CO, formyl, dioxomethane, and methoxy, as intermediates, has been illustrated. In summary, here it is proposed an innovative combination of nitro functionalized UiO-66 solids with mixed-metal Zr(IV)/Ti(IV) nodes and supported RuO_x NPs as co-catalyst to progress towards solar-driven photocatalytic CO_2 methanation. The authors consider that this work will open new possibilities for the development of multifunctional MOFs as solar-driven photocatalysts for selective CO_2 transformations.

5.6 Author contribution

Celia María Rueda Navarro performed the synthesis of all the materials under study and performed all the photocatalytic tests. She measured XRD, and SEM for the characterization of the solids and assisted with TEM analyses. Additionally, she handled data analysis for other characterizations conducted by technicians, such as BET, TGA, XPS, and UV. She also conducted the photocurrent and EIS experiments and participated in the photoluminescence experiments. She participated in several meeting with researchers in charge of both femtosecond TAS and *operando* FT-IR measurements. It should be also noted that she acquired further experience on *operando* FT-IR during a three-month period of research at the University of Caen under the supervision of Dr. Mohamad El-Roz and Professor Marco Daturi.

5.7 References

(1) Bosa, K.; Gupta, J. Stranded assets and stranded resources: Implications for climate change mitigation and global sustainable development. *Energy Res. Soc. Sci.* **2019**, *56*, 101215.

(2) Paraschiv, S.; Paraschiv, L. S. Trends of carbon dioxide (CO_2) emissions from fossil fuels combustion (coal, gas and oil) in the EU member states from 1960 to 2018. *Energy Rep.* **2020** *6*,237-242.

(3) Østergaard, P. A.; Duic, N.; Noorollahi, Y.; Mikulcic, H.; Kalogirou, S. Sustainable development using renewable energy technology. *Renew. Energ.* **2020**, *146*, 2430–2437.

(4) Sherwood, J. The significance of biomass in a circular economy. *Bioresour. Technol.* **2020**, *300*, 122755.

(5) Radovanović, M.; Filipović, S.; Vukadinović, S.; Trbojević, M.; Podbregar, I. Decarbonisation of eastern European economies: monitoring, economic, social and security concerns. *Energy Sustain. Soc.* **2022**, *12*, 16.

(6) de Kleijne, K.; Hanssen, S. V.; van Dinteren, L.; Huijbregts, M. A. J.; van Zelm, R.; de Coninck, H. Limits to Paris compatibility of CO_2 capture and utilization. *One Earth* **2022**, *5*, 168-185.

(7) Mac Dowell, N.; Fennell, P. S.; Shah, N.; Maitland, G. C. The role of CO_2 capture and utilization in mitigating climate change. *Nat. Clim. Change* **2017**, *7* (243-249).

(8) Mikkelsen, M.; Jørgensen, M.; Krebs, F. C. The teraton challenge. A review of fixation and transformation of carbon dioxide. *Energ. Environ. Sci.* **2010**, *3*, 43-81.

(9) Ding, M.; Flaig, R. W.; Jiang, H.-L.; Yaghi, O. M. Carbon capture and conversion using metal–organic frameworks and MOF-based materials. *Chem. Soc. Rev.* **2019**, *48*, 2783-2828.

(10) Zhang, Z.; Pan, S.-Y.; Li, H.; Cai, J.; Olabi, A. G.; Anthony, E. J.; Manovic, V. Recent advances in carbon dioxide utilization. *Renewable Sustainable Energy Rev.* **2020**, *125*, 109799.

(11) Artz, J.; Müller, T. E.; Thenert, K.; Kleinekorte, J.; Meys, R.; Sternberg, A.; Bardow, A.; Leitner, W. Sustainable conversion of carbon dioxide: An integrated review of catalysis and life cycle assessment. *Chem. Rev.* **2018**, *118*, 434–504.

(12) Dhakshinamoorthy, A.; Navalón, S.; Primo, A.; García, H. Selective gas-phase hydrogenation of CO_2 to methanol catalysed by metal-organic frameworks. *Angew. Chem. Int. Ed.* **2023**, e202311241.

(13) Bellabarba, R.; Johnston, P.; Moss, S.; Sievers, C.; Subramaniam, B.; Tway, C.; Wang, Z.; Zhu, H. Net zero transition: possible implications for catalysis. *ACS Catal.* **2023**, *13*, 7917–7928.

(14) De, S.; Dokania, A.; Ramirez, A.; Gascon, J. Advances in the design of heterogeneous catalysts and thermocatalytic processes for CO_2 utilization. *ACS Catal.* **2020**, *10*, 14147-14185.

(15) Lin, H.; Luo, S.; Zhang, H.; Ye, J. Toward solar-driven carbon recycling. *Joule* **2022**, *6*, 294–314.

(16) Lewis, N. S. Research opportunities to advance solar energy utilization. *Science* **2016**, *351*, 1920.

(17) Lewis, N. S.; Nocera, D. G. Powering the planet: Chemical challenges in solar energy utilization. *Proc. Natl. Acad. Sci. USA* **2006**, *103*, 15729-15735.

(18) Ciocarlan, R.-G.; Blommaerts, N.; Lenaerts, S.; Cool, P.; Verbruggen, S. W. Recent trends in plasmon-assisted photocatalytic CO_2 reduction. *ChemSusChem* **2023**, *16*, 202201647.

(19) Wang, Q.; Domen, K. Particulate photocatalysts for light-driven water splitting: Mechanisms, challenges, and design strategies. *Chem. Rev.* **2020**, *120*, 919-985.

(20) Halmann, M. Photoelectrochemical reduction of aqueous carbon dioxide on p-type gallium phosphide in liquid junction solar cells. *Nature.* **1978**, *275*, 115–116.

(21) Thampi, K. R.; Kiwi, J.; Graetzel, M. Methanation and photo-methanation of carbondioxide at room-temperature and atmospheric-pressure. *Nature.* **1987**, *327*, 506-508.

(22) Chen, D.; Zhang, X.; Lee, A. F. Synthetic strategies to nanostructured photocatalysts for CO_2 reduction to solar fuels and chemicals. *J. Mater. Chem. A* **2015**, *3*, 14487-14516.

(23) Li, X.; Yu, J.; Jaroniec, M.; Chen, X. Co-catalysts for selective photoreduction of CO_2 into solar fuels. *Chem. Rev.* **2019**, *119*, 3962−4179.

(24) Ulmer, U.; Dingle, T.; Duchesne, P. N.; Morris, R. H.; Tavasoli, A.; Wood, T.; Ozin, G. A. Fundamentals and applications of photocatalytic CO_2 methanation. *Nat. Commun.* **2019**, *10*, 3169.

(25) Mateo, D.; Albero, J.; Garcıa, H. Titanium-perovskite-supported RuO2 nanoparticles for photocatalytic CO_2 methanation. *Joule* **2019**, *3*, 1949-1962.

(26) Mateo, D.; Albero, J.; García, H. Photoassisted methanation using Cu_2O nanoparticles supported on graphene as a photocatalyst. *Energy Environ. Sci.* **2017**, *10*, 2392-2400.

(27) Mateo, D.; Albero, J.; García, H. Graphene supported NiO/Ni nanoparticles as efficient photocatalyst for gas phase CO_2 reduction with hydrogen. *Appl. Catal. B.-Environ.* **2018**, *224*, 563-571.

(28) Barrio, J.; Mateo, D.; Albero, J.; García, H.; Shalom, M. A heterogeneous carbon nitride-nickel photocatalyst for efficient low-temperature CO_2 methanation. *Adv. Energy Mater.* **2019**, *9*, 1902738.

(29) Jelle, A. A.; Ghuman, K. K.; O'Brien P.G.; Hmadeh, M.; Sandhel, A.; Perovic, C. D. D.; Singh, V.; Mims, C. A.; Ozin, G. A. Highly efficient ambient temperature CO_2 photomethanation catalyzed by nanostructured RuO_2 on silicon photonic crystal support. *Adv. Energy Mater.* **2018**, *8*, 1702277.

(30) Albero, J.; Peng, Y.; García, H. Photocatalytic CO_2 reduction to C_{2+} products. *ACS Catal.* **2020**, *10*, 5734-5749.

(31) Navalón, S.; Dhakshinamoorthy, A.; Álvaro, M.; Ferrer, B.; García, H. Metal–organic frameworks as photocatalysts for solar-driven overall water splitting. *Chem. Rev.* **2023**, *123*, 445-490.

(32) Younas, M.; Loong Kong, L. L.; Bashir, M. J. K.; Nadeem, H.; Shehzad, A.; Sethupathi, S. Recent advancements, fundamental challenges, and opportunities in catalytic methanation of CO_2. *Energ. Fuels* **2016**, *30*, 8815-8831.

(33) Walspurger, S.; Haije, W. G.; Louis, B. CO_2 reduction to substitute natural gas: Toward a global low carbon energy system. *Isr. J. Chem.* **2014**, *54*, 1432-1442.

(34) Khan, S.; Dai, X.; Ali, T.; Mahmood, S.; ul Haq, M.; Riaz, M. S.; Hu, Y. Recent advances on photo-thermo-catalysis for carbon dioxide methanation, . *Int. J. Hydrog. Energy* **2022**, *48*, 24756-24787.

(35) Zhao, J.; Liu, J.; Li, Z.; Wang, K.; Shi, R.; Wang, P.; Wang, Q.; Waterhouse, G. I. N.; Wen, X.; Zhang, T. Ruthenium-cobalt single atom alloy for CO photo-hydrogenation to liquid fuels at ambient pressures. *Nat. Commun.* **2023**, *14*, 1909.

(36) Cabrero-Antonino, M.; Remiro-Buenamañana, S.; Souto, M.; García-Valdivia, A. A.; Choquesillo-Lazarte, D.; Navalón, S.; Rodríguez-Diéguez, A.; Mínguez-Espallargas, G.; García, H. Design of cost-efficient and photocatalytically active Zn-based MOFs decorated with Cu_2O nanoparticles for CO_2 methanation. *Chem. Commun.* **2019**, *55*, 10932-10935.

(37) Férey, G.; Mellot-Draznieks, C.; Serre, C.; Millange, F.; Dutour, J.; Surblé, S.; Margiolaki, I. A chromium terephthalate-based solid with unusually large pore volumes and surface area. *Science* **2005**, *23*, 2040-2042.

(38) Furukawa, H.; Cordova, K. E.; O'Keeffe, M.; Yaghi, O. M. The chemistry and applications of metal-organic frameworks. *Science* **2013**, *341*, 1230444.

(39) Kitagawa, S.; Kitaura, R.; Noro, S.-I. Functional porous coordination polymers. *Angew. Chem. Int. Ed.* **2004**, *43*, 2334-2375.

(40) Dhakshinamoorthy, A.; Asiri, A. M.; García, H. Metal-organic framework (MOF) compounds: Photocatalysts for redox reactions and solar fuel production. *Angew. Chem. Int. Ed.* **2016**, *55*, 5414-5445.

(41) Li, R.; Zhang, W.; Zhou, K. Metal–organic-framework-based catalysts for photoreduction of CO_2. *Adv. Mater.* **2018**, *30*, 1705512.

(42) Kolobov, N.; Goesten, M. G.; Gascon, J. Metal–Organic Frameworks: Molecules or Semiconductors in Photocatalysis? . *Angew. Chem. Int. Ed.* **2021**, *60*, 26038-26052.

(43) Wang, S.; Cabrero-Antonino, M.; Navalón, S.; Chen-chen Cao, C.; Tissot, A.; Dovgaliuk, I.; Marrot, J.; Martineau-Corcos, C.; Yu, L.; Wang, H.; et al. A robust titanium isophthalate metal-organic framework for visible-light photocatalytic CO_2 methanation. *Chem* **2020**, *6*, 3409-3427.

(44) Cabrero-Antonino, M.; Ferrer, B.; Baldoví, H. G.; Navalón, S. Toward solar-driven photocatalytic CO_2 methanation under continuous flow operation using benchmark MIL-125(Ti)-NH_2 supported ruthenium nanoparticles. *Chem. Eng. J.* **2022**, *445*, 136426.

(45) Liu, H.; Cheng, M.; Liu, Y.; Zhang, G.; Li, L.; Du, L.; Li, B.; Xiao, S.; Wang, G.; Yang, X. Modified UiO-66 as photocatalysts for boosting the carbon-neutral energy cycle and solving environmental remediation issues. *Coord. Chem. Rev.* **2022**, *458*, 214428.

(46) Duflot, M.; Marchal, C.; Caps, V.; Artero, V.; Christoforidis, K.; Keller, V. Optimization of NH_2-UiO-66/TiO_2/Au composites for enhanced gas-phase CO_2 photocatalytic reduction into CH_4. *Catal. Today* **2023**, *413-415*, 114018.

(47) Melillo, A.; García-Aboal, R.; Navalon, S.; Atienzar, P.; Ferrer, B.; Álvaro, M.; Garcia, H. Photoactive Zr and Ti metal-organic-frameworks for solid-state solar cells. *ChemPhysChem* **2021**, *22*, 842-848.

(48) Santiago-Portillo, A.; Baldoví, H. G.; Fernandez, M. T. G.; Navalón, S.; Atienzar, P.; Ferrer, B.; Alvaro, M.; Garcia, H.; Li, Z. Ti as mediator in the photoinduced electron transfer of mixed-metal NH_2–UiO-66(Zr/Ti): transient absorption spectroscopy study and application in photovoltaic cell. *J. Phys. Chem. C* **2017**, *121*, 7015-7024.

(49) Rada, Z. H.; Abid, H. R.; Sun, H.; Shang, J.; Li, J.; He, Y.; Liu, S.; Wang, S. Effects of -NO_2 and -NH_2 functional groups in mixed-linker Zr-based MOFs on gas adsorption of CO_2 and CH_4. *Prog. Nat. Sci.: Mater. Int.* **2018**, *28*, 160-167.

(50) Dai, S.; Montero-Lanzuela, E.; Tissot, A.; Baldoví, H. G.; García, H.; Navalón, S.; Serre, C. Room temperature design of Ce(IV)-MOFs: from photocatalytic HER and OER to overall water splitting under simulated sunlight irradiation. *Chem. Sci.* **2023**, *14*, 3451–3461.

(51) Rueda-Navarro, C. M.; Ferrer, B.; Baldoví, H. G.; Navalón, S. Photocatalytic hydrogen production from glycerol aqueous solutions as sustainable feedstocks using Zr-based UiO-66 materials under simulated sunlight irradiation. *Nanomaterials* **2022**, *12*, 3808.

(52) Cabrero-Antonino, M.; Melillo, A.; Montero-Lanzuela, E.; Álvaro, M.; Ferrer, B.; Vayá, I.; Baldoví, H. G.; Navalón, S. Solar-driven gas phase photocatalytic CO_2 methanation by multimetallic UiO-66 solids decorated with RuO_x nanoparticles. *Chem. Eng. J.* **2023**, *468*, 143553.

(53) Wu, X.-P.; Gagliardi, L.; Truhlar, D. G. Metal doping in cerium metal-organic frameworks for visible-response water splitting photocatalysts. *J. Chem. Phys.* **2019**, *150*, 041701.

(54) Rueda-Navarro, C. M.; Cabrero-Antonino, M.; Escamilla, P.; Díez-Cabanes, V.; Fan, D.; Atienzar, P.; Ferrer B.; Vayá, I.; Maurin, G.; Baldoví, H. G.; et al. Solar-assisted photocatalytic water splitting using defective UiO-66 solids from modulated synthesis. *Nano Res.* **2023**, 1-17.

(55) Shearer, G. C.; Chavan, S.; Bordiga, S.; Svelle, S.; Olsbye, U.; Lillerud, K. P. Defect engineering: tuning the porosity and composition of the metal−organic framework UiO-66 via modulated synthesis. *Chem. Mater.* **2016**, *28*, 3749−3761.

(56) Cavka, J. H.; Jakobsen, S.; Olsbye, U.; Guillou, N.; Lamberti, C.; Bordiga, S.; Lillerud, K. A new zirconium inorganic building brick forming metal organic frameworks with exceptional stability. *J. Am. Chem. Soc.* **2008**, *130*, 13850-13851.

(57) Santiago-Portillo, A.; Navalón, S.; lvaro, M.; García, H. Generating and optimizing the catalytic activity in UiO-66 for aerobic oxidation of alkenes by post-synthetic exchange Ti atoms combined with ligand substitution. *J. Catal.* **2018**, *365*, 450-463.

(58) Sun, D.; Liu, W.; Qiu, M.; Zhang, Y.; Li, Z. Introduction of a mediator for enhancing photocatalytic performance via post-synthetic metal exchange in metal–organic frameworks (MOFs). *Chem. Commun.* **2015**, *51*, 2056-2059.

(59) Santaclara, J. G.; Olivos-Suarez, A. I.; Gonzalez-Nelson, A.; Osadchii, D.; Nasalevich, M. A.; van der Veen, M. A.; Kapteijn, F.; Sheveleva, A. M.; Veber, S. L.; Fedin, M. V.; et al. Revisiting the Incorporation of Ti(IV) in UiO-type metal–organic frameworks: metal exchange versus grafting and their implications on photocatalysis. *Chem. Mater.* **2017**, *29*, 8963-8967.

(60) Wang, Y.; Li, H.; Zhou, W.; Zhang, X.; Zhang, B.; Yu, Y. Structurally disordered RuO_2 nanosheets with rich oxygen vacancies for enhanced nitrate electroreduction to ammonia. *Angew. Chem. Int. Ed.* **2022**, *61*, e202202604.

(61) Kandiah, M.; Nilsen, M. H.; Usseglio, S.; Jakobsen, S.; Olsbye, U.; Tilset, M.; Larabi, C.; Quadrelli, E. A.; Bonino, F.; Lillerud, K. P. Synthesis and stability of tagged UiO-66 Zr-MOFs. *Chem. Mater.* **2010**, *22*, 6632-6640.

(62) Zhu, J.; Wu, L.; Bu, Z.; Jie, S.; Li, B.-G. Polyethyleneimine-modified UiO-66-NH_2(Zr) metal–organic frameworks: preparation and enhanced CO_2 selective adsorption. *ACS Omega* **2019**, *4*, 3188–3197.

(63) Nasalevich, M. A.; Van Der Veen, M.; Kapteijn, F.; Gascon, J. Metal-organic frameworks as heterogeneous photocatalysts: Advantages and challenges. *CrystEngComm* **2014**, *16*, 4919-4926.

(64) Hendrickx, K.; Vanpoucke, D. E. P.; Leus, K.; Lejaeghere, K.; Van Yperen-De Deyne, A. V.; Van Speybroeck, V.; Van Der Voort, P.; Hemelsoet, K.

Understanding intrinsic light absorption properties of UiO-66 frameworks: A combined theoretical and experimental study. *Inorg. Chem.* **2015**, *54*, 10701-10710.

(65) Wu, X.-P.; Gagliardi, L.; Truhlar, D. G. Cerium metal–organic framework for photocatalysis. *J. Am. Chem. Soc.* **2018**, *140*, 7904-7912.

(66) Zhang, J.; Chen, H.; Duan, X.; Sun, H.; Wang, S. Photothermal catalysis: from fundamentals to practical applications. *Mater. Today* **2023**, *268*, 234-253.

(67) Zhang, X.; Li, X.; Zhang, D.; Su, N. Q.; Yang, W.; Everitt, H. O.; Liu, J. Product selectivity in plasmonic photocatalysis for carbon dioxide hydrogenation. *Nat. Commun.* **2018**, *8*, 14542.

(68) Luo, S.; Lin, H.; Wang, Q.; Ren, X.; Hernández-Pinilla, D.; Nagao, R.; Xie, Y.; Yang, G.; Li, S.; Song, H.; et al. Triggering water and methanol activation for solar-driven H_2 production: Interplay of dual active sites over plasmonic ZnCu alloy. *J. Am. Chem. Soc.* **2021**, *143*, 12145−12153.

(69) Ren, J.; Ouyang, S.; Xu, H.; Meng, X.; Wang, T.; Wang, D.; Ye, J. Targeting activation of CO2 and H2 over Ru-loaded ultrathin layered double hydroxides to achieve efficient photothermal CO_2 methanation in flow-type system. *Adv. Energy Mater.* **2016**, 1601657.

(70) Guo, C.; Tang, Y.; Yang, Z.; Zhao, T.; Liu, J.; Zhao, Y.; Wang, F. Reinforcing the efficiency of photothermal catalytic CO_2 methanation through integration of Ru nanoparticles with photothermal $MnCo_2O_4$ nanosheets. *ACS Nano* **2023**, *17*, 23761−23771.

(71) Xiong, K.; Wang, Y.; Zhang, F.; Li, X.; Lang, X. Linker length-dependent photocatalytic activity of β-ketoenamine covalent organic frameworks. *Appl. Catal. B.-Environ* **2023**, *322*, 122135.

(72) Yan, X.; Cao, M.; Li, S.; Duchesne, P. N.; Sun, W.; Mao, C.; Song, R.; Lu, Z.; Chen, X.; Qian, W.; et al. Visualizing the birth and monitoring the life of a bimetallic methanation catalyst. *J. Am. Chem. Soc.* **2023**, *145*, 27358−27366.

(73) Beuls, A.; Swalus, C.; Jacquemin, M.; Heyen, G.; Karelovic, A.; Ruiz, P. CO_2 hydrogenation at low temperature over Rh/γ-Al_2O_3 catalysts: Effect of the metal particle size on catalytic performances and reaction mechanism. *Appl. Catal. B* **2012**, *113–114*, 237-249.

(74) Mateo, D.; Santiago-Portillo, A.; Albero, J.; Navalón, S.; Alvaro, M.; García, H. Long-term photostability in terephthalate metal organic frameworks. *Angew. Chem. Int. Ed.* **2019**, *58*, 17843-17848.

(75) Mateo, D.; Cerrillo, J. L.; Durini, S.; Gascon, J. Fundamentals and applications of photo-thermal catalysis. *Chem. Soc. Rev.* **2021**, *50*, 2173-2210.

(76) Khan, I. S.; Garzon-Tovar, L.; Mateo, D.; Gascon, J. Metal-organic-frameworks and their derived materials in photo-thermal catalysis. *Eur. J. Inorg. Chem.* **2022**, *28*, e202200316.

(77) Song, C.; Wang, Z.; Yin, Z.; Xiao, D.; Ma, D. Principles and applications of photothermal catalysis. *Chem Catalysis* **2022**, *2*, 52–83.

(78) Ruckebusch, C.; Sliwa, M.; Pernot, P.; de Juan, A.; Tauler, R. Comprehensive data analysis of femtosecond transient absorption spectra: A review. *J. Photochem. Photobiol. C* **2012**, *13*, 1-27.

(79) Ma, X.; Wang, L.; Zhang, Q.; Jiang, H.-L. Switching on the photocatalysis of metal–organic frameworks by engineering structural defects. *Angew. Chem. Int. Ed.* **2019**, *58*, 12175 –12179.

(80) Xiao, J.-D.; Shang, Q.; Xiong, Y.; Zhang, Q.; Luo, Y.; Yu, S.-H.; Jiang, H.-L. Boosting photocatalytic hydrogen production of a metal–organic framework decorated with platinum nanoparticles: The platinum location matters. *Angew. Chem. Int. Ed.* **2016**, *128*, 9535-9539.

(81) Cabrero-Antonino, M.; Melillo, A.; Montero-Lanzuela, E.; Álvaro, M.; Ferrer, B.; Vayá, I.; Baldoví, H. G.; Navalón, S. Solar-driven gas phase photocatalytic CO_2 methanation by multimetallic UiO-66 solids decorated with RuO_x nanoparticles. *Chem. Eng. J.* **2023**, *468*.

(82) Melillo, A.; Cabrero-Antonino, M.; Navalón, S.; Álvaro, M.; Ferrer, B.; García, H. Enhancing visible-light photocatalytic activity for overall water splitting in UiO-66 by controlling metal node composition. *Appl. Catal. B* **2020**, *278*.

(83) Bhattacharyy, A.; Gutiérrez, M.; Cohen, B.; Szalad, H.; Albero, J.; Garcia, H.; Douhal, A. Unraveling the optimal cerium content for boosting the photoresponse activity of mixed-metal Zr/Ce-based metal−organic frameworks through a photodynamic and photocurrent correlation: Implications on water splitting efficiency. *ACS Appl. Mater. Interfaces* **2023**, *15*, 36434−36446.

(84) Bhattacharyya, A.; Gutiérrez, M.; Cohen, B.; Valverde-González, A.; Iglesias, M.; Douhal, A. How does the metal doping in mixed metal MOFs influence their photodynamics? A direct evidence for improved photocatalysts. *Mater. Today Energy* **2022**, *29*, 101125.

(85) Yu, X. M.; Li, J.; Du, M. H.; Song, X. J.; Huang, H. L.; Nie, L. Adaptive lattice-matched MOF and COF core−shell heterostructure for carbon dioxide photoreduction. *Cell Rep. Phys. Sci.* **2023**, *4*, 101657.

(86) L., M.; Schirato, A.; Montini, T.; Alabastri, A.; Naldoni, A.; Fornasiero, P. Challenges in temperature measurements in gas-phase photothermal catalysis. *Joule* **2022**, *6*, 1727–1742.

(87) Liu, L.; Zhong, K.; Meng, L.; Hemelrijck, D. V.; Wang, L.; Glorieux, C. Temperature-sensitive photoluminescent CdSe-ZnS polymer composite film for lock-in photothermal characterization. *J. Appl. Phys.* **2016**, *119*, 224902.

(88) Douma, F.; Lakiss, L.; Lebedev, O. I.; Cardin, J.; Kostov, K. L.; El Fallah, J.; Valtchev, V.; El-Roz, M. Silver quasi-nanoparticles: bridging the gap between molecule-like clusters and plasmonic nanoparticles. *Mat. Adv.* **2021**, *2* (16), 5453-5464.

(89) Hadjiivanov, K.; Lavalley, J.-C.; Lamotte, J.; Maugé, F.; Saint-Just, J.; Che, M. FT-IR Study of CO Interaction with Ru/TiO_2 Catalysts. *J. Catal.* **1998**, *176* (2), 415-425.

(90) Su, B.; Kong, Y.; Wang, S.; Zuo, S.; Lin, W.; Fang, Y.; Hou, Y.; Zhang, G.; Zhang, H.; Wang, X. Hydroxyl-bonded Ru on metallic TiN surface catalyzing CO_2 reduction with H_2O by infrared light. *J. Am. Chem. Soc.* **2023**, *145*, 27415−27423.

(91) Wang, Y.; Liu, Y.; Tan, L.; Lin, X.; Fang, Y.; Lu, X. F.; Hou, Y.; Zhang, G.; Wang, S. Confining ultrafine Pt nanoparticles on In_2O_3 nanotubes for enhanced selective methanol production by CO_2 hydrogenation. *J. Mater. Chem. A* **2023**, *11*, 26804–26811.

(92) Kattel, S.; Liu, P.; Chen, J. G. Tuning selectivity of CO_2 hydrogenation reactions at the metal/oxide interface. *J. Am. Chem. Soc.* **2017**, *139*, 9739–9754.

(93) El-Roz, M.; Lakiss, L.; Telegeiev, I.; Lebedev, O.; Bazin, P.; Vicente, A.; Fernandez, C.; Valtchev, V. High-visible-light photoactivity of plasma-promoted vanadium clusters on nanozeolites for partial photooxidation of methanol. *ACS Appl. Mater. Interfaces* **2017**, *9* (21), 17846-17855.

(94) Hamoud, H.; Wolski, L.; Abdelli, H.; Chtourou, R.; Lebedev, O.; Martin, C.; Fan, D.; Maurin, G.; Maignan, A.; El-Roz, M. Earth-abundant-based photocatalysts for efficient and selective H_2 production through reforming of formic acid under visible light. *ACS Catal.* **2023**, *13* (24), 16266-16278.

(95) Guglielminotti, E.; Boccuzzi, F.; Manzoli, M.; Pinna, F.; Scarpa, M. Ru/ZrO_2 Catalysts: I. O_2, CO, and NO Adsorption and Reactivity. *J. Catal.* **2000**, *192* (1), 149-157.

(96) Hamoud, H. I.; Wolski, L.; Abdelli, H.; Chtourou, R.; Lebedev, O.; Martin, C.; Fan, D.; Maurin, G.; Maignan, A.; El-Roz, M. Earth-Abundant-Based Photocatalysts for Efficient and Selective H_2 Production through Reforming of Formic Acid under Visible Light. *ACS Catal.* **2023**, *13* (24), 16266-16278.

(97) El-Roz, M.; Lakiss, L.; Telegeiev, I.; Lebedev, O. I.; Bazin, P.; Vicente, A.; Fernandez, C.; Valtchev, V. High-visible-light photoactivity of plasma-promoted vanadium clusters on nanozeolites for partial photooxidation of methanol. *ACS Appl. Mater. Interfaces* **2017**, *9* (21), 17846-17855.

(98) Aldana, P. U.; Ocampo, F.; Kobl, K.; Louis, B.; Thibault-Starzyk, F.; Daturi, M.; Bazin, P.; Thomas, S.; Roger, A. Catalytic CO_2 valorization into CH_4 on Ni-based

ceria-zirconia. Reaction mechanism by operando IR spectroscopy. *Catal. Today* **2013**, *215*, 201-207.

(99) Morgan Jr, G. A.; Sorescu, D. C.; Zubkov, T.; Yates Jr, J. T. The Formation and Stability of Adsorbed Formyl as a Possible Intermediate in Fischer− Tropsch Chemistry on Ruthenium. *J. Phys. Chem. B* **2004**, *108* (11), 3614-3624.

(100) Finocchio, E.; Daturi, M.; Binet, C.; Lavalley, J.; Blanchard, G. Thermal evolution of the adsorbed methoxy species on $Ce_xZr_{1-x}O_2$ solid solution samples: a FT-IR study. *Catal. Today* **1999**, *52* (1), 53-63.

(101) Schild, C.; Wokaun, A.; Baiker, A. On the mechanism of CO and CO_2 hydrogenation reactions on zirconia-supported catalysts: a diffuse reflectance FT-IR study: Part I. Identification of surface species and methanation reactions on palladium/zirconia catalysts. *J. Mol. Catal.* **1990**, *63* (2), 223-242.

(102) Issa Hamoud, H.; Wolski, L.; Pankin, I.; Bañares, M. A.; Daturi, M.; El-Roz, M. In situ and operando spectroscopies in photocatalysis: Powerful techniques for a better understanding of the performance and the reaction mechanism. *Top Curr Chem* **2022**, *380* (5), 37.

5.8 Supporting Information

5.8.1 Synthesis of the MOF-based materials

Synthesis of UiO-66(Zr)-NH_2. The solid was prepared using a solvothermal method previously reported[1-3]. Briefly, $ZrCl_4$ (0.862 g, 3.699 mmol), amino- terephthalic acid (0.677 g, 3.701 mmol) and Mili-Q H_2O (0.200 mL, 11.10 mmol) were mixed with DMF (100 mL, 1291 mmol) in 250 ml volumetric flask. The system was heated at 70 °C and stirred during the preparation to ensure complete dissolution of the reagents. Once all reagents were dissolved, the stirring magnet was removed from the system and the flask was closed. Then, it was placed in a pre-heated oven at 120 °C for 72 hours. The resulting precipitate

was recovered by filtration. Then, it was washed three times with DMF and three more with CH_3OH. It was further washed in a Soxhlet for 4 h using CH_3OH as the solvent. And finally, the powder was dried under vacuum at 150 °C overnight.

Synthesis of UiO-66(Zr)-NO_2[1-3]. Briefly, $ZrCl_4$ (0.862 g, 3.699 mmol), nitro- terephthalic acid (0.790 g, 3.701 mmol) and Mili-Q H_2O (0.200 mL, 11.10 mmol) were mixed with DMF (100 mL, 1291 mmol) in 250 ml volumetric flask. The system was heated at 70 °C while stirring to ensure the complete dissolution of the reagents. Once all reagents were well dissolved, the flask was placed in a pre- heated oven at 120 °C for 72 hours after removing the stirring magnet and closing the system. The resulting precipitate was recovered by filtration. Then, it was washed three times with DMF and subsequently, three more with CH_3OH. It was further washed in a Soxhlet for 4 h using CH_3OH as the solvent. Finally, the powder was recovered drying it under vacuum at 150 °C overnight.

UiO-66(Zr/Ti)-NH_2 and UiO-66(Zr/Ti)-NO_2. Both solids were prepared following a PSM[4, 5] using $TiCl_4(THF)_2$ as Ti source under inert atmosphere. 0.45 mmol of previously synthesized UiO-66(Zr)-NH_2 or UiO- 66(Zr)- NO_2, respectively were mixed with 0.135 mmol $TiCl_4(THF)_2$ and suspended in 2.5 mL anhydrous DMF. The mixture was incubated through stirring and under argon atmosphere for 4 days at 120 °C. After cation exchange, the corresponding UiO-66(Zr/Ti) solids were recovered by filtration and sequentially washed with DMF and CH_3OH. Finally, the photocatalysts were dried at 100 °C for 24 h.

Deposition of RuO_x nanoparticles on the mentioned solids. RuO_x NPs were deposited in the as-prepared MOFs using the so-called photodeposition method[6]. Succinctly speaking, the material (50 mg) was introduced in a quartz tube and dispersed in a mixture of Milli-Q water (8 mL) and CH_3OH (13 mL). Subsequently, the corresponding amount of potassium perruthenate (1 % wt of Ru) previously dissolved in water (1 mL) was added to the dispersion. Then, the system was purged with Ar for 30 min and immediately irradiated using a UV-vis light lamp for 4 h. Finally, the resulting solid was filtered and washed several times with Milli-Q water, dried in an oven at 100 ºC overnight and then, left under vacuum at 150 ºC, 24 h.

5.8.2 Characterization techniques

Most of the characterization techniques (PXRD, UV-Vis, TGA, XPS, SEM, TEM, Isothermal N_2 adsorption) have already been discussed in the third chapter in Section 3.8.2, while fluorescence spectroscopy is described in section 4.8.1. Therefore, the techniques that are described here are the ones that have been varied or not used for the materials of the above chapters.

Photoelectrochemical analysis including EIS and photocurrent measurements were performed using a Gamry Instruments potentiostat (model Interface 5000E). A standard three-electrode configuration was used in a home-made quartz electrochemical cell with a platinum wire as counter electrode and a saturated Ag/AgCl electrode as the reference. The working electrode was prepared as follows. Firstly, a paste of each material was obtained by mixing 20 mg of photocatalyst with 0.2 mL of terpineol and 0.5 mL of acetone. Secondly, the mixture was left stirring until complete dispersion. Afterwards, the mixture was left under stirring and incubation at 90 ºC overnight. After letting cool down,

25 µL of each sample was spread onto an area of 1.0 x 1.0 cm^2 using doctor blade technique though a conductive carbon Toray paper with dimensions of 2.0 x 1.0 cm^2. Finally, the electrode was thermally treated at 150 °C for 1 hour.

The photocurrent generated by the electrodes was measured by chopped LSV with an electrolyte of 0.1 M NBu_4PF_6 acetonitrile solution. The applied potential was 0.9 V. And for some LSV measurements, CH_3OH (0.3 mL) was added as a hole scavenger.

EIS was carried out with frequencies ranging from 0.1 Hz to 100 kHz at 0.2 V. Prior to the measurements, the electrolyte solutions were purged with argon for 10 minutes. UV-Vis irradiation of the working electrodes was carried out with a spot light Hamamatzu Xe lamp (Lightnincure LC8 model, 800–200 nm, 1000 W/m^2, fiber optic light guide with a spot size of 0.5 cm).

Femtosecond transient absorption spectroscopy. Ultrashort laser pulses are generated in an oscillator-regenerative amplifier laser system (Coherent, Mantis- Legend) providing of 35 fs pulses at 800 nm. UV pump pulses (267 nm) are produced as the third harmonic of the fundamental beam. The white light continuum probe is produced by focusing (f=100 mm) a small fraction of the amplifier output on a 2 mm thick CaF_2 window. Pump probe delay is achieved with a translation stage (Thorlabs, DDS220) that allows a maximum range of 2 ns. Transient absorbance is measured with a fiber-coupled spectrometer (Avantes, Avaspec) as a function of the pump probe delay. The spot radii of the pump and probe beams are 0.35 mm and 0.1 mm, respectively. Pump pulse energies were varied in the range 2.5-5 µJ. The samples, prepared in a 2 mm quartz cuvette, were continuously stirred and scanned across the focal plane to avoid thermal effects on the sample.

The decay kinetics was analyzed by means of a two exponential decay including an offset to account for the longer-lived contributions. Global decay analysis was performed including decays at 10 different wavelengths in the range 550-725 nm. Average lifetimes were determined as the average of the decay constants weighted with the pre-exponential parameters resulting from the fitting averaged from all measured wavelengths.

Laser Flash Photolysis. Measurements were performed using a pulsed Nd:YAG L52137 V LOTIS TII at λ_{exc} = 266 nm. The single pulses were *ca*. 10 ns duration, and the energy was ~12 mJ/pulse. The LFP system consisted of the pulsed laser, a 77250 Oriel monochromator and an oscilloscope DP04054 Tektronix. The output signal from the oscilloscope was transferred to a personal computer. Absorbances of all solutions were adjusted at ~0.30 at the excitation wavelength in acetonitrile (HPLC grade). Measurements were done using 10 × 10 mm^2 quartz cuvettes at room temperature in argon atmosphere (25 min Ar bubbling). Control experiments indicated that the degree of decomposition of the samples after photolysis was lower than 2%. The LFP decay traces were fitted using a multi-exponential function following the Levenberg-Marquardt iteration algorithm (equation 1):

$$F(t,\lambda) = \sum_{i=1}^{n} a_i(\lambda) e^{\left(-\frac{t}{\tau_i}\right)} + y_0 \quad \text{(Eq. S1)}$$

with n = 2 or 3

The photoluminescence measurements were conducted using commercially available CdSe-ZnS core-shell quantum dots. A spectrofluorimeter was used to analyze the photoluminescence spectrum of either CdSe/ZnS core-shell QDs or

RuO_x@UiO-66(Zr/Ti)-NO_2-CdSe/ZnS upon excitation at 450 nm. To achieve this, 1 mg of CdSe/ZnS QDs was dissolved in 3 mL of CH_3CN for each case. Adding 2 mg of RuO_x@UiO-66(Zr/Ti)-NO_2 for the analysis of the MOF. 40 µL of both solutions were applied dropwise onto 2 sets of quartz supports, where the solvent was evaporated using a heating plate at 90 ºC during 5 min. One of the samples for each material supported on a quartz holder were then heated for 5 min on a hot plate to the appropriate temperature (from 200 to 280 ºC) and then measured using the spectrofluorimeter. The other two samples were irradiated during 13 min at the reference temperature of the photocatalysis experiments (T=200 ºC) under different light intensities (385, 220, 140, 85 mW/cm^2) with a xenon lamp containing a visible light filter.

ScanTemp410 Infrared-thermometer was used to monitor the temperature for PL experiments. The range to measure the temperature is within -3°C to 500°C.

5.8.3 Photocatalytic activity

Photocatalytic experiments under batch reaction conditions were carried out using a quartz reactor (50 mL) equipped with a heating mantle and thermocouple. The UiO-66 based photocatalyst is placed on the bottom of the reactor and, then, the system purged with H_2 for 15 min and then CO_2 was introduced to obtain a H_2:CO_2 ratio 4:1 and 1.5 bar pressure. Irradiations were performed using a Hg-Xe lamp (150 W, Hamamatsu ref. L8253; Hamamatsu spot light source L9566-04 and light guide A10014-50–0110) with or without an AM 1.5G type filter (Lasing ref. 81094) to obtain simulated sunlight irradiation. The influence of radiation intensity on the photocatalytic activity was carried out by using transmittance filters (Newport, ref. FSQ-OD30, FSQ-OD15 or FSQ-QD05). The course of the reaction was followed by analyzing gas phase reaction aliquots

in an Agilent 490 MicroGC equipped with a thermal conductivity detector. A MolSieve 5 Å column is used to analyse H_2, O_2, N_2, and CO while a Pore Plot Q column to analyse the CO_2, CH_4, and short-chain hydrocarbons (ethane, ethylene, propane, propylene, and butane). Quantification was obtained by calibration plots with commercially available gas mixtures.

***Operando* FT-IR photocatalytic tests.** Photocatalytic tests were performed using an *operando* FT-IR setup, which allows to monitor through real time both the gas phase products and the surface of the catalyst during the reaction. For that, a "Sandwich" IR cell reactor was used and the photocatalytic experiments were conducted under the following conditions: 4:1 molar ratio of H_2 to CO_2 with a total flow rate of 10 cm^3 min^{-1}; visible light irradiation (Xe lamp LC8 Hamamatsu with cut-UV filter λ >390 nm) irradiance= 71 mW/cm^2); and 20 mg of photocatalyst. The sample was preactivated under H_2 at 200 °C with a heating flow rate of 5 °C· min^{-1}. Then the reaction was conducted at different temperatures in dark and under irradiation. The catalyst surface as well as the composition of the output gas from the reactor were simultaneously analyzed by an IR spectrometer (ThermoNico-letNEXUS670FT-IR) equipped with a mercury cadmium telluride detector with a spectral resolution of 4 cm^{-1} and accumulating 64 scans. Mass spectrometry (Quadru-pole Pfeiffer Omnistar GSD301) was also used to monitor the gas composition during the reaction. The produced gases were also confirmed by online gas chromatography (Compact-GC) with a Rtx-1-5u (30 m - 0.32 mm) capillary column equipped with a flame ionization detector and using commercially available samples (methane and ethane).

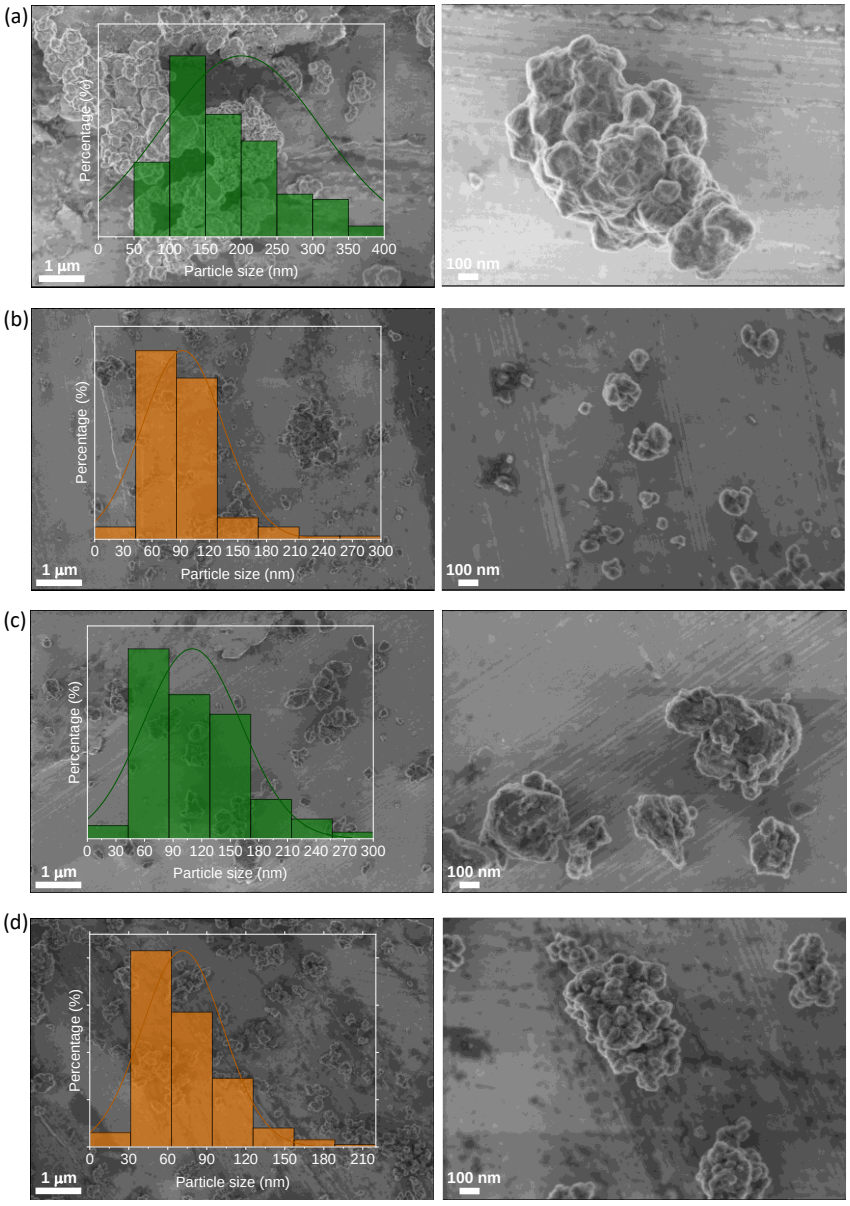

Figure S1. SEM images of (a) UiO-66(Zr)-NH_2, (b) UiO-66(Zr)-NO_2, (c) UiO- 66(Zr/Ti)- NH_2, (d) UiO-66(Zr/Ti)-NO_2. Legend: MOF average particle size and standard deviation of UiO-66(Zr)-NH_2 (200 ± 111 nm), UiO-66(Zr/Ti)-NH_2 (110 ± 51 nm), UiO-66(Zr)-NO_2 (92 ± 42 nm), UiO-66(Zr/Ti)-NO_2 (71 ± 31 nm).

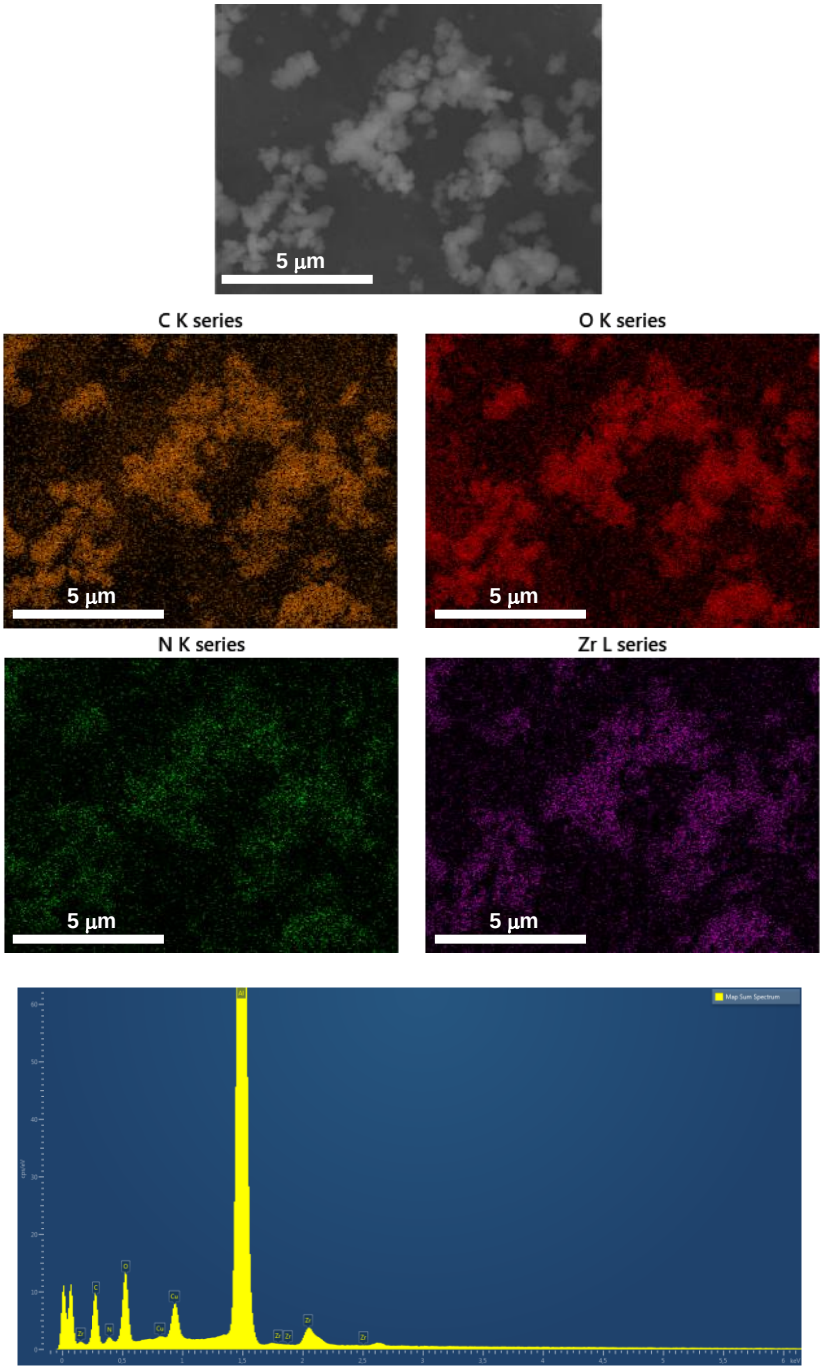

Figure S2. SEM-EDX of UiO-66(Zr)-NH_2.

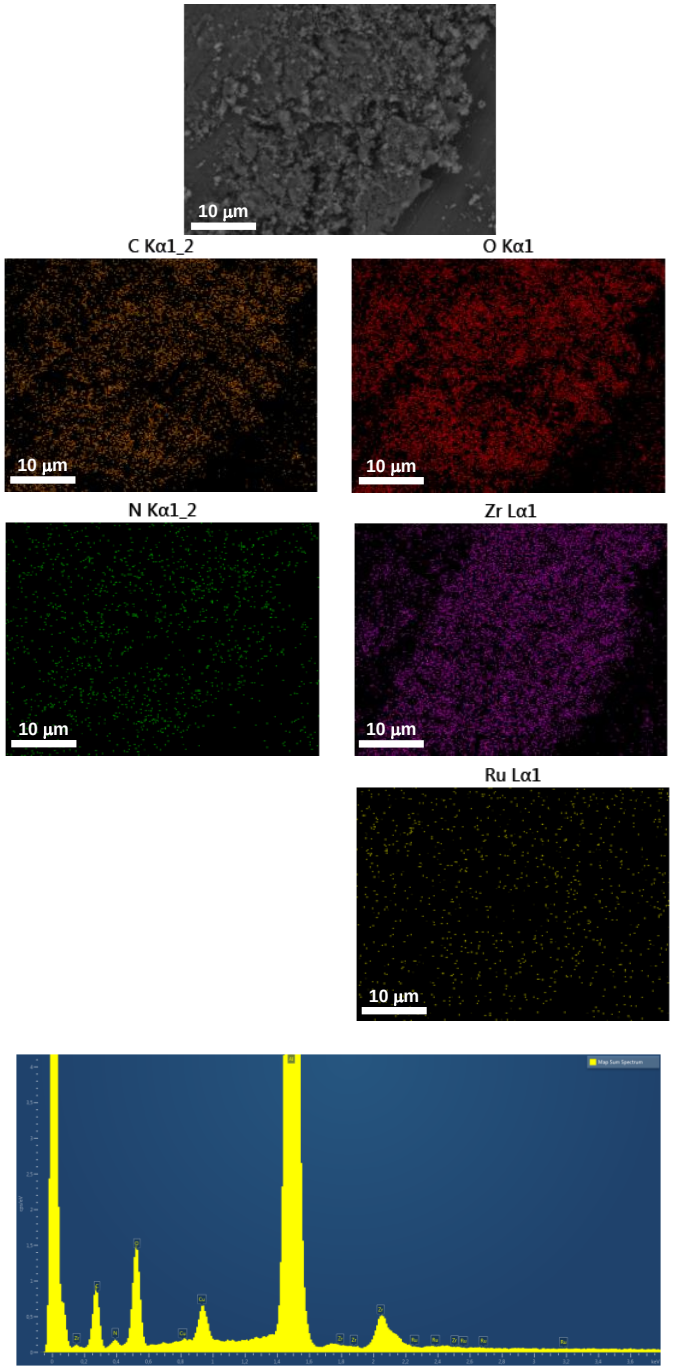

Figure S3. SEM-EDX of RuO_x@UiO-66(Zr)-NH_2.

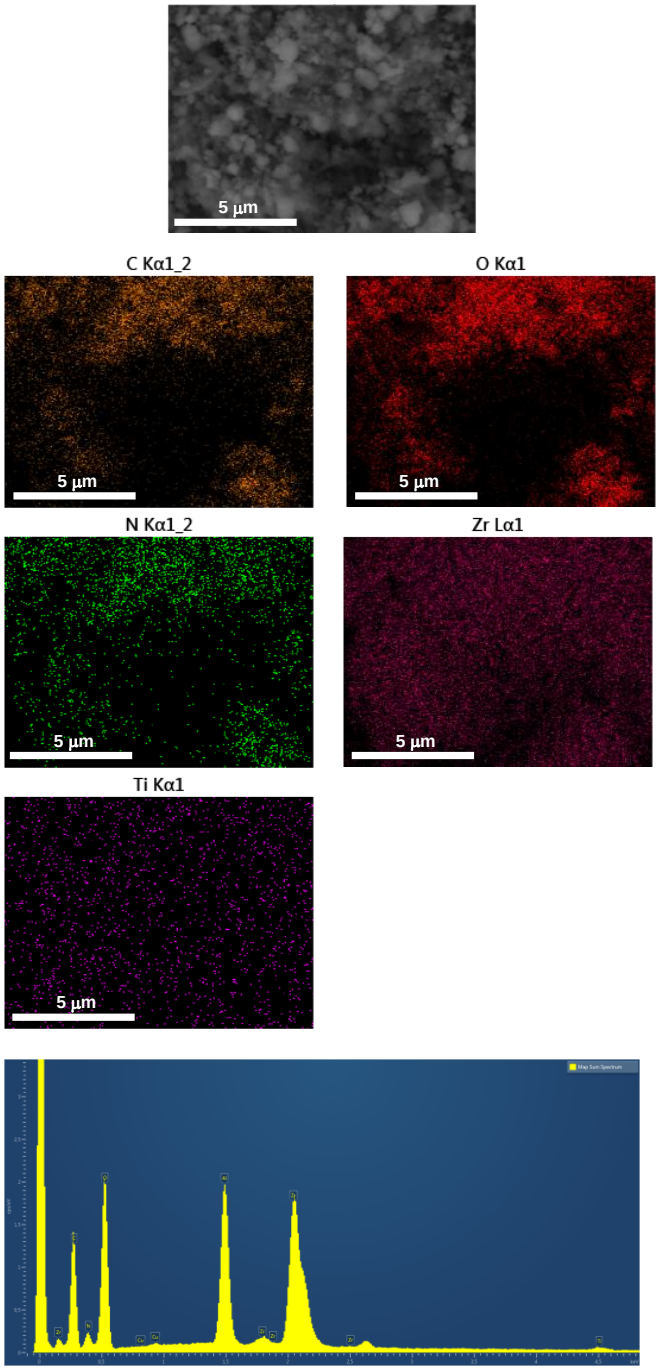

Figure S4. SEM-EDX of UiO-66(Zr/Ti)-NH_2.

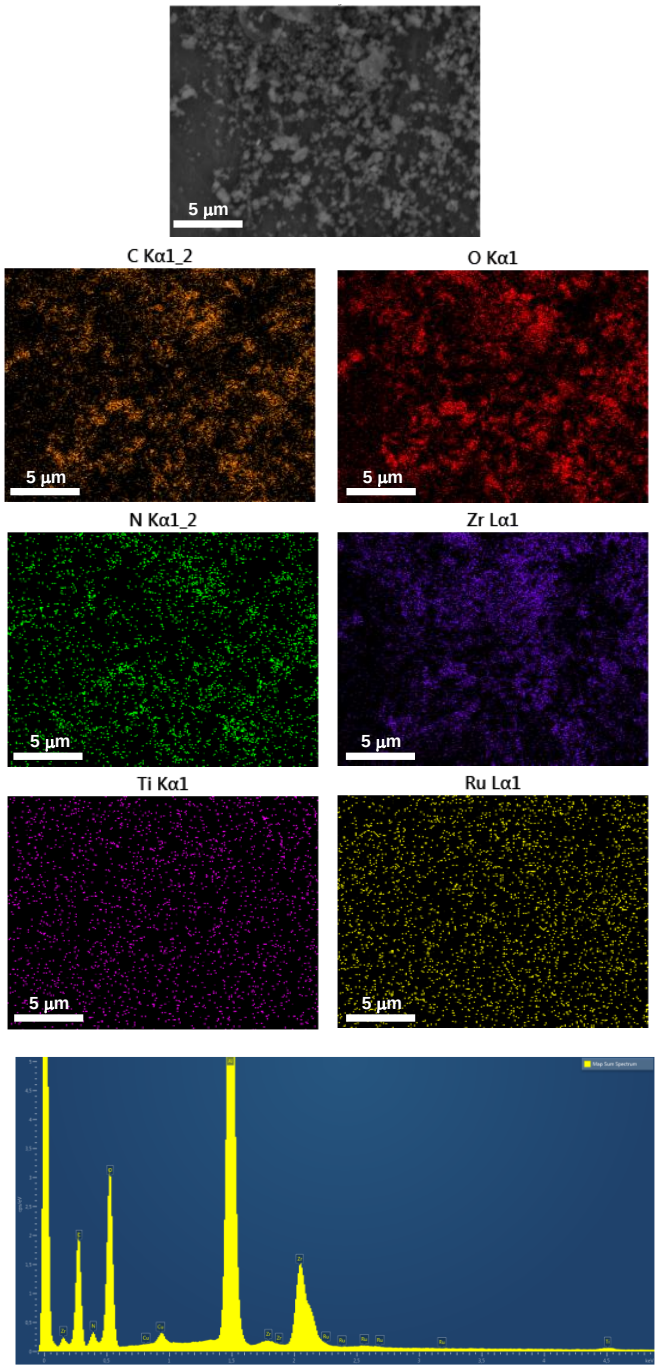

Figure S5. SEM-EDX of RuO_x@UiO-66(Zr/Ti)-NH_2.

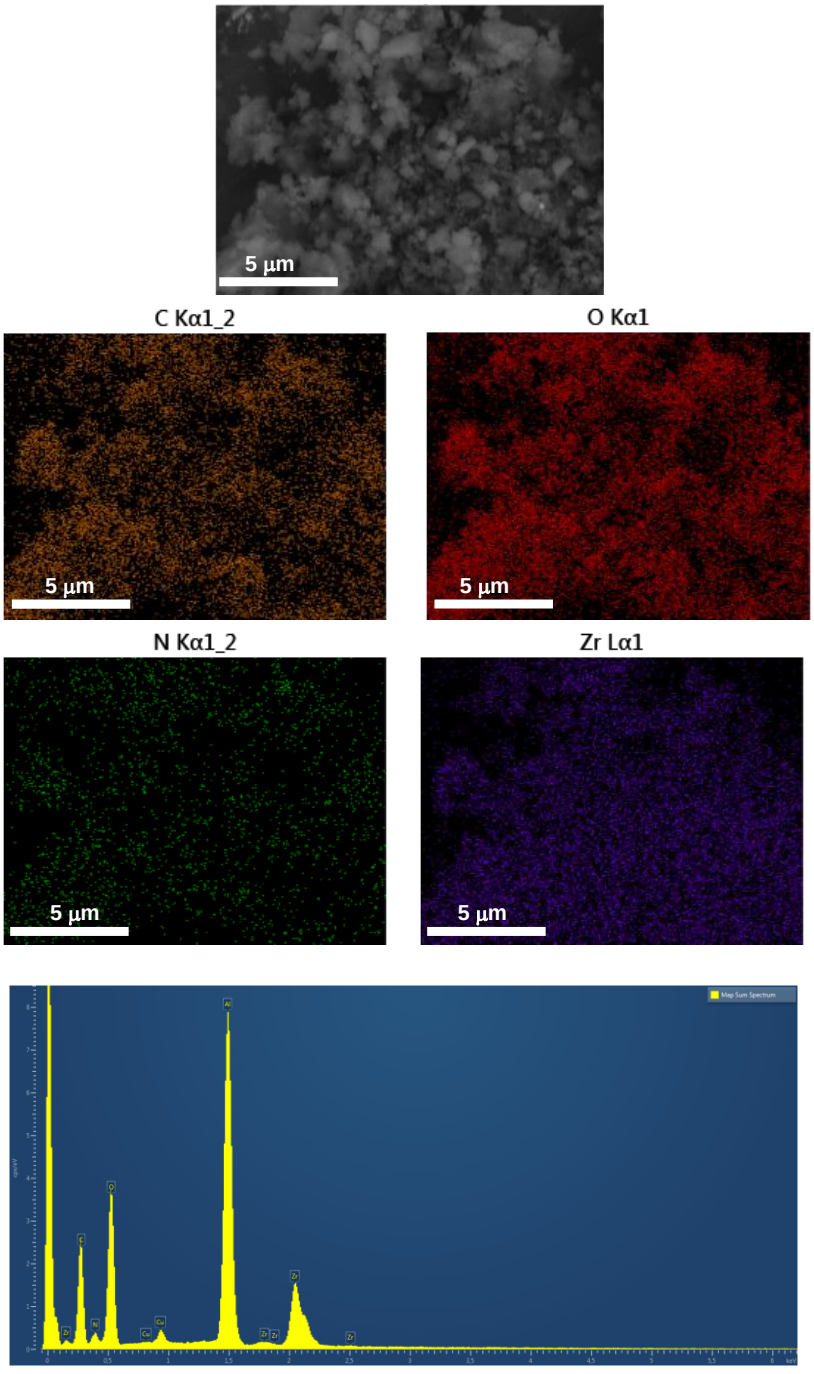

Figure S6. SEM-EDX of UiO-66(Zr)-NO_2.

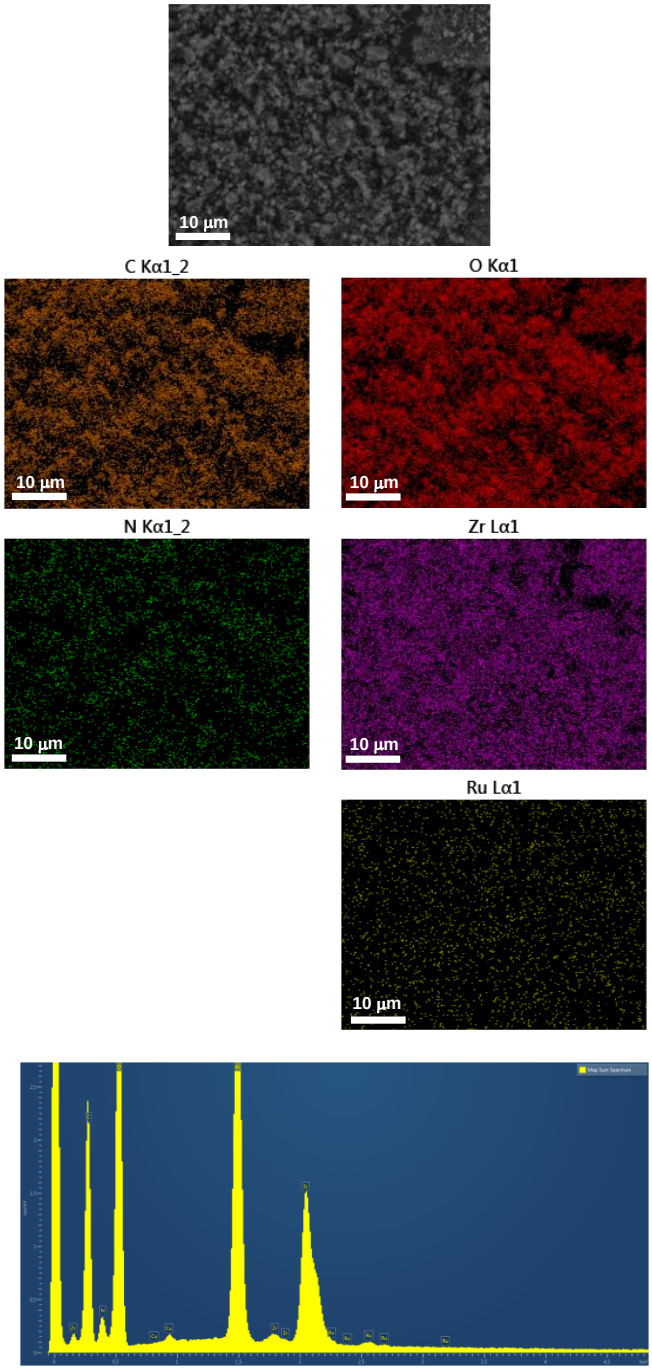

Figure S7. SEM-EDX of RuO_x@UiO-66(Zr)-NO_2.

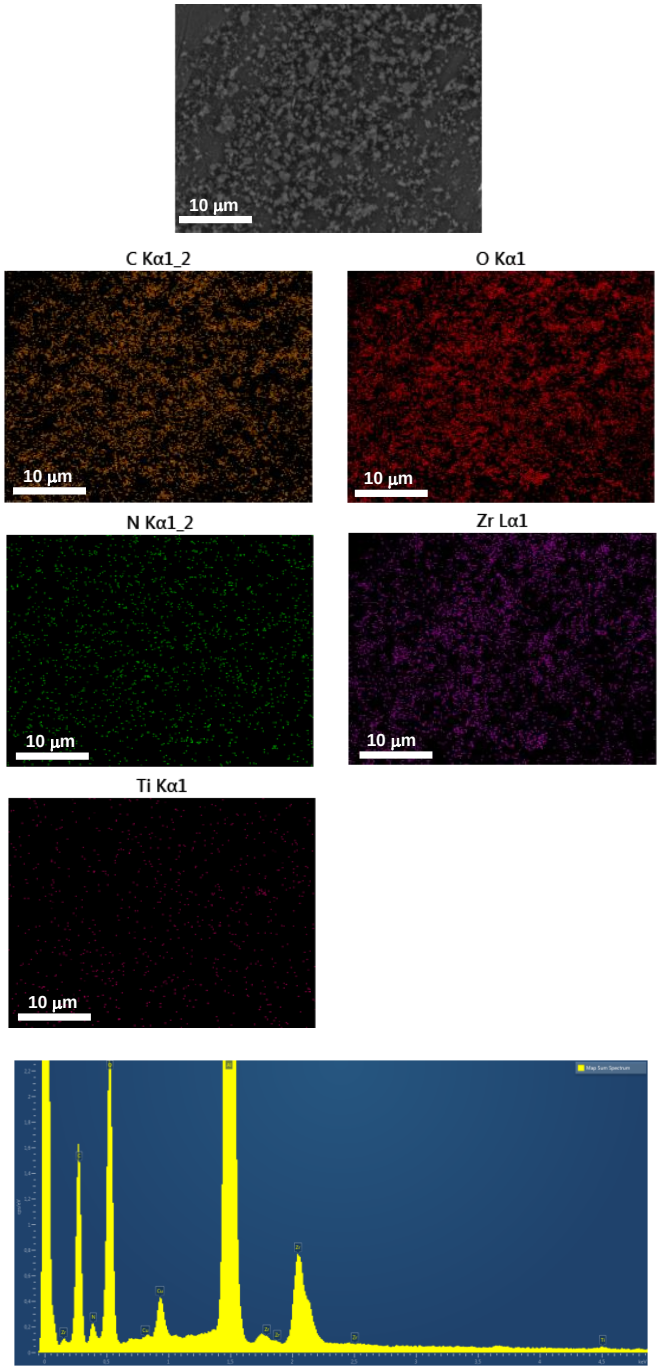

Figure S8. SEM-EDX of UiO-66(Zr/Ti)-NO_2.

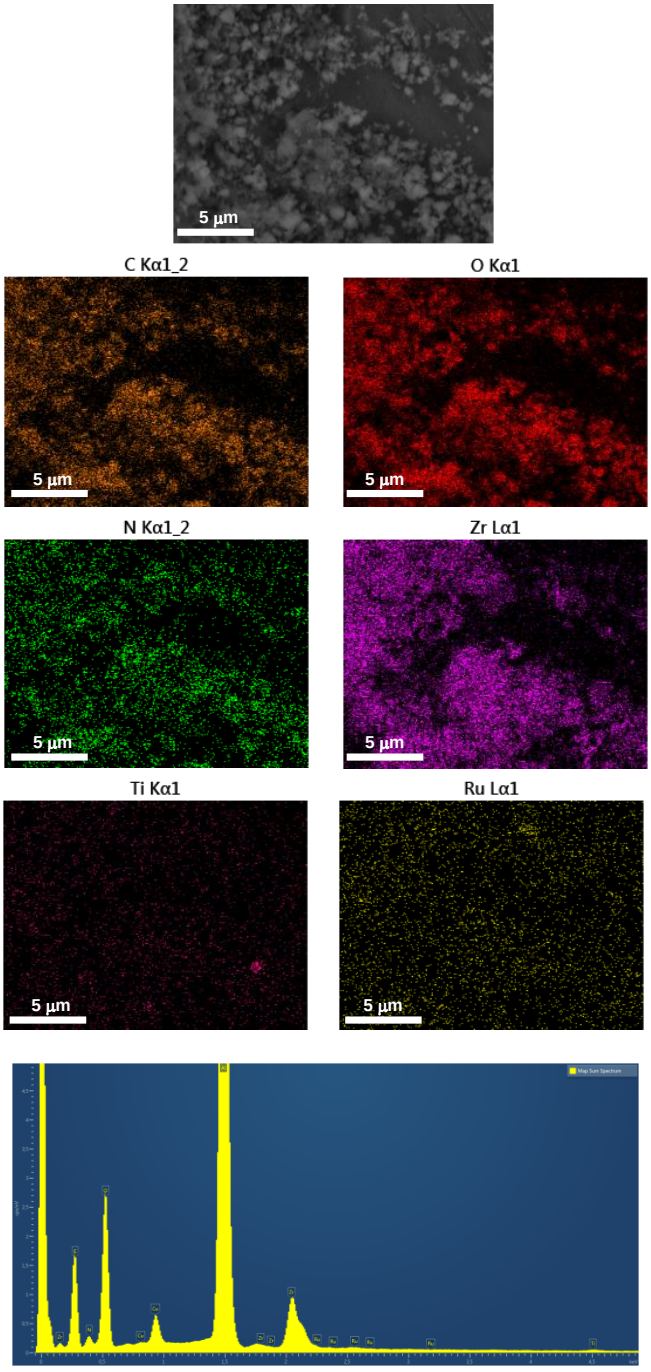

Figure S9. SEM-EDX of RuO_x@UiO-66(Zr/Ti)-NO_2.

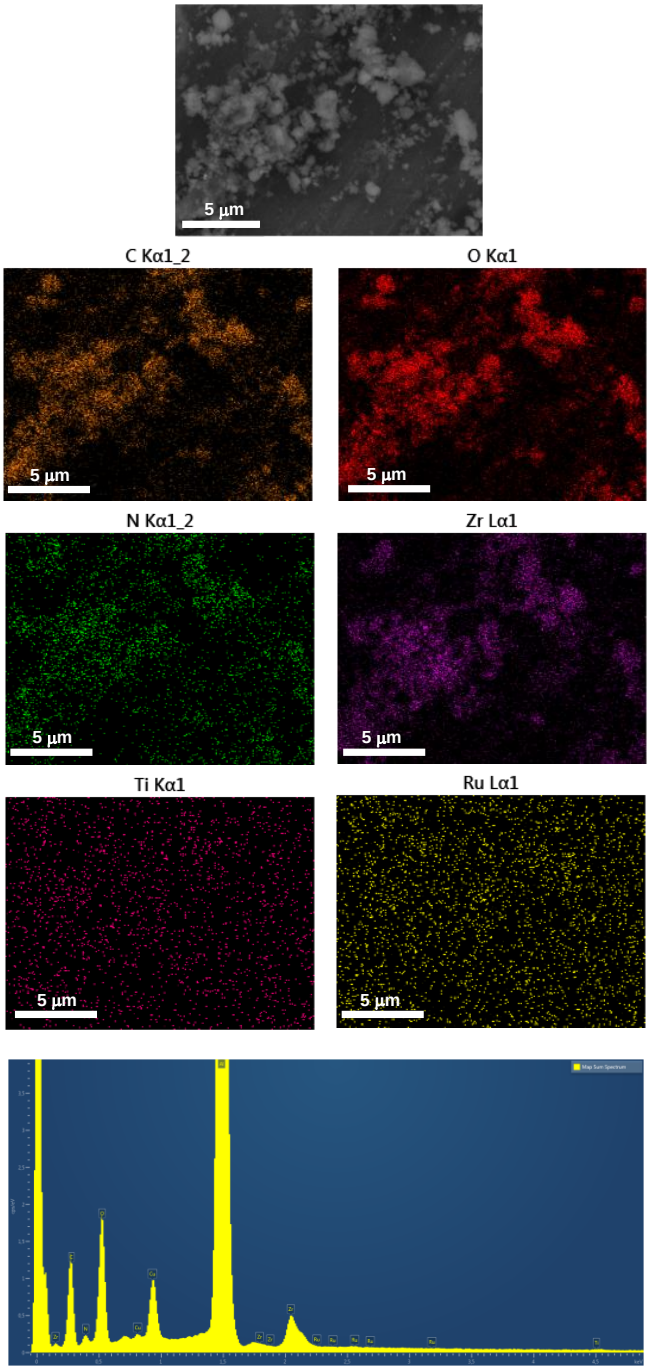

Figure S10. SEM-EDX of used RuO_x@UiO-66(Zr/Ti)-NO_2.

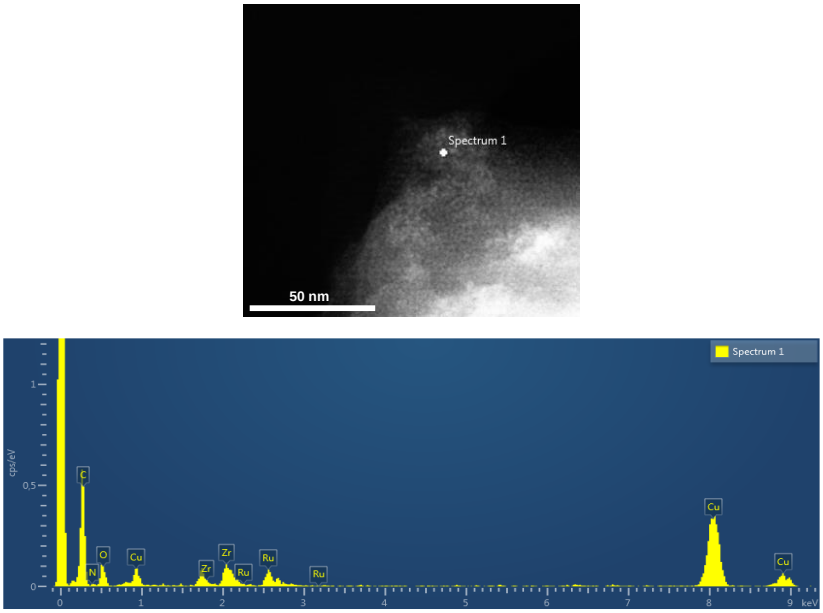

Figure S11. EDX image of RuO_x@UiO-66(Zr)-NH_2.

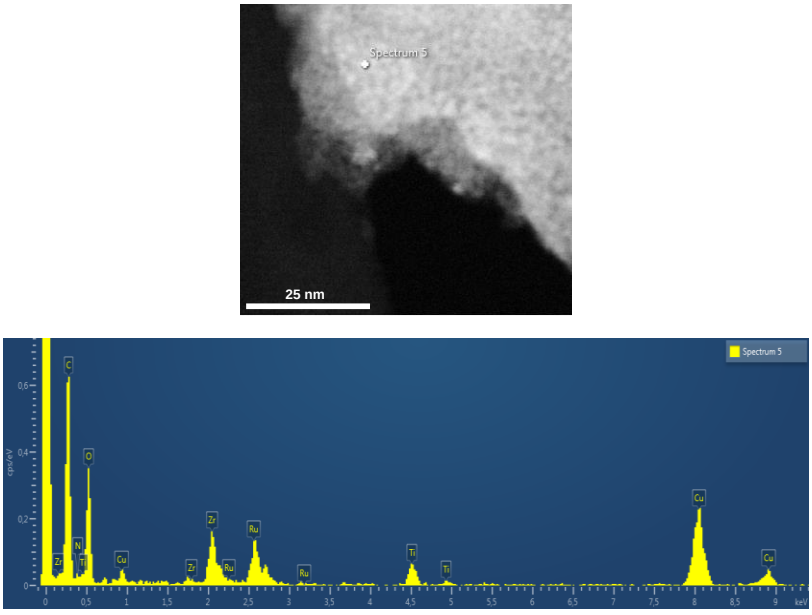

Figure S12. EDX image of RuO_x@UiO-66(Zr/Ti)-NH_2.

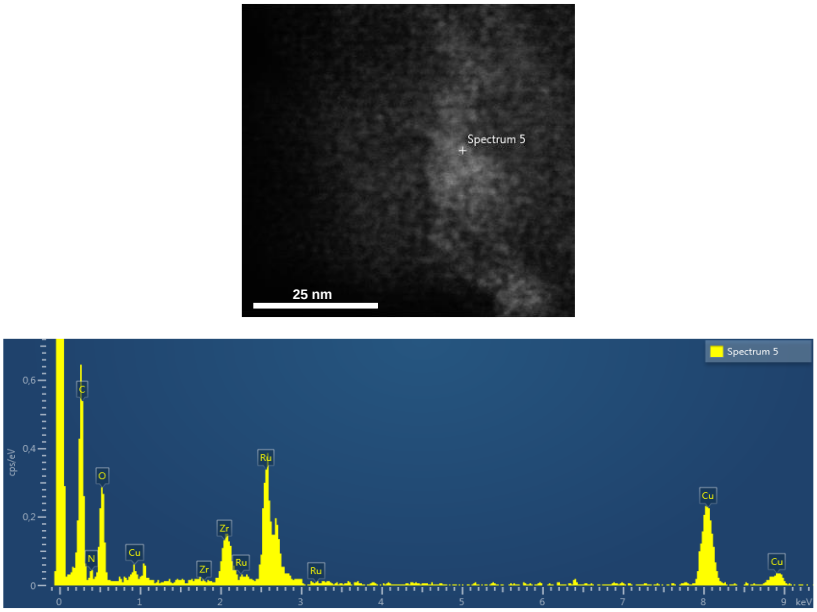

Figure S13. EDX image of RuO_x@UiO-66(Zr)-NO_2.

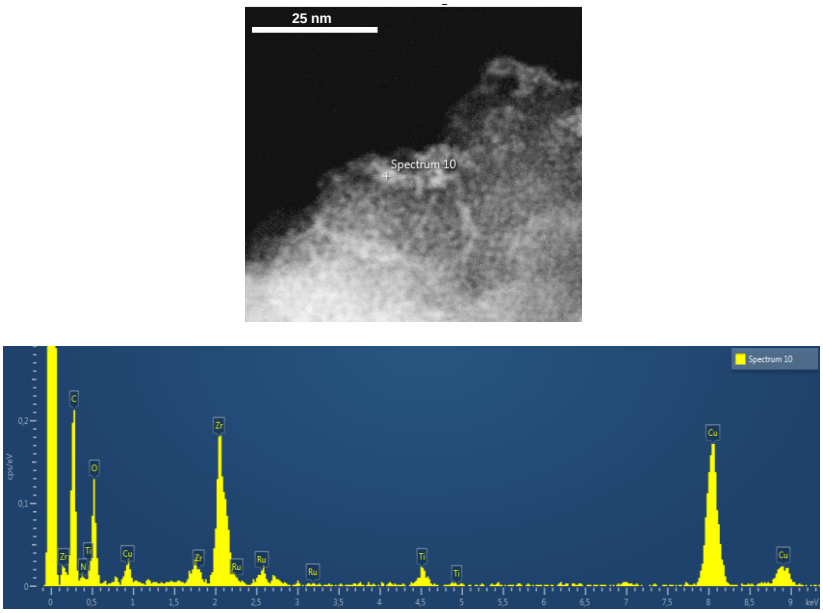

Figure S14. EDX image of RuO_x@UiO-66(Zr/Ti)-NO_2.

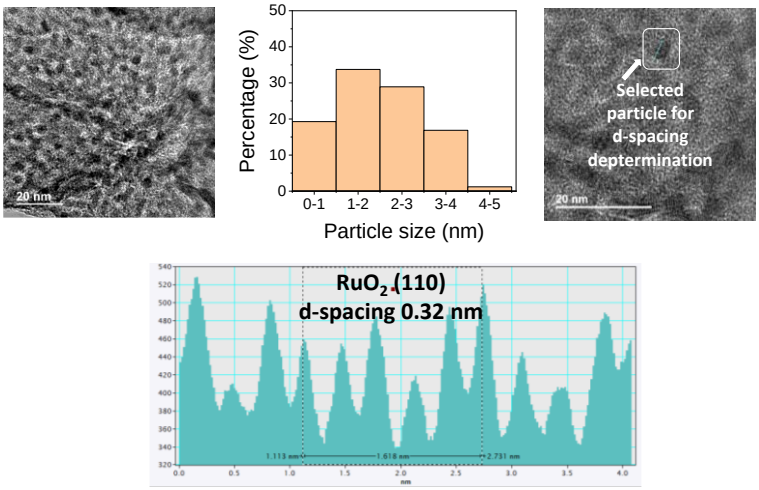

Figure S15. TEM image of RuO_x@UiO-66(Zr)-NH_2 to show the selected region to measure the interplane distance. Average particle size and standard deviation of 2.17 ± 1.04 nm.

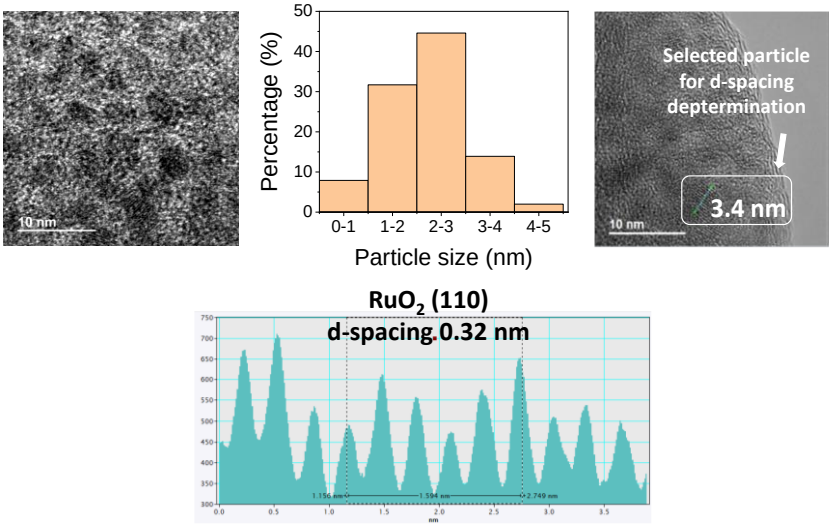

Figure S16. TEM image of RuO_x@UiO-66(Zr)-NO_2 to show the selected region to measure the interplane distance. Average particle size and standard deviation of 2.16 ± 0.87 nm.

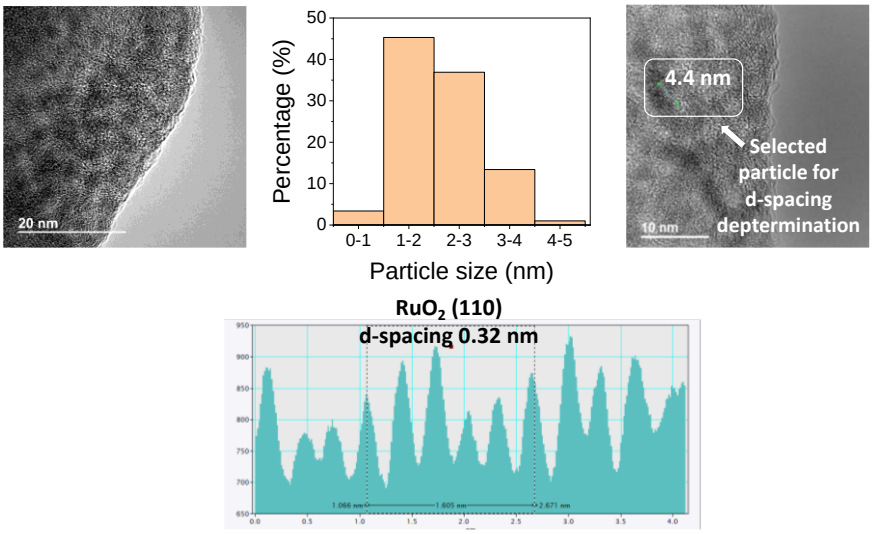

Figure S17. TEM image of RuO_x@UiO-66(Zr/Ti)-NH_2 to show the selected region to measure the interplane distance. Average particle size and standard deviation of 2.15 ± 0.71 nm.

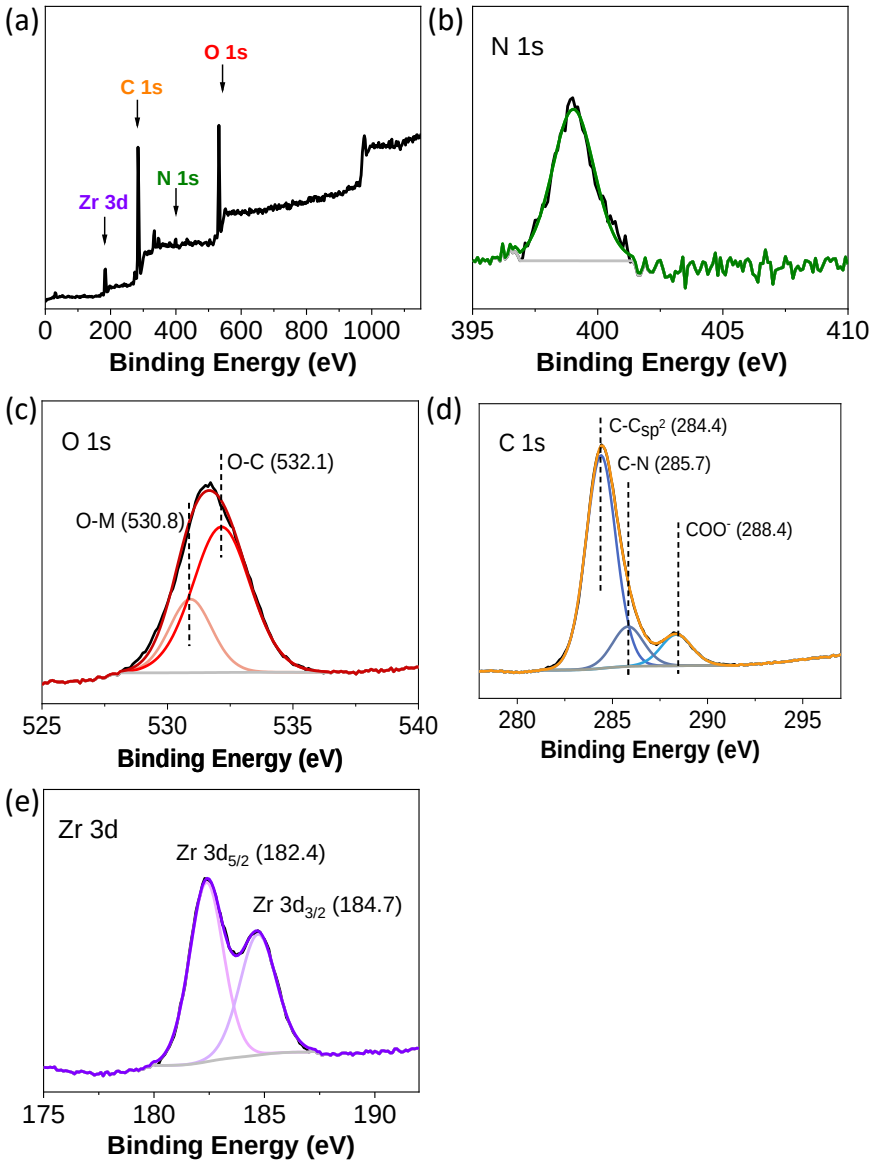

Figure S18. XPS Survey (a), C 1s (b), O 1s (c), N 1s (d) and Zr 3d (e) for UiO-66(Zr)-NH_2.

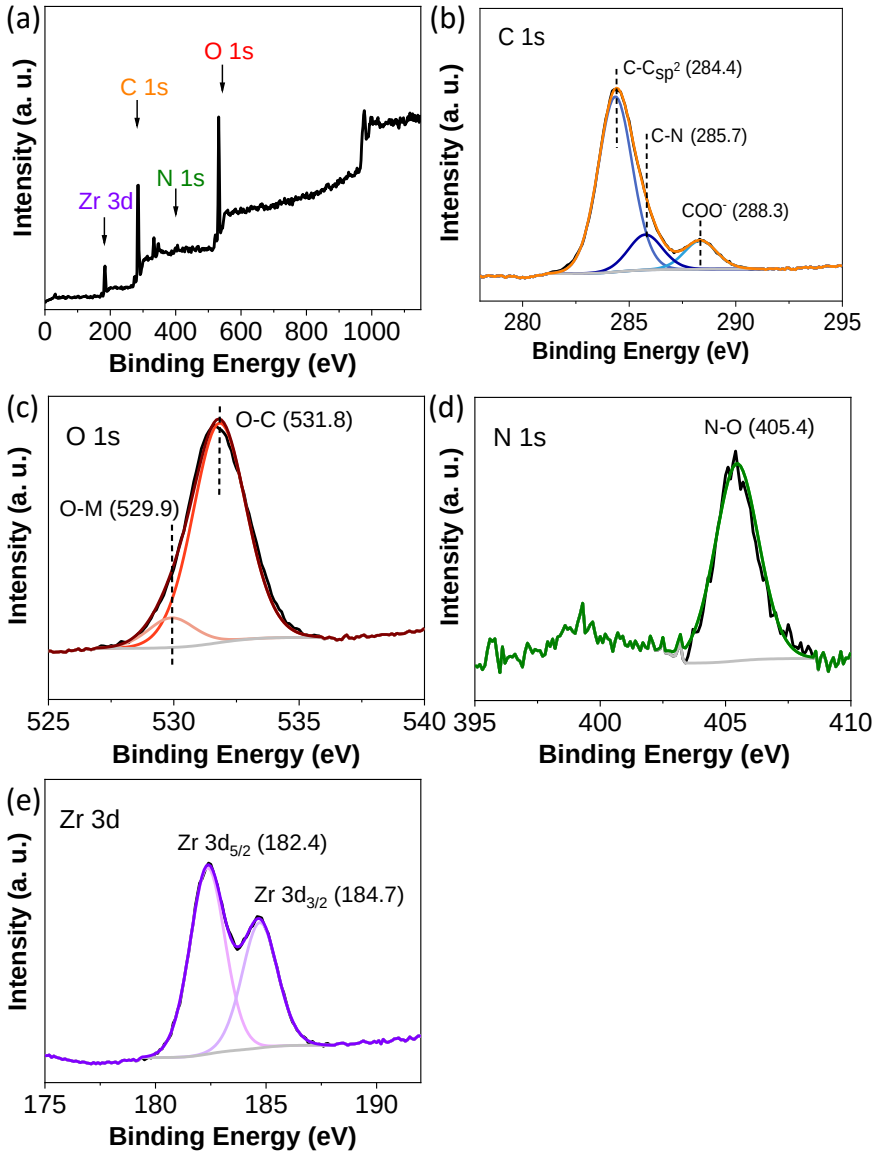

Figure S19. XPS Survey (a), C 1s (b), O 1s (c), N 1s (d) and Zr 3d (e) for UiO-66(Zr)-NO_2.

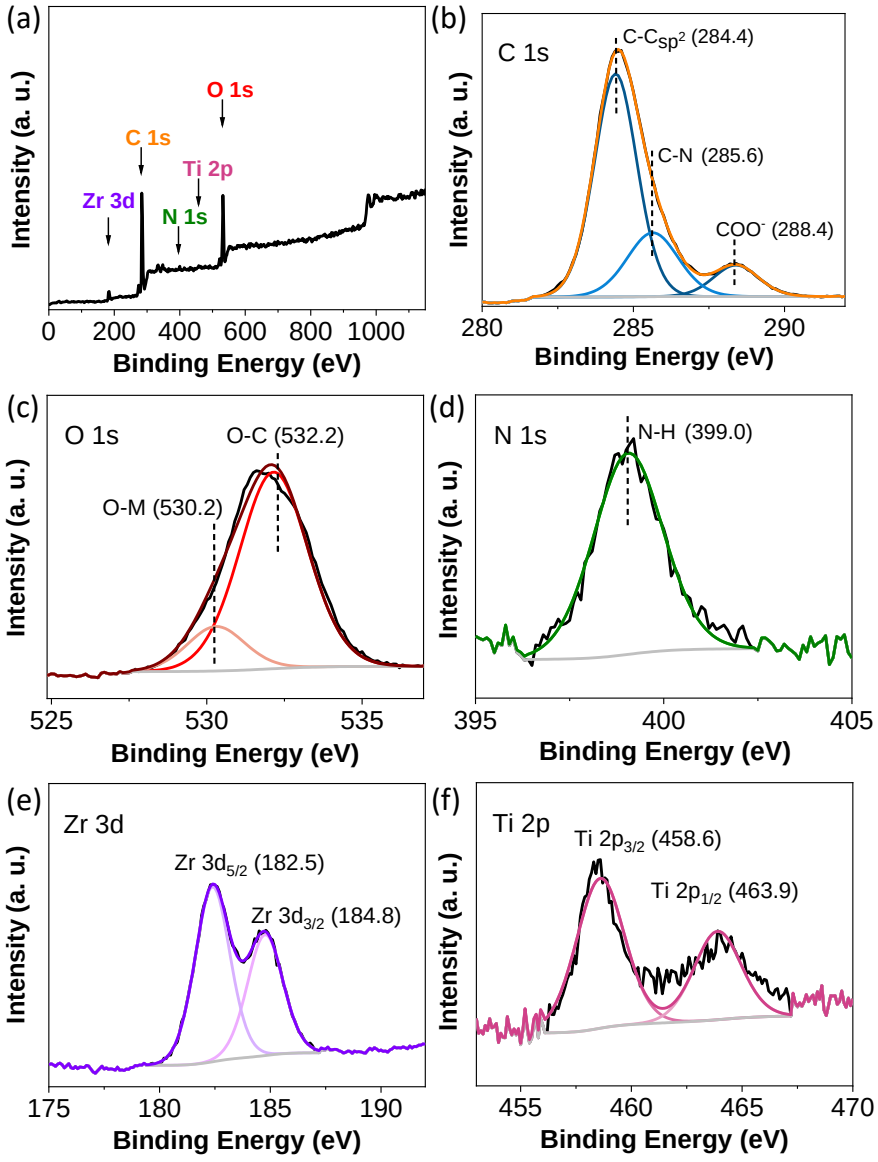

Figure S20. XPS Survey (a), C 1s (b), O 1s (c), N 1s (d) and Zr 3d (e) for UiO-66(Zr/Ti)-NH_2.

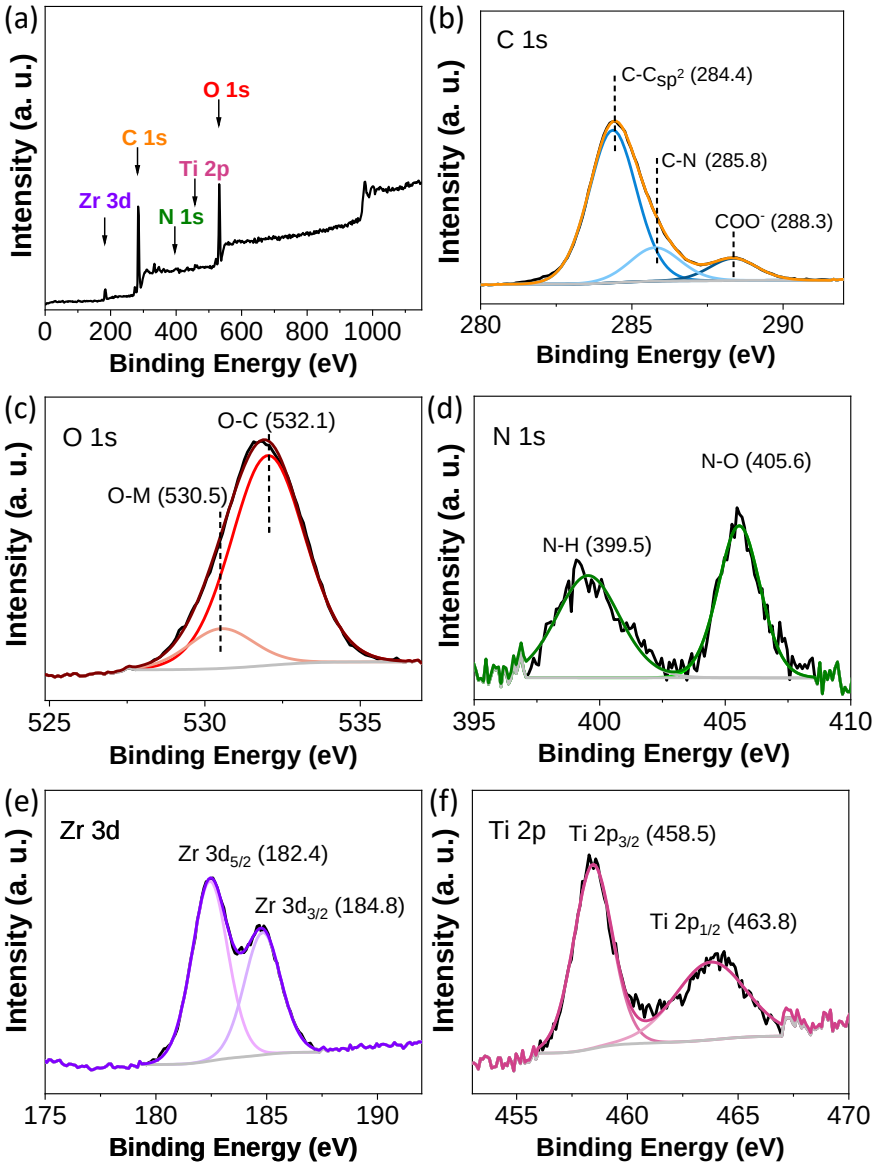

Figure S21. XPS Survey (a), C 1s (b), O 1s (c), N 1s (d) and Zr 3d (e) for UiO-66(Zr/Ti)-NO_2.

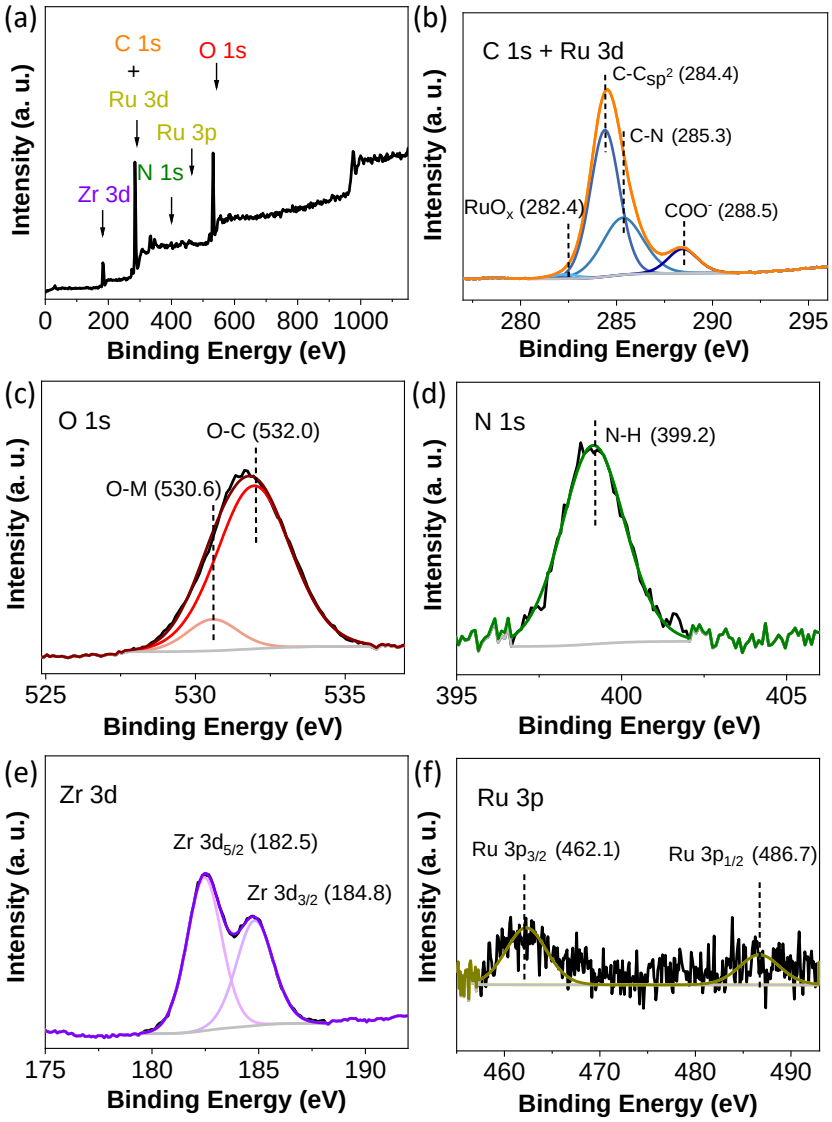

Figure S22. XPS Survey (a), C 1s (b), O 1s (c), N 1s (d) and Zr 3d (e) for RuO_x@UiO-66(Zr)-NH_2.

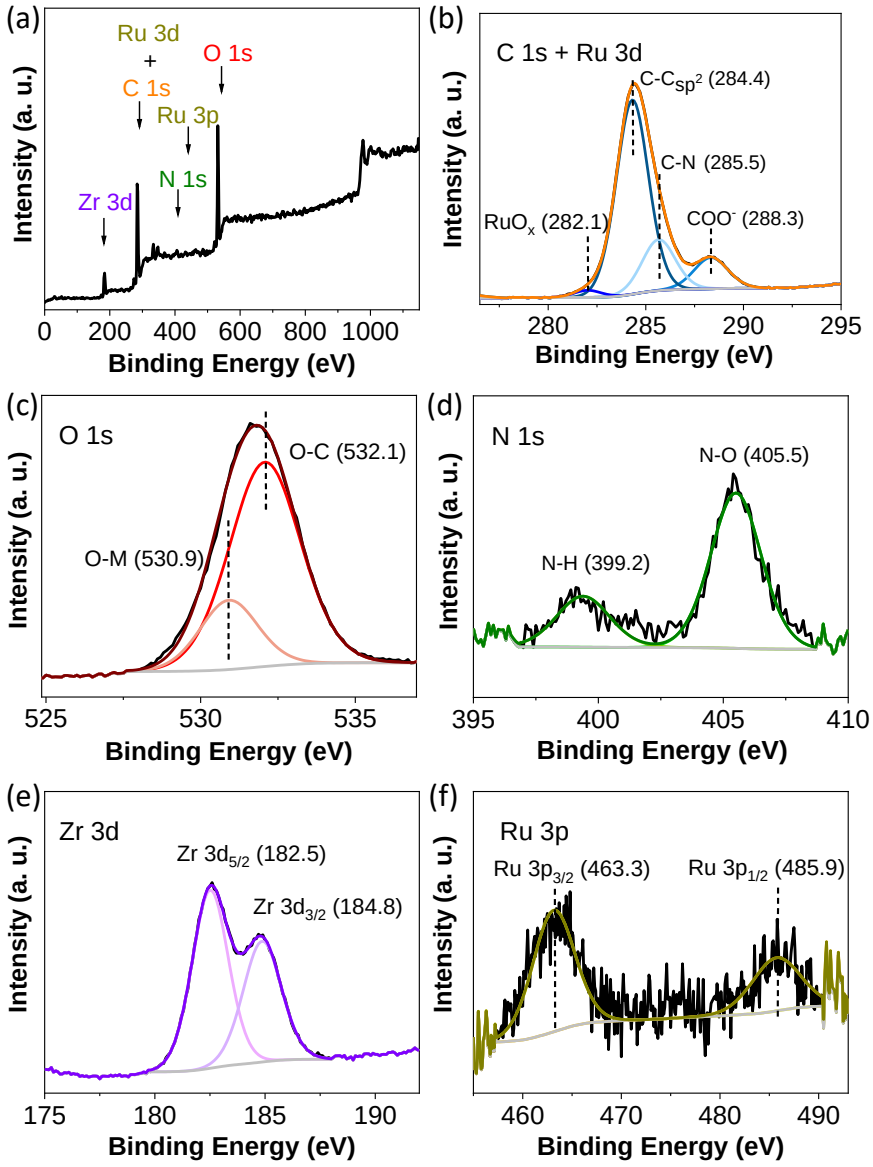

Figure S23. XPS Survey (a), C 1s (b), O 1s (c), N 1s (d) and Zr 3d (e) for RuO_x@UiO-66(Zr)-NO_2.

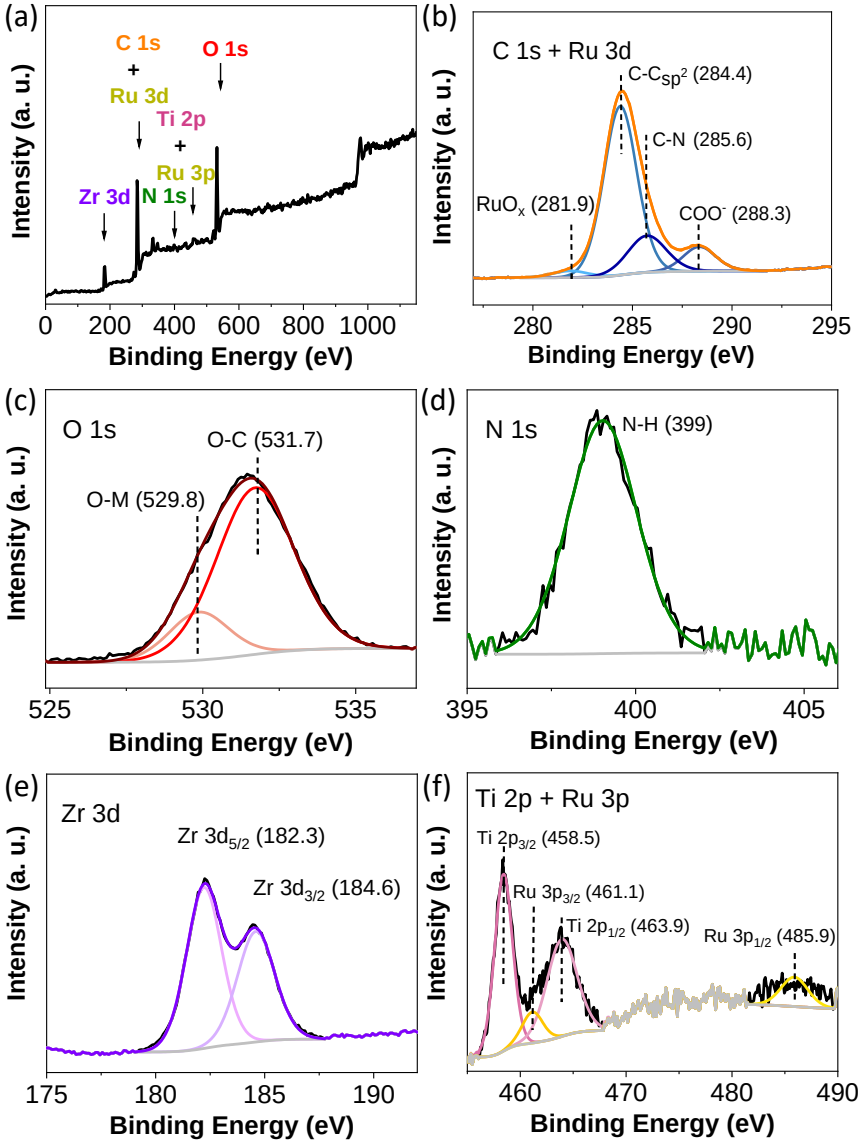

Figure S24. XPS Survey (a), C 1s (b), O 1s (c), N 1s (d) and Zr 3d (e) for RuO_x@UiO-66(Zr/Ti)-NH_2.

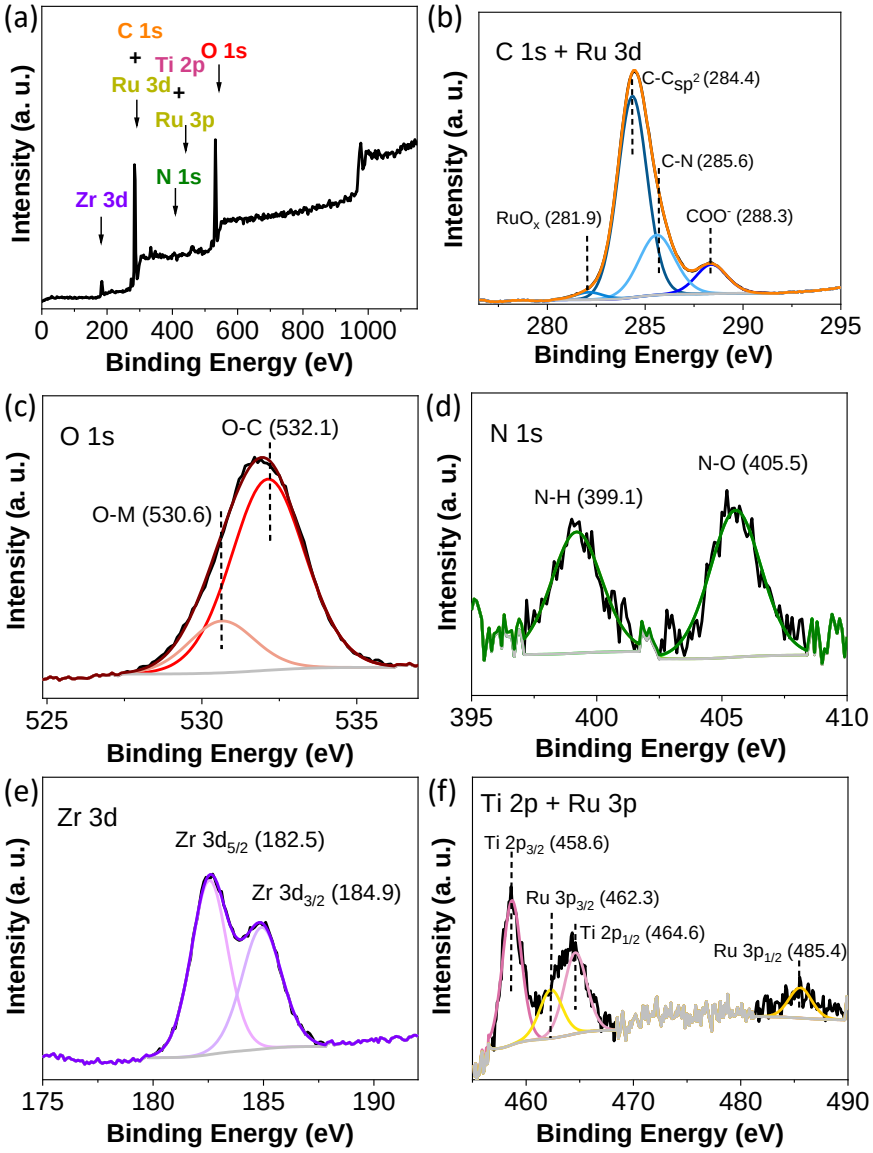

Figure S25. XPS Survey (a), C 1s (b), O 1s (c), N 1s (d) and Zr 3d (e) for RuO_x@UiO-66(Zr/Ti)-NO_2.

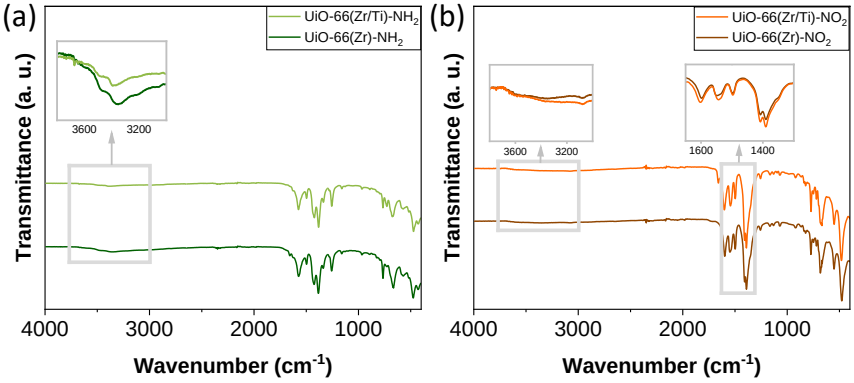

Figure S26. FT-IR of solids as indicated.

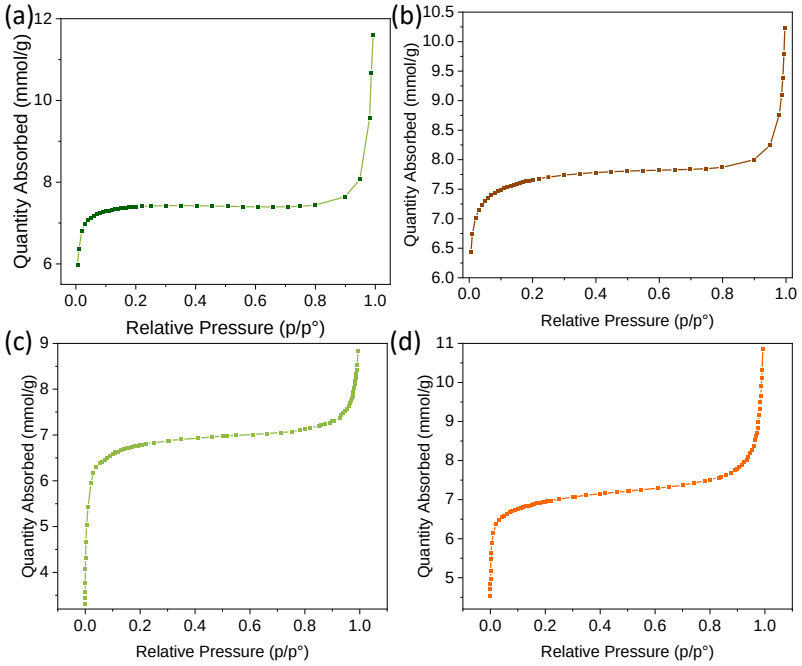

Figure S27. Isothermal N_2 adsorption curve of (a) UiO-66(Zr)-NH_2, (b) UiO-66(Zr)-NO_2, (c) UiO-66(Zr/Ti)-NH_2 and (d) UiO-66(Zr/Ti)-NO_2.

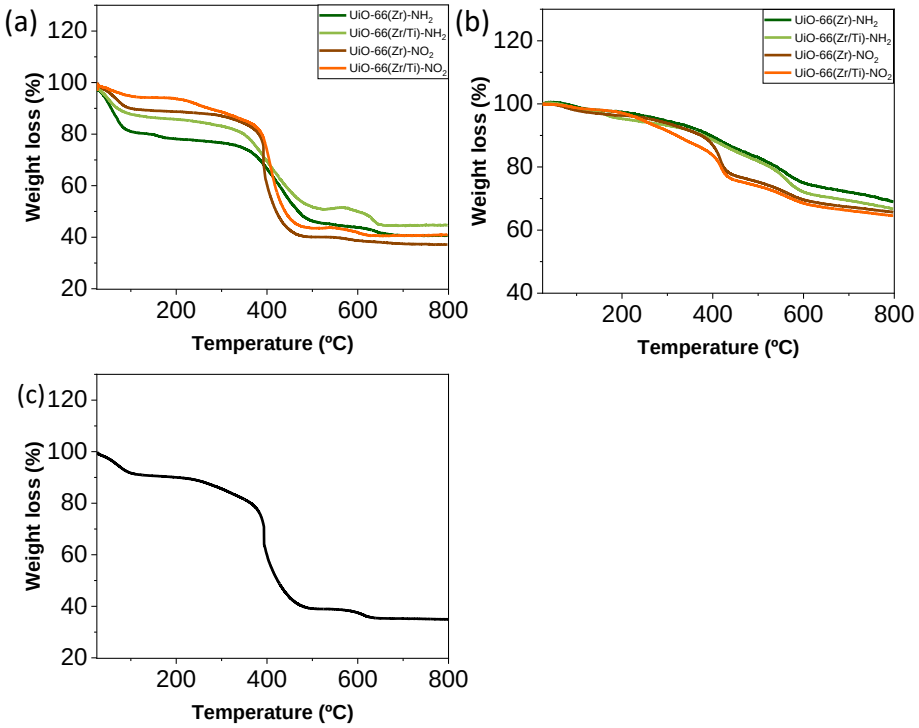

Figure S28. TGA analyses of UiO-66(Zr)-NH_2, UiO-66(Zr)-NO_2, UiO-66(Zr/Ti)-NH_2, UiO-66(Zr/Ti)-NO_2 as indicated under (a) air or (b) N_2 atmosphere. (c)TGA analysis of UiO-66(Zr/Ti)-NO_2, previously submitted to photocatalytic treatment at 200 ºC under H_2:CO_2 molar ratio for 22 h, under air atmosphere.

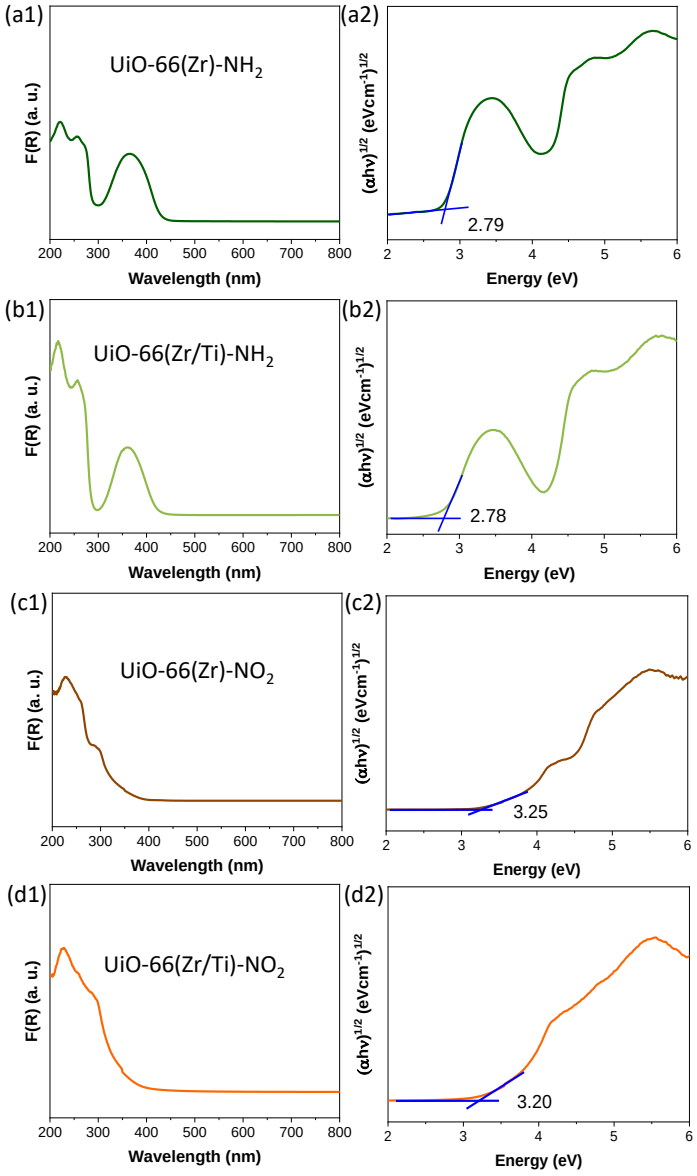

Figure S29. UV-Vis diffuse reflectance (left side) and Tauc plot (right side) of (a) UiO-66(Zr)-NH_2, (b) UiO-66(Zr/Ti)-NH_2, (c) UiO-66(Zr)-NO_2 and (d) UiO-66(Zr/Ti)-NO_2.

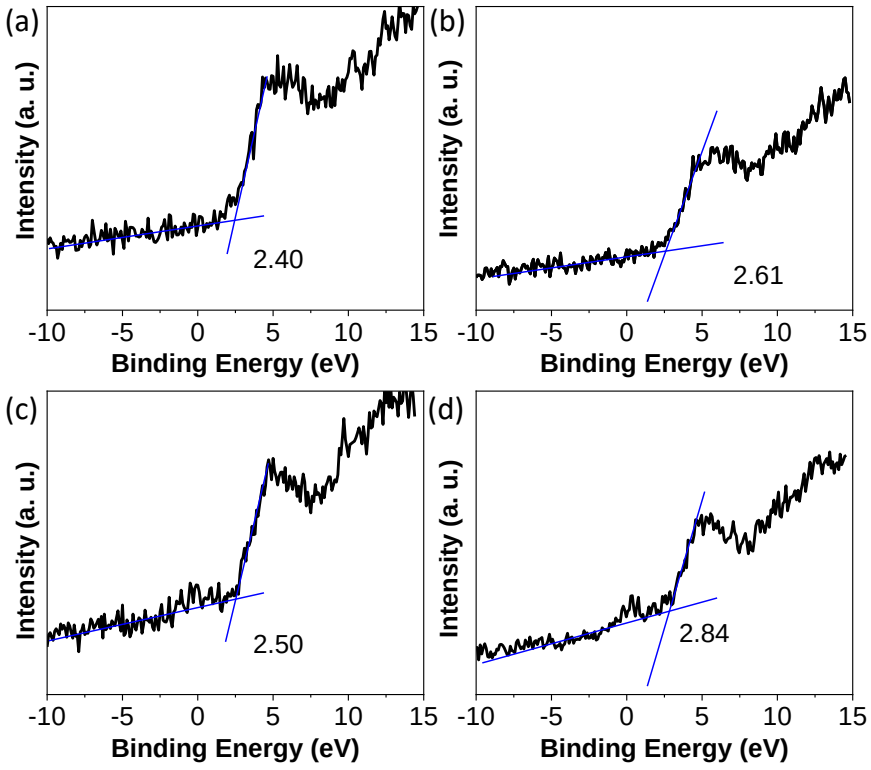

Figure S30. HOCO band XPS for (a) UiO-66(Zr)-NH_2, (b) UiO-66(Zr)-NO_2, (c) UiO-66(Zr/Ti)-NH_2, (d) UiO-66(Zr/Ti)-NO_2.

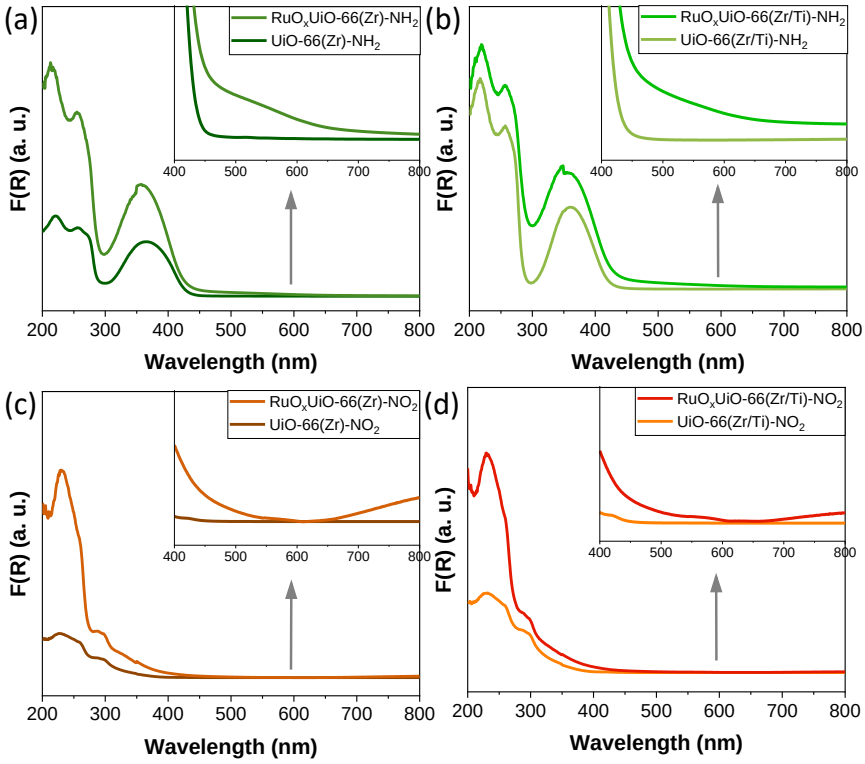

Figure S31. UV-Vis diffuse reflectance of RuO_x NPs on UiO-66 solids: (a) UiO-66(Zr)-NH_2, (b) UiO-66(Zr/Ti)-NH_2, (c) UiO-66(Zr)-NO_2 and (d) UiO-66(Zr/Ti)-NO_2. The inset shows the resonance plasmon band of these NPs.

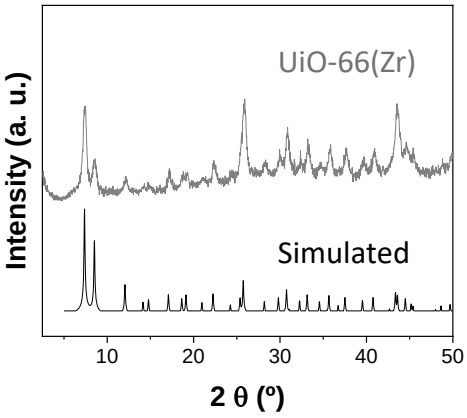

Figure S32. XRD of simulated UiO-66 and PXRD of UiO-66(Zr) material.

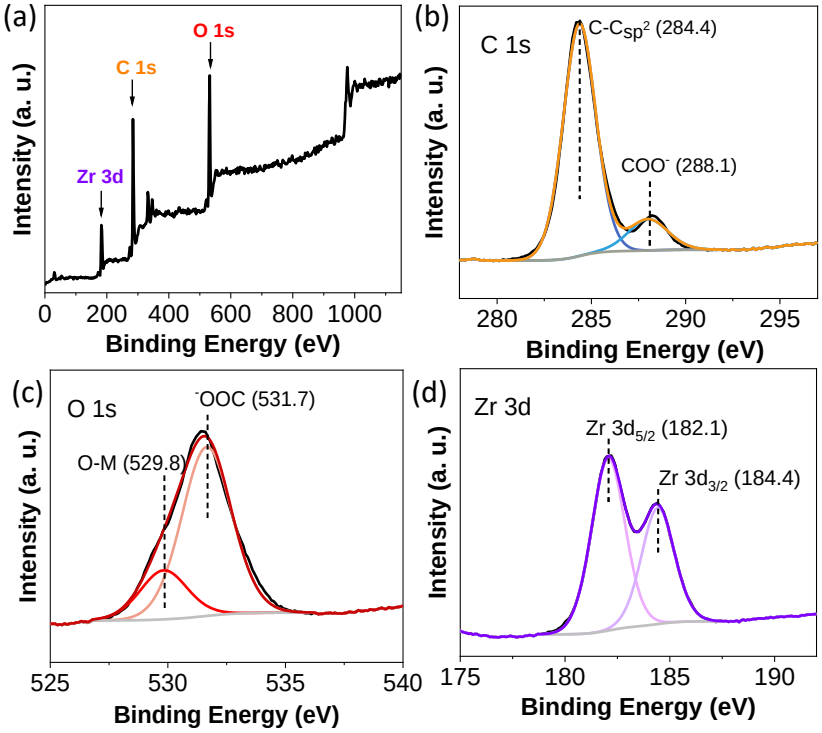

Figure S33. XPS survey (a), C 1s (b), O 1s (c), and Zr 3d (d) of UiO-66(Zr).

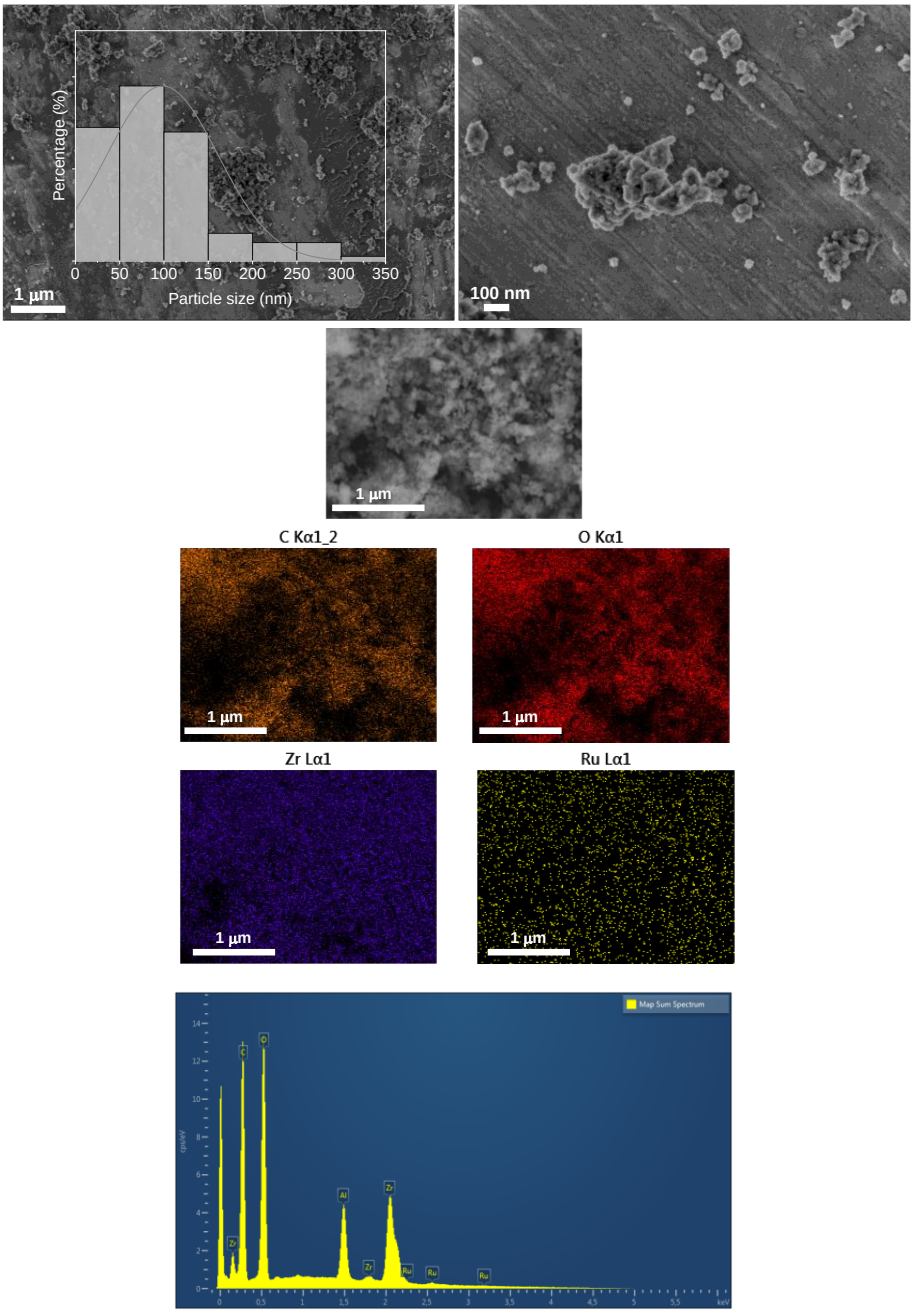

Figure S34. SEM-EDX of RuO_x@UiO-66. The average particle size and standard deviation is 98 ± 63 nm.

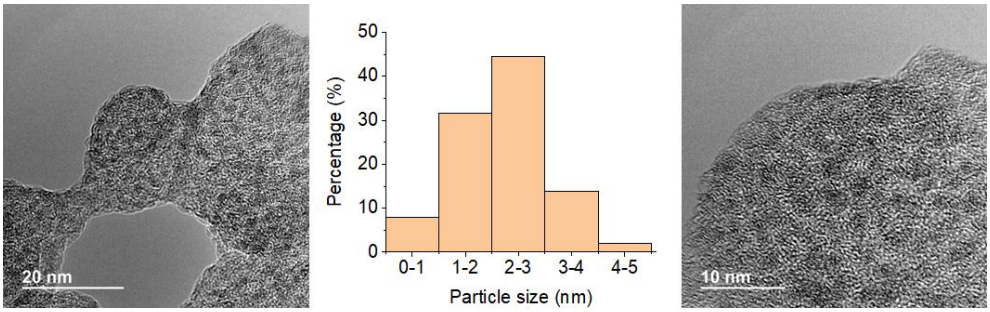

Figure S35. HRTEM image and RuO_x particle size distribution of RuO_x@UiO-66(Zr); average particle size and standard deviation of 2.4 ± 0.8 nm.

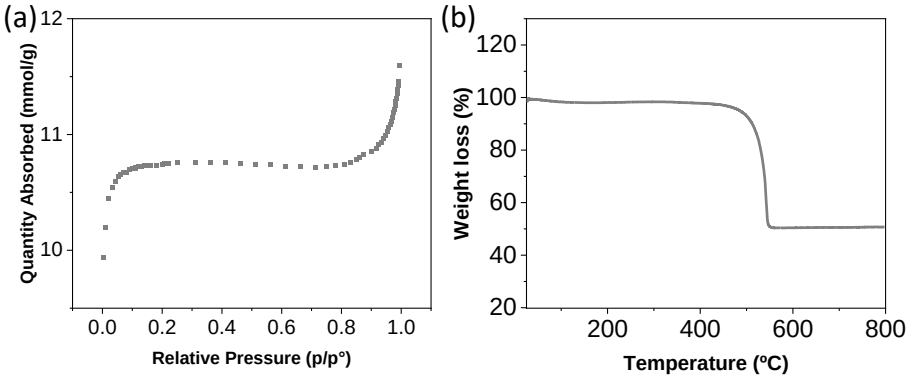

Figure S36. (a) Isothermal N_2 adsorption curve and (b) TGA of UiO-66(Zr).

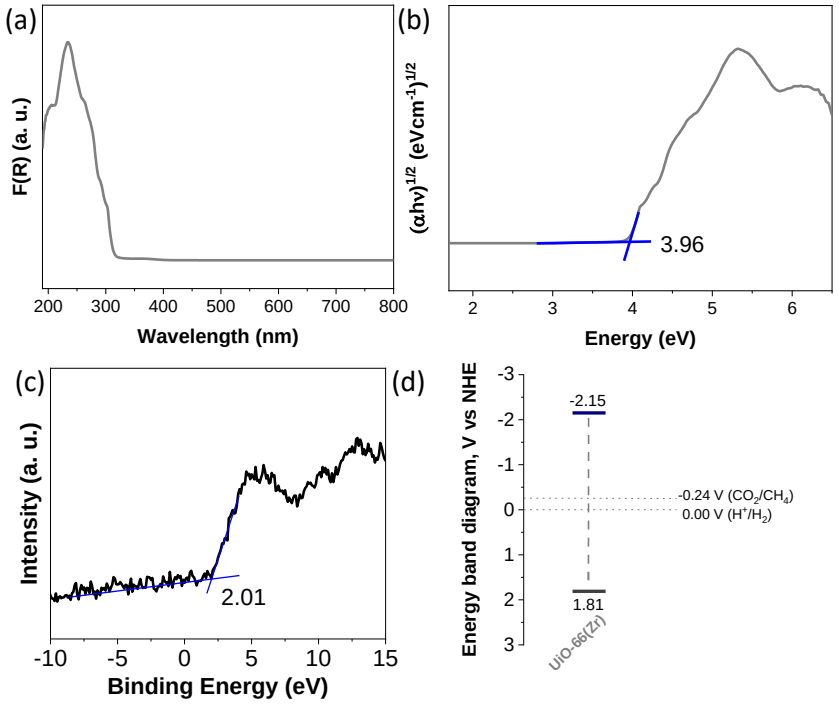

Figure S37. (a) UV-Vis DRS, (b) Tauc plot and, (c) XPS HOCO band and (d) Energy band level diagram of UiO-66 solid.

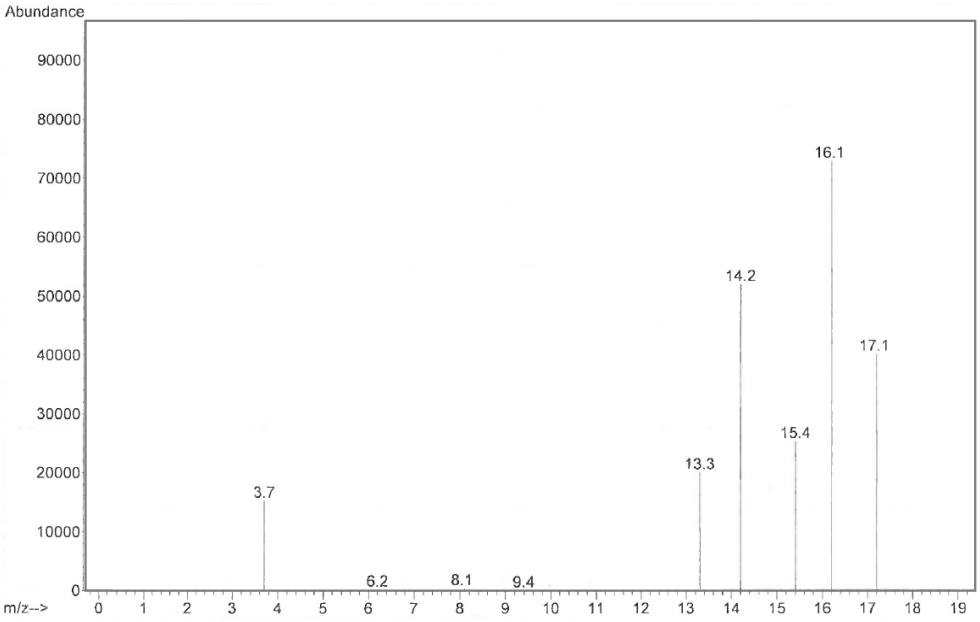

Figure S38. GC-MS obtained after the photocatalytic reaction using $^{13}CO_2$ and RuO_x@UiO-66(Zr/Ti)-NO_2.

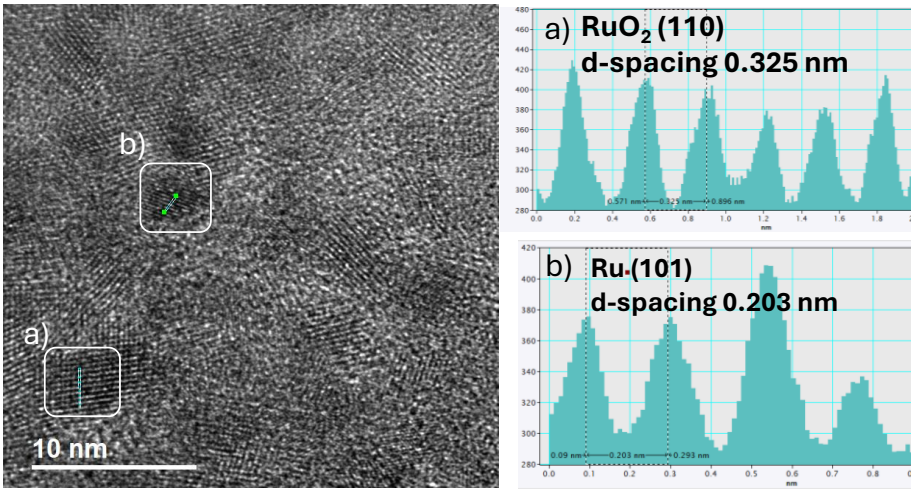

Figure S39. d-spacing estimation from HRTEM image show in main text of the manuscript (Figure 1d).

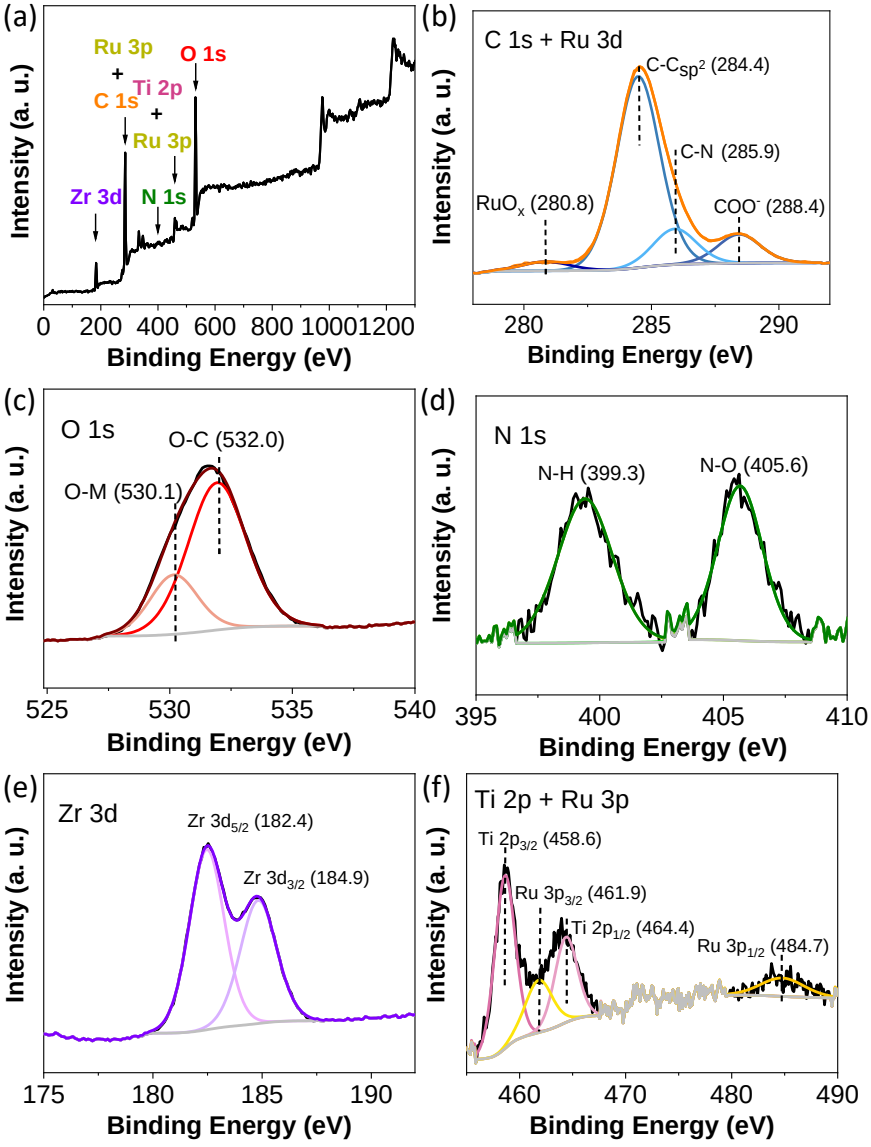

Figure S40. XPS Survey (a), C 1s (b), O 1s (c), N 1s (d) and Zr 3d (e) for used RuO_x@UiO-66(Zr/Ti)-NO_2.

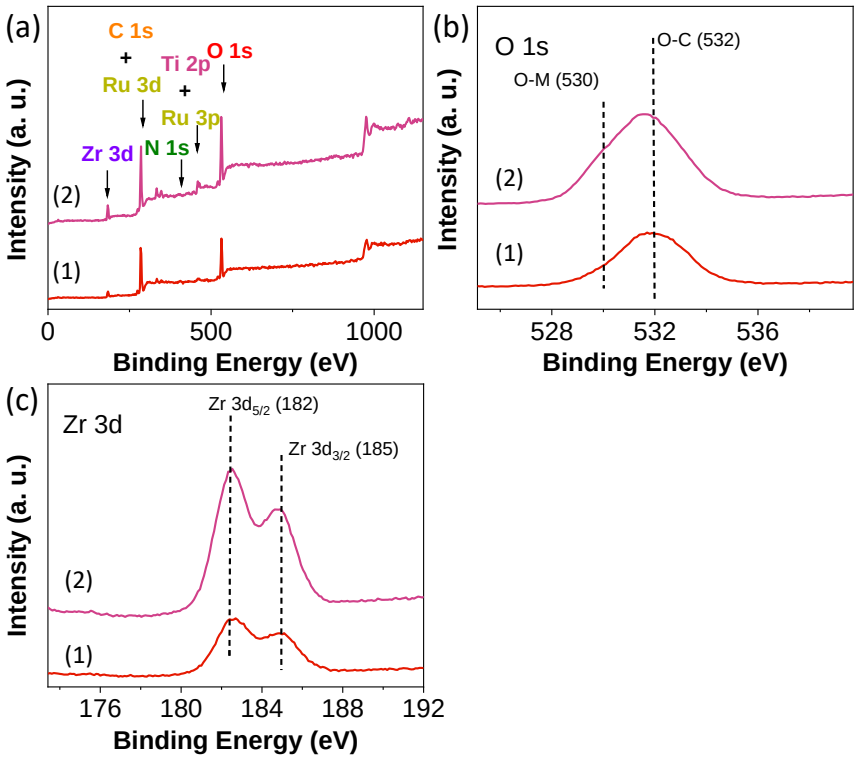

Figure S41. XPS comparison between fresh (red, below) and used (pink, up) Survey (a), O 1s (b), Zr 3d (c) RuO_x@UiO-66(Zr/Ti)-NO_2.

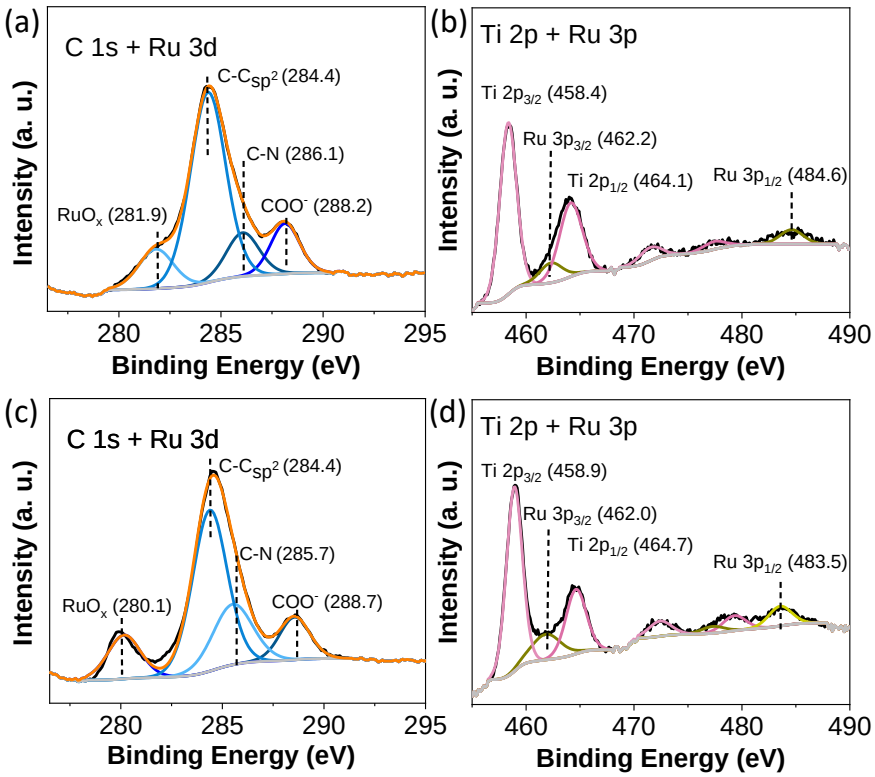

Figure S42. XPS C 1s + Ru 3d (a, c) and XPS Ti 2p + Ru 3p (b, d) of RuO_x@UiO-66(Zr/Ce/Ti) before (a, b) and after a H_2 treatment at 200 °C for 1 h (c, d)

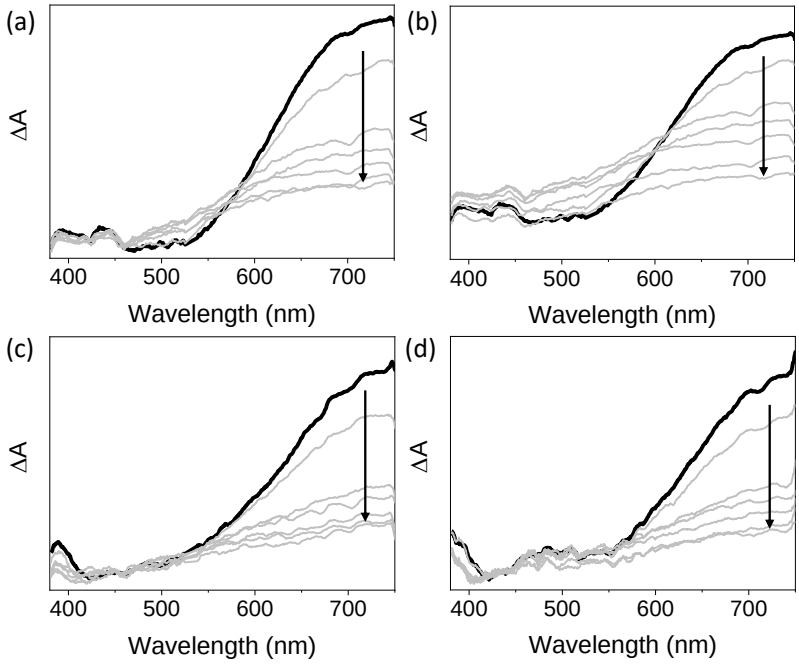

Figure S43. Femtosecond transient absorption spectra from 5 ps to 1 ns for (a) UiO-66(Zr)-NH_2, (b) UiO-66(Zr/Ti)-NH_2, (c) RuO_x@UiO-66(Zr/Ti)-NH_2 and (d) reused RuO_x@UiO-66(Zr/Ti)-NH_2 after excitation at 267 nm in MeCN.

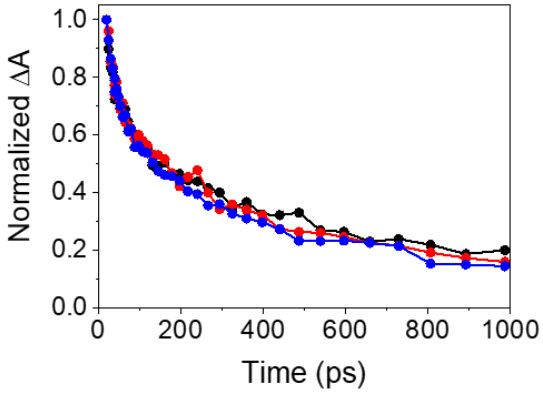

Figure S44. Femtosecond transient absorption decay traces for UiO-66(Zr)-NH_2 (black), @UiO-66(Zr/Ti)-NH_2 (red) and RuO_x@UiO-66(Zr/Ti)-NH_2 (blue) at λ_{exc} = 267 nm in aerated MeCN.

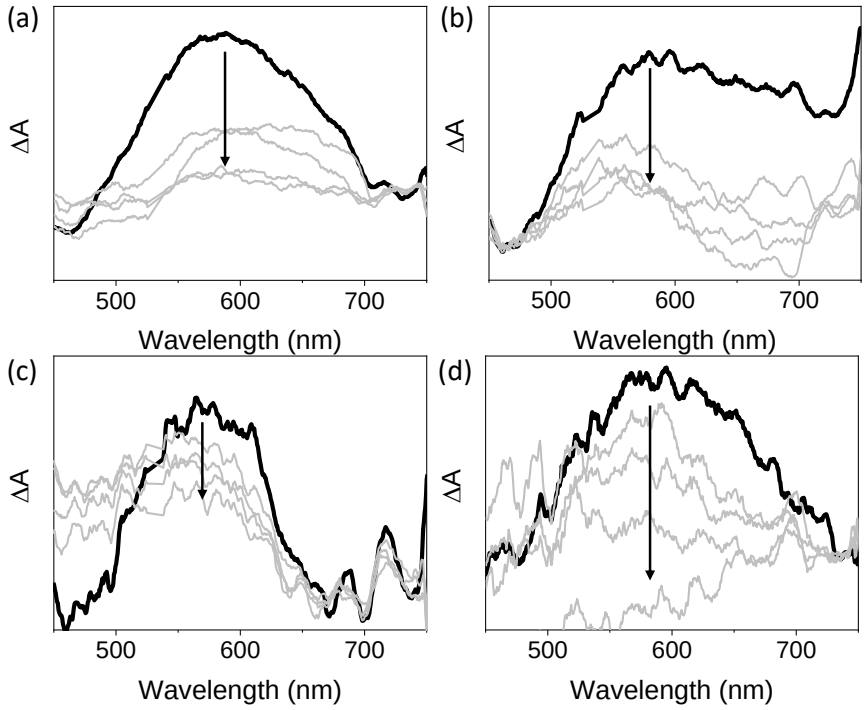

Figure S45. Femtosecond transient absorption spectra from 5 to 100 ps for (a) UiO-66(Zr)-NO_2, (b) UiO-66(Zr/Ti)-NO_2, (c) RuO_x@UiO-66(Zr/Ti)-NO_2 and (d) reused RuO_x@UiO-66(Zr/Ti)-NO_2 after excitation at 267 nm in MeCN.

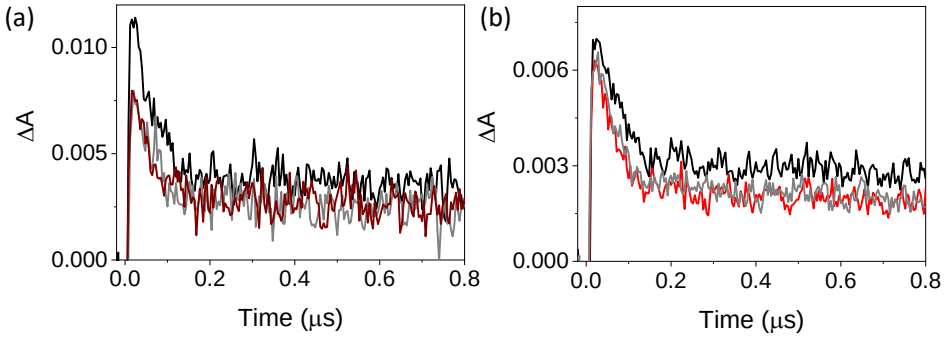

Figure S46. (a) LFP decay traces at 680 nm for UiO-66(Zr)-NO_2 (black), UiO-66(Zr/Ti)-NO_2 (gray) and RuO_x@UiO-66(Zr/Ti)-NO_2 (dark red) after excitation at 266 nm in MeCN under Ar atmosphere. (b) LFP decay traces at 520 nm for UiO-66(Zr/Ti)-NO_2 (black), RuO_x@UiO-66(Zr/Ti)-NO_2 (red) and reused RuO_x@UiO-66(Zr/Ti)-NO_2 (gray) after excitation at 266 nm in MeCN under Ar atmosphere.

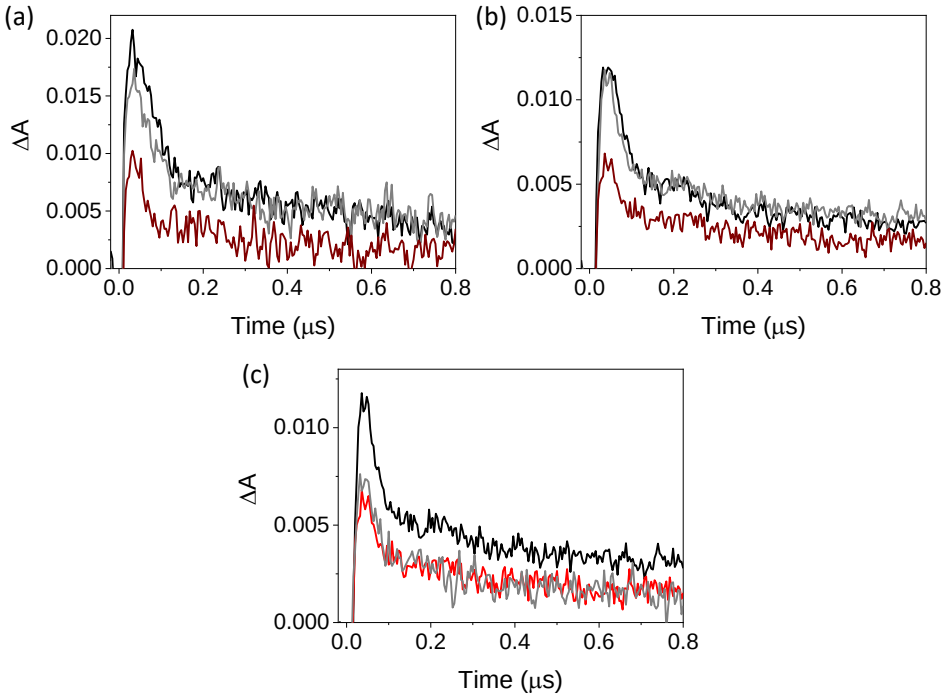

Figure S47. LFP decay traces at (a) 680 nm or (b) 520 nm for UiO-66(Zr)-NH_2 (black), UiO-66(Zr/Ti)-NH_2 (gray) and RuO_x@UiO-66(Zr/Ti)-NH_2 (dark red) after excitation at 266 nm in MeCN under Ar atmosphere, and (c) 520 nm for UiO-66(Zr/Ti)-NH_2 (black), RuO_x@UiO-66(Zr/Ti)-NH_2 (red) and reused RuO_x@UiO-66(Zr/Ti)-NH_2 (gray) after excitation at 266 nm in MeCN under Ar atmosphere.

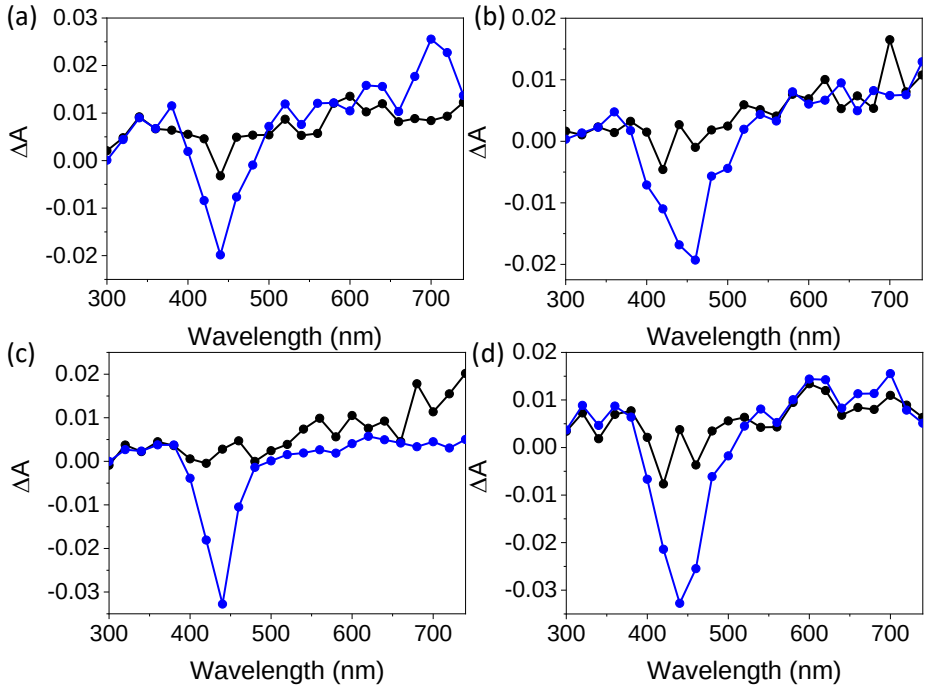

Figure S48. LFP spectra in acetonitrile (black) and in acetonitrile in the presence of 20 % CH_3OH (blue) recorded 32 ns after the laser pulse for (a) UiO-66(Zr)-NH_2, (b) UiO-66(Zr/Ti)-NH_2, (c) RuO_x@UiO-66(Zr/Ti)-NH_2 and (d) reused RuO_x@UiO-66(Zr/Ti)-NH_2. All measurements were performed in argon atmosphere at λ_{exc} = 266 nm.

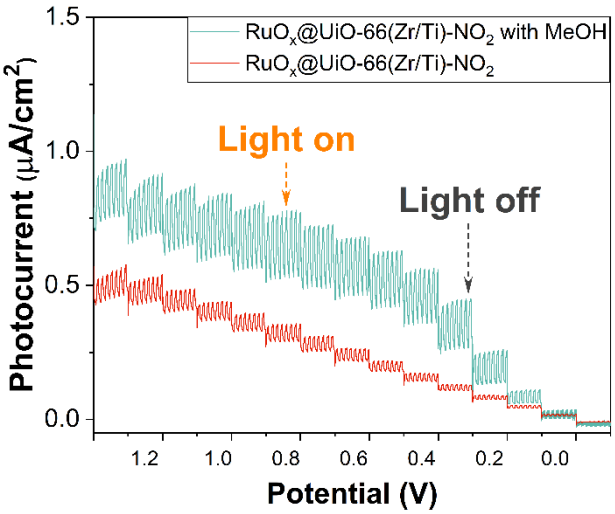

Figure S49. Current respond of RuO_x@UiO-66(Zr/Ti)-NO_2 supported on a carbon paper substrate electrode and immersed in acetonitrile (0.1 M, NBu_4PF_6) solution or in a mixture of acetonitrile and CH_3OH (0.3 mL CH_3OH) solution upon polarization from 1.3 to -0.1 V *vs.* Ag/AgCl during consecutive on/off cycles with simulated sunlight.

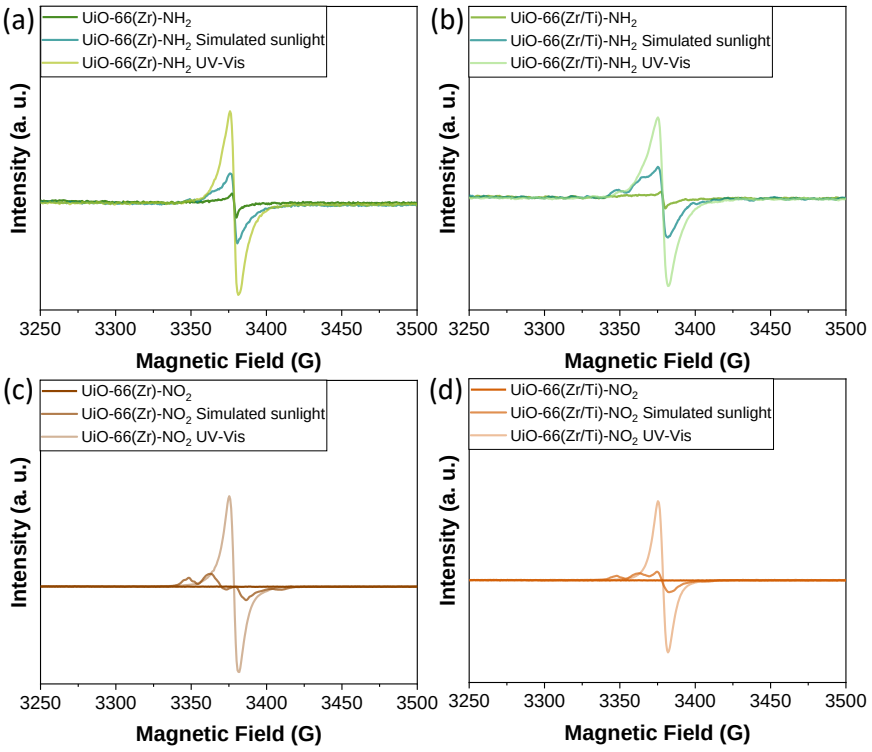

Figure S50. EPR spectra of UiO-66(Zr)-NH_2 (a), UiO-66(Zr/Ti)-NH_2 (b), UiO-66(Zr)-NO_2 (c) or UiO-66(Zr/Ti)-NO_2 (d) under dark or irradiation conditions as indicated.

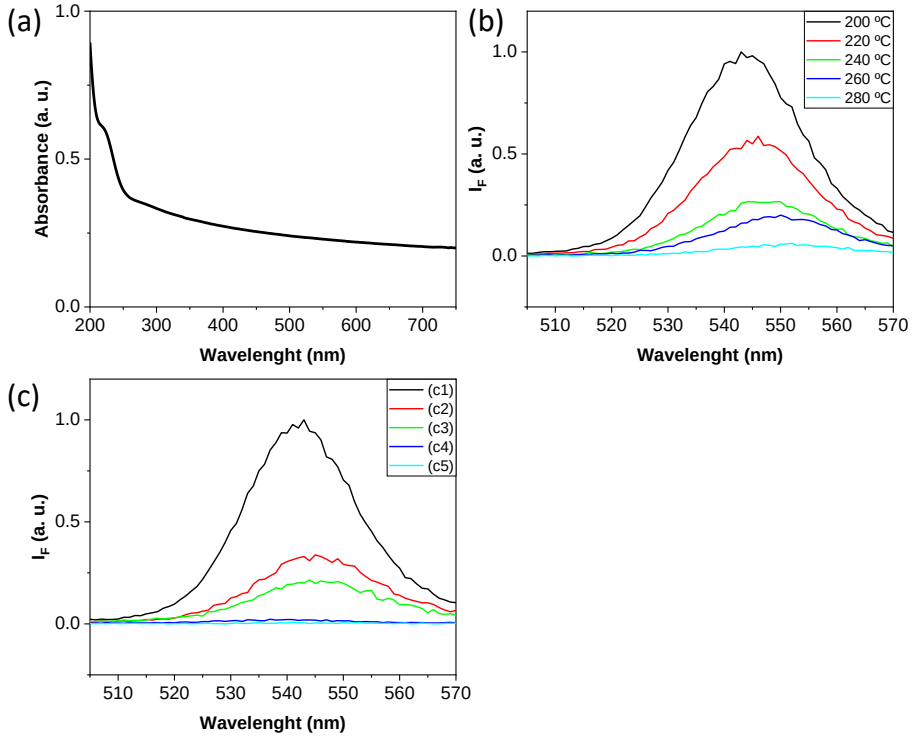

Figure S51. (a) UV-Vis spectrum of CdSe/ZnS QDs suspended in acetonitrile. (b) Photoluminescence spectra of CdSe/ZnS QDs supported on a quartz holder upon excitation at 450 nm and previously heated at different temperatures from 200 to 280 ºC as indicated. (c) Photoluminescence spectra CdSe/ZnS QDs supported on a quartz holder upon excitation at 450 nm and previously heated at 200 ºC under dark conditions (c1) or under simulated sunlight irradiation with an irradiance of (c2) 85, (c3) 140, (c4) 220, (c5) 385 mW/cm^2.

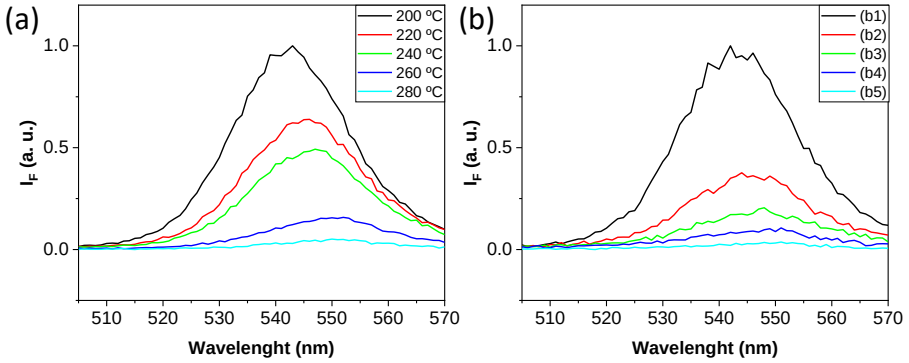

Figure S52. (a) Photoluminescence spectra of used RuO_x@UiO-66(Zr/Ti)-NO_2 supported CdSe/ZnS QDs deposited on a quartz holder upon excitation at 450 nm and previously heated at different temperatures from 200 to 280 ºC as indicated. (b) Photoluminescence spectra of used RuO_x@UiO-66(Zr/Ti)-NO_2 supported CdSe/ZnS QDs deposited on a quartz holder upon excitation at 450 nm and previously heated at 200 ºC under dark conditions (b1) or under simulated sunlight irradiation with an irradiance of (b2) 85, (b3) 140, (b4) 220, (b5) 385 mW/cm^2.

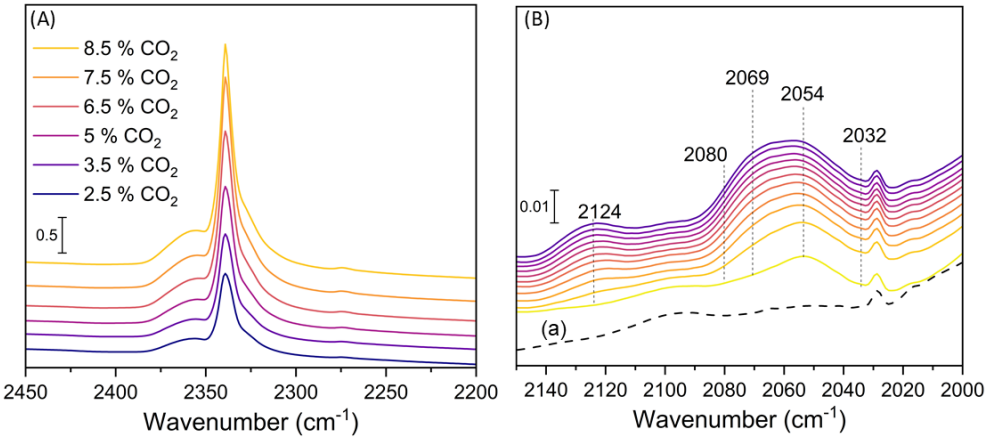

Figure S53. (a) Direct spectra of chemisorbed CO_2 over RuO_x@UiO-66(Zr/Ti)-NO_2 versus different concentrations of CO_2 in Argon and (b) the direct spectra of adsorbed CO (0.05 %) over RuO_x@UiO-66(Zr/Ti)-NO_2 versus time (1) is the reference spectrum recorded after activation under H_2 at room temperature. The assignments of the different bands are summarised in Table S3.

Table S1. Photocatalytic CO_2 methanation by H_2 using MOF-based photocatalysts reported in the literature.

Entry	**Photo catalyst**	**Co-catalyst**	**Irradiation source**	**Reaction conditions**	**CH_4 (mmol g^{-1})**	**Ref**
1	UiO-66(Zr/Ti)-NO_2	RuO_x (1 wt %)	Simulated solar light irradiation (150 W Hg-Xe lamp equipped with an AM 1.5 filter)	P(H_2)= 1.3 bar, P(CO_2)= 0.2 bar, 200°C, 22 h	5.03	This work
2	UiO-66(Zr/Ce/Ti)	RuO_x (1 wt %)	Simulated solar light irradiation (150 W Hg-Xe lamp equipped with an AM 1.5 filter)	P(H_2)= 1.05 bar, P(CO_2)=0.25 bar, 200°C, 22 h	1.80	7
3	MIL-125(Ti)-NH_2	RuO_x (1 wt %)	Simulated solar light irradiation (150 W Hg-Xe lamp equipped with an AM filter)	P(H_2)=1.05bar, P(CO_2)=0.25bar, 200°C, 22 h	0.92	6
4	MIL-125(Ti)-NH_2	RuO_x (2 wt %)	Simulated solar light irradiation (150 W Hg-Xe lamp equipped with an AM 1.5 filter)	P(H_2)=1.05 bar, P(CO_2)=0.25 bar, 200°C, 22 h	2.20	6
5	MIP-208(Ti)	RuO_x (0.76 wt %)	Simulated solar light irradiation (150 W Hg-Xe lamp equipped with an AM filter)	P(H_2)=1.05 bar, P(CO_2)=0.25 bar, 200°C, 22 h	0.79	8
6	MOF-Zn(1)	Cu_2O (1 wt %)	UV-Vis light irradiation (300 W Xe lamp)	P(H_2)=1.05 bar, P(CO_2)=0.25 bar, 215°C, 24 h	0.046	9

Table S2. Global fit analysis			
	t_1 (ps)	**t_2 (ps)**	**t_{avg} (ps)**
UiO-66(Zr)-NH_2	18	597	408
UiO-66(Zr/Ti)-NH_2	27	830	407
RuO_x@UiO-66(Zr/Ti)-NH_2	27	419	338
RuO_x@UiO-66(Zr/Ti)-NH_2 Used	15	736	353
UiO-66(Zr)-NO_2	10	896	369
UiO-66(Zr/Ti)-NO_2	11	557	358
RuO_x@UiO-66(Zr/Ti)-NO_2	99	448	309
RuO_x@UiO-66(Zr/Ti)-NO_2 Used	7	464	317

Table S3. Different vibrational modes of adsorbed CO over RuO_x@UiO-66(Zr/Ti)-NO_2 based on literature. [10, 11]

Species	Frequencies (cm^{-1})	Support	Reference
$Ru^{3+}(CO)_2$	2124, 2054, 2069	ZrO_2	[11]
$Ru^{2+}(CO)$	2079, 2032	SiO_2	[10, 11]
$Ru^{2+}(CO)_2$	2070, 2004, 1970	ZrO_2	[11]
$Ru^{\sigma+}(CO)$	1995, 1987, 1955	TiO_2	[10]
$Ru^0(CO)$	2023, 2080	SiO_2	[10]

Table S4. Vibrational modes of different adsorbed species over RuO_x@UiO-66(Zr/Ti)-NO_2 during the CO_2 methanation reaction based on literature.[12-15]

Band position with $^{12}CO_2$ (cm^{-1})	Band position with $^{13}CO_2$ (cm^{-1})	Δ (cm^{-1})	Possible Assignment	Ref.
1175	1171	4	H-CO bend. (formyl)	[12]
1172	1169	3	H-CO bend. (formyl)	[12]
1160	1056	4	Stretching (CO) of linear methoxys on Zr(IV)	[13]
1147	1144	3	rocking of methoxys	[15]
1130	1127	3	Dioxymethylene	[14]
1060	1057	3	Bridged methoxys on Zr(IV)	[13,15]

5.8.4 References

(1) Rueda-Navarro, C. M.; Cabrero-Antonino, M.; Escamilla, P.; Díez-Cabanes, V.; Fan, D.; Atienzar, P.; Ferrer B.; Vayá, I.; Maurin, G.; Baldoví, H. G.; et al. Solar-assisted photocatalytic water splitting using defective UiO-66 solids from modulated synthesis. *Nano Res.* **2024**, 17, 4134–4150

(2) Shearer, G. C.; Chavan, S.; Bordiga, S.; Svelle, S.; Olsbye, U.; Lillerud, K. P. Defect engineering: tuning the porosity and composition of the metal−organic framework UiO-66 via modulated synthesis. *Chem. Mater.* **2016**, *28*, 3749−3761.

(3) Cavka, J. H.; Jakobsen, S.; Olsbye, U.; Guillou, N.; Lamberti, C.; Bordiga, S.; Lillerud, K. A new zirconium inorganic building brick forming metal organic frameworks with exceptional stability. *J. Am. Chem. Soc.* **2008**, *130*, 13850-13851.

(4) Santiago-Portillo, A.; Navalón, S.; lvaro, M.; García, H. Generating and optimizing the catalytic activity in UiO-66 for aerobic oxidation of alkenes by post-synthetic exchange Ti atoms combined with ligand substitution. *J. Catal.* **2018**, *365*, 450-463.

(5) Sun, D.; Liu, W.; Qiu, M.; Zhang, Y.; Li, Z. Introduction of a mediator for enhancing photocatalytic performance via post-synthetic metal exchange in metal–organic frameworks (MOFs). *Chem. Commun.* **2015**, *51*, 2056-2059.

(6) Cabrero-Antonino, M.; Ferrer, B.; Baldoví, H. G.; Navalón, S. Toward solar-driven photocatalytic CO_2 methanation under continuous flow operation using benchmark MIL-125(Ti)-NH_2 supported ruthenium nanoparticles. *Chem. Eng. J.* **2022**, *445*, 136426.

(7) Cabrero-Antonino; M.Melillo, A.; Montero-Lanzuela, E.; Álvaro, M.; Ferrer, B.; Vayá, I.; Baldoví, H. G.; Navalón, S. Solar-driven gas phase photocatalytic CO_2 methanation by multimetallic UiO-66 solids decorated with RuO_x nanoparticles. *Chem. Eng. J.* **2023**, *468*, 143553.

(8) Wang, S.; Cabrero-Antonino, M.; Navalón, S.; Chen-chen Cao, C.-c.; Tissot, A.; Dovgaliuk, I.; Marrot, J.; Martineau-Corcos, C.; Yu, L.; Wang, H.; et al. A robust

titanium isophthalate metal-organic framework for visible-light photocatalytic CO_2 methanation. *Chem* **2020**, *6*, 3409-3427.

(9) Cabrero-Antonino, M.; Remiro-Buenamañana, S.; Souto, M.; García-Valdivia, A. A.; Choquesillo-Lazarte, D.; Navalón, S.; Rodríguez-Diéguez, A.; Mínguez-Espallargas, G.; García, H. Design of cost-efficient and photocatalytically active Zn-based MOFs decorated with Cu_2O nanoparticles for CO_2 methanation. *Chem. Commun.* **2019**, *55*, 10932-10935.

(10) Hadjiivanov, K.; Lavalley, J.-C.; Lamotte, J.; Maugé, F.; Saint-Just, J.; Che, M. FT-IR Study of CO Interaction with Ru/TiO2Catalysts. *J. Catal.* **1998**, *17*, 415-425.

(11) Guglielminotti, E.; Boccuzzi, F.; Manzoli, M.; Pinna, F.; Scarpa, M. Ru/ZrO2 Catalysts: I. O_2, CO, and NO Adsorption and Reactivity. *J. Catal.* **2000**, *192*, 149-157.

(12) Morgan Jr, G. A.; Sorescu, D. C.; Zubkov, T.; Yates Jr, J. T. The formation and stability of adsorbed formyl as a Possible Intermediate in Fischer− Tropsch chemistry on ruthenium. *J. Phys. Chem. B* **2004**, *108*, 3614-3624.

(13) Finocchio, E.; Daturi, M.; Binet, C.; Lavalley, J.; Blanchard, G. Thermal evolution of the adsorbed methoxy species on $Ce_xZr_{1-x}O_2$ solid solution samples: a FT-IR study. *Catal. Today* **1999**, *52*, 53-63.

(14) Schild, C.; Wokaun, A.; Baiker, A. On the mechanism of CO and CO_2 hydrogenation reactions on zirconia-supported catalysts: a diffuse reflectance FT-IR study: Part I. Identification of surface species and methanation reactions on palladium/zirconia catalysts. *J. Mol. Catal.* **1990**, *63*, 223-242.

(15) Panayotov, D. A.; Burrows, S. P.; Morris, J. R. Photooxidation mechanism of methanol on rutile TiO_2 nanoparticles. *J. Phys. Chem. C* **2012**, *116*, 6623-663

Chapter 6. Conclusions

Based on the results obtained in this thesis, it can be generally concluded that MOFs with UiO-66 topology are potential heterogeneous photocatalysts to produce solar fuels like H_2 from water or aqueous glycerol solutions as sustainable feedstocks or like CH_4 from gas-phase CO_2 hydrogenation. The conclusions of each chapter are listed below.

The zirconium-based MOF UiO-66(Zr)-NH_2 can be used as heterogeneous photocatalyst for H_2 production from aqueous glycerol solutions under simulated sunlight irradiation. The higher activity of UiO-66(Zr)-NH_2 compared to UiO-66(Zr)-X (X: H or NO_2) or MIL-125(Ti)-NH_2 associated to the adequate energy band level diagram of the former. Deposition of platinum NPs as co-catalyst within UiO-66(Zr)-NH_2 enhances its photocatalytic activity and produced 2.3 mmol g^{-1} H_2 in 3 h. This photocatalyst retained its structural integrity after its use for 70 h, as revealed by PXRD and TEM measurements. Furthermore, it was proposed that the presence of Pt NPs within UiO-66(Zr)-NH_2 favours the operation of this photocatalyst under a photoinduced charge separation mechanism based on the characterization TA and PL spectroscopies together with photocurrent measurements.

UiO-66(Zr)-NH_2 and UiO-66(Zr)-NO_2 defective MOFs prepared by modulated synthesis using AA or TFA exhibit higher photocatalytic activities for HER or OWS under simulated sunlight irradiation. The highest activities were obtained with UiO-66(Zr)-X (X: NH_2 or NO_2) solids prepared using 12 AA equivalents. A volcano-trend relationship was found between the number of defects and the photocatalytic HER. Besides, the most active UiO-66(Zr)-NH_2-12AA sample achieved an estimated AQYs for the

photocatalytic OWS upon irradiations at 350, 400 and 450 nm of 0.13, 0.06 and 0.04 %, respectively. The photocatalytic activity of UiO-66(Zr)-NH_2-12AA can be enhanced by the deposition of Pt NPs (1 wt%) as a co-catalyst. The observed order of photocatalytic activity was correlated with the inherent photoinduced charge separation efficiency of the solids based on EIS, PL and LPF measurements. DFT calculations confirmed that the thermodynamics of both HER and OER processes are favoured when using defective UiO - 66(Zr) - NH_2 samples prepared with AA or TFA modulators respect to non-modulated ones.

A series of multifunctional and photocatalytically active UiO-66 solids supported by RuO_x NPs were developed for gas-phase CO_2 hydrogenation to CH_4 under simulated concentrated sunlight irradiation. Unlike most reports highlighting the photocatalytic activity of UiO-66(Zr)-NH_2 prepared using the 2-aminoterephthalate ligand, this study shows the importance of using UiO- 66(Zr)-NO_2 prepared with 2-nitroterephthalate ligands to further increase the resulting activity. This concept was also validated for analogous and even more active mixed-metal Zr(IV)/Ti(IV) solids compared to Zr(IV)-based ones. RuO_x@UiO-66(Zr/Ti)-NO_2 was found to be a reusable photocatalyst that exhibited record activity (5.03 mmol g^{-1} after 22 hours) compared to others MOF-based photocatalysts. Based on the results of several spectroscopic, electrochemical and photocatalytic experiments, it is proposed that RuO_x@UiO-66(Zr/Ti)-NO_2 operates in a dual photochemical and photothermal reaction pathway.

Chapter 7. Abstract

Abstract

This PhD thesis has investigated the development of heterogeneous MOF- type photocatalysts with UiO-66 and MIL-125 topology to obtain solar fuels from water and CO_2. Initially, the introduction has reviewed the current state of the art on the use of fossil fuels, renewable energies and solar fuels as energy carriers. In this section, emphasis has been placed on photocatalysis processes based on inorganic semiconductors and MOFs to obtain solar fuels. The results of the thesis indicate that the MOF-type material UiO-66(Zr)-NH_2 is a more efficient photocatalyst than the analogues UiO-66(Zr)-X (X: H or NO_2) or the titanium MOF MIL-125(Ti)-NH_2 for obtaining H_2 from the mixtures of water and glycerol. On the other hand, the possibility of developing UiO-66(Zr)-X (X: NH_2 or NO_2) materials with structural defects introduced with AA or TFA as modulators and presenting enhanced photocatalytic activities and photoinduced charge separation efficiencies for the generation of H_2 from water and/or CH_3OH mixtures has been demonstrated. This thesis has also demonstrated the importance of the 2-nitroterephthalate ligand in the preparation of mono- or bimetallic Zr(IV) and Zr(IV)/Ti(IV) active photocatalysts with UiO-66 topology with respect to the analogues prepared with the 2-aminoterephthalate ligand. The RuO_x@UiO-66(Zr/Ti)-NO_2 material showed the highest activity compared to RuO_x@UiO-66(Zr/Ti)-NO_2 material, for the gas-phase hydrogenation reaction of CO_2 to CH_4 and it was proposed that it operates under a dual photochemical and photothermal mechanism.

Resum

La present tesi doctoral ha investigat el desenvolupament de fotocatalitzadors heterogenis tipus MOF amb topologia UiO-66 i MIL-125 per a l'obtenció de combustibles solars a partir de l'aigua i del CO_2. Inicialment, en la introducció s'ha revisat l'estat de l'art actual sobre l'ús de combustibles fòssils, les energies renovables i els combustibles solars com a vectors energètics. En esta secció s'ha emfatitzat sobre els processos de fotocatàlisis basats en semiconductors inorgànics i MOFs per a obtindre combustibles solars. Els resultats de la tesi indiquen que el material UiO-66(Zr)-NH_2 és un fotocatalizador més eficient que els anàlegs UiO- 66(Zr)- X (X: H o NO_2) o que el referent de MOF de titani MIL-125(Ti)-NH_2 per a l'obtenció d'hidrogen a partir de mescles d'aigua i glicerol. D'altra banda, s'ha demostrat la possibilitat de desenvolupar materials UiO-66(Zr)-X (X: NH_2 o NO_2) amb defectes estructurals introduïts amb àcid acètic o trifluoroacètic com a moduladors i que presenten activitats fotocatalítics i eficiències de separació de càrrega fotoinducida millorades per a la generació d'hidrogen a partir de mescles d'aigua i/o metanol. En esta tesi també s'ha demostrat la importància del lligant 2- nitrotereftalat en la preparació de fotocatalitzadors actius mono- o bimetàl·lics de Zr(IV) i Zr(IV)/Ti(IV) amb topologia UiO-66 respecte als anàlegs preparats amb el lligant 2-aminoteftalat. El material RuO_x@UiO-66(Zr/Ti)-NO_2 va mostrar la màxima activitat fotocatalítica per a la reacció d'hidrogenació en fase gas de CO_2 a CH_4 i es va proposar que opera per un mecanisme dual fotoquímic i fototérmic.

Resumen

La presente Tesis Doctoral ha investigado el desarrollo de fotocatalizadores heterogéneos tipo MOF con topología UiO-66 y MIL-125 para la obtención de combustibles solares a partir del agua y del CO_2. Inicialmente, en la introducción se ha revisado el estado del arte actual sobre el empleo de combustibles fósiles, las energías renovables y los combustibles solares como vectores energéticos. En esta sección se ha enfatizado sobre los procesos de fotocatálisis basados en semiconductores inorgánicos y MOFs para obtener combustibles solares. Los resultados de la Tesis indican que el material tipo MOF UiO-66(Zr)-NH_2 es un fotocatalizador más eficiente que sus análogos UiO- 66(Zr)-X (X: H o NO_2) o que el MOF de referencia de titanio MIL-125(Ti)-NH_2 para la obtención de hidrógeno a partir de la mezcla de agua y glicerol. Por otro lado, se ha demostrado la posibilidad de desarrollar materiales UiO- 66(Zr)-X (X: NH_2 o NO_2) con defectos estructurales introducidos con ácido acético o trifluoroacético como moduladores y que presentan actividades fotocatalíticias y eficiencias de separación de carga fotoinducida mejoradas para la generación de hidrógeno a partir de mezclas de agua y/o metanol. En esta Tesis también se ha demostrado la importancia del ligando 2- nitrotereftalato en la preparación de fotocatalizadores activos mono- o bimetálicos de Zr(IV) y Zr(IV)/Ti(IV) con topología UiO-66 respecto a los análogos preparados con el ligando 2-aminoteftalato. El material RuO_x@UiO- 66(Zr/Ti)-NO_2 mostró la máxima actividad fotocatalítica para la reacción de hidrogenación en fase gas de CO_2 a CH_4 y se propuso que opera bajo un mecanismo dual fotoquímico y fototérmico.

Annexure

I Journal publications

I.I Published articles

1. Celia M. Rueda-Navarro, Zahraa Abou Khalil, Arianna Melillo, Belén Ferrer, Raúl Montero, Asier Longarte, Marco Daturi, Ignacio Vayá, Mohamad El-Roz, Virginia Martínez-Martínez, Herme G. Baldoví, Sergio Navalón. **solar gas-phase CO_2 hydrogenation by multifunctional UiO-66 photocatalysts.** ***ACS Catalysis 2024, vol. 14, p. 6470-6487.***

2. Celia M. Rueda-Navarro, María Cabrero-Antonino, Paula Escamilla, Valentín Díez-Cabanes, Dong Fan, Pedro Atienzar, Belén Ferrer, Ignacio Vayá; Guillaume Maurin, Herme G. Baldoví, Sergio Navalón. **Solar-assisted photocatalytic water splitting using defective UiO-66 solids from modulated synthesis.** ***Nano Research 2024, vol. 17, no 5, p. 4134-4150.***

3. Celia M. Rueda-Navarro, Belén Ferrer, Herme G. Baldoví, Sergio Navalón. **Photocatalytic hydrogen production from glycerol aqueous solutions as sustainable feedstocks using Zr-based UiO-66 materials under simulated sunlight irradiation.** ***Nanomaterials 2022, vol. 12, no 21, p. 3808.***

4. Celia M. Rueda-Navarro; Marta González-Fernández; María Cabrero-Antonino; Amarajothi Dhakshinamoorthy; Belén Ferrer; Herme G. Baldoví, Sergio Navalón. **Solar-assisted CO_2 methanation via photocatalytic**

Sabatier reaction by calcined titanium-based organic framework supported RuO_x nanoparticles. *ChemCatChem* 2024, e202400991.

I.II Submitted articles or under preparation

1. Bingbing Chen, Asma Mansouri, Celia M. Rueda-Navarro, Iurii Dovgaliuk, Philippe Boullay, Gilles Patriarche, Beibei Xiao, Dong Fan, Arianna Melillo, Guillaume Maurin, Sergio Navalón, Hermenegildo Garcia, Georges Mouchaham, Christian Serre. **A novel Ti12-based metal-organic framework for photocatalytic hydrogen evolution** (preprint).

II Participation in conferences

- **29th PhotoIUPAC Symposium on Photochemistry.** 2024, Valencia (Spain).

Poster contribution: Metal-organic frameworks as photocatalysts for hydrogen generation from glycerol aqueous solutions under simulated sunlight irradiation. Celia M. Rueda-Navarro, Belén Ferrer, Herme G. Baldoví, Sergio Navalón.

Oral Communication: Solar-driven photocatalytic water splitting and CO_2 reduction using metal-organic frameworks. Sergio Navalón, Celia M. Rueda-Navarro, Eva Montero-Lanzuela, Amarajothi Dhakshinamoorthy, Herme G. Baldoví.

- **International Symposium SPECTROCAT.** 2024, Caen (France).

Attendance without contribution.

- **XXXIX Reunión Bienal de la Real Sociedad Española de Química.** 2023, Zaragoza, España.

Poster contribution: Photocatalytic Hydrogen Production from Glycerol Aqueous Solutions as Sustainable Feedstocks Using Zr-Based UiO-66 Materials under Simulated Sunlight Irradiation. Celia M. Rueda-Navarro, Belén Ferrer, Herme G. Baldoví, Sergio Navalón.

- **Solar2Chem Winter School. Materials and Methods for Solar Chemical Production.** 2023, Valencia, España.

Poster contribution: Photocatalytic Hydrogen Production from Glycerol Aqueous Solutions as Sustainable Feedstocks Using Zr-Based UiO-66 Materials under Simulated Sunlight Irradiation. Celia M. Rueda-Navarro, Belén Ferrer, Herme G. Baldoví, Sergio Navalón.

- **International Solar Fuels Conference.** 2021, online.

Poster contribution: Photoactive Zr and Ti metal-organic-frameworks for solid-state solar cells. Arianna Melillo, Celia M. Rueda-Navarro, Herme G. Baldoví, Sergio Navalón, Belén Ferrer.

- **E-MRS Fall Meeting.** 2021, online.

Oral Communication: Bifunctional metal-organic frameworks for the hydrogenation of nitrophenol using methanol as the hydrogen source. Celia M. Rueda-Navarro, Arianna Melillo, Cristina Vallés-García, Belén Ferrer, Herme G. Baldoví, Sergio Navalón.

III Research stay

Three months as a visiting PhD in "Laboratoire Catalyse et Spectrochime" placed in the "Université de Caen Normandie", Caen (France) under the supervision of Dr. Mohamad El-Roz and Professor Marco Daturi.

Study of the hydrogenation of CO_2 through IR *operando* using MOF with topology MIL-101(Cr) and MIL-100(X), where X: Cr, Fe, Al, In, Sc.